Developmental Biomechanics Through Image Analysis : The Dynamics of Pulsatile Actomyosin During Drosophila Dorsal Closure

Nilankur Dutta

Université Grenoble Alpes

THÈSE

Pour obtenir le grade de

DOCTEUR DE LA COMMUNAUTE UNIVERSITE GRENOBLE ALPES

Spécialité : **2MGE : Matériaux, Mécanique, Génie civil, Electrochimie**

Arrêté ministériel : 25 mai 2016

Présentée par

Nilankur DUTTA

Thèse dirigée par **Jocelyn ETIENNE**, CNRS et

Guy Blanchard, Université de Cambridge et

Pierre RECHO, CNRS

préparée au sein du **Laboratoire Interdisciplinaire de Physique** dans **l'École Doctorale I-MEP2 - Ingénierie - Matériaux, Mécanique, Environnement, Energétique, Procédés, Production**

Biomécanique du développement par l'analyse d'images : La dynamique de l'actomyosine pulsatile pendant la fermeture dorsale de la *Drosophile*

Developmental Biomechanics Through Image Analysis: The Dynamics of Pulsatile Actomyosin During *Drosophila* Dorsal Closure

Thèse soutenue publiquement le **21 novembre 2019**,
devant le jury composé de :

Monsieur **JOCELYN ETIENNE**
CHARGE DE RECHERCHE, CNRS DELEGATION ALPES, Directeur de thèse
Monsieur **FRANÇOIS GALLET**
PROFESSEUR DES UNIVERSITES, UNIVERSITE PARIS 7, Rapporteur
Monsieur **FRANÇOIS NEDELEC**
PROFESSEUR, UNIVERSITE DE CAMBRIDGE - ROYAUME-UNI, Rapporteur
Madame **MARIA LEDESMA**
PROFESSEUR ASSOCIE, UNIV. POLYTECHNIQUE DE MADRID - ESPAGNE, Examinateur
Monsieur **JACQUES OHAYON**
PROFESSEUR DES UNIVERSITES, UNIVERSITE SAVOIE, Président

Developmental Biomechanics Through Image Analysis

The Dynamics of Pulsatile Actomyosin During Drosophila Dorsal Closure

Nilankur Dutta

Acknowledgements

I would like to acknowledge my parents, Sikha and Nihar Kumar Dutta, who provided most of the genetic material required for this thesis, and my sister Upali Dutta, for ensuring its use in science.

I owe a debt of gratitude to my supervisors, Dr. Jocelyn Etienne, Université Grenoble-Alpes and Dr. Guy Blanchard, Cambridge University, who introduced me to developmental bio-mechanics with wisdom, enthusiasm, and patience. To the experimentalists, Dr. Nicole Gorfinkiel and Dr. Julia Duque at the Universidad-Europea, Madrid, without whom this work would not have been possible.

To my friends, fellow thesards and post-doctorants, Adel, Brenna, Heather, Thomas, Katharina, Erik and Saranath, for valuable scientific discussions and frivolity. This work was completed despite their ardent efforts to keep me in the bar. To Esther, who supported me through the most stressful parts of the thesis.

To the good people at sci-hub and stack overflow, for making science open and accessible, and having the answers to (almost) all questions.

Finally, to the 13 *Drosophila* embryo who provided the rest of the genetic material for this work, and who were excellent flies.

Contents

Introduction and Literature

0.1 Mechanics in Development

Over the last 50 years, mechanics has emerged as a necessary discipline to understand embryogenesis, complementing genetic signalling [36]. The effect of mechanical forces in tissue development and determination of cell fate has been demonstrated from the compaction of the morula [14] [27], to gastrulation [56], to organogenesis. In all cases, one finds that cells are able respond to forces and mechanical cues, similar to how they can sense chemical gradients [46].

However, since the effect of physical structures cannot be turned off in the same way that individual genes can be mutated, the role of mechanics is generally studied through perturbations: either molecular - by inhibiting or over-expressing certain molecules, or mechanical - by imparting various mechanical forces and studying their proximal effects [46]. A third way, that couples the first two approaches, is the inference of forces through the known effect of certain molecular interactions, for example tissue shape change through the force transmitting effect of actomyosin [56].

The *Drosophila melanogaster* has become a model organism to study mechanics in development, with exhaustive experimental studies and computational predictions showing the mechanical control of cell shape, tissue patterns and morphogenesis [28] [34] in various developmental contexts such as ventral furrow formation [57] [8], germ band extension [9] and germ band retraction [39]. Mechanical tensions generated in the cell cytoskeleton, manifested through cell-cell or cell-extra cellular matrix interactions, have been shown to produce global effects on the developmental process [53]. More specifically, in recent years, the actin cortex has attracted increasing attention as a key regulator of cell mechanics and shape changes [60].

Let us now examine a specific biological system in *Drosophila*, that of dorsal closure, to further elucidate the role of the various mechanical forces acting in concert during morphogenesis.

0.2 Dorsal Closure in *Drosophila*

Dorsal closure (DC) is a late morphogenetic process in *Drosophila* embryogenesis, first described in the 1990's [70]. This process has been studied extensively due to its similarities with other constricting tissues in vertebrates, and to wound healing.

Dorsal closure involves the closing of an epidermal gap in the embryo, by the contraction of the amnioserosa, the extra-embryonic tissue covering the gap. As dorsal closure continues, cells delaminate from the amnioserosa, but there are no cell intercalations, migrations or divisions. This simplicity makes it an ideal system to study pulsatile cellular contractions.

During this process, the area of the amnioserosa shrinks at the time scale of 10s to minutes [22] [23]. Dorsal closure literature describes its progression in three phases, early, slow and fast, starting 45 minutes after germband retraction, and lasting up to 2+ hours after this [4].

It has been shown that amnioserosa (AS) cell areas fluctuate at a time scale of a few minutes, and that they contract more along the dorso-ventral (DV) axis than the anterior-posterior (AP) axis [22]. Dorsal closure is also characterised by the appearance of a supra-cellular actin cable in the late phase at the interface of the amnioserosa and the epidermis [64] [26]. It also has been shown that as the *Drosophila* embryo progresses through dorsal closure, the amnioserosa increases in stiffness, and the contractile strain rate increases [18] [40]. Dorsal closure is characterised by an attenuation in the amplitude of apical area oscillations of single cells, and an increase in the average dominant oscillation frequency over time [41].

There are several forces that have been shown to act concurrently, contributing to the process of dorsal closure, being :

- A tension arising from a supracellular actin cable, which appears during late dorsal closure. This cable brings the two edges of the epidermis together, applying a tension tangentially along the lateral edges of the amnioserosa, zippering it like a 'purse-string'. It is also thought to dampen the fluctuation of cells, preventing their expansion [16] [4].
- The contraction of the AS tissue which can be further considered to have three contributions [13],
  - a contracting active force due to Myosin activity, [32]
  - a sporadic force due to cell delaminations, which increases as the process continues [32] [59],
  - and the cellular pressure that opposes these two forces.
- The tension generated by the epidermis, that acts normally along the lateral edges of the AS.

In this work, we are concerned mainly with the contractile Myosin activity on the actin cortex, which is observed as pulses of Myosin II mini-filaments on the cell apical surface, known as Myosin foci. Such kind of activity manifests itself in a variety of biological systems in development, across organisms, which are presented in the following section.

In DC, observations show that Myosin is concentrated in two areas at the subcellular scale, in a cortical ring and in the apico-medial surface of the cell: these are called the junctional and the medial Myosin populations, respectively. Cell shape fluctuations have been shown to be driven by medial Myosin foci [4], while the function of the junctional population, which is relatively low in fluorescence intensity, is yet unknown (although it has been posited that it has an increasing effect as DC progresses [65]).

Previous work quantifying fluorescence intensity of foci in the AS show that fluorescence gain is faster than fluorescence loss, suggesting differences in the mechanism of focus assembly and disassembly. Average apico-medial Myosin fluorescence intensity is inversely correlated with cell radius. The peak in Myosin fluorescence intensity precedes the trough of cell radius (the subcellular nature of the fluctuations is demonstrated by simultaneous expansion and contraction at opposite ends of a cell, and where the greatest extent of Myosin fluorescence occurs mid-wave) [4].

Several studies have been performed attempting to model the forces causing DC, and these works can be divided under two main headings, those that model the closure through the activity of the whole AS tissue, and those that model the closure through the collective activity of individual cells.

Whole AS Modelling of Dorsal Closure

The first modelling attempts of the amnioserosa tissue during dorsal closure [26] were based on the imbalance of the forces described above creating the closure dynamics.

In general, these considered ad-hoc zipping rates [33] or constant forces [2] for the actin cable. They were limited to two dimensions and did not consider the temporal evolution of forces. More recently other works [59] have included the three dimensional shape of the tissue, and time varying forces, the geometry of the closure being approximated by two symmetrical circular arcs. These models have generally treated the tissue as a continuous homogeneous material, and did not consider the geometry of individual cells.

Individual Cell Modelling

Other works considered the shape fluctuations of individual cells in the AS as a basis of their biophysical model. In these models the contractile force is generated actively in the cells by Myosin-II, which acts on an elastic substrate. The pulsatile nature of these fluctuations is derived either from making the contractile force stretch dependent [64] [29], or by the turnover and the binding and unbinding dynamics of the motors [68] [15].

In this work, we will follow the approach of looking at experimental data of individual cells to investigate pulsatile actomyosin.

0.3 Morphogenetic Events Involving Pulsatile Actomyosin

Though we use dorsal closure as our model biological system to investigate pulsatile actomyosin, such activity is seen across organisms in various developmental contexts. Some examples of actomyosin driven cell shape changes can be found in the following biological systems (reviewed in [21]):

- Mesoderm invagination on the ventral side of the *Drosophila* embryo, lasting 5 minutes during early embryogenesis
- Germband extension in *Drosophila*, a mid stage embryogenetic event in which the germband extends around the posterior of the embryo, lasting 2 hours
- Basal cells of *Drosophila* follicular epithelium, which enlarge 1.7 fold in 2 hours
- Convergence and extension movements of the ectoderm and mesoderm cells of the *Xenopus* embryo
- Cortical flow in early *Caenorhabditis elegans* embryo [50]
- Elongation and neural tube closure in vertebrate embryo [71]

In all of the cases mentioned in the previous section, phenomena of assembly and disassembly of Myosin into periodic subcellular 'foci' are found. It is observed that the time-period of these focus fluctuations are similar across organisms, between 1 and 5 minutes.

0.4 Biochemical and Mechanical Bases for Apical Myosin Focal Pulsation

Actomyosin dependent contractile forces are essential to the process of dorsal closure, and disruption of amnioserosa contractility leads to a failure in dorsal closure and to a dorsal open phenotype [61] [10].

Medial actomyosin oscillatory activity is controlled biochemically by Myosin phosphorylation on its regulatory light chain, so that the motors can assemble into bipolar Myosin mini-filaments, which can produce contraction. Myosin phosphorylation, in turn, is regulated by Myosin kinases (Rok) and Myosin phosphatases [49]. It has been shown in amnioserosa cells *in vivo* with a Rok inhibitor, Myosin focus oscillations are greatly attenuated [17].

It is observed that in both *Drosophila* epidermal cells [17] and the amnioserosa [49], both Rok and Mbs (Myosin binding subunit) of Drosophila, MLCK (Myosin light chain phosphatase) colocalize with medio-apical Myosin foci. It has also been shown that Rho1/A, which regulates Rok and Mbs, also displays pulsatile dynamics [58] [49].

Further upstream, the activity of Rho1/A has been shown to be upregulated by RhoGEF, with oscillatory behaviour of its own [45], and downregulated by RhoGAPs [58].

Though the biochemical Rho1/A oscillator is found sufficient in many cases to create and sustain focal pulsation, mechanical feedback is also asssumed to contribute to this. For example, during the actomyosin initiated posterior mid-gut invagination in *Drosophila*, it is seen that Myosin activation may be rescued in Snail mutant embryos (Snail is a transcriptional repressor that restricts neural fate in the invaginating mesoderm) by the application of tissue tension [48]. It is also observed that the rate of Myosin focus nucleation and their life-times are both reduced when targeting the linking protein, α-catenin [31], which is responsible for connecting the actin cortex to the adherens junctions at the cell membranes.

Finally, Ca^{2+} ions are known to increase actomyosin activity, and thus contractile forces during dorsal closure, suggesting that mechanically gated ion channels have a role in coordinating cell shape fluctuations during this process [25].

0.4.1 Physical and Biochemical Models for Pulsatility

Different models have described the origin of Myosin focal pulsations in different ways, but they can be broadly classified as ones with biochemical origin and ones with mechanical origin, and ones that involve a mixture of both. We briefly present three such complementary models:

- Rho1/A oscillator: Some authors have attributed the origin of pulsatility to a RhoA pacemaker [51] (in the *C. elegans* zygote). Interestingly these authors have also reported that speed of Myosin foci takes a pulsatile pattern with a period of about 50 seconds and amplitudes between 0.1 and 0.5 $\mu m/s$. In the same organism, other authors [58] have cited the accumulation of F-actin dependent protein RGA-3/4 providing the necessary negative feedback to RhoA pulsatility.

- MLCP regulated oscillations: In *Drosophila* follicular cells, it has been shown [67] that Myosin Light Chain Phosphatase subunit *flapwing (flw)* is the regulator of basal Myosin oscillations and cell contractions. These authors also note that actin oscillates in the same way as Myosin in this system. This work cites cooperative actin bundling as the reason of focus assembly, and the disassociation of actin fibres due to Myosin induced tension as the reason for focus disassembly.

- Rho1/A oscillator as an emergent property: Instead of a hard-coded oscillator [51], certain works [49] suggest that in the *Drosophila* germband extension, Rho, ROK, Mbs pulsatility instead is dependent on Myosin-II activity, arising as an effect of biomechanical feedback between Myosin advection and dissociation rates. In this work, focus disassembly is modelled by the breakdown of actin network at high actin concentrations. In this model, the pulsatility is generated through an interplay of mechanics and biochemistry.

0.5 Dynamics of Myosin Foci

Though a lot has been said about the temporal properties and pulsatility of Myosin foci, their spatial properties are less well known. In this section we outline the spatial factors important to the force generating apparatus of foci, and what is known of their kinetics, a theme that will absorb us for the rest of this work.

0.5.1 Forces due to Myosin Foci

Myosin-II foci impart a contractile 'pre-stress' by deforming the actin substrate locally. To transmit this at the scale of the tissue, three factors are important [3]

- Properties of actin substrate : the actin substrate is a polarized and dynamic network that turns over continuously (with a half-life of 50 seconds in the *Drosophila* germband, for instance). To transmit the local, focal stress at the cell scale, it has to be connected to the cell membrane. Slippage between the actin cortex and cell-membrane has been shown in *C. elegans* and the *Drosophila* mesoderm [1]. The mechanism has been described as a sort of 'clutch', which, when engaged, transfers the focal pre-stress into effective cell deformation, and when disengaged, contracts the cortex without cell shape change[49].

- Adhesion complexes to connect actin between cells : To transfer stress at the tissue scale the cell membranes have to be connected effectively amongst themselves by adhesion complexes. Laser ablation studies have shown that Myosin foci are connected to cell membranes [55], and that targeting adhesion reduces focus' ability to cause cell deformation [31]. It has also been implied that there are mechanical communications between neighbouring cells, by induced focal activity [69]

- Tissue boundary conditions : Finally, generating cell deformations is dependant on tissue stiffness. Myosin pre-stress acts either to build up tissue stress in stiff tissues, or to create deformations, in compliant tissues. It has been shown in the *Drosophila* ventral furrow, that by reducing tension along a particular axis of tissue by performing laser incisions, the organisation of the actomyosin meshwork could be made more isotropic [11], changing the directionality of the pre-stress.

In addition to regulating force or stress production, actomyosin is responsible for establishing the mechanical properties of the embryo that resist stress and guide tissue deformation. For instance, actomyosin controls much of the viscoelastic properties of *Xenopus* during gastrulation and neuralization as dorsal axial tissues converge and extend [47].

0.5.2 Flow of Myosin Foci

In many of the systems described in section 0.3, flow of Myosin foci across cell surfaces is observed. Where flow is seen, during germband extension and dorsal closure in *Drosophila* as well as in *Xenopus* and *C elegans*, one finds that flow rates are strikingly similar across organisms, between 0.5 and 1.5 $\mu m/s$ [21].

It has been suggested [21] that where cells are planar polarised due to the localisation of junctional proteins like E-Cadherin, (*Drosophila* germband), focus flow follows the cell polarity [64], which is perpendicular to the arrangement of actin bundles in the cell. In the biological system concerned in this work, the amnioserosa, the cells are not polarized due to junctional proteins, but do experience anisotropic stress (greatest along the Anterio-Posterior axis) [40] [44]. Similar phenomenon is observed in the *Drosophila* mesoderm. It has been suggested that in these systems [21], the tension biases the recruitment of actin in a direction parallel to it, and focus flow occurs perpendicular to it. An alternative explanation is that the tension results in anisotropy in cell shapes [44], with the long axis oriented perpendicular to maximal tension, and focus flow follows the long axis of the cell [22].

Biophysical modelling suggests various modes of motion such as advection via contraction of actin substrate [49], or diffusion due to disassociation from actin [67], but the kinetics of these foci are poorly understood. This will be the central theme of this work.

0.6 A Working Hypothesis for Focus Kinetics

Observing the kinetics of Myosin signal we can make hypothesis on plausible biochemical or mechanical causes.

If we consider a random cell in the amnioserosa over its life-time, we begin by observing, at some specific time, an increase in the average apical Myosin signal. This diffuse cell-wide signal is then concentrated into one or more foci at specific subcellular regions. The available biochemical mechanism that can explain this is a high local rate of recruitment of Myosin into foci, due to high concentration of Myosin upregulating species (Rho, ROK) at that region, or low concentration of Myosin downregulating species (Mbs) at the region. Since it is known that ROK diffuses from the cell membranes, this concentration phase is likely to be accompanied by high rates of focus formation close to membranes, and lower rates further away.

Alternatively, one can explain this concentrating phase by a mechanical hypothesis, the contractile activity of Myosin foci. A focus contracts the actin meshwork, bringing the actomyosin closer together. Myosin foci may also be associated with actin foci that assemble on top of a pre-existing actin web [67]. In such a case, using the deformation of the cell membranes as a proxy for the flow of the substrate (under a fully engaged clutch), one would expect focus formation to be simultaneous with maximum cell deformation. It is likely that both these effects play a role in focus formation, combined in a yet unknown proportion.

After concentration, we observe foci travelling on the apical surface. This can be due to the imbalance of strain rates in the front and at back of foci. In such a case, due to its connection with the cell membranes, Myosin could be pulled to one direction with the actin network that it rests on. One could again examine the deformation of membranes, and one would hope to see a difference in deformations to the front and back of foci.

Another explanation that offers such kinetics is loss of Myosin at the back of the foci, and recruitment in the front. This could be the same Myosin that detaches in the back and and re-attaches in the front, setting a flow under the apical surface. Or perhaps the focus draws Myosin from the bulk pool of Myosin at differing rates in the front and back. The biochemical reasons driving this are unknown, but could again be related to different gradients of Myosin upregulating and downregulating species at the two ends of a focus. In such a case, the motion of the focus would follow the gradient of these chemical cues.

Finally, we see the end of focus propagation and activity. This can be due to dissociation of Myosin under the action of a biochemical clock, which could be a property at the cell scale, assuming the 'hardcoded Rho oscillator' hypothesis. In this case one would see a regular periodic pattern in focus disassociation. Another available hypothesis is the local high concentration of Myosin which could trigger a downregulation mechanism. This could be either biochemical, such as the control of Mbs, or mechanical, such as the breakdown of the substrate. In the second case, one would expect the cessation of focus activity to be followed by a local quiescent phase, as the substrate recovers.

Having laid out the various hypotheses that might be generating the apparent flow of Myosin foci, we note that the literature lacks a detailed quantification of these kinetics. We posit that flow needs to be understood mechanistically if we are to have any future hope of understanding its function.

0.7 Layout of This Thesis

In this work, I will present a range of data processing and image analysis tools, which will progressively characterize focus behaviour. These were developed over the last three years to analyse a set of amnioserosa time-lapse movies. These analyses allowed us to investigate the kinetics of Myosin foci during dorsal closure. This thesis is divided into four main chapters, based on the methods.

In chapter 1, I will describe the dataset of two channel (E-cadherin and Myosin II) fluorescent time-lapse movies of the amnioserosa [41] that will be analysed in this work. The first channel will let us see the cell membranes, and we will identify and confirm the various cellular properties during DC. The second channel lets us see the foci, and we will define a method of pre-processing necessary for their uniform identification over the whole dataset. This will account for the changes in absolute levels of intensity between different time-lapse movies, as well as the changes in intensity over long time-scales (10s of minutes) in the same movie. Once identified, the focus static properties will be quantified.

Then, in chapter 2, using a home-made automated image-tracking algorithm, we will temporally link the identified foci, thus observing their motion. We will find that such linkage reveals merging and splitting behaviour of foci. Under a point particle ansatz, we will outline their kinematic properties, such as speeds, durations and angles of deviations.

Chapter 3 is devoted to further point-particle analysis of the trajectories of focus paths, namely quantifying their directions and their travelling distances. We will examine these features and attempt to relate them to known laws of motion. We will check the effect of geometry on these focus paths, by correlating the properties of the foci with the cell and tissue properties that they are concurrent with.

The final chapter 4, sees a return to the continuous description of the Myosin signal from the point wise analysis. Here we will visualize the apical features of florescence in the known spatio-temporal neighbourhoods of foci, through space time kymographs. We will define a way to average our visualizations, so we can look at the properties of the apical cell or tissue Myosin signal in the regions where a focus has been, and will be. We will verify our conclusions from the previous chapters, and offer new insights.

Chapter 1

Normalization of Intensities and Focus Identification

1.1 Introduction

To study the kinetics of pulsatile actomyosin foci, we use as our model biological system the amnioserosa tissue of *Drosophila* during dorsal closure. I worked on a dataset with multiple time lapse movies of the same over from our collaborators Julia Duque and Nicole Gorfinkiel from Centro de Biologia Molecular, Madrid, which was analysed and curated in [41].

1.2 Amnioserosa Time Lapse Movies

I describe briefly the process of imaging. A stock carrying ubiECad-GFP [52] and zipperCPTI002907 (available from KyotoStock Center) were used. The embryos were dechorionated, mounted in coverslips with the dorsal side glued to the glass and covered with Voltalef oil 10S. The amnioserosa was imaged at 25–28 $^{\circ}C$ using an inverted laser scanning microscope. The emitted signal between 495 and 620 nm was collected at five or six z-sections 1 μm apart. Signals specific to green fluorescent protein and yellow fluorescent protein were extracted using the linear unmixing tool. The movies are imaged at two different resolutions of 0.439 $\mu m/pixel$ and 0.264 $\mu m/pixel$ at the apical plane respectively.

From this, we obtained 13 movies, 9 of them at 0.264 $\mu m/pixel$ resolution, and 4 of them at 0.439 $\mu m/pixel$. All movies had a time resolution of 10 $s/frame$.

1.3 Extraction of Cell Membrane Properties

The resulting confocal images are then segmented in a semi-automated manner using custom software written in Interactive Data Language (IDL, Exelis). This software senses the shape of the surface of the embryo in each z position of the image stack, and then uses these shapes to extract curved image layers of constant radial depth within the embryo. In this case the layers were extracted through the apical zonula adherens of the ectoderm [5]. The software then tracks cells over time in these pseudo-2D layers, based on the identification of the cell membranes. At each time point, the following quantities are recorded: the pixelated shape described by the fluorescent cell membrane; the location of the cell centroid (centre of mass); and cell identity. Parts of tracked cells that do not meet criteria for reasonable behaviour, such as anomalously high rates of volume change or cell displacement compared to the immediate cell neighbourhood, are excluded. We exclude these badly tracked cells to ensure high quality data, but then develop analyses that are designed to not be affected by missing cells. Cells that touch the edge of the field of view are also excluded from the analyses because they may be incomplete [4]. The final result gives us the membranes for 476 cells over 13 *Drosophila* embryos. The following table shows the total duration and total number of cells associated with each embryo:

Tissue Name	Duration (in frames)	Number of cells
2a early	240	32
2a fast	240	46
3a early	240	42
3a fast	360	30
4a early	240	24
4a fast	240	25
3LU	80	39
4LU	392	38
5LU	754	49
7LU	226	40
slow2	200	35
slow3	360	20
slow4	360	53

Using the open-source computer vision library, openCV, [7], these pixelated shapes of the cell membrane is transformed into closed numerical contours, and stored. This allows us to access at each time-instant the properties of the contours such as area and perimeter, and also fit the contour with ellipses to calculate anisotropy. We can now use these to extract and statistically analyse essential cell properties during dorsal closure of the *Drosophila* in the next section.

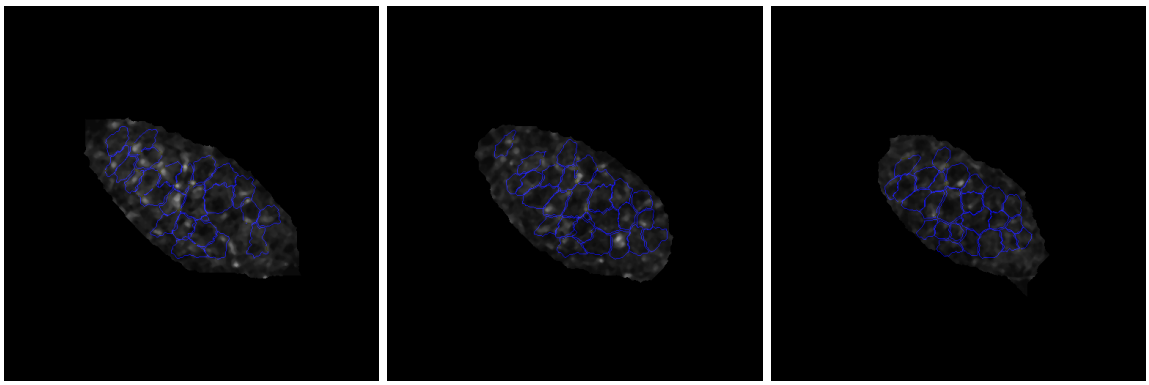

(a) $t = 45$ minutes (b) $t = 61$ minutes (c) $t = 78$ minutes

Figure 1.1: **The amnioserosa with Myosin and Cadherin:** Panels (a), (b) and (c) show a tissue (4LU) with Myosin channel (grey) and cell outlines from the Cadherin channel (blue) as dorsal closure progresses

1.4 Cell Properties

In this section we describe our model tissue, the amnioserosa, through the data made available from analysing the cell membrane. We confirm data of [22] and [41] and offer some new insights.

1.4.1 Cell Shape Variation in Development

The cell fluctuations of the amnioserosa tissue during dorsal closure (DC) of *Drosophila* has been quite well described in the literature. During this time, the cells of the amnioserosa tissue fluctuate at a time scale of a few minutes, which is described as three phases of DC - early, slow and fast. During the early phase, which lasts 45 minutes from the end of germ-band retraction to the start of DC, amnioserosa cells fluctuate with a long cycle length (4 minute cycles) and high amplitude ($8 - 10\%$ of cell radius) [4].

Then, as whole tissue contraction starts, both cycle length and amplitude of fluctuations are attenuated: this is the slow phase. The beginning of this phase (and equally, the end of the early phase) marks the

reference 'developmental time', $t = 0$, following conventions found in literature [22]. In this period the amplitude ($6 - 7\%$ of cell radius) and cycle length decreases (3 minute cycles).

Finally, 50 minutes after tissue contraction onset, zippering starts, marking the fast phase of dorsal closure, where cells fluctuate with low amplitude and short cycle length. During this phase, the supracellular actin cable that initiates zippering is also visible in our time-lapse movies, and Myosin focus pulsations are replaced by more and more continuous activity. An illustration of this is shown in figure 1.2 for the early, slow and fast phases of dorsal closure.

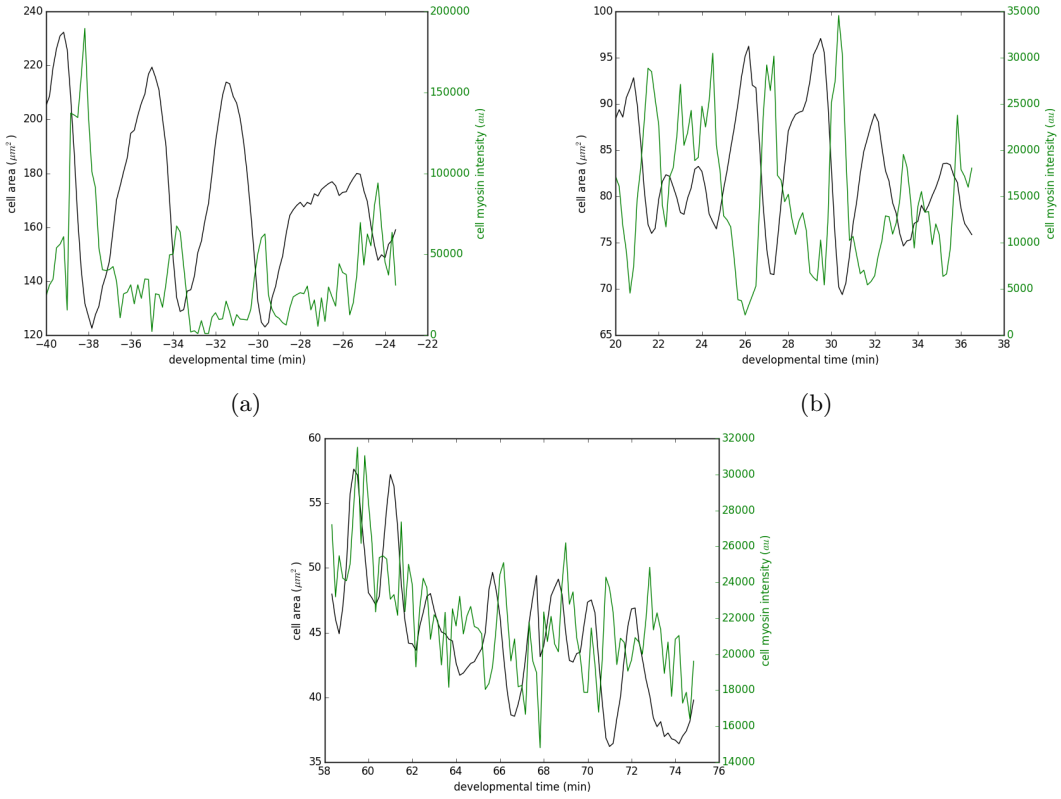

Figure 1.2: **Cell area and Myosin intensity fluctuations in individual cells:** Panels (a), (b) and (c) show the early, slow and fast phases of dorsal closure respectively

Since we are interested in the slow-varying trends of cell-shape oscillations during this whole period, we calculate the average cell area for all cells across all embryos for each developmental time-instant, and plot them in the figure 1.3.

From the plot 1.3, we can confirm that the beginning of effective contraction of cell areas starts around development time $t = 0$, before which the cells on average increase their area by $\sim 20\ \mu m^2$.

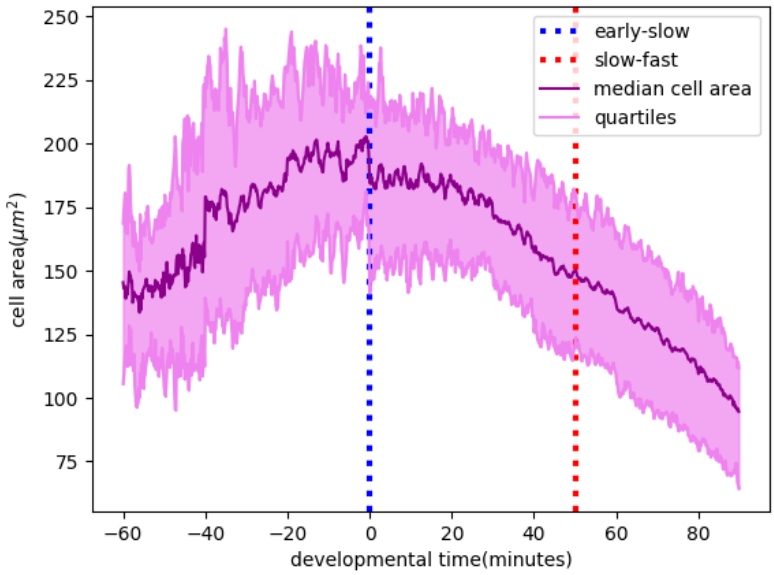

Figure 1.3: **Long timescale cell area variations over 13 embryos during dorsal closure**

1.4.2 Cell Shape Eccentricity and Orientations in Development

We also want to confirm the anisotropy in the cell shapes. This can be done by approximating the cell outline at every instant, as an ellipse, and then determining its eccentricity, which is defined as:

$$\epsilon = \sqrt{1 - \frac{b^2}{a^2}} \tag{1.1}$$

where, b and a are the lengths of the short and long axes respectively.

We also determine and store the orientation of the long axis of the cell with respect to the anterio-posterior (AP) axis of the embryo, at each time instant (we will find them to be useful in chapter 3).

Plotting the evolution of the cell eccentricities in time, in the figure 1.4, we observe the long timescale trends in the anisotropy of cell shape during DC. We note that the eccentricity is high, around 0.8, in the beginning, and it takes a constant value upto the the start of effective contraction ($t \sim 0$ minute). After this, the cells become more and more circular through the slow and fast phases of dorsal closure, never reaching quite the circle (eccentricity$= 0$), and have a minimum eccentricity of 0.5 at the end of DC.

Similarly, plotting the evolution of the cell long axes with respect to the anterio-posterior (AP) axis of the embryo in figure 1.5, we find that as DC progresses the cells become less and less polarized along the Dorso-Ventral (DV) axis of the embryo.

We note that the jump seen in the last three figures (1.5, 1.4 and 1.3) at $t = 0$, are due to the collation of data from various movies, some of which start or stop at this time.

Having thoroughly characterised all relevant cell properties during the biological process, we are now ready to pre-process the movies to identify the foci.

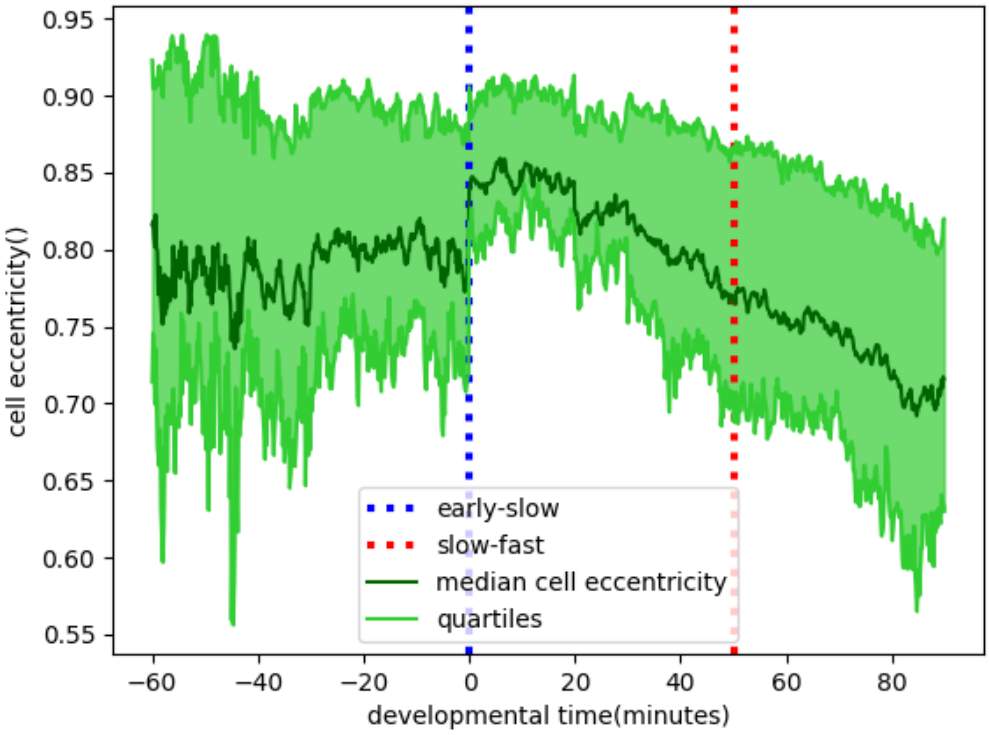

Figure 1.4: **Cell eccentricities over 13 embryos during dorsal closure**

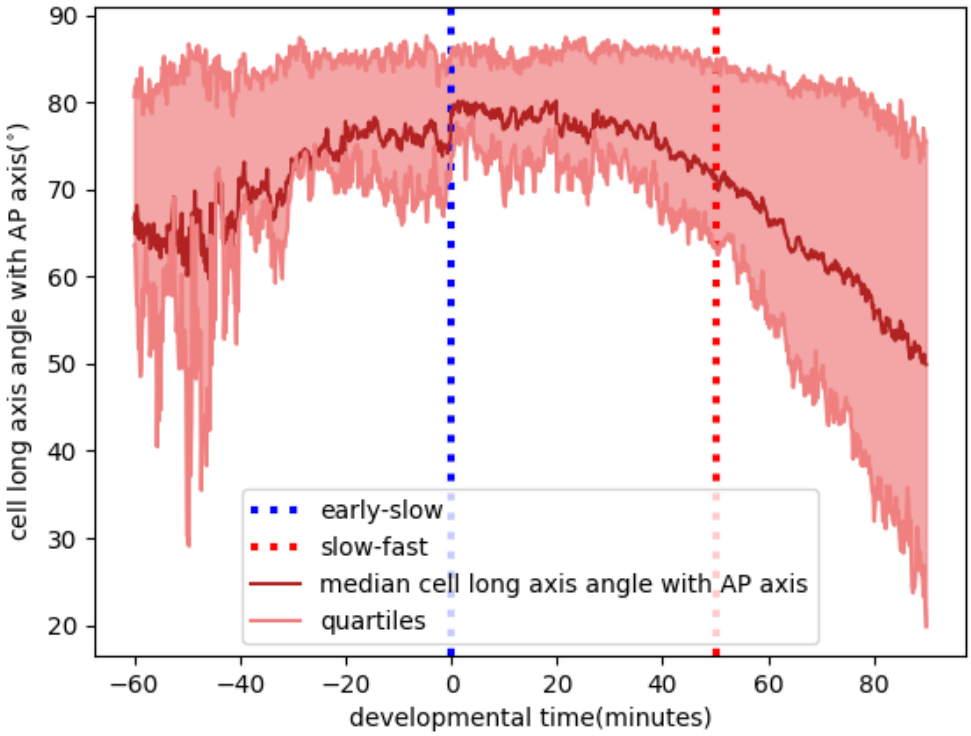

Figure 1.5: **Cell long axis orientations with respect to the tissue AP axis, over 13 embryos during dorsal closure**

1.5 Pre-processing Movies for Focus Identification

Now we are armed with two sets of Myosin movies, the whole AS movies as obtained from microscopy, as well as the per-cell movies obtained by segmenting these via the cadherin signal. Before we can identify foci, we must pre-process them in two ways, namely, noise removal, and signal normalization.

1.5.1 Noise Removal

As a first step of identifying foci, we need to remove noise from our time-lapse Myosin movies. This noise presents itself mainly in three forms. Firstly, we observe 'specks' of Myosin of 1-2 pixel diameter: which represent diffuse Myosin before and after focus assembly and disassembly respectively. There is also the junctional Myosin localised to 1-2 pixels around cell edges, which generally present brightnesses greater than medial Myosin, which we know from the literature as having little or no effect in cell-shape fluctuations during dorsal closure [4]. Finally, towards the end of dorsal closure, we observe supracellular actin cable at the edges of the amnioserosa, oriented along the anterio-posterior axis, which is much brighter than the Myosin foci.

We will deal with these issues sequentially:

Since we are interested in the quantification of the properties of large ($10 - 20\ pixel^2$ in area, depending on the resolution), mobile Myosin foci, we first need to remove the speckling phenomenon, while preserving the strength, and the slowly-varying properties of the signal at the stage of pre-processing the movies. For highly intense pixels present in close proximity, we would like to 'smear out' their signal so identify them as a signal focus. All the while, we want to preserve the brightness in our movies. This entails applying a filter to 'smooth' the Myosin movies.

During this process, we have to also deal with the problem of smearing out the edges/contours of our cells/tissues. We want to be able to still extract the precise geometrical features of the edges, which are an important feature of our analysis.

A broad range of signal processing literature [6] [37] suggests that a median filter is the most appropriate choice for preserving edges while suppressing noise. Using a median filter also possesses the benefit of being less influenced by extreme values of intensity than a linear filter. The drawback to this process is that such a filter is non-linear, and recovering the original signal is not possible after the application of this smoothing process.

We choose to use a square median kernel, $\mathbf{K}$ of size $2\mu m^2$, corresponding to 4 and 9 $pixel^2$ respectively in our movies of different resolutions. We modify this kernel at the edges of our cells/ tissues, adapting the kernel size to consider only in-cell and in-tissue pixels. Algorithmically, the process may thus be described as, deriving the smoothed signal $I_s(\mathbf{i})$ from the original signal $I(\mathbf{i})$:

$$I_s(\mathbf{i}) = Median\{I(\mathbf{j}) : \forall \mathbf{j} \in \mathbf{i} + \mathbf{K_i}, \mathbf{j} \in tissue\} \tag{1.2}$$

where $\mathbf{i} + \mathbf{K_i}$ refers to all on-tissue or on-cell pixels within the kernel $\mathbf{K}$ centered on the pixel $\mathbf{i}$. We reserve 0 intensity as a protected pixel value, which now denotes off-cell/ off-tissue.

Then, to exclude the non relevant part of the signal that is in the form of junctional Myosin, we trim the pixels around a contour of 2 pixels into the cell edge.

Following the same procedure for the tissue-movies, particularly those that comprise the late epoch of dorsal closure, we can now exclude most of the signal from the supra-cellular actin cable. However, it must be noted that near the end of DC, the task of identifying foci is particularly difficult since the Myosin signal changes in quality from discrete pulses of focal activity to a more and more continuous sheet of Myosin.

Having mitigated the noise in each focus movie, we then progress to define a method that would permit us to compare these movies with each other.

1.5.2 Percentile Normalization

As seen in figure 1.6, each of the 13 movies of dorsal closure have a different absolute fluorescence level. Moreover, within each movie we see a gradual fall in the Myosin intensity normalized by tissue area, that takes place at the time scale of hours (knowing that focus activity has a time-scale of minutes). This can be attributed to photo-bleaching phenomena. While some of this, no doubt, arises from the wide range

of Myosin activity that accompanies the process of dorsal closure, we find that movies during the same developmental epoch, present us with Myosin signals that have big differences.

To develop statistics of foci across embryos, and in time points separated by hours in the same embryo, we need thus to create a method that normalizes the Myosin intensity for the long-timescale deviations, while preserving the minute time-scale fluctuations that are the signature of focal activity.

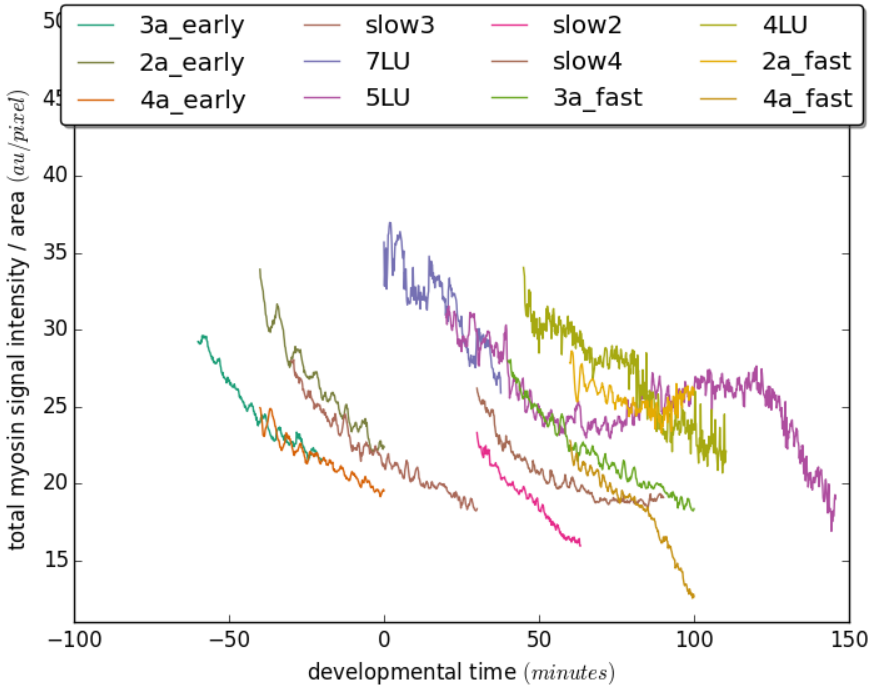

Figure 1.6: **Total Myosin signal per unit tissue area across various tissue movies**

To do this, we first observe that the 'structure' of the deciles of the Myosin signal, or the relative number of pixels at a particular fraction of the total signal intensity remain fairly uniform throughout the developmental process, and across different embryos.[1] Said otherwise, the frequency histograms of fluorescence intensity are similar at any time for any movie, but the values of intensity change in time (figure 1.7). Using this observation, we decided to define one of the deciles as a level of 'background' Myosin intensity, and scale the remaining deciles to normalize the signal at each time point, using a linear fit.

So, if we define the observed Myosin intensity at the $n-th$ decile at a time instant t for an embryo E as $myo_{obs}(n,t,E)$, as being composed of two parts, a time-embryo dependent background Myosin $b(t,E)$, and a time-embryo dependant 'signal Myosin' which varies linearly with the signal deciles $a(t,E)\times n$, then we can write the equation :

$$myo_{obs}(n,t,E) = a(t,E)\times n + b(t,E) \tag{1.3}$$

Fitting this with the slope $a(t,E)$ and the intercept, $b(t,E)$ for every time, we can then obtain from it the normalized 'signal' Myosin at particular pixel (x,y), defined as $myo_{norm}((x,y),t,E)$, as:

$$myo_{norm}((x,y),t,E) = \frac{myo_{obs}((x,y),t,E) - b(t,E)}{a(t,E)} \tag{1.4}$$

To use the entire range of available pixel intensities 0-255, we then scale this by a scalar multiplier (10).

[1] All but one of the experimental movies analysed in this work have roughly the same separation among decile necessary more this method of normalization. 3LU, which doesnt obey this rule, has therefore to be normalized differently. For this reason, we do not consider results from 3LU in the main work.

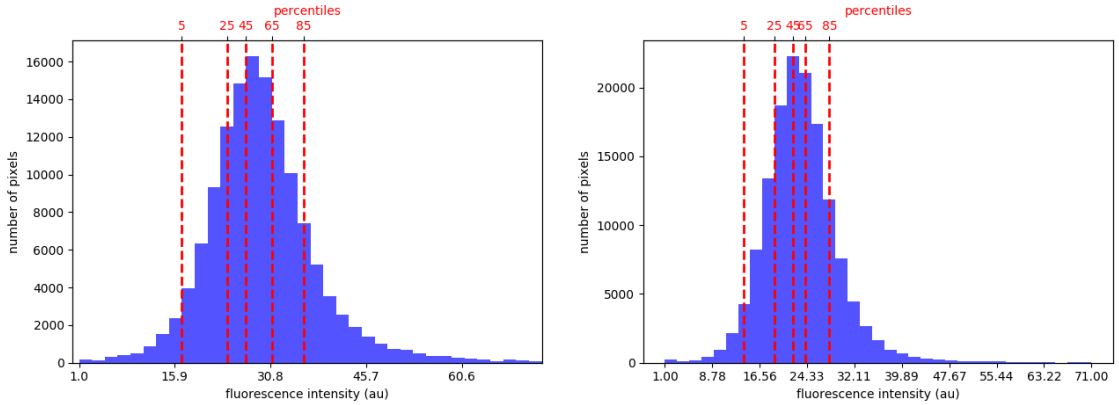

(a) Histogram of fluorescence intensities for 3a early at $t = -60$ minutes

(b) Histogram of fluorescence intensities for 3a early at $t = -26.66$ minutes

Figure 1.7: **Evolution of percentiles with time:** Panels (a) and (b) show the time evolution of the distribution fluorescence intensities for a tissue (3a early) at two different time points. Some of the percentiles are marked with dotted red lines.

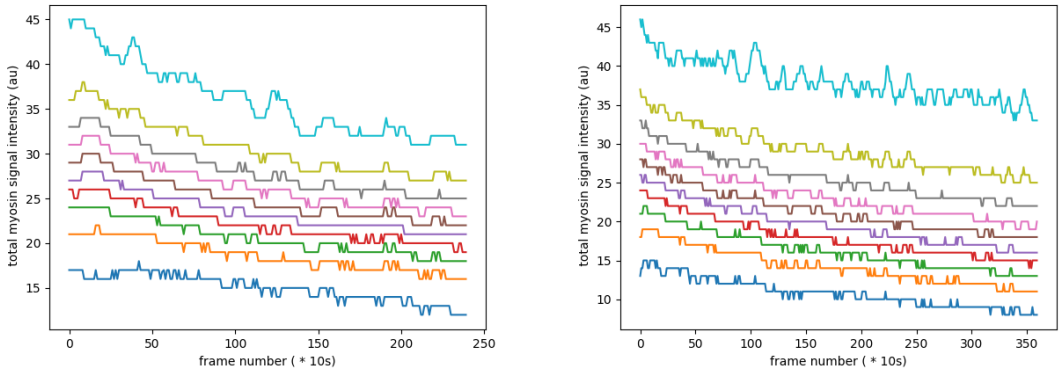

(a) Deciles of 3a early

(b) Deciles of 3a fast

Figure 1.8: **Demonstrating the structure of the deciles:** Panels (a) and (b) show the time evolution of the fluorescence intensity of the deciles of two movies from early and fast phases of dorsal closure, respectively.

Thus, choosing appropriate decile values as background and maximum, we can then normalize the signal between these for all the movies. In this work, we always chose the maximum at the $95th$ percentile of total Myosin signal intensity. We explore a range of different choices for the background from the $45th$ to the $65th$ percentile, and repeat all experiments over these values. Extracting normalization parameters from whole AS tissue movies, we apply this process to the tissue movies, as well as the segmented cell movies.

We see the effect of the normalization with the $45th$ percentile background on the deciles in figure 1.9, and on the total signal per unit area in figure 1.10. A visual idea of the effect of this normalization can be seen in the figure 1.11.

Thus, having smoothed the movies for noise removal, and having normalized intensities to compare statistics across movies and developmental time, we are now ready to move towards the identification of foci.

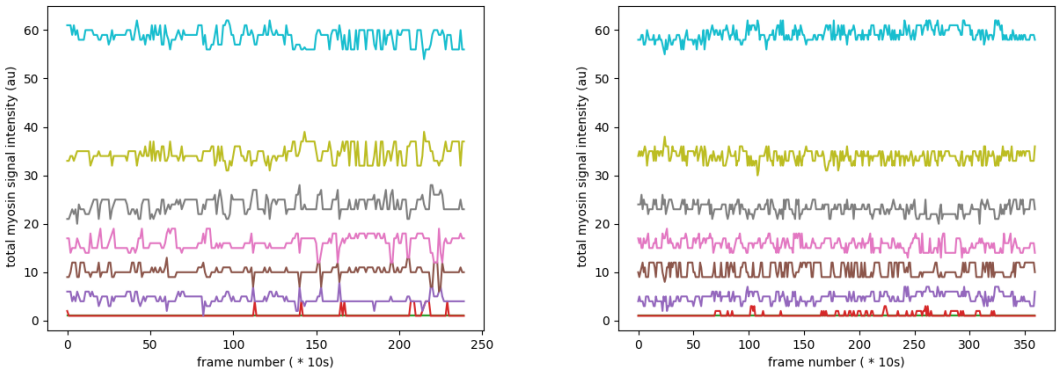

(a) Normalized deciles of 3a early

(b) Normalized deciles of 3a fast

Figure 1.9: **Structure of the deciles after normalization:** Panels show the structure of the deciles from same movies as figure 1.8 after the normalization procedure is applied using the 45th quantile as background.

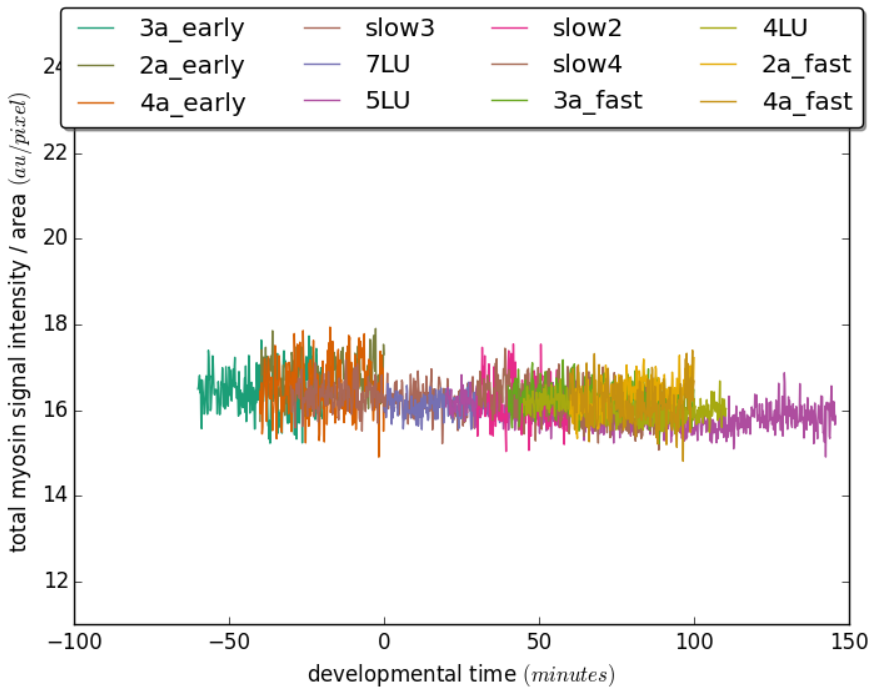

Figure 1.10: **Total Myosin signal per unit tissue area across various tissue movies after normalization with 45th percentile background**

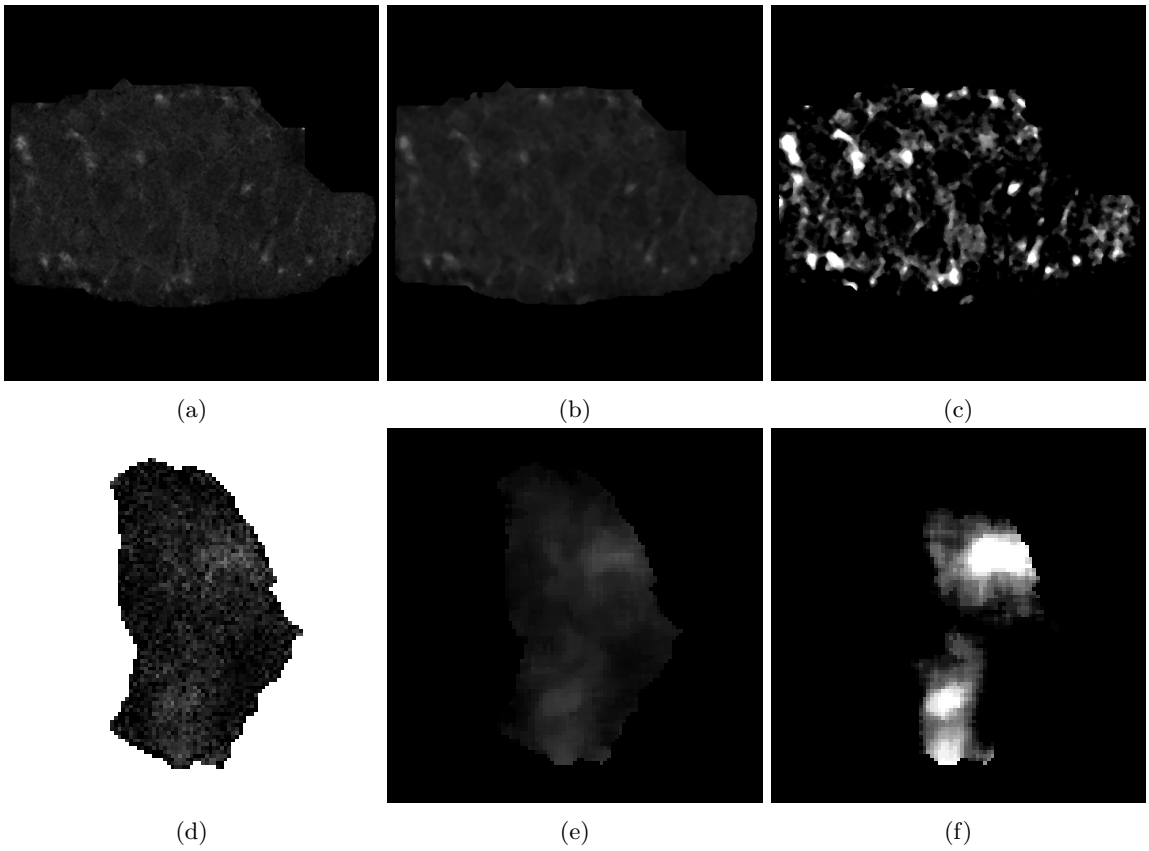

(a) (b) (c)

(d) (e) (f)

Figure 1.11: **Effect of normalization:** Frame from embryo movie showing pre-processing from raw in panel (a) to smoothed in panel (b) to intensity normalized in panel (c), and analogous frames from an individual cell in this embryo in panels (d), (e), (f).

1.6 Focus Identification

The first step in focus identification is to define what exactly constitutes a focus. For example, studying the literature we get estimates of size, speed and lifetime of foci [21] [17] [13] [54], and we can then ask our algorithm to isolate structures within a certain range of areas, moving within a certain range of speeds, and persisting for a certain amount of time. However, these values are specific to the biological system being studied, but we would like to have a method of detection that is general for all foci. So, while we will allow values cited in literature to guide our detection, we will not want our algorithm be biased by them.

The most typical signature of a general focus is the intensity of the pixels contained in it, which are much brighter than their neighbours. However, to be a focus, these bright pixels also must be assembled together in proximity. Furthermore, if there are a number of close bright pixels separated by a small 'island' of dark pixels, we would like to identify this as a single focus.

Isolating structures that adhere to these three criteria involves three distinct morphological operations, which are described in the subsequent subsections.

1.6.1 Thresholding

First, using a binary threshold we create a mask, which captures all the pixels greater than a lower bound of pixel brightness. The equation describing this process can be written as :

$$dest(x,y) = \begin{cases} maxval, & \text{if } src(x,y) \geq thresh \\ 0, & \text{if otherwise} \end{cases} \tag{1.5}$$

where $thresh$ is the value of the lower threshold, whereas $maxval$ is any value of white chosen for the mask color. Having normalized the movies to relatively uniform levels of total intensity in time, we can now pick the same value of the lower threshold to identify the foci, and apply it to all movies. We find that lower thresholds between $65th$ to $98th$ percentile of pixel intensities are appropriate. Lower than that and we capture the non-focus Myosin signals, higher and we capture only the brightest part of the foci, missing their birth and death processes, as described in chapter 2.

The lower threshold is an important parameter in our focus definition, and though the smoothing and the normalization processes remove a great deal of randomness in the Myosin signal, a good choice of the lower threshold is important for the complete characterization of all focus activity. Therefore, we sample the movies through a range of lower thresholds, and repeat our statistics for every value[2].

1.6.2 Closing

Having obtained a binary image where the bright regions represent the positions of candidate foci, we need to then 'despeckle' this image, getting rid of small isolated bright spots, as well connecting together small spots in close proximity. This is done by applying the morphological operation of 'closing' to the image, which is a dilation operation followed by an erosion operation.

The dilation of a binary image A by the structuring element B is defined by:

$$A \oplus B = \bigcup_{b \in B} A_b.. \tag{1.6}$$

The erosion of the binary image A by the structuring element B is defined by:

$$A \ominus B = \{z \in E | B_z \subseteq A\}, \tag{1.7}$$

where B_z is the translation of B by the vector z, i.e.,

$$B_z = b + z | b \in B, \forall z \in E. \tag{1.8}$$

Together, they have the effect of removing all bright spots smaller than the radius of the erosion structuring element, and then enlarging all remaining bright regions by the radius of the dilation structuring

[2] A sample of these statistics are presented in the appendix A

element. We use the same structuring element for both erosion and dilation, which is a circular structuring element with a radius of 1.317 μm is suitable for us in all cases. This is about 25% compared to the size of the largest foci detected without any closing operator.

As in the case of median smoothing in section 1.5.1, care is taken to restrict the 'closed' mask to the in-cell/in-tissue region, by performing a 'bitwise and' operation on this 'closed' binary mask by a binary image of the cell/tissue. This has the effect of removing all regions in the mask that are outside the cell/tissue, while keeping the rest unchanged. Using the contours of the mask thus obtained we are able to identify all Myosin foci.

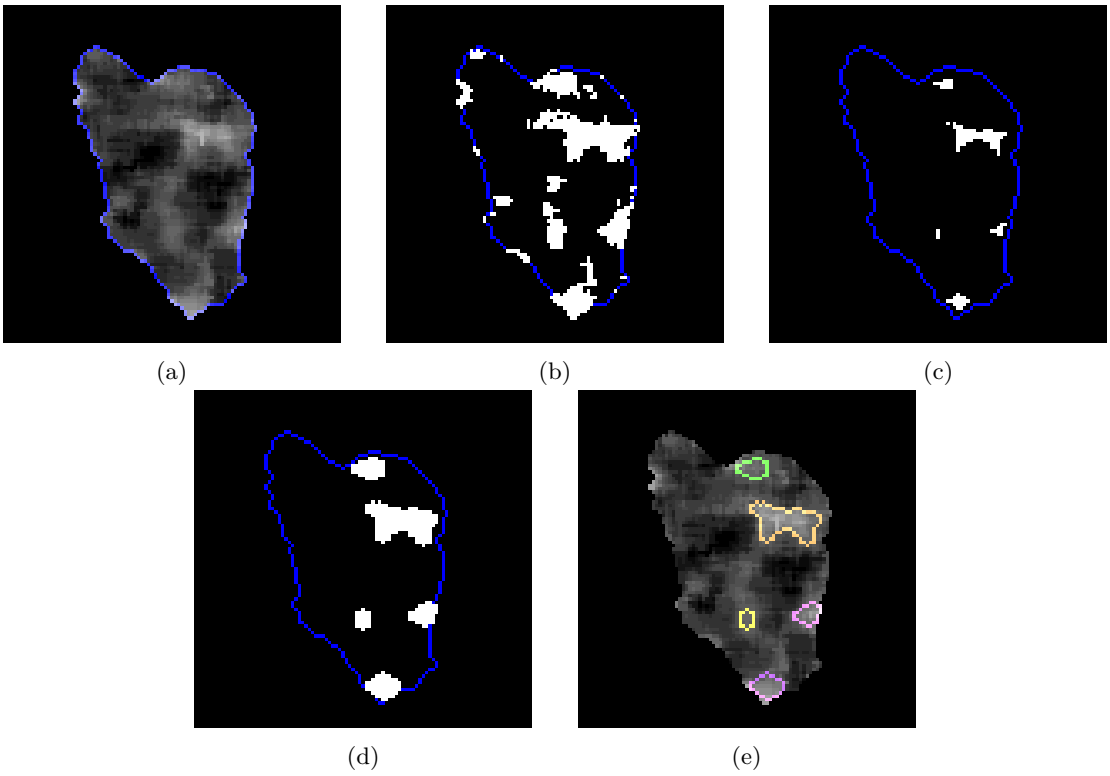

Figure 1.12: **All processes in the idenfication of foci:** from the original image in panel (a), which is then thresholded between a lower threshold (30% of the maximum) and the maximum gray value possible in panel (b), then eroded in panel (c) and dilated in panel (d), to complete the closing operation. The final image in panel (e) shows the different foci outlined by contours of different colors. In all cases the cell outline has been marked in blue.

1.6.3 Other Operations and Focus Identification

While these morphological operations together constitute a complete process to identify Myosin foci at the apical surface of the cell, we are guided by the literature to further restrict the definition in of a focus in two ways:

Firstly, we discard all contours with an area smaller than 0.94 μm^2 (corresponding to 5 and 13 px^2 in our time-lapse movies of the two different resolutions, respectively), that remain after the closing operation, since these are much smaller than values cited for focus size in the literature [17].

Secondly, at rare occasions we detect annular foci with holes in the middle.Though ring-like organization of Myosin has been cited in the literature [66] in other systems such as posterior mid-gut invagination of *Drosophila*, we discard any such holes (by considering only the bright part, and ignoring the hole in the middle) for two reasons: they occur rarely, and their properties are far from the scope of this work.

Now, each focus is recorded a unique identification number, which is associated to its location in space and time. The foci have a distinct a number of properties, such as size, shape, fluorescence intensity. We

also locate the 'mass-center' **M**, of the focus on the 2D apical surface by calculating the mean of all pixels within the contour, weighted by the intensity at that pixel. This has a side effect of sometimes placing the center outside the contour, due to the nonconvexity in the shape of some foci.

Having performed all these, we have a list of foci for at every time instant on each cell, and we may look into their basic properties.

1.7 Goodness Test for Lower Threshold

Once we have identified the foci across all embryos, we can use that information as a test for goodness of the lower threshold chosen. Qualitatively, at any given developmental instant during dorsal closure, foci detected in the embryos differ only due to process of thresholding, and not due to a physical or biological reality. Thus, we can assume that, at the same time, focus properties should be equal (or at least similar) across embryos.

For example, if at the same time instant in DC in two different embryos, we find that the number of foci in each cell differ by an order of magnitude, we can be sure that this is an artefact induced by the identification processes defined in the previous section. We can thus, use difference the number of foci across embryos, and identify the lower thresholds that minimise this.

We extract three such statistics from identified foci: number of foci per cell, fraction of cell apical area covered by foci, fraction of cell Myosin signal contained inside foci, assuming in every case that this quantities are independent of the originating embryo, only depending on the developmental time of DC. We can then compare them across embryos at equivalent time instants. We plot an illustration of this in figure 1.13.

However, as caveat, it is important to realize the choice of lower threshold is also visual, since choosing a lower threshold at both 0% or 100% would give us exactly the same numbers and fractions of foci across all cells and embryos, (being 1 and 0) respectively. In practice, a minimum acceptable range of lower threshold is chosen visually (we find the value 60 or about 24% of maximum, acceptable for this). These numbers are then useful in confirming the best possible choice greater than that minimum. In all plots in the following chapters, a lower threshold of 70 has been used. However, we repeat all experiments over from 60 to 140 (at which point the focus numbers drop close to 0), and present these results in the appendix. No appreciable differences in results are found within this range.

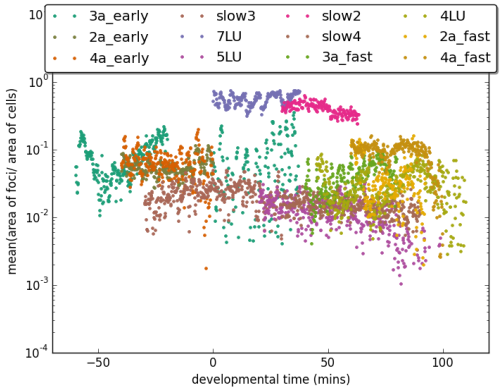

(a) Fraction of cell area in foci, lower threshold 40

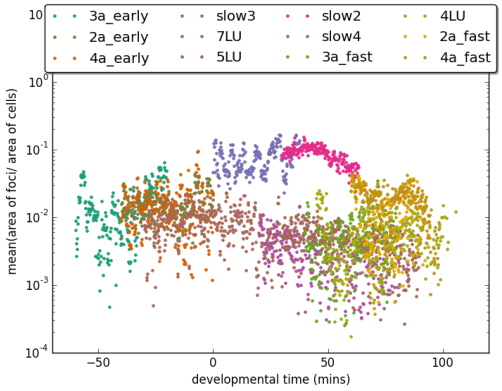

(b) Fraction of cell area in foci, lower threshold 80

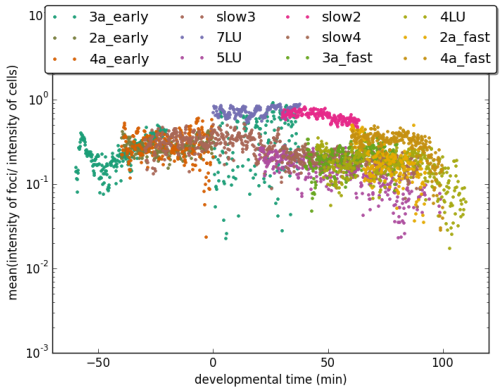

(c) Fraction of cell Myosin in foci, lower threshold 40

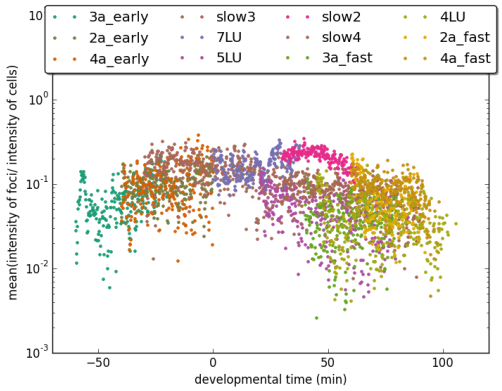

(d) Fraction of cell Myosin in foci, lower threshold 80

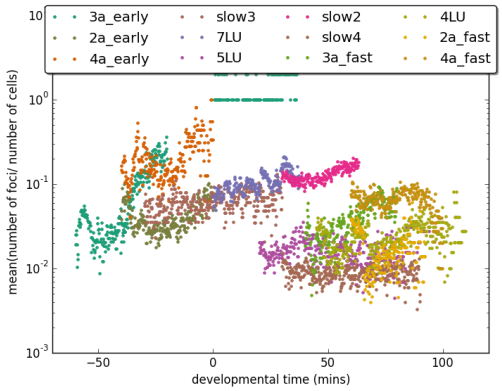

(e) Number of foci per cell, lower threshold 40

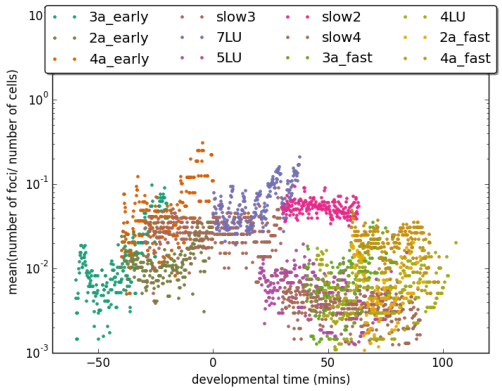

(f) Number of foci per cell, lower threshold 80

Figure 1.13: **Some quantities to check goodness of choice in lower threshold across tissues:**, left panels (a), (c), (e), at a lower threshold of 15% of permissible pixel intensity values, and bottom panels (b), (d), (f) at a lower threshold 30% of permissible pixel intensity values.

1.8 Focus Static Properties

Identifying all foci permits the derivation of several properties of the Myosin foci. We plot the distributions the most important out of these here, and show how the choice of parameters for focus identification affects

these distributions.

1.8.1 Focus Areas and Intensities

We plot the areas and the intensities of the identified foci in the form of histograms, in the figure 1.14.

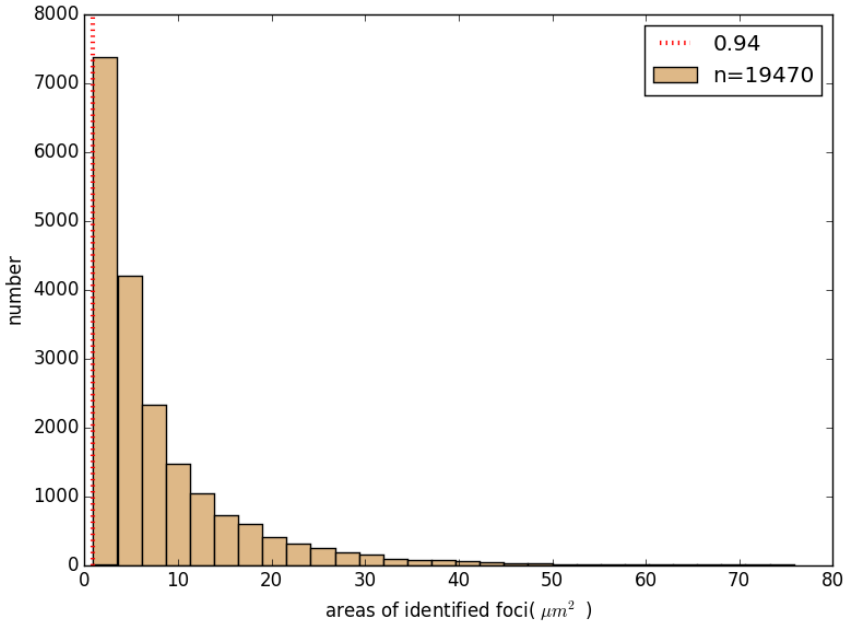

(a) Distribution of the areas of the identified foci, the dotted vertical line shows the minimum area among all foci

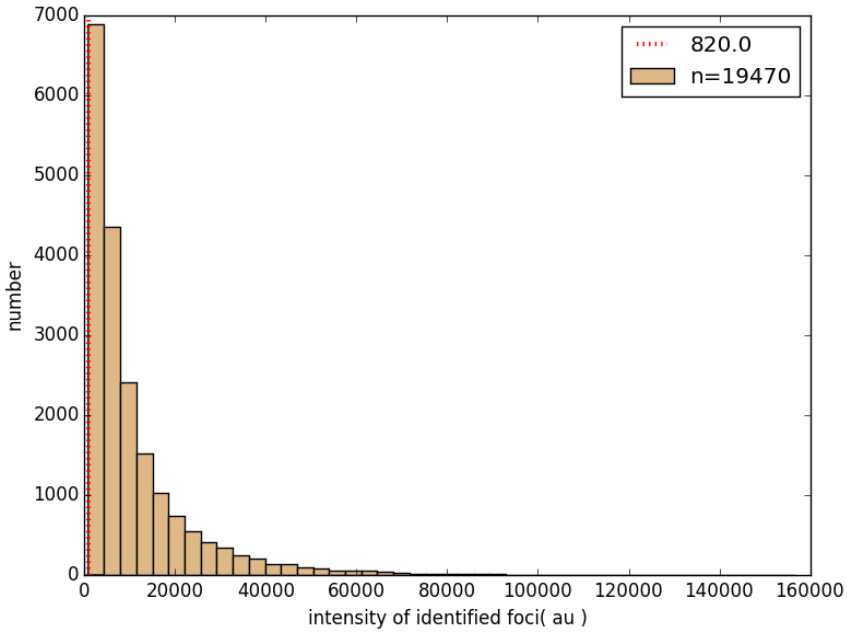

(b) Distribution of the intensities of the identified foci, the dotted vertical line shows the minimum intensity among all foci

Figure 1.14: **Areas and Intensities of identified foci**

We note in the figure 1.14a, the minimum area is about 0.94 μm^2 (which we have enforced in section 1.6.3), where as the minimum magnitude is about 820 au.

1.8.2 Focus Distribution on Cell Apical Surface

It is known that Rho-associated protein kinase (ROCK), which governs the activation of Myosin light chain kinase, flows from cell junctions where Rho, the upstream regulator of Myosin activity is located [54]. Thus, we are interested in finding out if foci occupy different parts of the cell preferentially. To do so, we can calculate the distance of every identified focus from closest point on the cell membrane. Since cells are of different sizes and eccentricities, to accumulate statistics, we normalize this distance by the by the length of the semi-minor axis of the ellipse fitted with the instantaneous cell contour.

Plotting this distribution in the form of a histogram, in the figure 1.15, we find that there is a high number of foci close to the cell membrane, as we move towards closer to the center (towards right in this histogram), the number of foci decreases. We find a non-zero minimum value of the closest distance at 0.02 times the semi-minor axis, due to the finite size of foci.

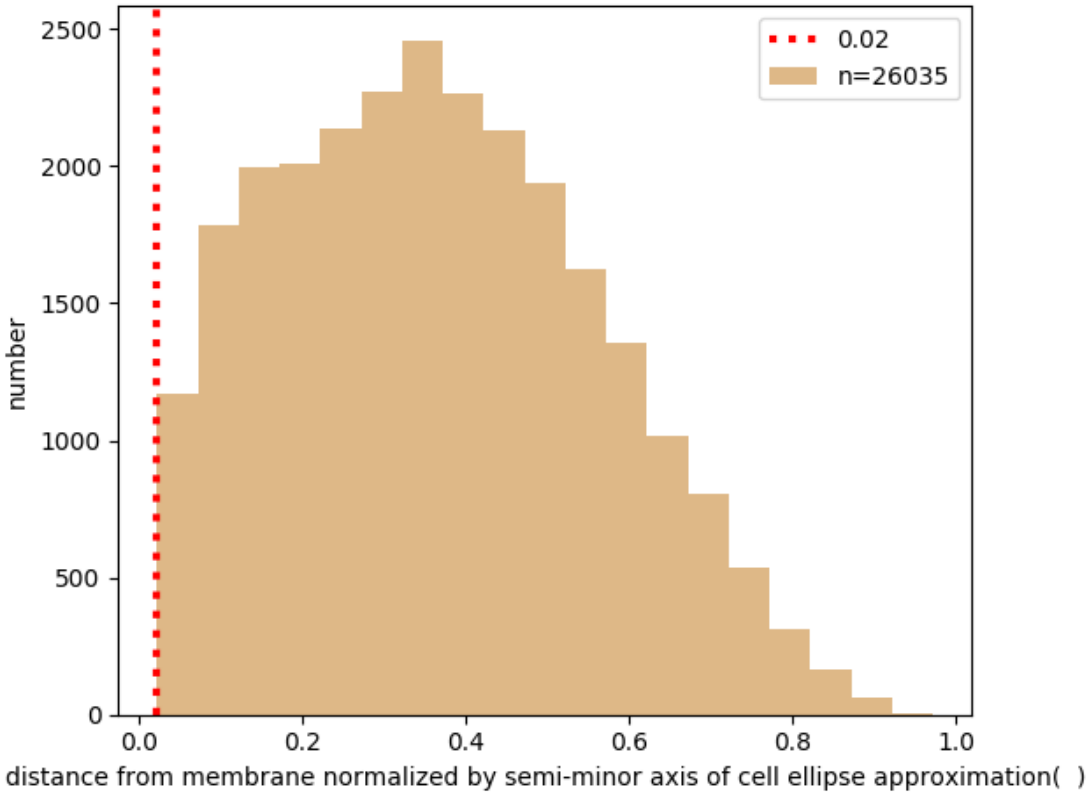

Figure 1.15: **Distance of foci from cell membrane, normalized by the length of the semi-minor axis of the cell-fitted ellipse**

1.9 Conclusion

In this chapter, we have reviewed the basic features of the morphogenetic process, dorsal closure in *Drosophila*. Using a tool to extract cell membranes, we have explored the basic properties of the cells of the amnioserosa, such as their area fluctuations and their anisotropy in shape.

We also saw that Myosin activity in the amnioserosa is in the form of focus pulsations, and we found a way to define these foci in an automated, algorithmic way using a couple of parameters. Comparing

their activity across different embryos, and compensation for photo-bleaching required a tool to normalize Myosin intensities, which we have developed. However, removing bleaching effect by normalization that we artificially hold total Myosin constant over long timescales of 10s of minutes. Previous analysis done with this dataset [41], had tentatively concluded that Myosin may be increasing in density over time (as cells get smaller). However, measuring the change over these long timescales is tricky from an imaging point of view. As a trade off, we are able to isolate and compare focus activity over these time-scales.

Coupling the normalization with the identification gave us a list of foci, whose basic properties we have looked into, confirming that they take comparable values across embryos. Finally, we saw their distribution on the apical plane of the cell.

However, we still lack an understanding of the dynamic properties of foci. For example, we have seen the pulsation frequency of Myosin foci, but we have said nothing about how these pulses are arranged spatio-temporally to synchronise changes at the tissue scale. We have seen the distribution of the areas and intensities, but we do not yet understand how they are arranged within the span of a single focus, or within the developmental epochs of dorsal closure.

Proper identification of foci provides us with a 'snapshot' of the regions and times of interest in each cell, however the task of dynamically linking these snapshots to create a complete picture of focus motion rests ahead of us. This will be our 'focus' in the following chapter.

Chapter 2

Kinetics of Apical Myosin Foci in Dorsal Closure

2.1 Introduction

From the previous chapters, we see that the local properties of acto-Myosin, and particularly of the foci at the cell apical surfaces, affect cell shapes in a manner that causes contraction at the scale of the tissue [4]. Thus, it is reasonable to assume that the mesoscopic spatial properties of the Myosin foci may shed light on shape changes at the scale of the tissue.

The focus formation consists in Myosin accumulation on the actin meshwork at the cell apical surface. It can be understood through various mechanical and biochemical models that include: cooperative Myosin binding, advection and concentration of acto-Myosin, force dependent activation of ROK, etc. Similarly, Myosin disassembly can be understood through the models including the disassembly of actin network at high actin or Myosin concentration, or elastic resistance to contraction arising from the surroundings (reviewed in [3]).

Myosin II molecules can self assemble into bipolar Myosin II mini-filaments, promoted by the action of Myosin Light Chain Kinases (MLCKs) in the unfolding of the inactive homodimers, and the action of actin in concentrating encounters between the Myosin molecules [42]. Similarly, the disassembly of the mini-filaments back into the homodimers is promoted by the dephosphorylation of Myosin Regulatory Light Chains (MRLCs), or the phosphorylation of Myosin Heavy Chains (MHCs). Since there is no flux of Myosin through the cell membrane, the amount of Myosin in the cell is conserved except the relative fluxes of assembly and disassembly.

However, as we image only the apical surface of the cell, it is worthwhile to consider the division of the amount of Myosin in a cell into two pools: an apical pool, that we observe experimentally, and a bulk-pool, which is out of our view. These two pools exchange fluxes of Myosin.

The assembled minifilaments are able to bind to the actin meshwork by their head-domain, and walk on the actin substrate by executing a power stroke. Mini-filament assembly is crucial in force generation by producing mechanical work on the actin substrate by consuming ATP energy. These mini-filaments can also unbind from the actin meshwork, which is followed by their diffusion into the surroundings.

Thus, within the apical pool we have two species of Myosin mini-filaments: force-generating, bound Myosin, and detached, unbound Myosin.

Another feature of Myosin activity at the apico-medial surface is flow, or advection of the actin cytoskeletal network, described in biological systems like the *C. elegans* cortex [20] [50], and *Drosophila* during cell intercalation [55]. In the time scale of 10s of seconds to minutes, this network shows a fluid-like behaviour. In this hypothesis, Myosin focus motion is explained by the flow of apical actin cytoskeleton to which it is bound [12]. This network continuously turns over, with disassembly that allows dispersal as well as assembly that allows incorporation of actin monomers at the barbed ends of actin filaments, as seen in the *Drosophila* ventral furrow formation [30].

Thus the processes that describe the apparent motion of Myosin foci at the apical cortex may be broadly

classified into the following three types: the motion of Myosin mini-filaments on polarized actin fibers through the 'power stroke', localized binding and unbinding of Myosin on the actin substrate followed by the diffusion of unbound Myosin, and advection of the substrate itself on the apical cell surface, combined with the turnover of both species in response to mechanical or biochemical cues. Given that all of these processes take place on the cortex, we may write a mass balance for the Myosin molecules at the surface of the cell, called the apical pool of Myosin.

In our system, the amnioserosa of *Drosophila*, we observe that the transient pulses of Myosin across the apical surface show sufficient spatio-temporal separation and are sufficiently long-lived to lend themselves to be analysed in a discrete way. Furthermore, we show in section 2.4.2, these transient pulses of Myosin show a distinct growth and decay pattern within the period of each pulse.

Thus, we are motivated to treat each Myosin pulse as a separate object, find a way to track it in space and time, and correlate its various properties statistically. A similar process has been performed in [17], via manual tracking. Other authors [55] have tracked foci in other systems (*Drosophila* germband extension). We extend this process by developing an automated tracking algorithm, which is able to link the foci identified in the chapter, and reconstruct them as discrete pulses of activity.

2.2 Focus Tracking

Our goal in this section is to develop an algorithm that allows us to temporally link the Myosin foci that we found (in chapter 1), and then reconstruct their paths. We do this by establishing a 'mother-daughter' relationship between foci in subsequent frames of our time lapse movies. To do so, we use a bitwise 'and' operation to compare each binarised frame f_i of the normalized Myosin movies (from section 1.2) to the previous one f_{i-1}. From this, we obtain ROOs, which are the 'regions of overlap'. In the reference frame of the cell, this is the common region in space-time where the candidate foci for 'mother-daughter' linkage exist. Therefore, the size and the relative signal intensity at this ROO at f_i and f_{i-1} are indications of mother-daughter linkage. We quantify this using the ROO to determine the Myosin signal intensities in each of the two frames, as well as the area of the ROO itself. We then find the ratio of the overlap area to the area of the mother focus to determine the 'fraction of area overlap.' We also calculate the 'speed' of a possible linkage by calculating the distance between the mass-center for the foci in different frames, participating in a particular region of overlap. Using a combination of these derived parameters, we are able to define a set of rules to link foci across frames.

Consider, for example, an ideal case where the thresholding and closing operation described in sections 1.6.1 and 1.6.2 detects one ROI ('regions of interest', or candidates for mother-daughter linkage) in each of N subsequent frames t_i, for $i \in 1..N$ of a particular time-lapse movie (figure 2.1b).

We will now define the set of rules that tell us algorithmically, whether or not two foci participate in a mother-daughter linkage.

Using these N ROIs, and with the methods described in section 1.6, we now identify a list of N foci, each with a contour Ω_i of area A_{Ω_i}, a mass-center $\mathbf{M_i}$ and signal intensity I_i $\forall i \in 1..N$.

Using a bitwise 'and' operator for every pair, $i, i+1th$ contour in this list, we obtain the regions $\Omega_{i\cap i+1}$ and their areas, $A_{\Omega_{i\cap i+1}} \forall i \in 1...N-1$. These, then, are the ROOs (figure 2.1c). Mapping each region $\Omega_{i\cap i+1}$ on to the frames t_i, t_{i+1} gives us the two intensity values of the region in both frames where it is present.

We can now define the fraction of area overlap, as:

$$r_i = \max\left\{\frac{A_{\Omega_{i\cap i+1}}}{A_{\Omega_i}}, \frac{A_{\Omega_{i\cap i+1}}}{A_{\Omega_{i+1}}}\right\},\ \forall i \in 1...N-1, \tag{2.1}$$

or the area of the region of overlap normalized by the area of smallest of the two foci participating in said overlap.

We can also define the speed of the possible linkage as:

$$u_i = |\mathbf{M_{i+1}} - \mathbf{M_i}|,\ \forall i \in 1...N-1, \tag{2.2}$$

which is simply the distance between the said foci in the two frames.

Thus, we define a set of rules for a linkage $\Lambda_{i,i+1}$ as a crenel function of r_i and u_i such that

$$\Lambda_{i,i+1} = \begin{cases} 1, & \text{if } r_i \geq r_{abs} \\ 1, & \text{if } r_i \geq r_{conditional} \text{ AND } u_i \leq u_{max} \\ 0, & \text{otherwise,} \end{cases} \tag{2.3}$$

where $r_{abs}, r_{conditional}$ and u_{max} serve as parameters. Thus, if and only if value of $\Lambda = 1$, we establish a mother daughter-linkage (figure 2.1d). Lower values of the r parameters allow us to expand the number of linked foci, to where even very loosely associated foci linked together, whereas higher values make linkages more restrictive so only highly associated foci linked together.

u_{max} ensures that two foci in which the main fractions of the signal are located in very different spatial locations, are not temporally linked. Though this puts an upper limit on the possible speed of a focus under the rules of our algorithm, the value for the parameter used is 3 times the value commonly cited in the literature [21] [17].

The parameter space for this is explored visually. However, proper choices of focus identification parameters such as lower-threshold and closing radius, described in section 1.6 ensures that these parameters do not bias the tracking too much. We use a combination of speed and the fraction of area overlap to determine a linkage: with a max speed of 2 $\mu m/s$ and a fraction of area overlap at least 0.3, or a fraction of area overlap at least 0.5

However, in general, more than one ROI can and will be detected in each frame, and thus for a frame i with n_i number of focus detected, the terminology generalises to contours Ω_i^j where $1 \leq j \leq n_i$ and we have to determine all linkages between Ω_i^j and Ω_{i+1}^k where $1 \leq j \leq n_i$ and $1 \leq k \leq n_{i+1}$.

Obtaining a 1 value for more than one linkage between three or more foci in subsequent frames leads to the detection of merging and splitting phenomenon. In all cases, very often, two or more foci in one frame fulfil all requisites to be linked to a single focus in the next frame, and vice versa. Thus, the reconstruction of paths for foci requires remembering all linkages, and associating them back in time.

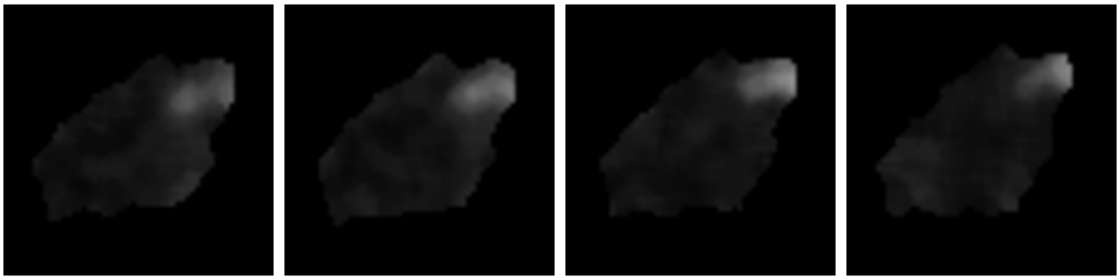

(a) 4 frames from a time-lapse movie of a cell, showing Myosin signal in levels of gray.

(b) Same frames after morphological operations have been performed to obtain the ROIs, with the cells outlined in blue.

(c) Regions of overlap between ROIs tracked in the current frame (in green, daughter foci), and ROIs tracked in previous frame(in red, mother foci), region of intersection in gray. From left to right, (r, u) are $(0.93, 0.02\mu m/s)$, $(0.70, 0.89\mu m/s)$ and $(0.89, 0.71\mu m/s)$

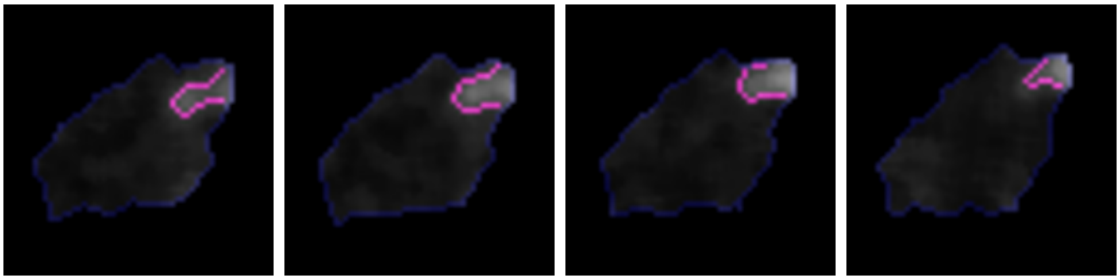

(d) Motion of the tracked branch, with the individual foci outlined.

Figure 2.1: **An illustration of the process of creating mother-daughter linkages between foci identified in different frames**

2.3 Path Reconstruction

Having defined and quantified temporal linkages for all tracked foci in a particular frame, we are now ready to reconstruct their paths in the apical surface of the cell.

As described in section 2.2, since linkages between more than two foci are found often, we need to make a choice on the strategy of path reconstruction. One option is to define a parameter that describes the likelyhood of the linkages previously described, and then choose the path that contains the most likely linkages. Otherwise, we must define the discrete events, merging and splitting, that keep track of all multiply linked foci. In both cases, we need to define the events of birth and death, which account for the first and last time a focus is detected.

We follow the second way, defining four 'events' that a focus may undergo: birth, death, merging at splitting. We will now describe them biologically:

- In the biological context, we see birth as the aggregation of a patch of diffuse Myosin into a prominent focus. This might be due to the preferred/selective recruitment of Myosin at a particular part of the cell, possibly followed by centripetal movements that concentrate it. This process might also involve the recruitment of more actin on top of a persistent apical network.

- Death is the opposite process of birth, which may be understood by the preferred/selective unbinding of a Myosin focus from its actin substrate, which then diffuses, resulting in dilution through centrifugal movements, or disappears from the cell apical surface by sinking into the bulk. This process might also involve the loss of actin from the apical network

- Merging is the process of coalescence of two or more Myosin foci into one single focus. This phenomenon has been reported in the literature in various developmental contexts [63]. For instance, in *Drosophila* ventral furrow cells, it has been reported that Myosin foci failed to coalesce in embryos treated with an actin disruptor Cytochalasin D [43]. Therefore, one possible hypothesis is that merging occurs due to actin-Myosin network contractions. One of the interesting questions raised during this analysis, is whether this occurs randomly or through some attractive property.

- Splitting is the opposite process of merging, which is defined as a single focus in one frame dividing into two or more distinct 'daughters' in the subsequent frame, separated by a region of lower Myosin concentration. This process is not very well-described in previous studies of Myosin foci, however we observe that it happens quite frequently in the *Drosophila* amnioserosa.

We need now to define these biological events in terms of our algorithm, so as to properly quantify and detect them.

- A focus birth is defined as the first occurrence of a focus in the movies, for which no mother daughter linkage can be established (as defined by equation 2.3) with any focus in the previous frame.

- Death is the opposite process of birth, that is when the Myosin intensity in a focus becomes so weak as to not be detectable by the thresholding operation described in section 1.6. Therefore, we might define it in a way that is opposite to the birth event, being a focus for which no mother-daughter linkage can be defined in the next frame.

- Merging occurs when two or more separate foci in one frame move sufficiently close together in the subsequent frame so as to be marked as a single one in our focus detection. Thus, algorithmically, it may be defined as a mother focus in one frame which has two or more daughter foci in the next frame, as defined by equation 2.3.

- Splitting is the opposite process of merging, which occurs when a single focus in one frame divides into two or more discrete 'daughters' in the subsequent frame, which are sufficiently distinct and retain large enough sizes to be detected as separate by the closing and despeckling operation during focus identification.

With our analysis we record 77040 unique cell-frames across all cells. Out of these, for the standard lower threshold used in this chapter (70), we found 6521 births, 6470 deaths, 1756 mergings and 1627 splittings.

Using these four events and already having obtained the temporal relationships between foci, we are now able to define focus 'branches': a time ordered list of the properties of foci that share ROOs. Thus, a branch

is defined as a list of linked foci through N subsequent frames, which is initiated by a birth or merging or splitting event, and ended by a death or merging or splitting event.

A 'branch' is a subset of a greater structure called a focus 'tree' : which is a list of all linked foci, including merging and splitting branches. In the diagram 2.3, all foci connected to the green branch, and all foci connected to the blue branch, make two different trees.

Thus each branch has a head, the 'oldest' focus detected, and a tail, the 'youngest' focus detected. As we have defined mothers and daughters in terms of individual foci, we may now do so for individual branches. If the head of the branch is not the result of a birth event, then the branch also possess two or more mother foci, which are at the tails of the previous branches participating in the splitting or merging event. Similarly, if the tail of the branch does not result in a death event, then the branch possess two or more daughter foci, which are at the heads of the next branches participating in the splitting or merging event.

A small but important distinction here, is that while an individual focus may possess a unique mother, a branch never can (a unique mother, in this case, would be defined as a focus that is not mother to any other branch). If it is the product of a birth event then it has no mothers (as seen at the head of the green tree in 2.3). If it is the product of a merging event, then it has two or more mothers. Similarly, a branch can never have a unique daughter. It either has none, or two or more.

Each branch is also defined by one or more 'matriarch foci.' The matriarchs for any focus branch are defined as all foci that maybe linked to that branch through equation 2.3, which has also participated in a birth events.We obtain this algorithmically by following the list of mother-daughter linkages for that branch up to birth events.

Similarly, each branch is defined by one or more 'grand-daughters', which are defined, analogously, as all foci linked to a particular branch that also participate in death events. We obtain this, analogously, by following the list of mother-daughter linkages up to death events.

It should be noted at this point, that a single focus may possess more than one appellation. Thus, it is possible for a single focus to be both mother and matriarch, (indeed, if a focus is a matriarch it is necessary for it to a mother), as seen in the schematic diagram 2.3.

At the lower threshold used for plots in this chapter (70), we track 6747 branches, and 4524 trees, for 434 distinct cells over 720 time points.

In addition to the list of properties possessed by its elements, each focus 'branch' also has now global properties, such its duration in time, as well as an exponent of motion and an average direction of propagation, (described in more detail in chapter 3). Now that we are able to reconstruct the path taken by a single focus branch in time, we are able to look at some of their dynamical properties.

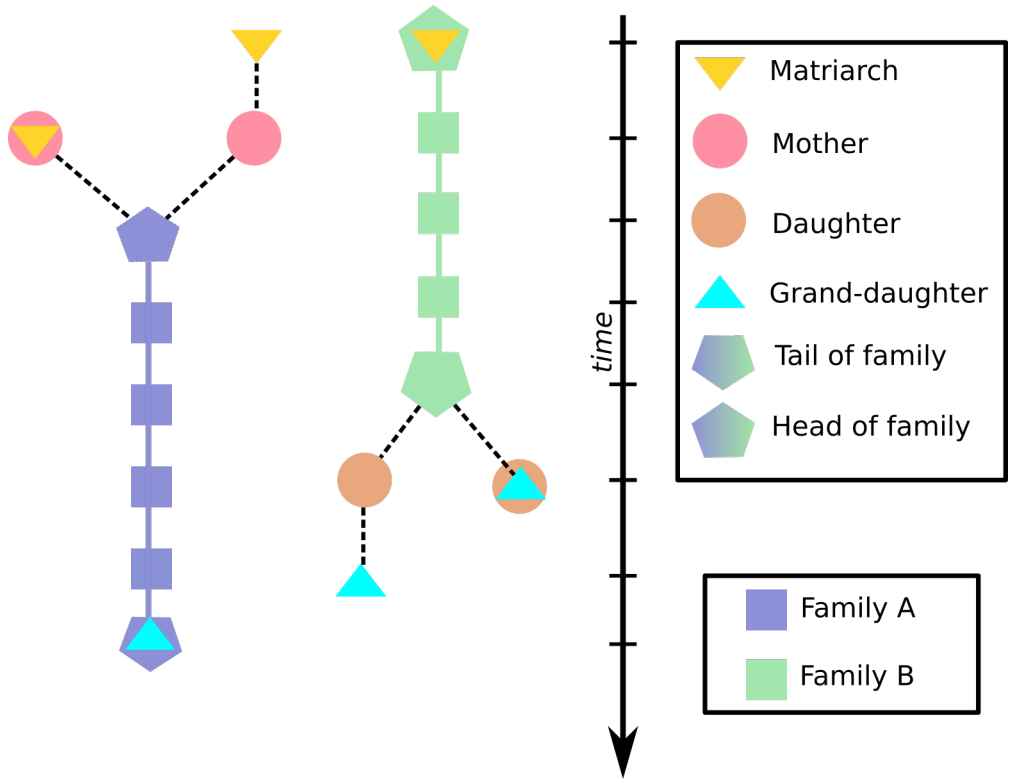

Figure 2.2: **Schematic diagram of two focus trees showing various branch appellations:** In this diagram, time points from top to bottom, and individual foci are denoted by green and violet shapes respectively. Intra-branch linkages are denoted by solid lines with the same color as the branch, where as inter-branch linkages are denoted by dashed black line. Birth events are denoted by colored shapes at the head of lines, where as death events are colored shapes at the end of lines. Merging and splitting are shown by converging and diverging dashed black lines respectively

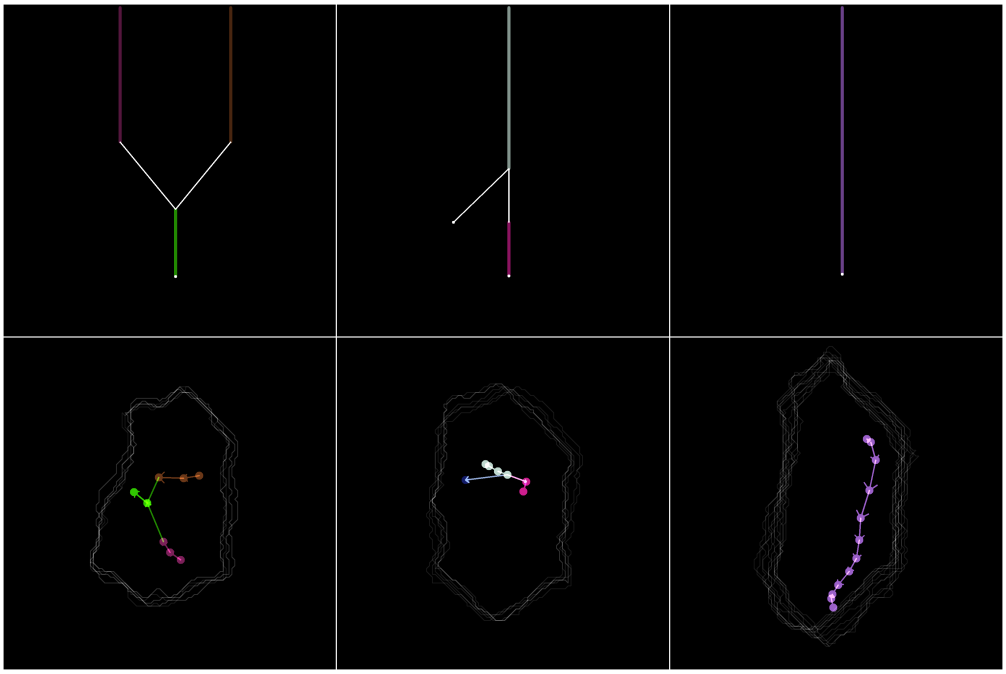

Figure 2.3: **Merging and Splitting Geneologies:** Cell from slow phase of dorsal closure with focus trees (top panel) and tracks (bottom panels) drawn by algorithm after tracking. Colors on tracks and branches correspond.

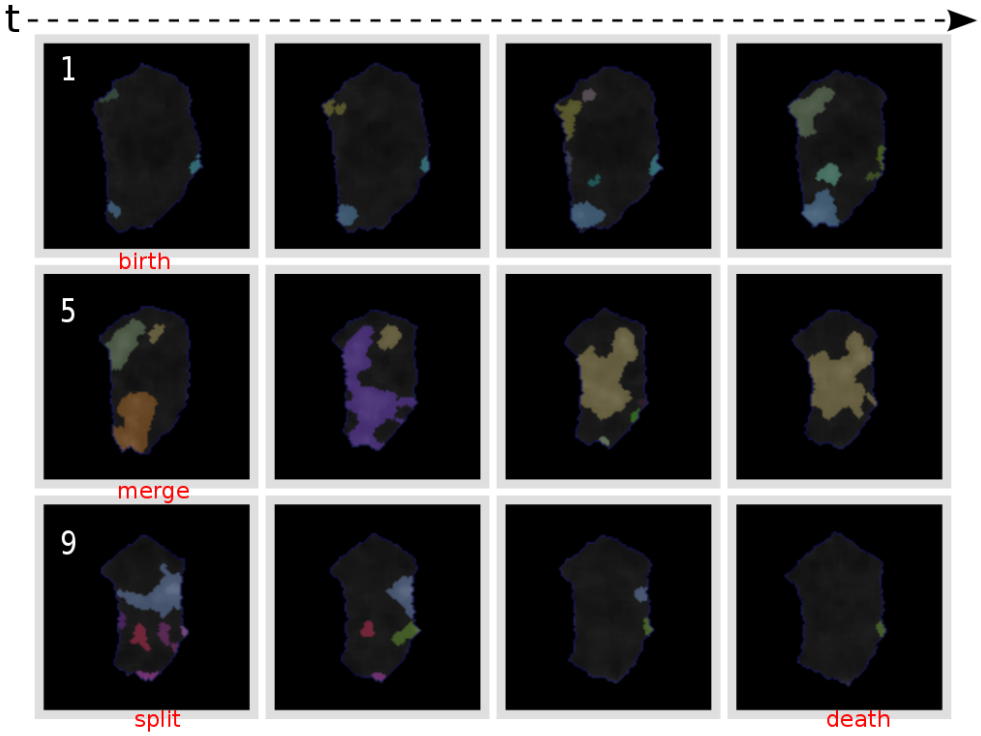

Figure 2.4: **Snapshots of births and merging followed by splitting and death:** 12 subsequent frames from a cell from slow phase of dorsal closure, with artificially colored foci drawn by algorithm, illustrating births, mergings, splittings and deaths. A change in branch identity followed by events is indicated by change in color. The frame number is marked on each left panel

2.4 Motion of Foci

We restrict our analysis at this stage to focus branches- that is, paths travelled by foci between any two events. The justification for this is twofold. Firstly, this is that branches vary sufficiently in their properties such as duration, speed, etc to merit analysis as separate objects, and not within a broader structure of trees. Secondly, it is more pragmatic to start at this level, as it is simple.

Branches may be of two kinds, lone branches: ones that begin with a birth event and end with a death event, or branches in trees: which are branches that may be connected to other branches through merging and splitting events. We quantify several dynamic properties of the focus branches, and correlate with other static properties/cell properties obtained in chapter 1

2.4.1 Durations of Focus Branches and Trees

Having obtained the time ordered lists of focus branches, we can now quantify the average duration of each branch.

Thus, for any focus branch j, we denote the duration as d_j. Algorithmically, this is calculated by the difference in time between the head and the tail of each branch. We can also analogously calculate the durations of trees, where we calculate the difference in time between at earliest matriarch and the latest grand-daughter for each tree. We plot these in the histogram 2.5

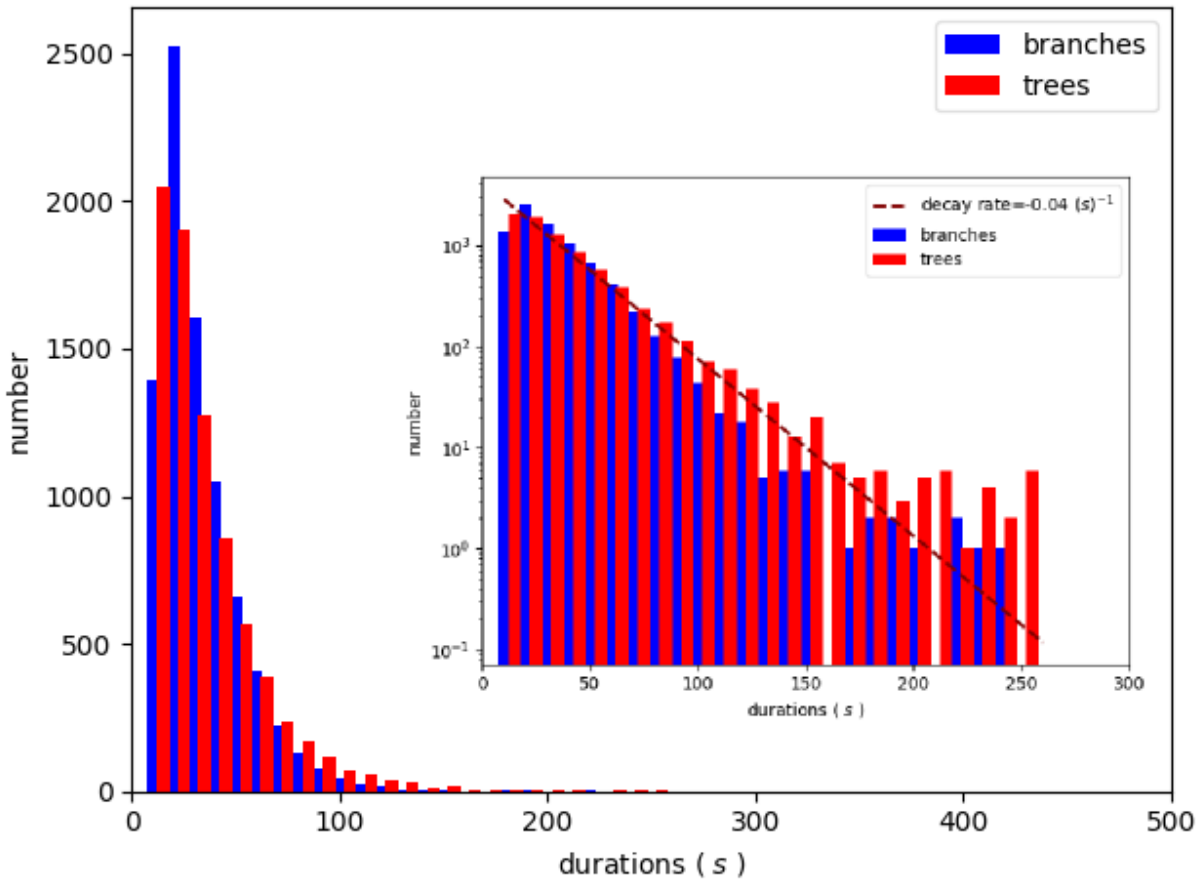

Figure 2.5: **Durations of focus branches and trees :** Histogram of branches in blue and trees in red. Inset shows same figure with log y scale, with the durations of trees between $20s$ and $100s$ fitted with linear rule, decay rate $= 0.04s^{-1}$.

Previous work in quantifying focus durations [17] on 17 cells of *Drosophila* wild type embryos, suggests a spread of durations between 30s and 4 minutes, with the peak of the distribution at 1m.

We find in our data the minimum duration of $10s$, which are foci found in just 1 frame of our time lapse movies. We find 2046 such trees, which correspond to foci that cannot be connected to any other foci in the previous or the next time instant. Since these 'single frame unconnected foci' possess no dynamic properties, we will exclude them from further analysis. We also find about 1395 such branches of duration $10s$. The difference between these two numbers is owed to single frame foci between merging and splitting events in a tree. For example, consider two foci at any time instant, which merge into one focus at the next instant, and then separate again in the next time instant after that. In our taxonomy, this constitutes one single tree, with five foci in it, but five separate branches, each with one focus.

From our data, we observe that the median duration of trees is $20s$, where as 90% of the trees have a duration under $70s$. We also observe that for branches, the median duration is at $30s$, with the $90th$ percentile at $60s$

We also find that 50% of all trees have durations greater than 30s, and this is where we choose to threshold our data, since we are more interested in the features of long-lived persistent foci. Also pragmatically, we have to make this choice because this corresponds to 3 recorded positions for a focus branch for out time lapse movies which have a temporal resolution of $10s$. This the minimum necessary to define a deviation from a particular direction, which we concern ourselves with while calculating angles and exponents in the following sections and chapters.

2.4.2 Myosin Intensity of Focus Branches

Looking at the intensity profile of a branch between birth and death events, and we find the evolution of intensities to be a Gaussian shaped curve. The areas, and concentrations also show similar trends (figure 2.6).

We are not surprised to see this shape of the intensity profile, since, due to the nature of thresholding described in section 1.6.1, we are only able to detect foci once their intensities rise above a particular 'sea-level' of signal, and we stop detecting them once their intensities fall below it.

However, the same trend in the shape of the area profile tells us that Myosin concentration into the focus occurs well into its flow phase, and only is overtaken by the disassembly about halfway into the duration of the pulse, which occurs on a time scale of 10s of seconds [35].

Comparing the intensity profiles to the concentration profiles, we see that the 75th percentile of total intensity of Myosin may vary between 20000 to 40000 units of fluorescence between birth and death, and the concentrations may vary between 4000 to 4500 units of fluorescence.

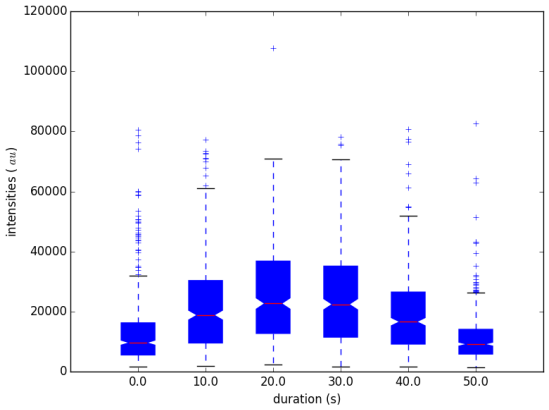

(a) Myosin intensity in $a.u.$ for focus branches of duration 50 s, notches on the box at 95 % confidence intervals

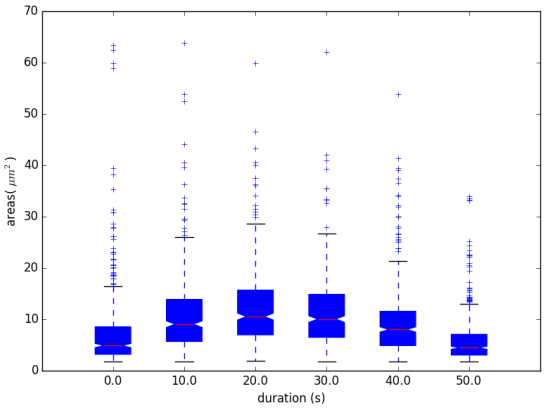

(b) areas in μm^2 for focus branches of duration 50 s, notches on the box at 95 % confidence intervals

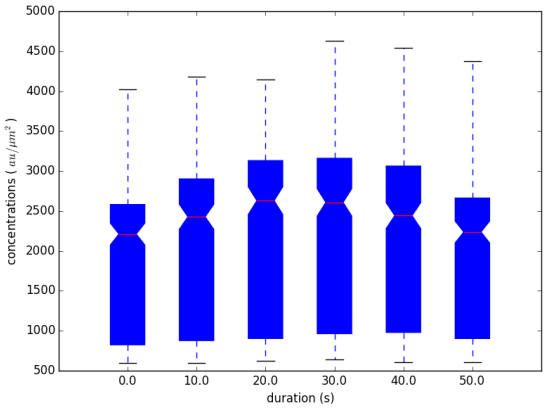

(c) Myosin concentration in $a.u./\mu m^2$ for focus branches of duration 50 s, notches on the box at 95 % confidence intervals

Figure 2.6: **Change of focus intensities, areas and concentrations (≡ intensity/area) during its lifetime.**

2.4.3 Speeds of Focus Branches

We can now calculate the speeds, or the magnitude of the displacement vector per frame.

Establishing the list of coordinates for a focus branch j as $\{x_i^j, y_i^j\}$ where $1 \leq i \leq d_j$, where d_j is the duration for that branch, we can define the average speed of the branch j as:

$$u^j = \langle |(x_{i+1}^j - x_i^j, y_{i+1}^j - y_i^j)| \rangle_i, \forall i \in 1..(d_j - 1) \tag{2.4}$$

We plot the histogram for these values in figure 2.7 and compare them to the values found in literature. For example, in the amnioserosa, the mean speed of the foci has been reported as $0.1\mu m/s$, and in the invaginating mesoderm in *Drosophila* ventral furrow formation, the speed has been reported as $0.04\mu m/s$ [43].

We find that the peak of the histogram, the most likely speed of foci to be around 0.04 $\mu m/s$, with 90% of foci with speeds above 0.03 $\mu m/s$, telling us that all foci are mobile. We find the median speed is around 0.08 $\mu m/s$. The mean speed is higher at 0.09 $\mu m/s$, owing to the long tail of the distribution because of a few fast moving foci.

We can also now calculate and plot (in figure 2.8) the end to end distances of foci, which are simply defined as :

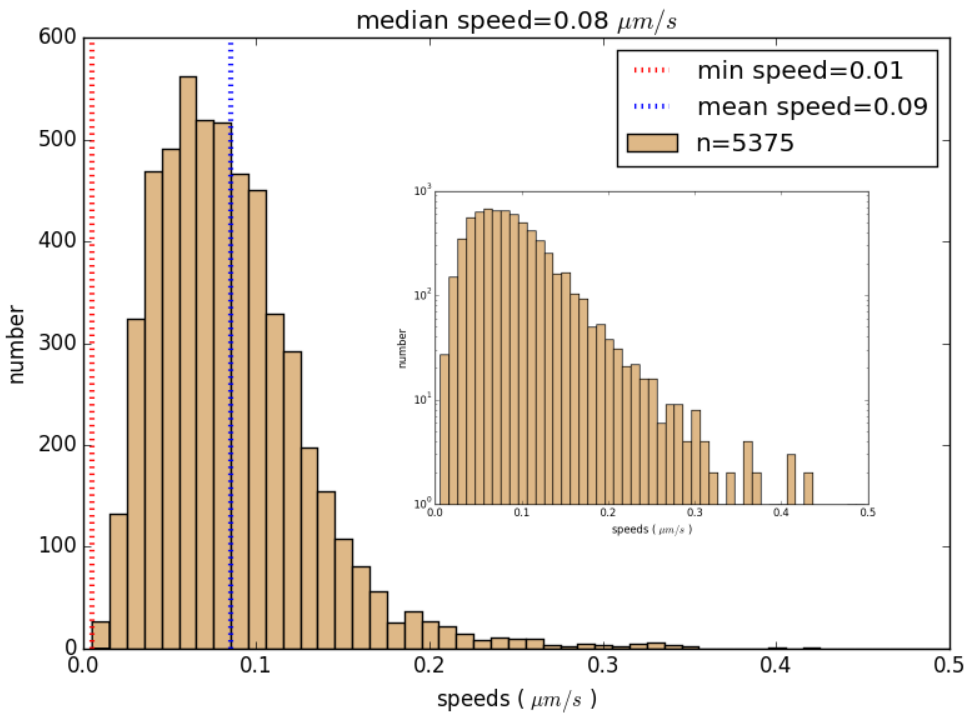

Figure 2.7: **Speeds of foci:** histogram, inset in log-y scale

$$s^j_{ete} = \sqrt{(x^j_{d_j} - x^j_1)^2 + (y^j_{d_j} - y^j_1)^2} \tag{2.5}$$

This gives us a measure of the displacements of the foci from their original position at the time of birth. The decay rate of the tail of this distribution, fitted by an exponential, tells us the probability of finding the focus as we move further and further away from its birth position.

We find the median displacement of foci to be 1.6 μm away from their original position, with 80 % of all foci to within 3.2 μm from their original position. Given that the most common speed of foci is 0.04 $\mu m/s$ and the most common duration is 30 s, this figure is close to the value we would expect if the motion of the foci was a directed, ballistic motion.

Correlating the speeds, to the end to end distances, and to the durations of foci, we find that the most mobile foci (for which end to end distances are greater than the median), travel at speeds between $0.1\mu m/s$ and 0.17 $\mu m/s$, This corresponds to 50 % of our tracked foci. These are also, in general, the most intense. We further find that the largest distribution of speeds corresponds to the most short-lived foci, and the spread in the distribution decreases for foci of longer durations, which again corresponds to the most intense foci. All these factors induced us to restrict our analysis to foci of durations at least 40 seconds in the following chapters. We have already learnt that the most intense foci generally live longer, and travel further.

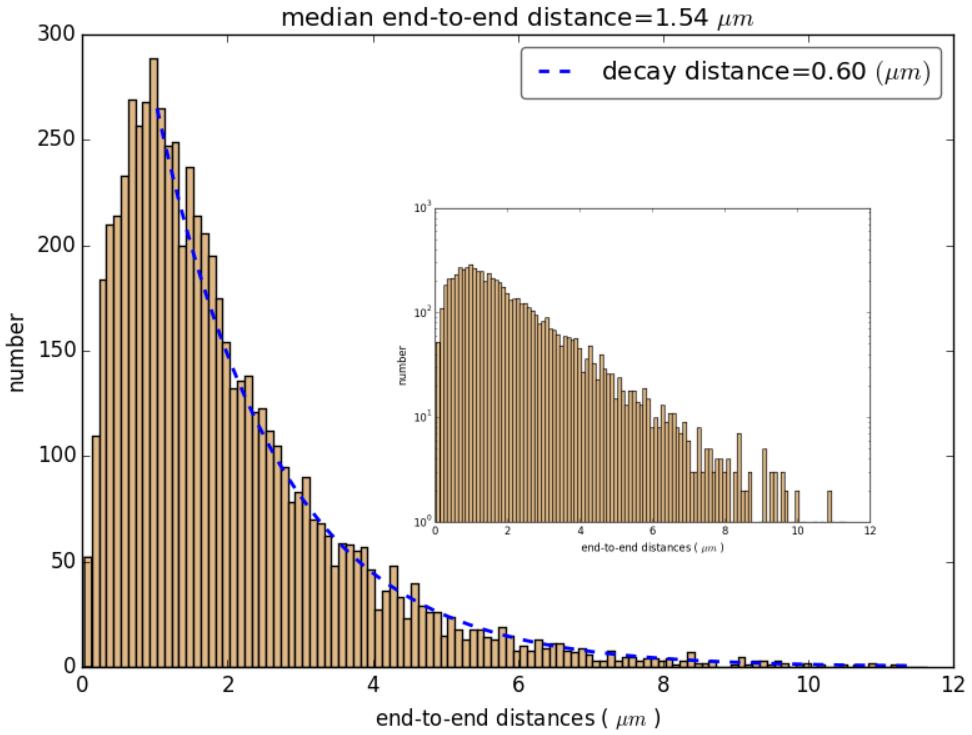

Figure 2.8: **End-to-end distances of focus branches:** histogram, inset in log-y scale

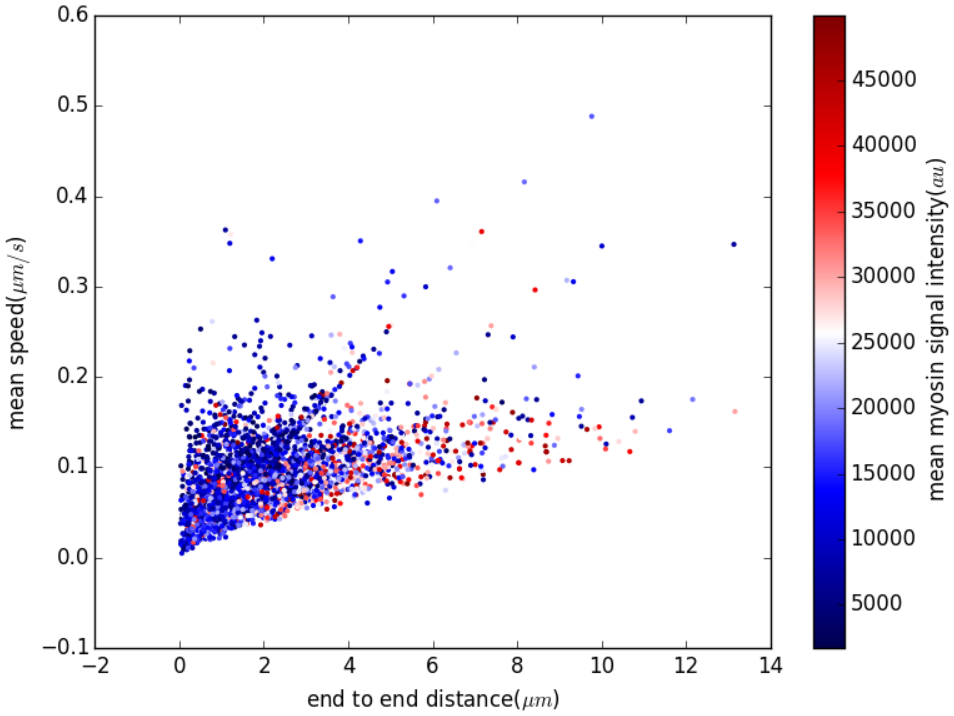

(a) focus mean speeds vs end to end distances color-coded by intensity

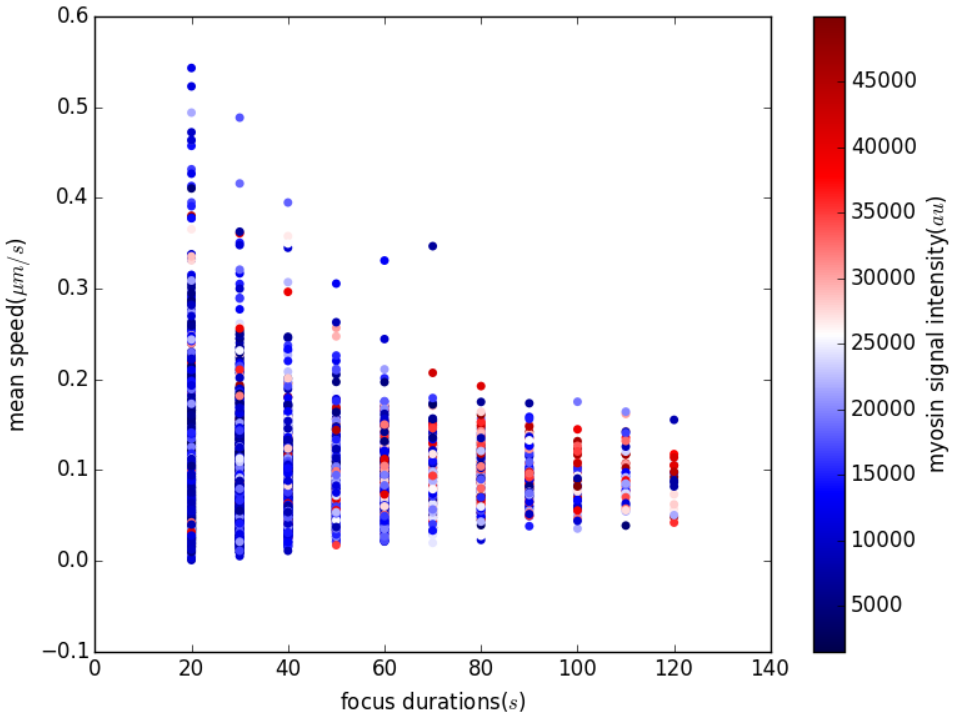

(b) focus mean speeds vs durations color-coded by intensity

Figure 2.9: **Plots showing relations between speeds, durations and end-to-end distances with mean intensity**

2.4.4 Angles of Deviation for Focus Branches

Looking at the paths taken by focus branches, we now want to find out whether foci travel in straight paths on the apical surface of the cell, and to quantify any deviation from this path. To do so, we calculate the angles of deviation of individual focus branches at subsequent points on their trajectories,

Thus, at every part of the trajectory taken by a focus branch, we calculate the angle between the vectors:

$$\theta_i^j = \cos^{-1}\left(\frac{(x_{i+1}-x_i, y_{i+1}-y_i)\cdot(x_{i+2}-x_{i+1}, y_{i+2}-y_{i+1})}{|(x_{i+1}-x_i, y_{i+1}-y_i)||(x_{i+2}-x_{i+1}, y_{i+2}-y_{i+1})|}\right), \forall i \in (1..d_j - 2) \tag{2.6}$$

This gives us the deviation at each 'step' (or the discrete time point when the location of a particular focus is imaged in the time lapse movies). If the branches were indeed travelling in straight lines, the distribution of these angles of deviation would be centered around 0°, where as if the motion of the branches was diffusive, would expect all angles in the range 0° to 180°, to be equally represented in the distribution.

We plot a histogram of these angles of deviations for all branches.

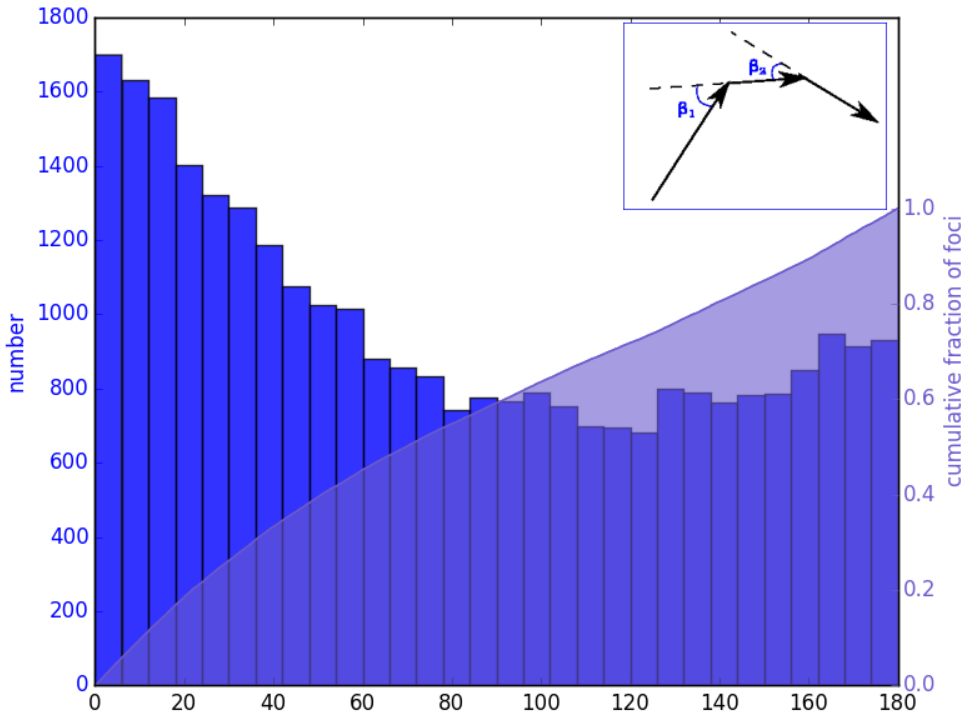

Figure 2.10: **Deviations along the path of a focus branch :** Panel shows histogram of distribution of angles of deviation. Inset shows diagram of a typical focus branch trajectory in black, illustrating how angles of deviation are calculated

We find that the distribution of the angles of deviations is somewhat between the two scenarios described above. While all angles are represented, the distribution is not isotropic and instead has a pronounced bias towards values near 0°, a sag in the middle, and another small but persistent peak at large angles around 180°.

The peak at 180° points to a curious feature of foci preferentially retracting their own path than travelling in a direction perpendicular to it. Repeating this calculation over different tissues in different developmental epochs of dorsal closure, we find similar results in all cases.

Overall however, these results argue that foci are persistent in their motion in a particular direction. We investigate this feature further by defining an preferred direction of focus propagation, which is described in 3.2, where we explore different kinematic rules for focus motion.

We can also define the mean angle of deviation for each focus branch as $\bar{\theta^j} = \langle \theta_i^j \rangle_i$, and this is a measure of the deviation of the foci from its original path. We find that the values of the mean angle of deviation $\bar{\theta^j}$ are distributed uniformly over the most common values of speeds, areas, durations and intensities. Thus at this stage, we find that the angles of deviations of foci are independent of their Myosin content or speed.

Plotting the mean angles of deviation against the end to end distance, s_{ete}^j, for each focus branch in figure 2.11, we see that for the most common end to end distances, between 1 to 2 μm, the mean angles of deviation are distributed equally among all possible values, but for higher end to end distances, the mean angles of deviation take small values. This may be understood intuitively, as on a 2D surface, the largest end to end distance possible for a trajectory of given speed, occurs when the mean angles of deviation are zero.

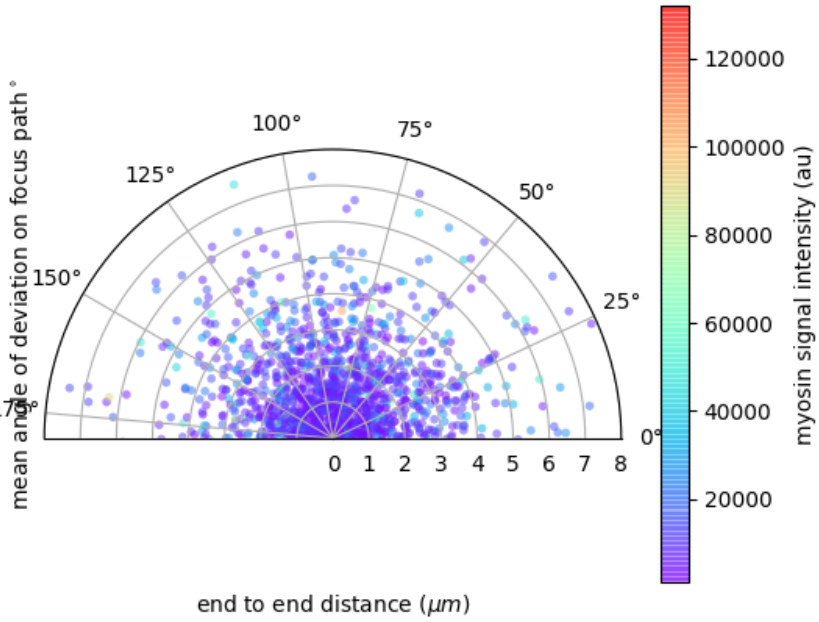

(a) Plot of angles of deviations vs end of end distances for foci

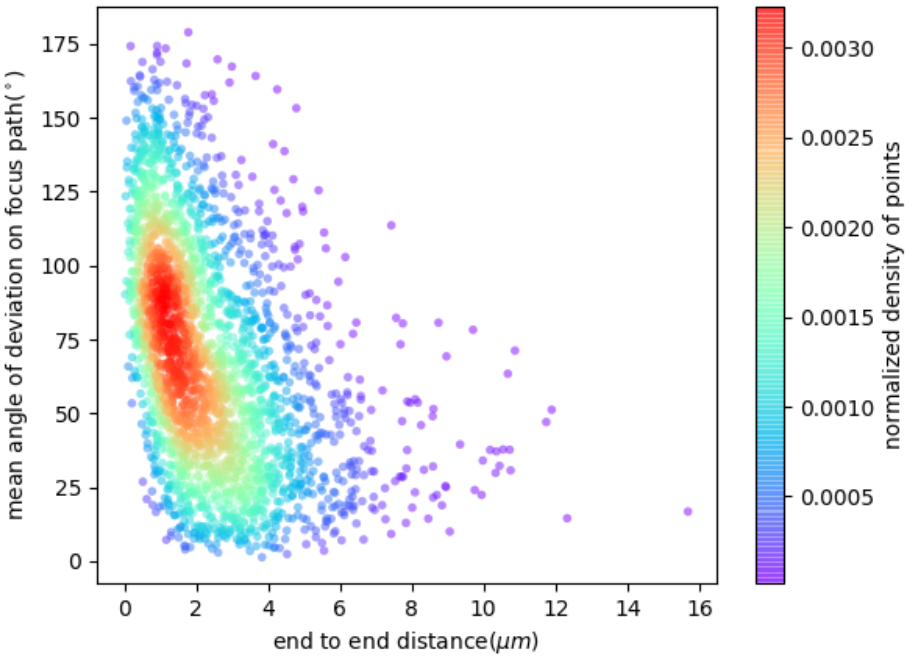

(b) Plot of angles of deviations vs end of end distances for foci

Figure 2.11: **Correlation between focus angles of deviations and end-to-end distances**

2.5 Focus Events in Developmental Time during Dorsal Closure

As we've seen before in section 1.4.1, cell pulsations during dorsal closure (DC) may be described in three distinct epochs. Having defined births and deaths for each focus branch, we now quantify this during the whole of developmental time for DC, to see whether these epochs are marked by different phases of focus activity. To do this, we plot a distribution in time for all birth and death events per cell per minute (in this section, we do not restrict for branch duration, however single-frame trees, which are both birth and death events, are discarded), happening during the process of dorsal closure, in figure 2.12.

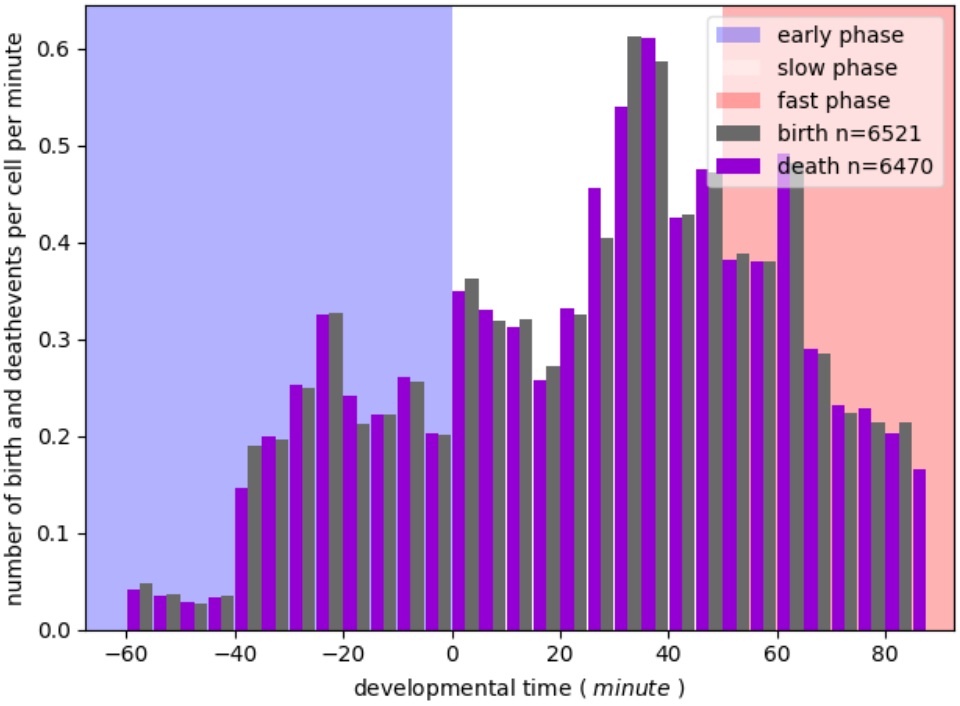

Figure 2.12: **Distribution of the number of birth and death events per cell per minute over DC:** Data sampled from 12 embryos in various stages of dorsal closure, each bar is $5min$ wide. $t = 0$ marks the start of effective tissue contraction. Red, White, and Blue represent the early, slow and fast phases of dorsal closure respectively.

We can analogously plot the distribution of other focus events, merging and splitting (figure 2.13).

We observe an increase in the frequency of all event types through early and slow phases of dorsal closure, finding a peak in number of events around $t = 30 - 35$ minutes. After that, the number of focus events falls (at $t = 90$ we have about one birth and one death event every ten minutes per cell). This can be attributed to the fact that around this time, the pulsatile focus activity is increased more and more by a continuous sheet of Myosin.

Here, we would also like to quantify the number of birth and death events as a function of distance from the cell membrane. As we have seen in figure 1.15, foci are more prevalent closer to the membranes than at the centre. Using the same normalization (the length of the semi-minor axis of the cell fitted ellipse), we now replot this for births and deaths, in the histogram 2.14.

The peak of this histogram corresponds to a distance between 1.5 to 2.5 μm from the cell membrane, after which we see the progressive drop in the number of events. This figure tells us that both birth and deaths are more common near the cell membranes.

We note here that our algorithm considers the foci present in the first frame of each cell movie, (if they can be linked to any other foci in the subsequent frames), as birth events. Similarly, linked foci present in the last frame are considered death events. However, given the number of foci polled, we consider that this

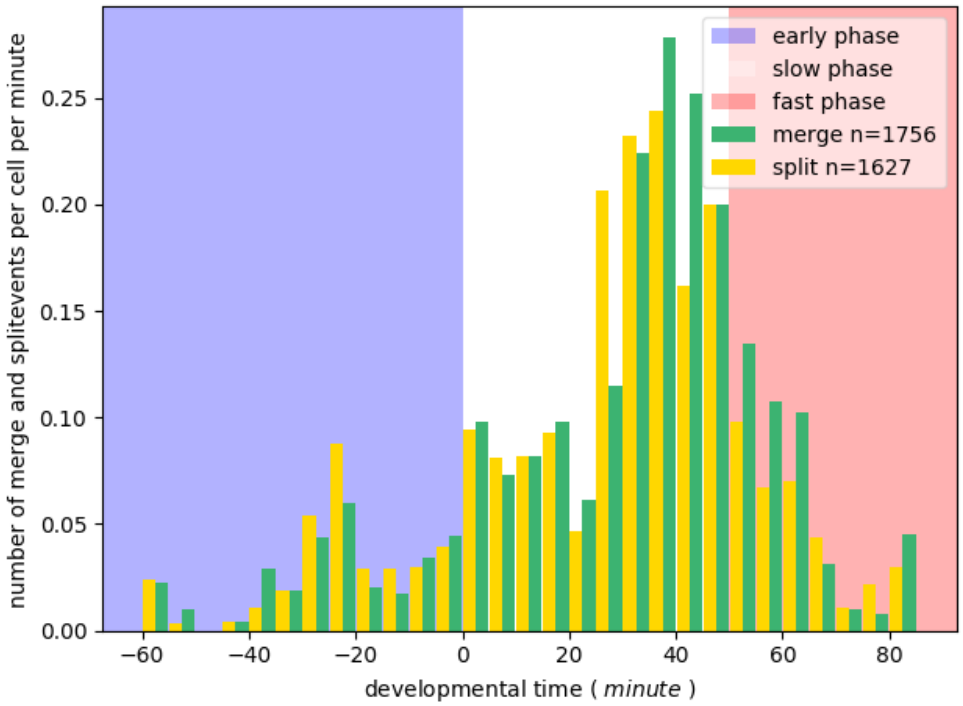

Figure 2.13: **Distribution of the number of merging and splitting events per cell per minute over DC:** Data sampled from 12 embryos in various stages of dorsal closure, each bar is $5min$ wide. $t = 0$ marks the start of effective tissue contraction. Red, White, and Blue represent the early, slow and fast phases of dorsal closure respectively.

artefact would have a negligible effect on our statistics.

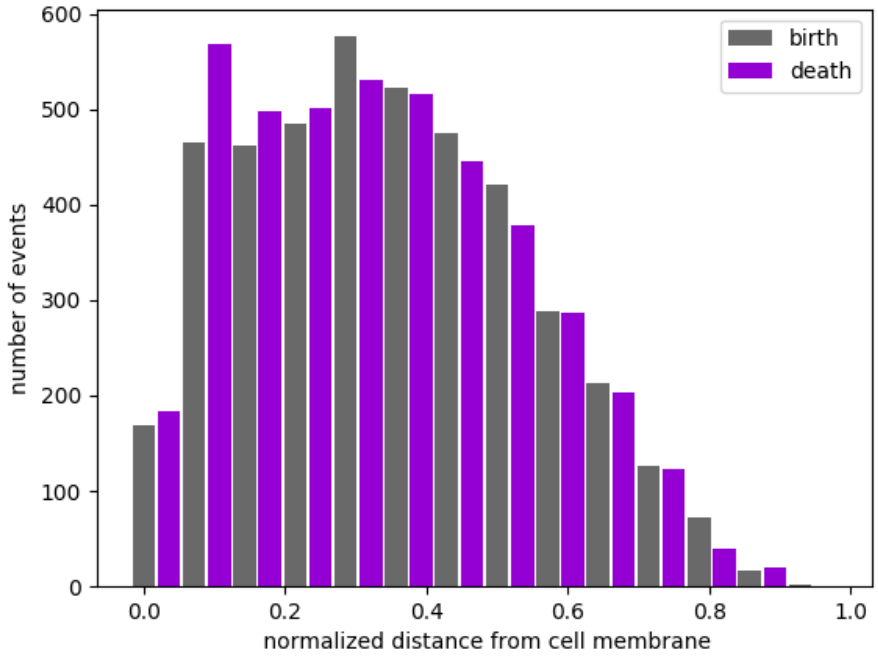

Figure 2.14: **Distance of births and deaths from cell membrane, normalized by the length of the semi-minor axis of the cell-fitted ellipse**

2.6 Conclusion

In this chapter, we have argued for treating the transient focal pulses as discrete objects with trajectories, and presented a way to track them in time, and reconstruct their motion. We have also observed (as a natural result of these assumptions, and elsewhere in other biological systems), the merging and splitting phenomena in foci. Then, we have obtained a phenomenological description of the basic kinematic features of foci, such as their relative changes in area and intensity during the course of their lifetimes. We have defined branch properties such as average speeds between subsequent frames, durations and end-to-end distances and we have seen the distribution of these quantities, as well as their evolution in time. What we found were mobile focus branches that endure between $20s$ to $1m$, and travel at speeds of the order of 0.1 $\mu m/s$. We note that between two frames, foci always possess a non-zero speed: there are no stationary foci. We also defined the angles of deviation on each branch, finding that these angles were not isotropic, instead being peaked at $0°$, telling us that the motion of foci might be directional, or even ballistic. But in the same distribution, we found a smaller peak at $180°$, telling us the foci retrace their paths, which does not correspond with the ballistic explanation.

In the chapters that follow, we shall be looking into the directionality in greater detail, describing a law of motion for the foci in mechanistic terms, and asking ourselves if we can predict their motion. We shall also ask ourselves what the factors are responsible for their directionality, and scrutinizing biochemical and mechanical explanations commonly cited in the literature.

Chapter 3

Statistical Features of Focus Paths

3.1 Introduction

From chapter 2 we have obtained a phenomenological description of the main focus properties. And now we are concerned with quantifying their motion in a more mechanistic framework, treating them as point particles located at their mass-centres and observing their motion. To investigate the mechanism of focus propagation, we follow focus branches along their trajectories, quantifying motion between birth, death, merge and split events. We will treat these trajectories as the point-wise motion of a discrete object on a 2-dimensional domain, the cell-cortex. As we have seen from the results of chapter 2, these trajectories have well defined speeds, and their deviations suggest that they might have directionality properties.

Thus, this chapter mainly deals with investigating the time evolution of the two features of the point-wise trajectory of the focus, their directionality, represented by angles of deviation, and their travelling distances, represented by their mean-squared distances.

In the previous chapter, we observed that the motion of the focus within a branch might be oriented along a certain direction. In this chapter, we are concerned with determining this direction. Asking ourselves if this is significant, we will quantify the motion of the foci that is aligned with, or that deviates from this direction. We will also investigate the geometrical constraints that might be responsible for setting this direction.

One of the strengths of the automated tracking of foci described in chapter 2 is that we poll a large number of foci, which enables the use of the tools of statistical mechanics. In this chapter, we will determine the known laws of motion that the foci obey, by calculating the mean-squared-displacements (MSDs) on the the observed trajectories. MSDs, first used to study the Brownian motion of molecules in a fluid, is the measure of the expected distances travelled by a particle over time. For any particle, fitting the observed squared-distances with a power-law, we arrive at a law of motion that the particle obeys. The exponent of this power-law tells us the measure of deviation from the behaviour of a diffusive particle, which would have an exponent value of 1. A ballistic particle, for example, that travels with a uniform speed in a particular direction, would have an exponent of 2 (since in this case, $d = vt$, thus $d^2 \propto t^2$). Such behaviour is called super-diffusive. Similarly particle with this exponent less than 1 is said to have a sub-diffusive behaviour.

Prediction of the motion of a single particle of gas in a large container is infeasible, however using the laws of thermodynamics, one can predict the average motion that the particles follow. Analogously, we will find that while the motion of a single focus trajectory is erratic, calculating the average of the squared displacements over all focus branches enables us to characterise their average behaviour.

3.2 Preferred Direction for Foci

In section 2.4.4, we found that the angles of deviation of foci are not isotropically distributed. This hints at the focus branches travelling along a preferred linear direction between two events. We attempt to quantify this by defining a preferred or mean direction for focus movement.

Thus for the set of focus branches, $\mathbf{F}$, obtained through tracking we have the positions in each frame as $\{(x_i^j, y_i^j)_{i,\,1\le i\le d_j},\ \forall j \in \mathbf{F}\}$ where the branch j has a duration of d_j.

We calculate the end to end vector for each branch as :

$$\mathbf{v}_{e2e}^j \equiv (x_{e2e}^j, y_{e2e}^j) = (x_{d_j}^j - x_1^j, y_{d_j}^j - y_1^j) \tag{3.1}$$

We calculate the mean position for each branch,

$$\bar{\mathbf{v}}^j \equiv (\bar{x}_j, \bar{y}_j) =< x_i^j, y_i^j >_i = \frac{\sum_{i=1}^{d_j} x_i^j}{d_j}, \frac{\sum_{i=1}^{d_j} y_i^j}{d_j} \tag{3.2}$$

and the second order variances in the postions of each focus branch, (dropping the j superscript),

$$\sigma_x^2 = \frac{\sum_{i=1}^{d_j}(x_i^j - \bar{x}_j)^2}{d_j} \tag{3.3}$$

$$\sigma_y^2 = \frac{\sum_{i=1}^{d_j}(y_i^j - \bar{y}_j)^2}{d_j} \tag{3.4}$$

$$\sigma_{xy}^2 = \frac{\sum_{i=1}^{d_j}(x_i^j - \bar{x}_j)(y_i^j - \bar{y}_j)}{d_j} \tag{3.5}$$

Then, the eigen-vector associated with the largest eigen-value of the matrix $\begin{bmatrix} \sigma_x^2 & \sigma_{xy}^2 \\ \sigma_{xy}^2 & \sigma_y^2 \end{bmatrix}$ gives us the orientation of the largest spread of the coordinates. This axis, taken in the direction of $\mathbf{v}_{e2e}$ of each focus branch, tells us the preferred direction of that branch $\mathbf{v}_{\text{pref}} \equiv (v_{\text{pref}}^x, v_{\text{pref}}^y)$.

We can then calculate the angles of deviation $\forall j \in \mathbf{F}$ from this preferred direction of motion as,

$$\theta_{\text{dev}}{}_i^j = \cos^{-1}\left(\frac{\mathbf{v}_i^j \cdot \mathbf{v}_{\text{pref}}^j}{|\mathbf{v}_i^j||\mathbf{v}_{\text{pref}}^j|}\right) \qquad \forall i \in (2..d_j) \tag{3.6}$$

where $\mathbf{v}_i^j \equiv (x_i^j - x_{i-1}^j, y_i^j - y_{i-1}^j)$, the displacement vector at each point in the trajectory. We plot the distribution of these θ_{dev} in the form of a histogram 3.1 .

We see a histogram highly peaked towards zero, implying that focus branches have a high directionality along the vector $\mathbf{v}_{\text{pref}}$. Nearly half of all motion happens within a range less than 20° of this direction. The distribution plateaus for higher values, until angles close to 180°, where we find a curious, small peak. We find that at steps at 180° are 100s more than the steps at 90°. We had also observed this feature in chapter 2 , figure 2.10, which told us that successive steps separated by a deviation of 180°, are more common than those separated by a deviation of 90°. Thus, this peak might be due to back and forth motion of foci.

We are interested in comparing this empirical directionality in the motion of foci with the directionality we would see in four known types of motion, ballistic, diffusive, self avoiding random-walk and drift-diffusive:

- Ballistic motion corresponds to the motion of a particle with inertia, where the velocity vector has a continuous time evolution, and thus tends to be identical between two successive small time steps. Thus, over a sufficiently small time window, direction and speed are conserved and distance travelled grows linearly in time. This means that each step in the trajectory is highly correlated with the previous, and the distance grows linearly in time in along a certain direction. In this case, we expect the histogram to be highly peaked at zero. Our histogram has such of feature of a high peak at 0°, corresponding to half of the steps. However, the small peak at 180°, as well is the histogram of angular deviations at each step (chapter 2 , figure 2.10) where we see many instances of high angles, tells us that this explanation is either not complete or not adequate.

- For a random-walk, or a diffusive motion, each step in the trajectory is completely uncorrelated from another, or, at any given time instant the focus is free to move in any direction. But this may be subject to external constraints due to confinement in cell, lack of substrate etc. In the unconfined version, the distance grows as the square root of time. In this case, we do not expect the line of

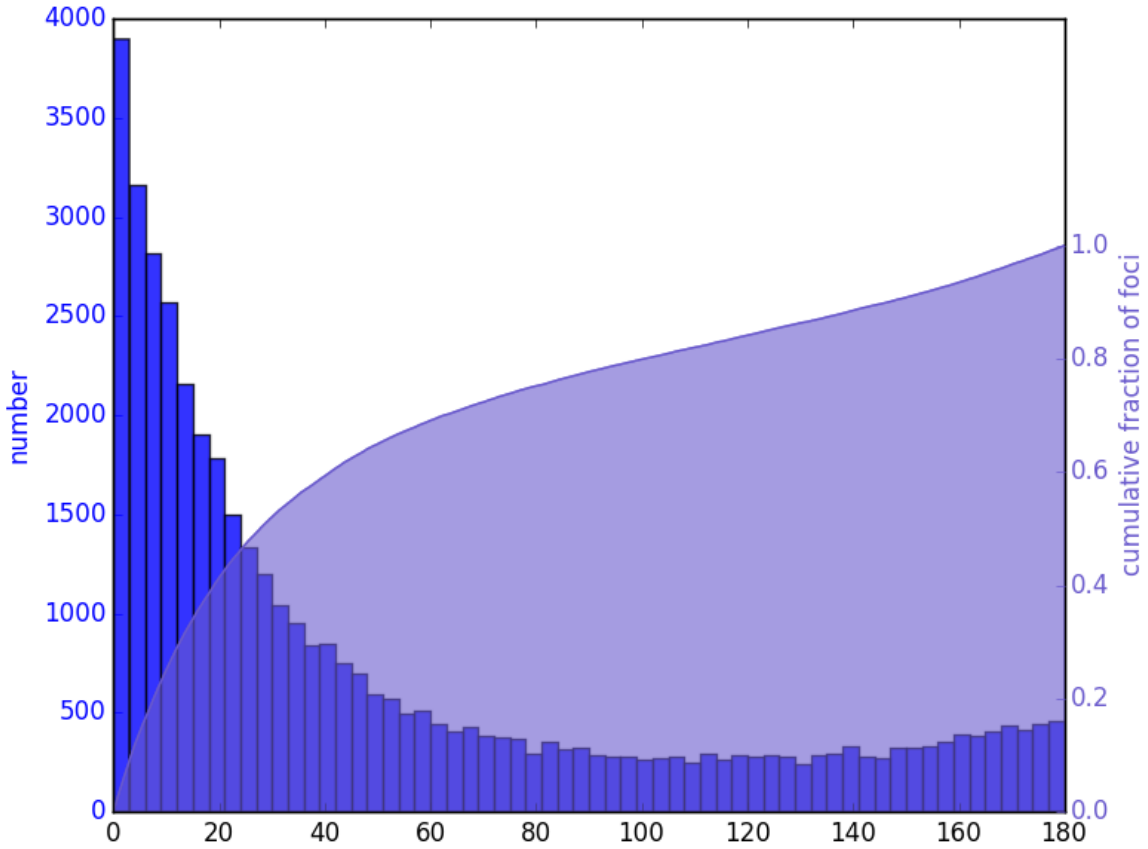

Figure 3.1: **Deviation from focus preferred direction :** Histogram of distribution of angles of deviation from defined preferred focus direction, $\mathbf{v}_{\text{pref}}$, in dark-blue. Cumulative distribution overlaid in light-blue.

preferred direction to possess any special meaning for a trajectory (except the meaning attributed to in the definition, which is the orientation corresponding to the greatest spread). Thus, though any given part of the walk ($\mathbf{v}_i^j$) is likely to deviate from any other part ($\mathbf{v}_k^j$) , with all angles between 0° and 180°, we would still expect the peaked feature in deviations from the preferred direction ($\mathbf{v}_{\text{pref}}^j$), that is seen in our histogram. However, we would expect the distribution in figure 2.10 to be isotropic. We note that a confined diffusive behaviour, where some angles are not available to the focus due to geometrical constraint, can bias such a distribution towards a particular direction. We can explore this further by isolating the motion of focus under different constraints due to cell shape geometry, as we will do in subsection 3.2.1.

- Self-avoiding motion / self avoiding random walk is one kind motion between the above two scenarios, where steps are somewhat correlated, focus is free to move in all directions except where it came from. distance time proportionality is between ballistic and random-walk, and the distance grows as the $0.75th$ power of time in 2 dimensions [62] [24]. In this case, the graph would be peaked at zero, but not as much as the ballistic case. But we would expect the distribution in figure 2.10 to have a trough at 180°, and we see that this is not the case. Same as the previous case, geometrical constraints can bias the motion to a particular direction.

- Drift-diffusion corresponds to the motion of a diffusive particle being advected on a constant velocity field [38]. In such a case, the directionality is provided by the velocity field or the drift, and once this field is calculated and subtracted from the particle trajectory, one would expect the distances to follow a diffusive law, being the distances would then grow as the $0.5th$ power of time. Analogously,

the histogram 2.10 would present highly peaked value in the beginning, as we observe here, but once the drift is removed, we would expect it to correspond to the histogram of a diffusive particle.

At this stage, some simulations of 'walks' on a two-dimensional square lattice, were performed with the various regimes of motion (diffusive and self-avoiding) to try to replicate the observed results. All walks were of a fixed number of steps, and the preferred direction was calculated using the same formula as above. Finally, the angles of deviation from this preferred direction were calculated using a sub-walk of a fixed number of steps.

The diffusive regime was modelled by a walker on a square lattice, with equal probability to move in any of the four directions available to it at each point. The self avoiding regime was modelled by a walker with equal probablity to move in any of the three directions except the one it came from, and zero probability to move in the direction it came from (any walk that 'annihilated' itself before the requisite steps, by running into its own previous path, was discarded).

Further, the effect of confinement was checked in both cases by using a confined lattice as opposed to an infinite one. The results of the simulations are presented in the figure 3.2.

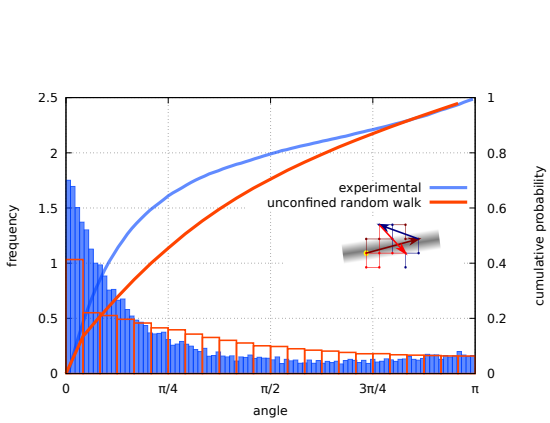

(a) Results of simulations with unconstrained random walk, or diffusive motion

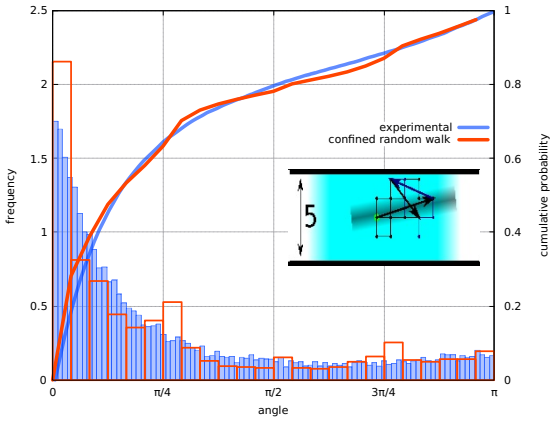

(b) Results of simulations with confined random walk, or confined diffusive motion

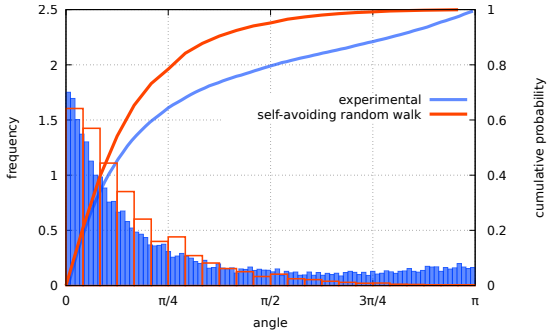

(c) Results of simulations with unconfined self avoiding random walk

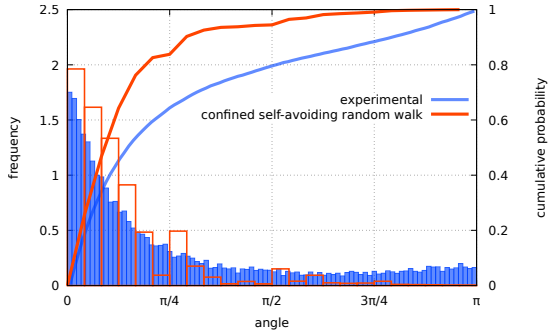

(d) Results of simulations with confined self avoiding random walk

Figure 3.2: **Deviations from mean direction of model particles**: Results of different types of simulations attempting to repeat the observed results. In each case, the observed angles (from figure 3.1) plotted with solid blue bars, results of simulations in hollow red bars. Respective cumulative distributions on the right y-axis.

Through this figure we find the closest correspondence between the experimental results and panel 3.2b, which is able to replicate many of the features of our observed histogram, including some of the backwards steps of 180°. We also note that figure 3.2a provides a good qualitative replication of the features in the observed histogram. However, this is hardly conclusive, and we proceed investigate mechanism of focus

directionality experimentally and not through simulations.

3.2.1 Orientation of Foci in Cell

To explore the confined diffusive hypothesis, we ask if foci move differently in cells of different degrees of confinement. Specifically, we want to see if high directionality in cell-shape implies more motion of focus along this direction.

To do this, we use information on the cell shape obtained in chapter 1, where we derived the instantaneous cell shapes (contour of the cell membrane) from every movie during the process of dorsal closure. We determine the ellipse that minimizes the least-squares error with each cell contour at each time instant through standard opencv libraries on C++ [19]. we then extract the orientation of the long axis, and the eccentricity of the ellipse. Then, using the number of segmented cells we have (number of unique cells = 434, with an average of 177.5 time points per cell), we can group them in quartiles of eccentricity.

We compare the average focus direction, defined in the previous section, with the orientation of ellipse-approximated long axis of the cell, at plot these distributions as histograms at the quartiles of eccentricity in the figure 3.3

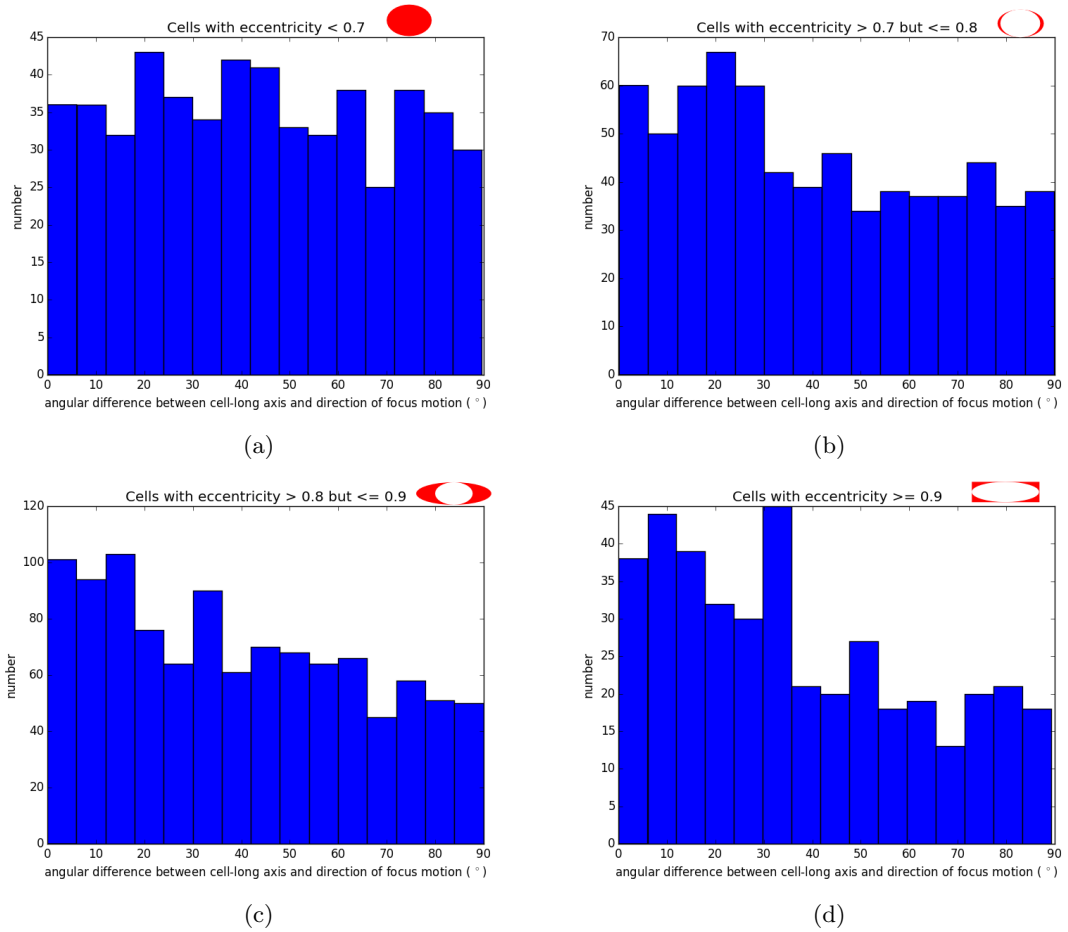

Figure 3.3: **Effect of confinement on focus directionality:** Histogram of angles between focus direction and cell long axis, for cells of different eccentricities, title legend shows ellipses in red that correspond to the values of eccentricity in each plot.

From these distributions, we observe that foci travel along the long axis of elliptical cells. This effect increases with the increase in ellipticity. Thus, confinement has a role in setting focus direction during DC. We can also explain small peak near 180° in figure 3.1 through confinement: when a focus reaches the edge

of elliptical cell, it has no choice but to retreat backwards or die.

From section 1.4.2, we know that that amnioserosa cells are quite elliptical, with average ellipticity around 0.8 through dorsal closure, decreasing as the process progresses. Thus we could hypothesize the motion of foci as a walk in confined domain, with the directionality set by the cell-shape orientation.

However, we see that the confinement effect is not enough to explain this completely. And that even in highly elliptical cells where, $\epsilon \geq 0.9$, half as many steps taken perpendicular to axis as along it (the figure 3.3d has 0.33% of steps greater than 45°). Thus, we have to explore other, additional mechanisms for directionality.

Replotting the figure 3.1 for cells of different eccentricities (figure 3.4), we find that backwards steps are more likely in highly eccentric cells, as compared to more circular cells. We see in figure 3.4(a), that in cells of eccentricity less than 0.7, these steps are as likely as intermediate steps.

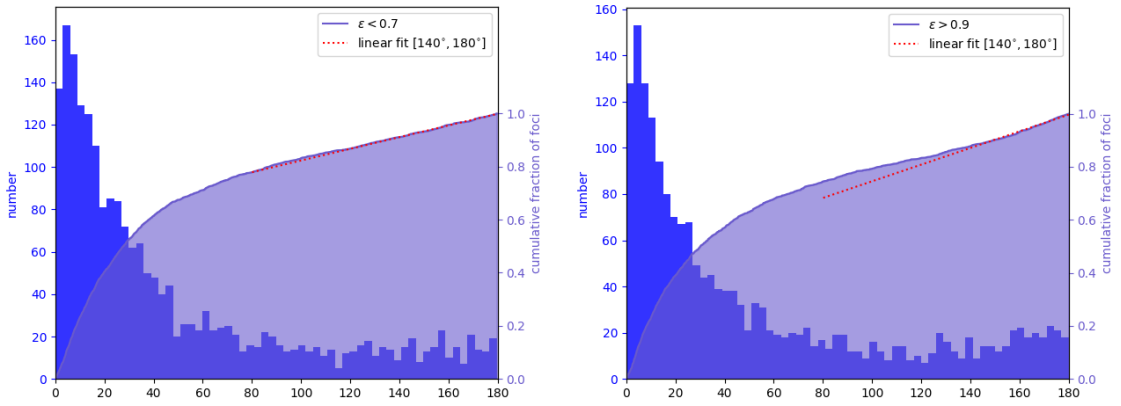

(a) Angles of deviation from focus preferred direction in cells of eccentricity < 0.7

(b) Angles of deviation from focus preferred direction in cells of eccentricity > 0.9

Figure 3.4: **Angles of deviation in different confinements:** Subsets of foci are chosen based on cell eccentricities, and figure 3.1 is replotted. The numbers of backwards steps (angles between 140° and 180°) are fitted with a line, showing deviation from the numbers of steps at intermediate angles.

3.2.2 Orientation of Foci in Tissue

We also repeat the question from the previous subsection 3.2.1, but now at the scale of the tissue. Specifically, we want to know if foci 'speak to each other' at scales greater than the single cell? More precisely, does motion of focus in one cell affect the motion of foci in neighbouring cell, and in cells further away?

So, in this subsection, we explore ordering of foci at tissue-scale. To do so, we need to take tracked focus data in the cell frame of reference, $\mathbf{F}$, and transform it to tissue frame $\mathbf{F}'$ using the following method:

From section 1.3, we have the instantaneous coordinates of the cell centroids, $\mathbf{M}_c(t)$ for every $c \in \{\text{cells}\}$ throughout dorsal closure, as well as time-instant corresponding to first appearance of cell $t_c(0)$.

Thus for each tracked focus f in cell c at location $\mathbf{M}_f, t_f$, we may find its position in the tissue using a simple Galilean transform like equation:

$$\mathbf{M}'_f = \mathbf{M}_f + \mathbf{M}_c(t) \tag{3.7}$$

$$t'_f = t_f + t_c(0) \tag{3.8}$$

where $\mathbf{M}'_f, t'_f$ now represent the focus' spatio temporal coordinates in the tissue frame of reference. We shall call this set in the tissue reference frame as $\mathbf{F}'$, and use it in the rest of this work.

Correlation with Tissue Orientation

We have seen that focus directionality is correlated with the cell orientations, and given that most cells are aligned with their long axis towards the dorso-ventral (DV) axis of the embryo, we can assume that focus motion might be aligned along the same axis.

Thus, in this section, we want to verify if this is true and focus motion aligns at the tissue scale. We find the orientation of the focus direction in anterio-posterior dorso-ventral (AP-DV) plane of the amnioserosa, and plot the distribution as the histogram 3.5.

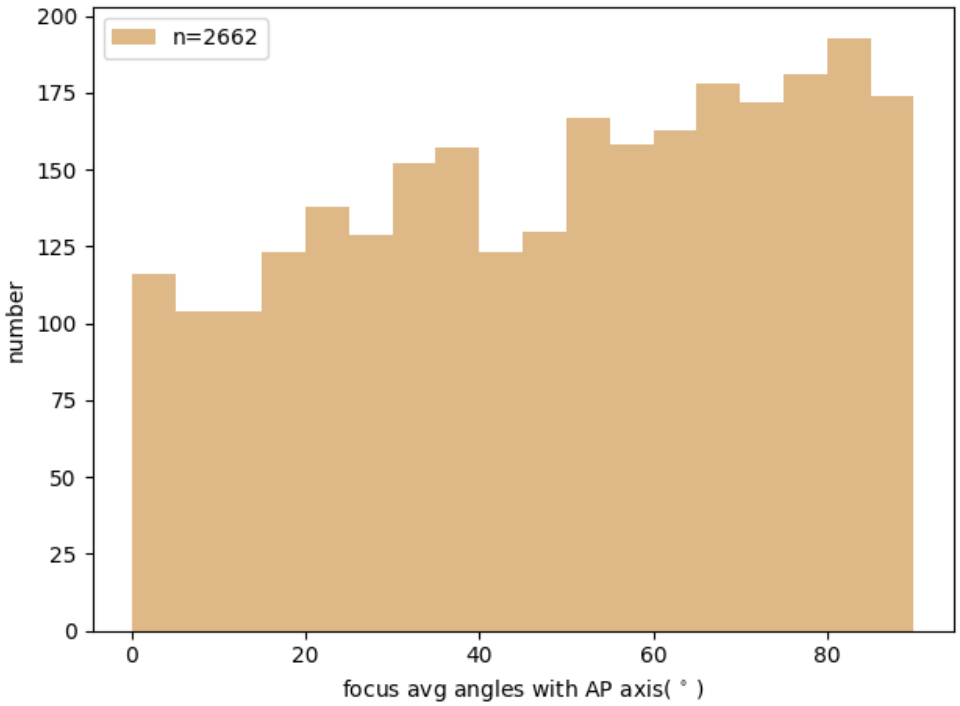

Figure 3.5: **Correlating focus directionality with tissue long axis:** histogram of relative angles of focus motion with the tissue AP direction.

We find the histogram has a small peak along the DV axis, implying foci travel along all directions almost equally, with a slight preference for DV. As mentioned, this can be due to confinement in cell, since most cells elongated around DV direction as shown in the figure 3.6.

But again, we find that correlation is not very strong, and as dorsal closure progresses, ellipticity decreases slightly, whereas focus activity increases.

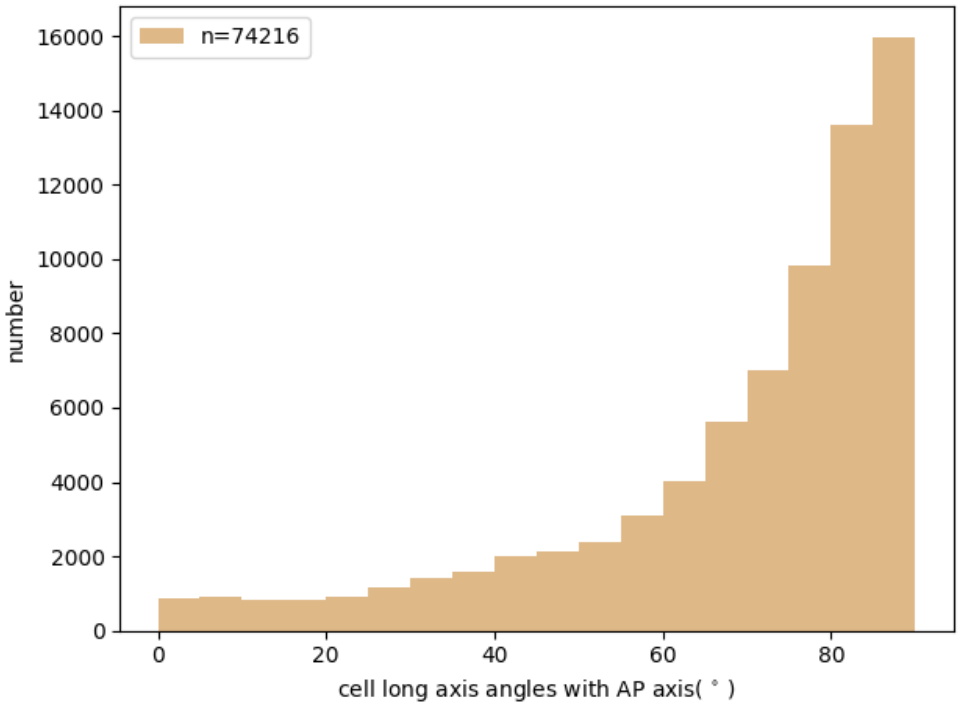

Figure 3.6: **Orientation of cells with respect to tissue long axis :** histogram of relative angles of cell long axis with tissue AP direction.

Correlation with Directionality of Other Foci

Asking if the motion of one focus influences another at the scale of tissue, we relate the direction of propagation of foci across the tissue, in the following manner:

for each focus branch $f' \in \mathbf{F}'$, we determine the distance with, and difference in the preferred angle of propagation with respect to, all other focus branches in $\mathbf{F}' \setminus \{f'\}$, and we plot this in the form of a 3d scatter plot, in the figure 3.7.

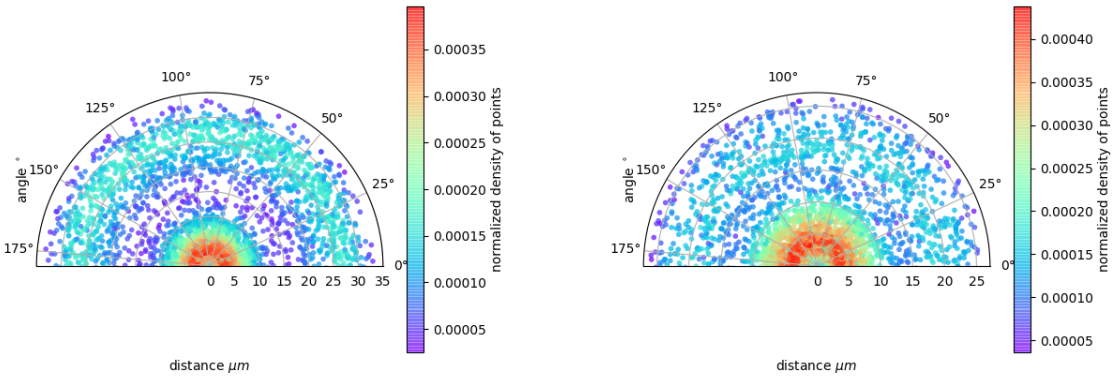

(a) Tissue 3a early

(b) Tissue 4a early

Figure 3.7: **Correlation between directions of all foci on tissue:** relative angles between foci, in $r - \theta$, for a tissue as a function of distance, for two different tissues from early dorsal closure.

We find that all angles are equally represented for all distances. To further visualize the uniformity of direction, we take three typical distances from the focus position, and calculate the distribution of the difference of angles, and plot these angles in the form of the histogram 3.8.

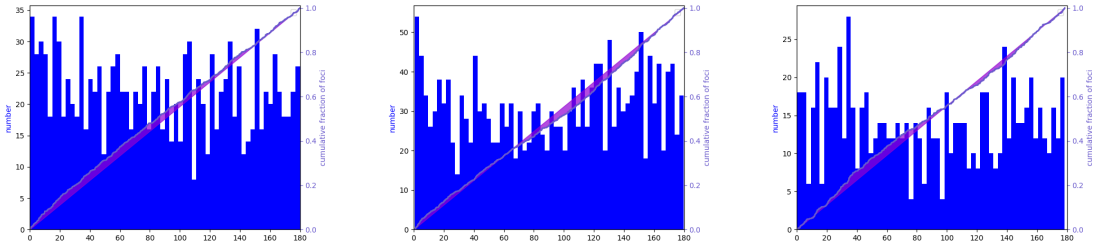

Figure 3.8: **Correlation between directions between foci at various distances:** histogram of the relative angles between foci at a distance between (a) 2 and 3 μm , (b) 4 and 6 μm, (c)15 and 20 μm between foci, for one tissue (3a early, figure 3.7a) in dark blue. Respective cumulative distribution overlaid in light blue line. its deviation from a uniform distribution is shown by the purple area. x-axis in °.

In these plots, we notice a small bias towards low angles in the closest distances, and another small bias towards high angles at intermediate distances. But apart from this, we find the angles represented more or less equally at all the three distances. This result is unexpected because if foci propagate due to a mechanical mechanism, we would expect them to influence each other through some kind of mechanical feedback at least at a short range. But there appears to be no correlation, even at small length-scales, in the direction of motion of foci. We consider this to be an important negative result, since this tells us that the focus directionality is something that is intrinsic to a particular branch, perhaps born as a result of the geometrical confinement that the focus is subjected to. Our analysis does not reveal any influence due to the interaction between a focus and its neighbours.

3.2.3 Trends in Focus Orientation over Developmental Time

Finally, in this section, we attempt to quantify any changes in focus directionality over developmental time. We determine the orientation of all focus branches over the mean developmental time at which that branch is tracked. Then, calculating the median and quartiles over developmental time, we visualise this in the form of a bar and whiskers plot 3.9

We find that the mean directionality of foci, staying between $40 - 60°$ remains largely independent of developmental time. We would expect the mean direction to be around 45° if the foci were oriented randomly on the tissue surface at each instant.

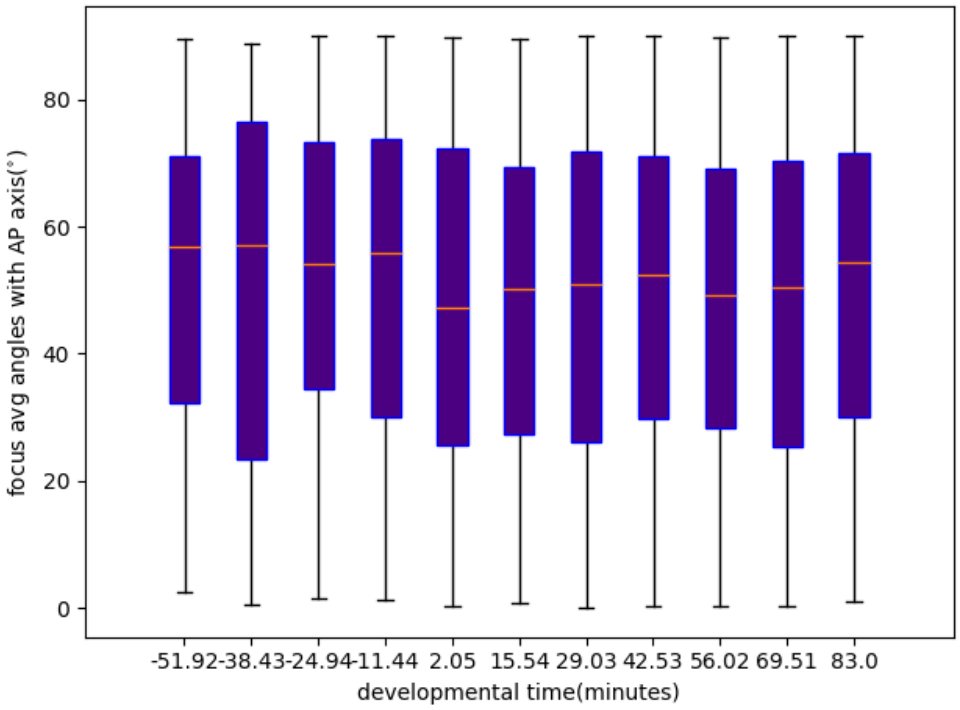

Figure 3.9: **Change in focus orientation with progress of dorsal closure:** Angles of focus motion during the course of developmental time. box width indicates the upper and lower quartiles, with red line at median.

3.3 Mean Squared Distances on Focus Trajectories

In this section we are again largely concerned with classifying the foci in the regimes of behaviour described in section 3.2 - ballistic, diffusive, self-avoiding and drift-diffusive (examples of the first three are illustrated in the figure 3.10). To recapitulate, these mean-squared distances grow differently with time passed, so to this end, we wish to derive the distance-time relation between foci at all points on their trajectory:

Thus for $\mathbf{F}$, the set of focus branches are obtained through tracking, $\forall j \in \mathbf{F}$ with a duration of d_j, we calculate the table of discrete time-lags $\{t_i^j\}$ and discrete distances travelled , $\{d_i^j\}$ for $1 \leq i \leq d_j$, for every $10s$ (which corresponds to the time-resolution of the time-lapse movies).

To this table we fit a power-law relation, as illustrated in figure 3.10:

$$d_i^j = (t_i^j)^{n^j} \forall j \in \mathbf{F} \tag{3.9}$$

Thus, the mean exponent is given as,

$$\bar{n} \equiv \langle n^j \rangle_j = \langle \frac{log(d_i^j)}{log(t_i^j)} \rangle_j$$

and the median, $\tilde{n}$ is defined analogously.

As argued in section 2.4.3, we restrict ourselves here to branches that last at least $40s$ or more, since the spread in speeds of focus branches decreases as the duration of the branch increases, so we can expect to have a more well-behaved distribution of exponents for higher durations. Pragmatically, we also find that mean error of fit goes up as the size of the branch decreases.

Plotting the distribution of all n in the form of a histogram D.2, we see wide range of exponents ranging between -2 to 4 implying that behaviour in all three regimes are presented by foci. About a third (34.7%) of foci behave diffusively or sub-diffusively, with an exponent less that 1. Going up to the self avoiding

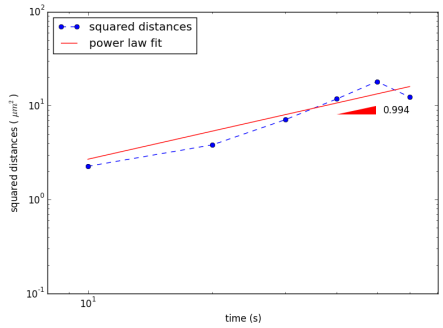

(a) squared distances versus lag, exponent = 1

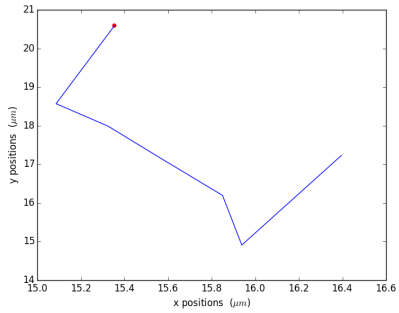

(b) Trajectory of branch on apical cell surface

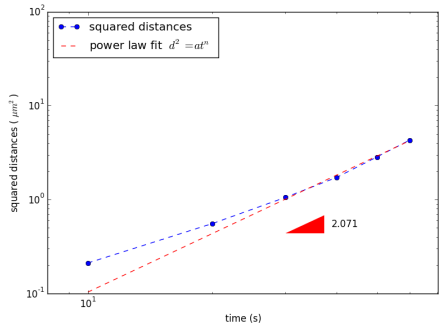

(c) squared distances versus lags, exponent = 2

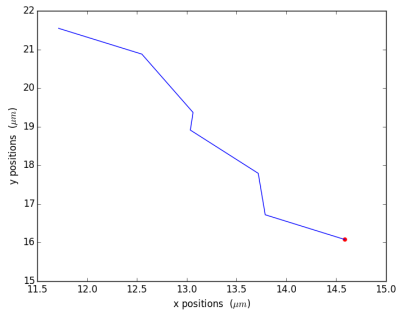

(d) Trajectory of branch on apical cell surface

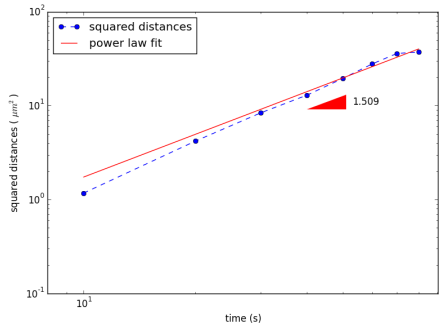

(e) squared distances versus lags exponent =1.5

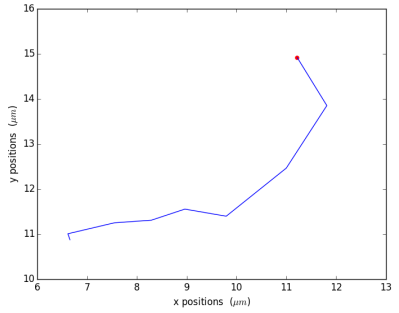

(f) Trajectory of branch on apical cell surface

Figure 3.10: **The different regimes of motion:** Squared distances versus lags, and trajectories in space, of a 3 different focus branches illustrating the three main regimes of motion, diffusive, with an exponent of 1, ballistic, with an exponent of 2, and self-avoiding, with an exponent of 1.5. the left panels (a), (c) and (e) show the poitwise squared distances vs lags in blue, and the power law fit on it in red. The right panels (b), (e) and (f) show the trajectory of the corresponding focus branch on the apical cell-surface, with each trajectory ending on the red point.

exponent of 1.5 accounts for approximately another third (64.5%), and another 20% are up to the ballistic exponent of 2. The remaining 15% have an exponent more than 2, showing a net acceleration. The median exponent is found to be 1.34, and the mean as 1.24.

We already have seen that diffusive dynamics is unlikely to entirely explain focus branch motion due to high directionality in section 3.2, and the high value of median exponent further confirms this hypothesis. We also recall the distribution of focus speed (chapter 2, figure 2.7), where we found between two-frames speeds clustered away from zero, with a minimum speed of 0.01 $\mu m/s$ among all foci. This is not compatible with purely diffusive dynamics, which, due to its lack of directionality, implies the peak of the speed at zero. However, the exponent is still too low for purely ballistic explanation.

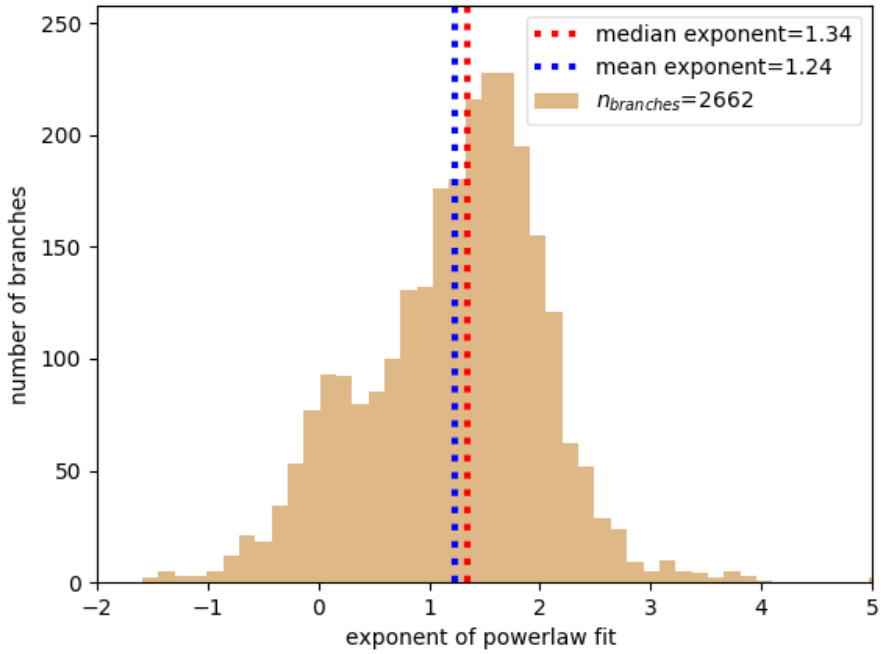

Figure 3.11: **Various regimes of motion for focus branches:** The distribution of the exponents of the laws of motion for the focus branches.

1.5 exponent value for 2D self avoiding walks is cited in literature [62] [24], so perhaps the motion of foci has something to do with self avoiding walk on 2D surface. As mentioned in section 3.2.1, confinement can have in changing the properties of motion, and it can equally change it exponent. For a self-avoiding walk confined domain, we can expect to have an exponent slightly lesser than the literature value, as seen from the simulations 3.2.

Here we take a slight detour from figure D.2, to explore the possibility of a drift-diffusive behaviour. To quantify this, we calculate a constant velocity drift field from the mean direction vector. We fit the projections of the focus positions on the mean direction vector with a linear law in time, giving us a drift velocity for each trajectory. The distribution of these velocities along the direction of the average vector is plotted in the figure D.3a. Then, calculating linear distances with time and subtracting them from the focus position, we find the new trajectory of the focus in a frame of reference co-moving with the drift field. Calculating the exponents of the MSD power-law in this new frame of reference, if drift-diffusion is indeed a valid hypothesis for our motion, we would expect to change the distribution of the exponents D.2 to a diffusive distribution centered at 1. Our empirical distribution following this process is shown in the figure D.3b.

Observing the speeds in the figure D.3a, we find them to be similar orders of magnitude as compared to the focus speeds in the figure 2.7. Observing the exponents, we find the distribution centered at 0, indicating that the focus behaviour in this frame of reference is sub-diffusive. We conclude from this that drift-diffusion cannot explain the observed focus trajectories. The combination of the comparable focus speeds and the small exponents tells us that most of the focus motion is along the mean direction vector, with very little motion happening perpendicular to it.

Coming back to the figure D.2, another feature of this distribution is that it can be expressed as the sum of two gaussian distributions, a low amplitude, high-variance distribution centered around 0.75, and another, high amplitude, low-variance distribution at 1.5 (figure D.5). As we increase the threshold of focus identification, this separation becomes more apparent. This led us to ask if we can consider two distinct populations of foci that move in different ways. A search was conducted over all observed properties of

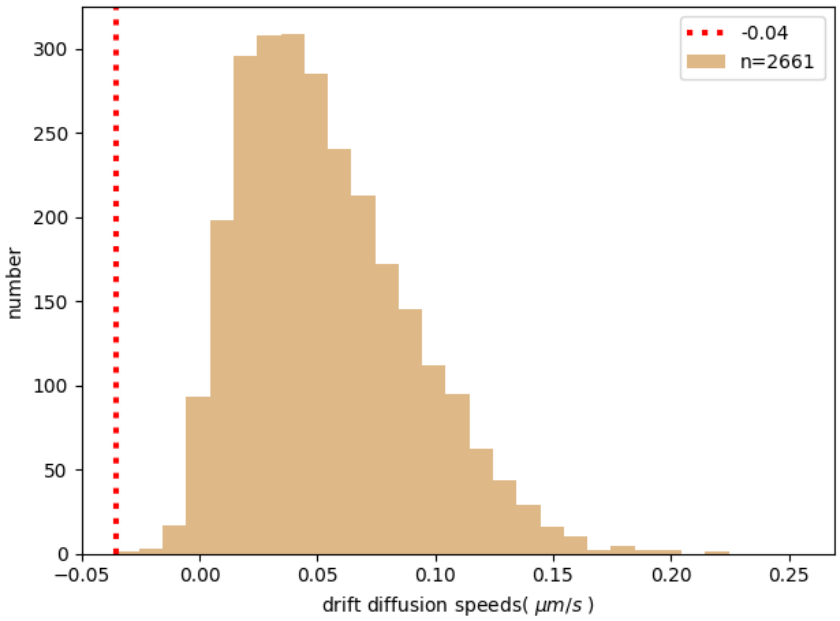

(a) Drift diffusion speeds

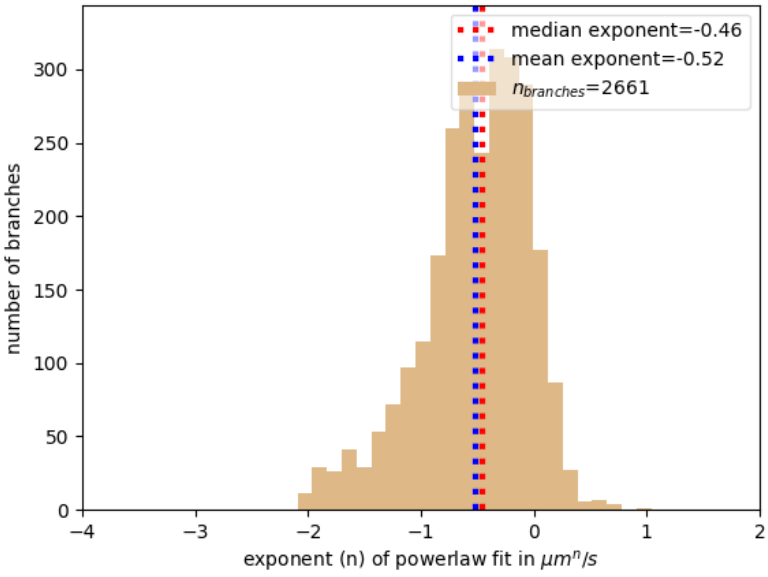

(b) Drift diffusion exponents

Figure 3.12: **Drift diffusion as mechanism of focus propagation**: Panel (a) shows the distribution of the constant speeds of each focus branch along its mean direction. Panel (b) shows the distribution of exponents in a frame of reference that travels with this constant velocity vector.

foci, such as their areas, intensities, durations, to see if there was at all a observable characteristic that differentiates the foci into these two populations[1]. But during the course of this work, no other focus properties were found that would confirm this hypothesis.

[1]The plots are presented in the appendix B

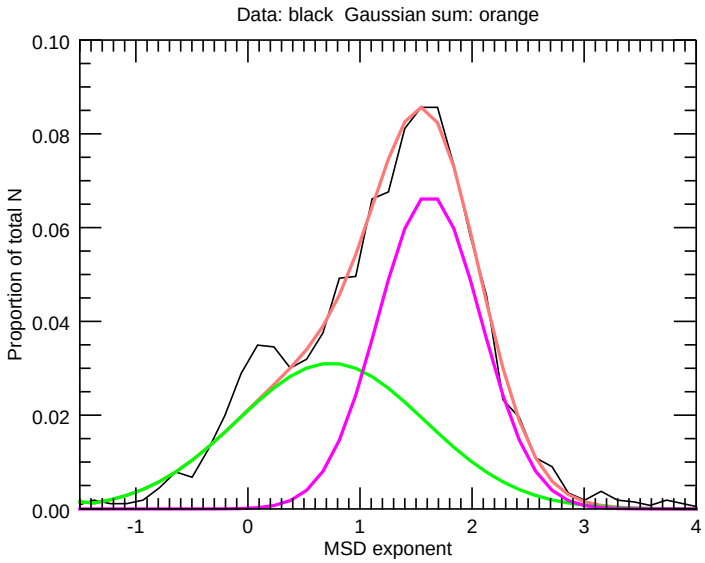

Figure 3.13: **Exponents of motion as a sum of two Gaussian distributions:** For the low exponent population $\mu_1 = 0.741, \sigma_1 = 0.833$, and for the high exponent population $\mu_2 = 1.619, \sigma_2 = 0.455$, fraction of area overlap between low and high $= 0.843$.

3.3.1 Trends in MSD due to Confinement

Since the motion of the Myosin foci are fundamentally linked to the actin cytoskeleton on which they propagate, and since this cytoskeleton is connected to the cell membranes via adhesion complexes, we can expect that the dynamics of Myosin will be influenced by the geometry of the cell in which it is present.

We thus expect the exponent of motion to be different in differently shaped and sized cells. Using the eccentricity of the cell fitted ellipse as a measure of the cell shape, we can correlate the exponent of focus motion to the mean eccentricity of the cell at that instant of time. We plot this in the figure D.6b. We also

check the influence of the mean area of the cell with the exponent of focus motion in the figure D.6a.

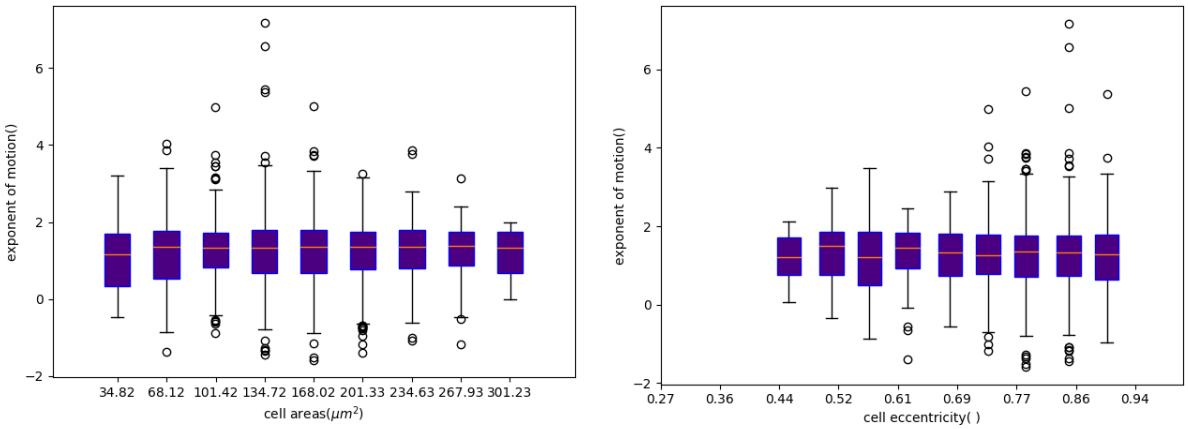

(a) exponents of motion vs cell area

(b) exponents of motion vs cell eccentricity

Figure 3.14: **Exponent of motion of focus branches due to confinement**

No apparent trends were found through this, though we note that in cells with high eccentricity, the spread in the exponent values is larger. A thorough search for the correlations of the distribution of exponents, with other cell and focus properties was done. however, no strong correlations were found in the course of this work. These figures are presented in the appendix B.

3.3.2 Trends in MSD over Developmental Time

Finally, we wish to check whether the dynamics of foci change over developmental time. It would be reasonable to think so since different epochs of dorsal closure show different modes of cell shape change, from slow to rapid as the process progresses, as seen in section 1.4.1. We have also seen that different epochs present different birth-rates (section 2.5) for focus branches.

Thus we correlate all the exponents of motion obtained over individual branch trajectories with the mean developmental time over which that branch is tracked.

However, we find no change in the exponent over the course of developmental time.

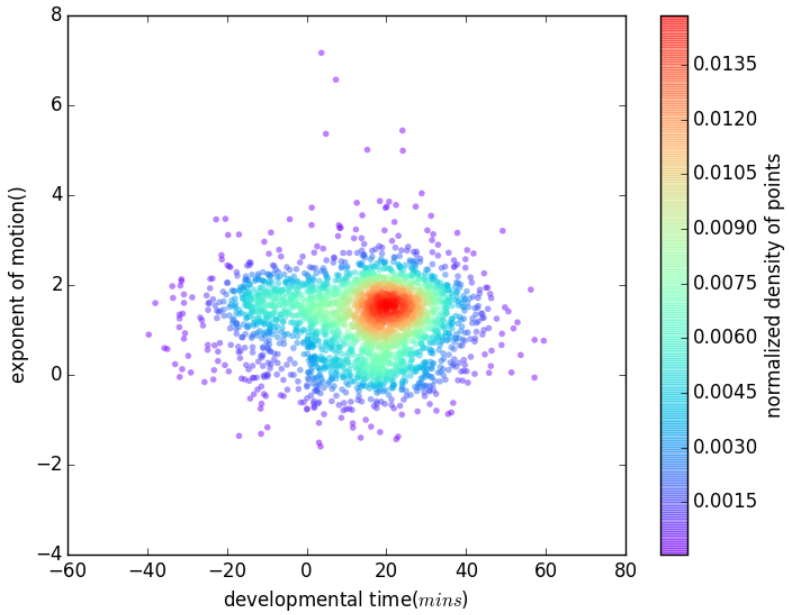

(a) Exponents of focus branches, vs developmental time of branch occurrence. Colorbar indicates the normalized density of points at each coordinate.

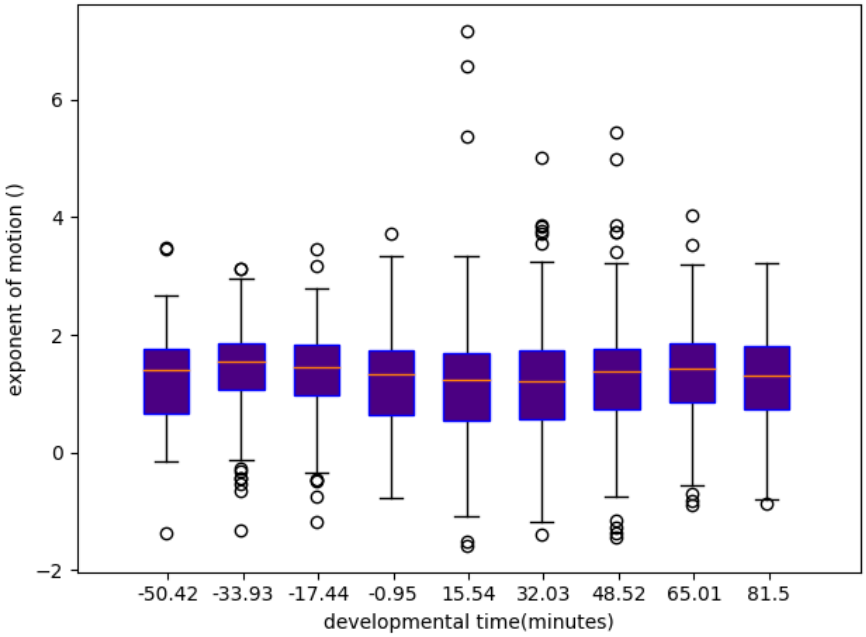

(b) Exponents of focus branches, vs developmental time, box width indicates the upper and lower quartiles, with red line at median

Figure 3.15: **Exponent of motion of focus branches with progress of dorsal closure:** Exponents of motions vs developmental times through D.8a scatter plot, showing the density of tracked foci in time. same plot in box and whisker formulation, D.8b showing roughly uniform distribution of exponents across time.

3.4 Conclusions

Thus, in this chapter we were concerned with quantifying the two degrees of freedom associated with every focus branch trajectory, namely its directionality, and the distances travelled by it. For the directionality, we have determined the 'average' direction of focus motion, finding that there is a strong preference for motion along that direction, and very little perpendicular to it. For the distances, we calculated the mean squared displacements of the foci, finding that while there was a rich array of behaviours associated with the branches, the mean of the exponents is around 1.5, which is the same as value in literature for self-avoiding random walks. We found that backwards steps were more likely than perpendicular steps, and this effect was more pronounced in foci present in more elliptical cells.

In both cases, we have tried to classify our trajectories with known regimes of motion, namely diffusive, ballistic and self-avoiding. With the non-zero speed of the branches seen in figure 2.7, and the high directionality seen in figure 3.1, we could conclude that the motion of the foci was not an unconstrained diffusive motion, but rather something that is more ballistic. We speculated that the histogram D.2, could be probably decomposed into two gaussians, hinting at the existence of different populations of foci, with different properties of motion.

We saw the effect of geometric constraints on the motion of focus branches, finding that in more anisotropic cells, foci predominantly travelled along the long axis of the cell. We also tried to correlate the directionality with the presence of other foci, but we saw no effect on propagation direction due to it. Finally, we found no correlation of the exponent of the squared distances with confinement or the change in developmental epoch.

Thus, at the end of this chapter we have obtained a global view of the motion of our focus centroids, and we note that these observations bias us towards a self-avoiding nature of these centroids. But, it is important to note that the centroid of the focus is not sure to correspond to any physical particle, since the motion of foci is a combination of advection as well as binding and unbinding dynamics.

Having followed the foci as they go by, we will, in the following chapter, change our frame of reference to one fixed on the tissue, change our formalism from discrete to continuous, and introduce a new framework to visualise apical Myosin activity.

Chapter 4

Space-time Features of Myosin Environment of Foci

4.1 Introduction

By the end of the previous chapter, we have hypothesized a self-avoiding behaviour for foci. In this chapter we want to put this hypothesis to a test and see in what measure the data we have allows to speculate on a mechanism explaining this behaviour. We do so by defining a method that will return us to a continuous focus Myosin signal, as opposed to the point particle based analysis that we have performed in chapters 2 and 3. At the same time, we will also define a method of point particle analysis to verify these new results.

The methods in this chapter also entail observing Myosin focus motion from the frame of reference fixed on the apical plane of the amnioserosa tissue, as opposed to a frame co-moving with each individual cell. We refer to these two frames as the tissue frame and the cell frame respectively.

We are also interested in including methods that are more independent of the success of tracking foci, than those described in chapter 3. Thus, in the continuous analyses described in this section, we will not be using the temporal relationships between foci that we derived in chapter 2, but only the positions of the foci identified in chapter 1.

To recapitulate, we have defined the four focus events as birth, death merging and splitting. In this chapter, we ask the question : are there some features in the Myosin signal around these specific events, that differentiate these points from any random point on the tissue? For example, for a specific birth event we want to verify if there are any identifying signatures of a focus birth in the Myosin signal in the parts of the cell or tissue localised around the event, at the times close to when the birth happened.

To do so, we investigate spatio-temporal features of the Myosin signal at the apical surface of the tissue around these events. Thus, the methods deal with isolation of the Myosin signal around a specific event, then sampling many such events during the duration of dorsal closure, then determining the central tendencies in all such signal obtained. Comparing these measures of central tendencies (which might be the average, for example), with the same measure from randomised parts of the tissue, or the average of the cell, we will be verifying if at all that event comes with an identifying signature. We will visualize this through a space-time kymograph.

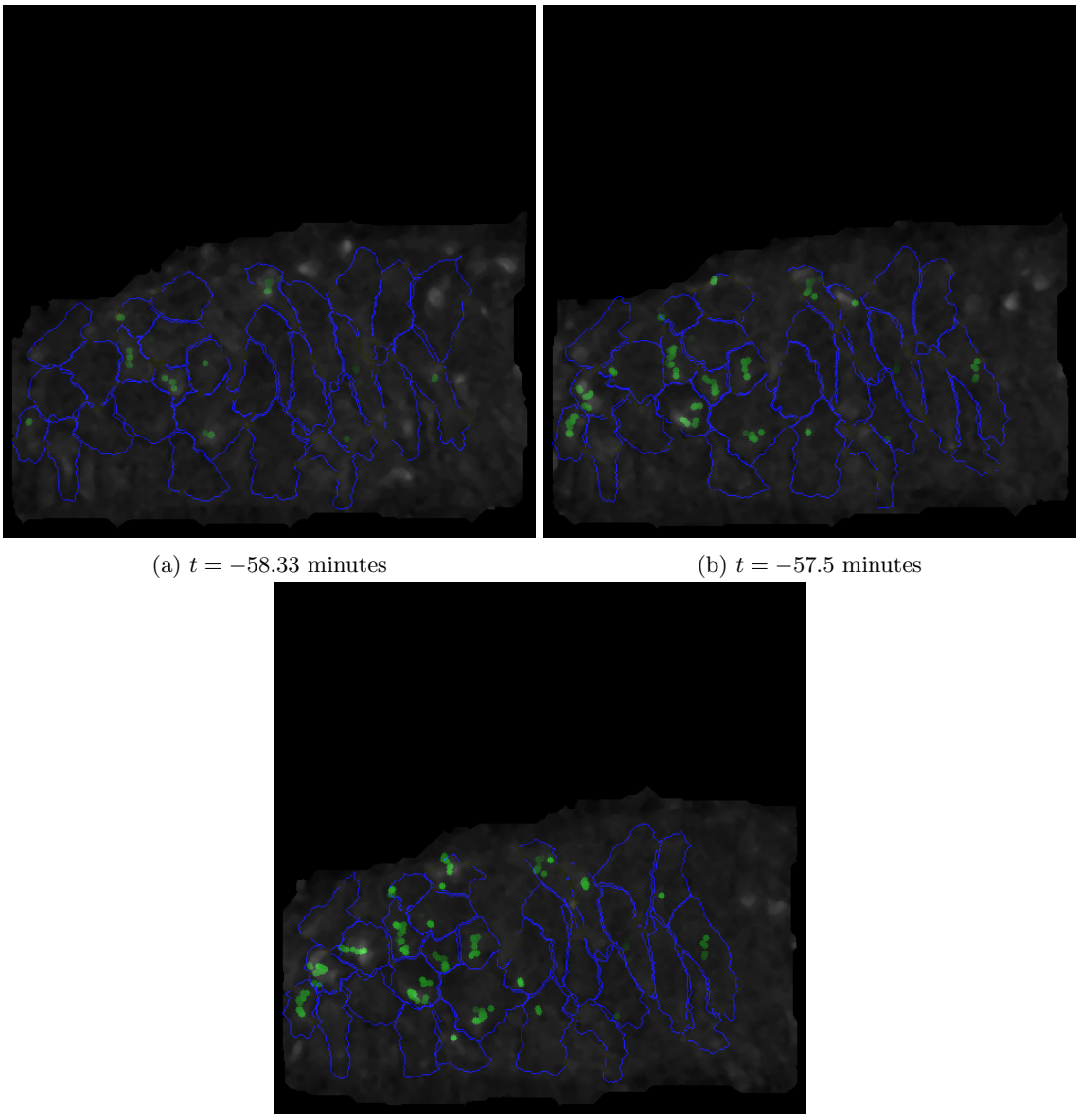

(a) $t = -58.33$ minutes

(b) $t = -57.5$ minutes

(c) $t = -56.66$ minutes

Figure 4.1: **Focus positions on the amnioserosa during dorsal closure:** Panel (a), (b) and (c) show the amnioserosa of one tissue (3a early) during three time points early dorsal closure, with cells outlined in blue. Tracked focus positions are overlaid as green dots, through the whole duration, to illustrate the progressive coverage of foci on the tissue.

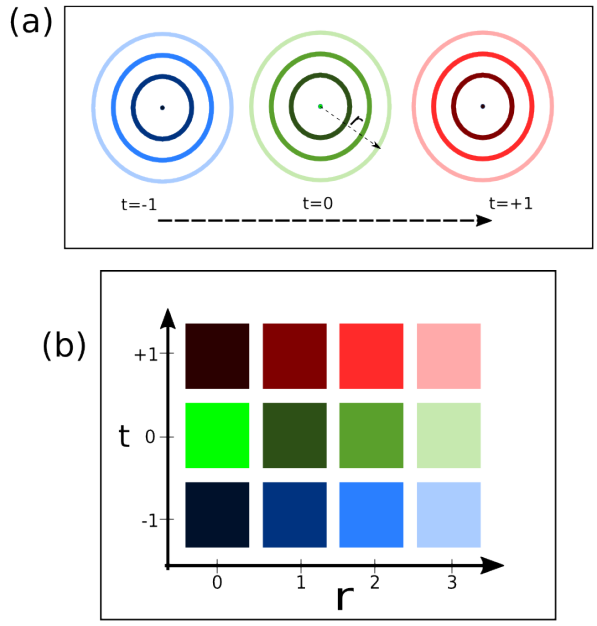

(a) Panel (a) shows a simple cartoon of a circular tissue, for three time points, containing four radial positions including the origin. We fix our origin at the centre of the tissue. As we move in time, the signal at each of these radial positions changes, illustrated by different colors. Panel (b) shows how this information would be visualised through a space time kymograph, where each of the 12 pixels corresponds to one of 4 radial rings, at one of 3 times.

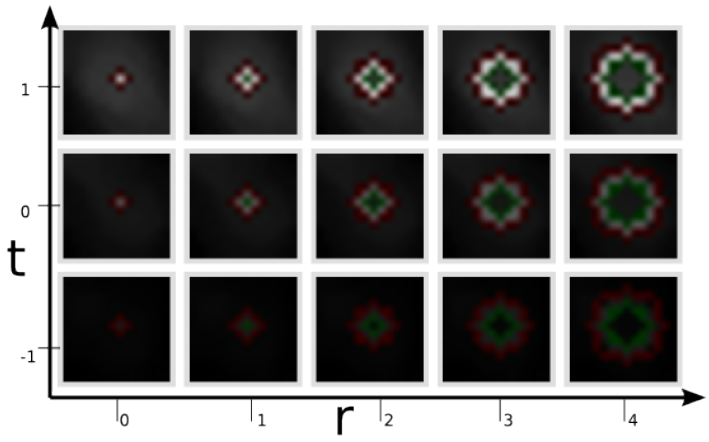

(b) A simple kymograph of 3 time points and 5 radial distances is illustrated, centered on a birth event. At each cell, the pixeleted circle between the green (where present) and the red circles is the region of interest, over which the Myosin signal is averaged. $t = 0$ marks a focus birth.

Figure 4.2: **How a kymograph encodes space time information**

4.2 Space-time Kymographs

The task of looking at the Myosin signal around foci can be performed through a kymograph, which is a space-time plot that shows us the signal value over some predetermined paths over time. However a two-dimensional kymograph, to accommodate a temporal dimension, must project the two spatial dimensions of the apical plane onto a line, and we have to be aware that we sacrifice spatial information in this analysis. Since we will be sampling many events across the tissue, and as we have shown at there is no privileged direction for focus motion at the tissue scale in section 3.2.2, we can assume that a radial projection around the focus would reveal the average trends. A major task in this analysis is the alignment of the spatial coordinates between events, and defining ways of averaging that reveal the trends at the correct spatial scales.

We begin with the set of spatial and temporal coordinates of all events on the tissue as defined as:

$$\mathbf{E}' = \mathbf{E}'_{\text{birth}} \cup \mathbf{E}'_{\text{death}} \cup \mathbf{E}'_{\text{merge}} \cup \mathbf{E}'_{\text{split}} \ , \tag{4.1}$$

where each term on the right hand side is defined as: $\mathbf{E}'_{\text{birth}} = \bigcup_i E'^i_{\text{birth}}$, where

$$E'^i_{\text{birth}} = \{(x, y, t)|\ \text{birth } i \text{ happens at}(x, y, t)\}$$

is the set of spatio-temporal coordinates of all birth events on that tissue, in the tissue frame of reference. And $\mathbf{E}'_{\text{death}} = \bigcup_i E'^i_{\text{death}}$, where

$$E'^i_{\text{death}} = \{(x, y, t)|\ \text{death } i \text{ happens at}(x, y, t)\}$$

is the set of spatio-temporal coordinates of all death events on that tissue, in the tissue frame of reference, and so on (here, we will mainly be looking at birth and death events, though merging and splitting lends itself to analysis that is exactly analogous).

Let us call each term on the right of equation 4.1 as $\mathbf{E}'_{\text{event}}$ in general, this standing as shorthand for the list of spatio-temporal coordinates of all events of that type on the tissue. Since we will only be working with one term at a time, this will be useful.

As described in chapter 2, we have also identified the positions of foci on the tissue during dorsal closure. We denote this spatio-temporal coordinate set as $\mathbf{F}'$, as before (section 3.2.2).

We can now proceed in two ways, which will be defined in the two following sections.

4.2.1 Centroid Kymographs

By compiling a list of all known events, $\mathbf{E}'_{\text{event}}$, across a specific tissue, and then using the list of our tracked foci $\mathbf{F}'$, we can determine, point-wise, the coordinates of all the foci in the spatio temporal neighbourhood of the event and their Myosin intensity. If we were to sum the presence of foci at all coordinates on the tissue around a specific event (for instance, the case where a focus presence at a particular coordinate is assigned a value 1, and focus absence is assigned a value 0), and normalize it by the number of such foci, we would obtain a probability density map of focus presence. However, such a map would give equal weight to high intensity and low intensity foci. Since we want to use this map not simply as measure of focus presence, but also as a measure of focus intensity, we can weight each focus by its Myosin intensity. Then averaging over the whole tissue then gives us a map of the probability density of foci weighted by their Myosin intensity.

Here, we sample through list of foci to obtain the list of the spatio-temporal coordinates $\mathbf{E}'_{\text{event}}$ of events as described. We further sample through the list to locate all the foci in the neighbourhood of the event $E \in \mathbf{E}'_{\text{event}}$. We name this list $\mathbf{F}'_E$.

Calculating the radial distance between the members of $\mathbf{F}'_E$ and the specific event $E \in \mathbf{E}'_{\text{event}}$ we can populate a kymograph. This is the method of centroids, since this method treats foci as point particle located at their mass-centers.

This has the advantage of being fast and efficient, since we are now dealing with foci as discrete point entities with associated intensities. This method is also low in noise, since we have (hopefully) already removed all non-focal Myosin signal from our dataset during focus identification (section 1.6). The trade-off is that it may be overly reliant on tracking methods developed in chapter 2, and a badly tracked focus is likely to pollute analysis through noise. Also, we have lost all detail on the spatial structure of the foci

when we describe them as point objects. **We will refer to this type of kymographs as "centroid kymographs"**. We provide an illustration of such a kymograph for a tissue in the figure 4.3.

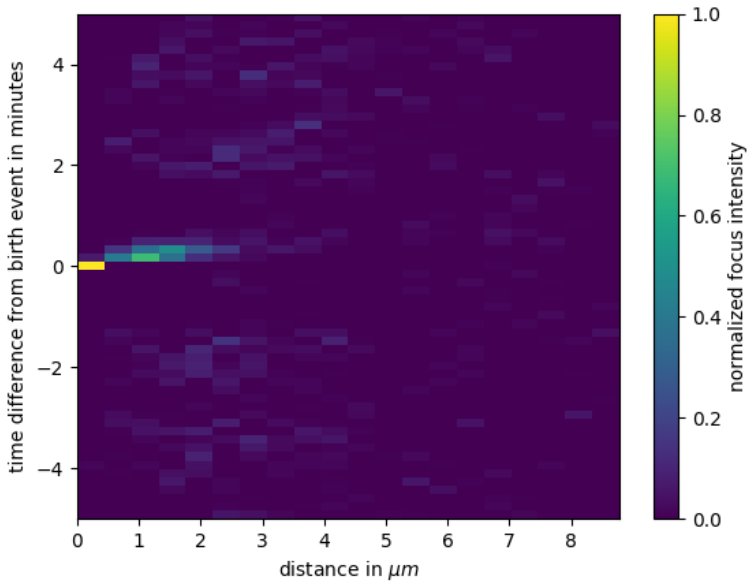

Figure 4.3: **Birth events on a centroid kymograph:** A centroid kymograph of all birth events that happen in one tissue (4LU) during dorsal closure.

Algorithmic Implementation

For an event $E \in \mathbf{E}'_{\text{event}}$ at x_E, y_E, t_E, we must decide how long before and after, and how far to look from the origin, to capture enough signal without being drowned in too much of it, and rendering the process computationally too cumbersome. Given that during dorsal closure, the inter-pulse duration is between $30s$ and 3 minutes, and in section 2.4.1 we find that our maximum duration of our foci at 5m (value in literature 4m [43]), limiting our time domain ($\equiv t_{max}$) to 7 to 10 minutes before and after the event seems sufficient to capture wide enough breadth of signal for this analysis. Since the focus end to end distances are around $1.6\mu m$ (with the $90th$ percentile at $3.2\mu m$), we restrict the size of our spatial domain to a maximum ($\equiv r_{max}$) of $6\mu m$ for single cell kymographs, and $8\mu m$ for all tissue kymographs.

Thus for all points, (x, y, t) that are on the embryo, we consider the signal from points such that.

$$\sqrt{(x - x_E)^2 + (y - y_E)^2} \leq r_{max} \tag{4.2}$$

$$|t - t_E| \leq t_{max} \tag{4.3}$$

For each event $E \in \mathbf{E}'_{\text{event}}$, we sub-sample our list of tracked foci to obtain all the information within a time $t_E \pm t_{max}$. Now, for x_F, y_F, t_F for every focus $F \in \mathbf{F}'$, we calculate the radial distance and time as

$$r = \sqrt{(x_E - x_F)^2 + (y_E - y_F)^2} \tag{4.4}$$

$$t' = t_F - t_E \tag{4.5}$$

Thus, the kymograph of a single event, E, may be defined as a mapping of intensities $f : I(x, y, t) \rightarrow I_{kymo}(r, t')$, and we can now use equation 4.4 to populate the $I_{kymo}(r, t')$ from $I(x, y, t)$. At each point on (r, t'), we place the total intensity of the focus from the corresponding (x, y, t). Thus bright foci contribute more than dim ones. We restrict our kymograph to the pre-decided value of $r = r_{max}$, for better visibility. The process is repeated for all $E \in \mathbf{E}'_{\text{event}}$ and averaged (figure 4.3).

4.2.2 Radial Myosin Kymographs

Another way to proceed is to use the list of known events, and then analyse the signal directly from the normalized embryo movies, obtained in chapter 1.

Thus, for any given event $E \in \mathbf{E}'_{\text{event}}$ on $\mathbf{\Omega}_{\text{tissue}}(t)$, we want to look at the radial distribution of Myosin in annular regions $\mathbf{A}^{\mathbf{E}}_{\mathbf{r}}$ of increasing radius, around that event before and after it happens. As before, kymograph of this single event, E, may be defined as a mapping of intensities $f : I(x, y, t) \to I_{kymo}(r, t')$.

$$I^E_{kymo}(r,t) = \frac{\sum_{(x,y)\in \mathbf{A}^{\mathbf{E}}_{\mathbf{r}} \cap \mathbf{\Omega}_{\text{tissue}}(t)} I^E(x,y)}{|\mathbf{A}^{\mathbf{E}}_{\mathbf{r}} \cap \mathbf{\Omega}_{\text{tissue}}(t)|} \tag{4.6}$$

where $\mathbf{A}^{\mathbf{E}}_{\mathbf{r}} \cap \mathbf{\Omega}_{\text{tissue}}(t)$ is the set of all on-tissue pixels contained in $\mathbf{A}^{\mathbf{E}}_{\mathbf{r}}$ at time t.

We average the kymographs over all events in $\mathbf{E}'_{\text{event}}$ to obtain the typical behaviour of the signal

$$I_{kymo}(r,t) \equiv \langle I^E_{kymo}(r,t)\rangle_E = \left\langle \frac{\sum_{(x,y)\in \mathbf{A}^{\mathbf{E}}_{\mathbf{r}} \cap \mathbf{\Omega}_{\text{tissue}}(t)} I^E(x,y)}{|\mathbf{A}^{\mathbf{E}}_{\mathbf{r}} \cap \mathbf{\Omega}_{\text{tissue}}(t)|} \right\rangle_E \tag{4.7}$$

We will refer to this type of kymographs as "average radial-Myosin kymographs"

Sometimes, we would also like to look at the maximum signal on the annulus, and not the average, since the maximum is a clearer indication of focus presence at large radii. We may then modify the equation 4.6 as :

$$I^E_{kymo}(r,t) = \max_{(x,y)\in \mathbf{A}^{\mathbf{E}}_{\mathbf{r}} \cap \mathbf{\Omega}_{\text{tissue}}(t)} I^E(x,y) \tag{4.8}$$

Averaging again over all events, we have the final kymograph :

$$I_{kymo}(r,t) \equiv \langle I^E_{kymo}(r,t)\rangle_E = \left\langle \max_{(x,y)\in \mathbf{A}^{\mathbf{E}}_{\mathbf{r}} \cap \mathbf{\Omega}_{\text{tissue}}(t)} I^E(x,y) \right\rangle_E \tag{4.9}$$

We will refer to this type of kymographs as "maximum radial-Myosin kymographs"

We also introduce here the terminology of 'original focus', defined as the focus that participates in the event E, and therefore is present at the origin of the kymograph. Analogously, we define the 'original cell', which is the cell that contains the original focus, and therefore the point (x_E, y_E, t_E).

In this work, we obtain results from three different sets of space time coordinates:

- Considering only the original cell,

$$(x,y,t) \in \mathbf{A}^{\mathbf{E}}_{\mathbf{r}} \cap \mathbf{\Omega}_{\text{original cell}}(t) \ , \tag{4.10}$$

- considering the whole tissue,

$$(x,y,t) \in \mathbf{A}^{\mathbf{E}}_{\mathbf{r}} \cap \mathbf{\Omega}_{\text{tissue}}(t) \tag{4.11}$$

- and considering the whole tissue except the original cell

$$(x,y,t) \in \mathbf{A}^{\mathbf{E}}_{\mathbf{r}} \cap \mathbf{\Omega}_{\text{tissue}}(t) \setminus \mathbf{\Omega}_{\text{original cell}}(t) \tag{4.12}$$

Together, the two equations 4.7 and 4.9 constitute the method of annular approximation of radial Myosin, or simply the **"radial-Myosin kymographs"**.

The direct use of signal makes this method more independent from the quality of tracking. We also retain foci as continuous objects of varying shapes and sizes. The downside ofcourse, is that we will have to deal with non-focus Myosin signal, as well as slower-processing time, since we must consider every pixel at the spatio-temporal neighbourhood of each movie for each event.

Algorithmic Implementation

We sub-sample our dataset of tracked focus locations in the tissue frame, F', to obtain a list of the events $\mathbf{E}'_{\text{event}}$. This, for example, corresponds to all the birth events on at tissue. These are also the points placed at the origin of our kymographs, corresponding with $(r, t') = (0, 0)$. Then, for each event $E \in \mathbf{E}'_{\text{event}}$, for each remaining pixel in the kymograph at (r, t') we use the relation 4.6 with the set of pixels (x, y, t) that are within the domain of the equation 4.2. The temporal requirement is met simply by looking at the movie and locating the frames in the times t_{max} before and after the event time t_E, giving us that,

$$t' = t - t_E \tag{4.13}$$

For the spatial part, for each such frame, we locate the point (x_E, y_E) corresponding to E, and we create a mask in the shape of an annular ring, $\mathbf{A}^{\mathbf{E}}_{\mathbf{r}}$(figure 4.4), of constant width and increasing radius r from 1 up to r_{max} . Because of the way the masks are created (by drawing a circle of radius $r+w$, and then subtracting from it a circle of radius r, for an annulus of width w), these annuli provide a partition of the entire space on the tissue up to the maximum chosen radius, meaning that the intersection of the set of annuli is a null set, and their union is the entire space.

We project this 2d signal onto a point by taking the average of all the Myosin signal contained in the annulus, $\mathbf{A}^{\mathbf{E}}_{\mathbf{r}} \cap \mathbf{\Omega}(t)$. For the average radial-kymograph, the number of on-tissue pixels contained in the annulus provides the normalization factor as the mask increases in size (the denominator in equation 4.6). Since the annular ring is of fixed width, the number of pixels contained in it scales with radius. This normalization allows us to compare the strength of the signal as we move further from the focus event.

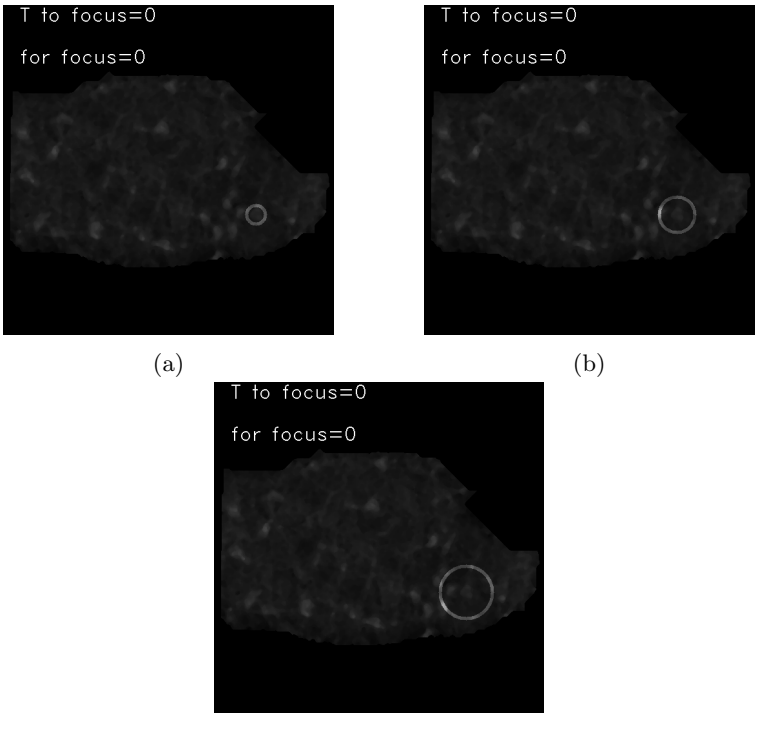

(a) (b)

(c)

Figure 4.4: **Illustration of process of annular approximation radial-Myosin:** Panels (a), (b) and (c) show three different annuli $\mathbf{A}^{\mathbf{E}}_{\mathbf{r}}$ at the same time point, with increasing radii r, centered on focus birth event position

We ensure that all pixels are on tissue by a bitwise-and operation of each frame in question with a binary mask of the tissue silhouette. Each kymograph is then stored, and averaged after repeating this process up to the end of set $\mathbf{E}'_{\text{event}}$ (via equation 4.7). This gives us a kymograph for each tissue. An illustration of this for births and deaths is shown in figure 4.5.

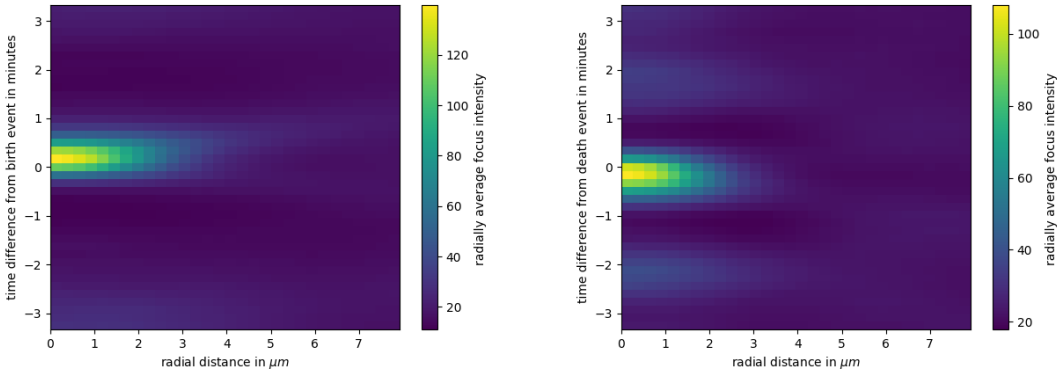

(a) Kymograph of all focus births for the tissue 2a early during early dorsal closure

(b) Kymograph of all focus deaths for the tissue 4a fast during fast dorsal closure

Figure 4.5: **Focus birth and death on two tissues, average radial-Myosin kymographs**

Calculating the average Myosin intensity on the annular region is not always sufficient to reveal all details of focus motion. As described above, we will use both the average and the maximum of the signal on the ring. Therefore, while iterating on the annular region we calculate these two measures to better visualize focus dynamics at different length scales. A qualitative description of what this does is provided below.

- average Myosin signal in annular region, normalized by radius : As described before, this measure is useful for looking at regions close to the event: for example, looking for a time pattern in the pixels located close to the y-axis of the kymographs. The average is also useful for looking for regions of low signal or non focus signal- since these regions generally have a markedly different average signal from focus regions. We can also directly compare these with centroid kymographs. However, at high radii, the average fails to provide enough contrast.

- maximum Myosin signal in annular region : At high radius average Myosin signal does not provide enough contrast on kymograph, since the few focus pixels are muddied by large number of non-focus pixels. In these cases using the maximum Myosin signal is more useful, since at high radius, the maximum intensity on the annulus is more likely to be in a focus. This measure lets us better visualize motion of foci by excluding non focus pixels. An illustration of this for births and deaths is shown in figure 4.5.

In the methods used in this chapter, though we have continued to use the positions of our foci as input for our analysis, but for many of the cases (radial-Myosin kymographs), we have neglected the exact temporal relationship between foci tracked in different frames, deducing it instead through the signal seen. Specifically, we used the coordinates for the events defined in section 2.3. But we only need to be approximately correct about the timing of these events, because of the large number of events we average over.

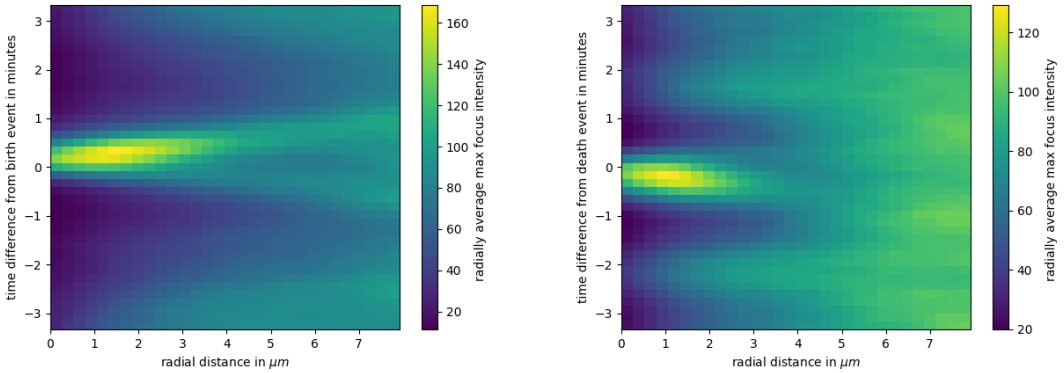

(a) Kymograph of all focus births for the tissue 4a fast during early dorsal closure

(b) Kymograph of all focus deaths for the tissue 2a early during fast dorsal closure

Figure 4.6: **Focus birth and death on two tissues, maximum radial-Myosin kymographs:** These are for the same events as those in figure 4.5, but now we are able to better see the motion of the focus far away from origin.

4.3 Randomisation

Finally, to check on unknown biases in the data we need to compare our kymographs of events to kymographs from random parts of the tissue. We develop this procedure for the radial-Myosin kymograph, by randomising the set $\mathbf{E}'_{\text{event}}$. For every $E \in \mathbf{E}'_{\text{event}}$, we pick random points in space as the origin of our kymograph. This is performed by choosing random positions on tissue, instead of positions associated with focus events, at the same times associated with focus events.

The procedure is then repeated and a random kymograph for every $E \in \mathbf{E}'_{\text{event}}$ for each tissue, is produced. This is then averaged over the same instances as the length of the set $\mathbf{E}'_{\text{event}}$. This then gives us an idea of the default Myosin signal on tissue, not associated specifically to foci. These kymographs can then be subtracted from each 'focus' kymograph to better see the focus motion patterns. Therefore, to visualize them here, we have used the same range of intensities on the color-bar as is present in the 'focus' kymographs, even though the intensity values contained in these kymographs are generally much lower. We plot such kymographs for the average, and the maximum Myosin flavours in the figure 4.7.

We see for figure 4.7a, a constant low value of Myosin, which is what we would expect. Due to the scaling of the color-bar, we cannot, in this figure, see the random fluctuations of Myosin intensity, which occur at amplitudes much lower than focus fluctuations. To better visualize this, we map the color-bar onto a log-scale, as seen in figure 4.7b

For figure 4.7c we see linear uniform increase of Myosin value with radial distance. This is because as the radius of the annular region is increased, the probability of finding a focus on it increases. We understand that in the ensemble average over the members of $\mathbf{E}'$ the high radius points carry more weight than the low radius points, and this provides contrast at high radii.

We will now see how, through a combination of the two methods: discrete and continuous, we are able to identify signal properties of focus events. In fact, a close correspondence between the results also enables us to gain confidence in the quality of the focus tracking.

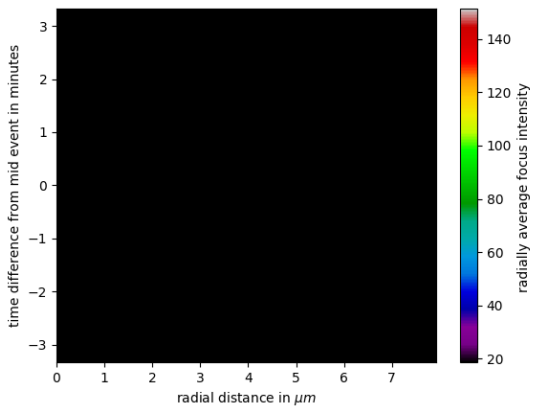

(a) Heatmap of radially average Myosin intensity for $N = 2616$ random points on the tissue

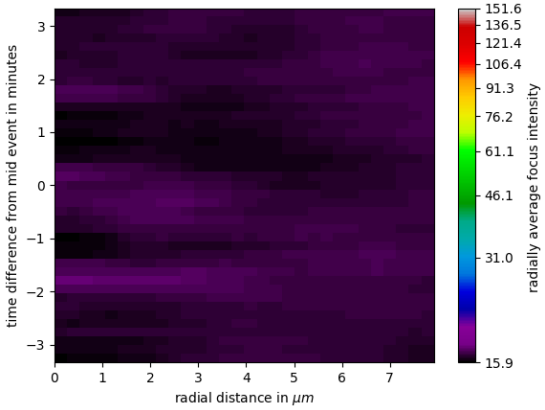

(b) Heatmap of radially average Myosin intensity for $N = 2616$ random points on the tissue, colorbar in logscale

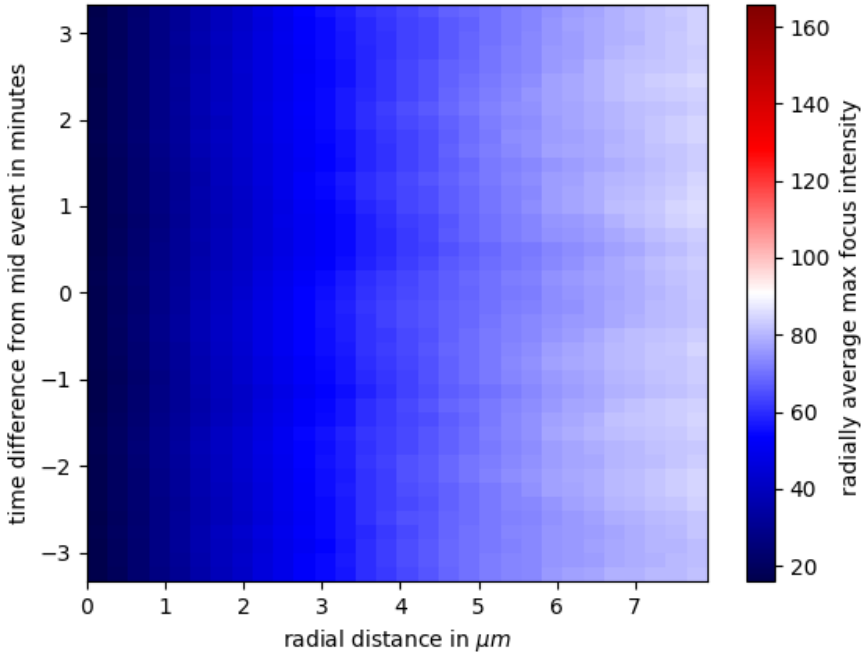

(c) Heatmap of radially maximum Myosin intensity for $N = 2616$ random points on the tissue

Figure 4.7: **Typical Myosin signal on the amnioserosa in a radial-Myosin kymograph :** Panel (a) and (b) show the kymograph of the 'typical' (meaning randomised, not necessarily associated with a focus event) Myosin signal on the tissue under the 'average' (equation 4.7) flavour of the radial-Myosin kymographs. Panel (c) shows the same view under the 'maximum' (equation 4.9) flavour of the radial-Myosin kymographs

4.4 Results

We will now present the main results of these parallel approaches. All kymographs presented in this section are additionally averaged over many tissues [1]

[1]Since our dataset consists of movies of two different spatial resolutions, we average them separately. In the sections that follow, the results from one variant are presented. Results from the other variant, as well as the kymographs for the individual

4.4.1 Motion of Original Focus in Cell

In the simplest case, we are interested in how a focus is born inside the cell, and we can obtain a statistical idea for this by looking at averaged kymographs containing information from only the original cell. With the centroid kymograph we can do this by simply restricting our look-up list $\mathbf{F'_E}$ to foci contained only in that cell.

We plot the centroid kymograph, for each tissue, and plot the average in the figure 4.8.

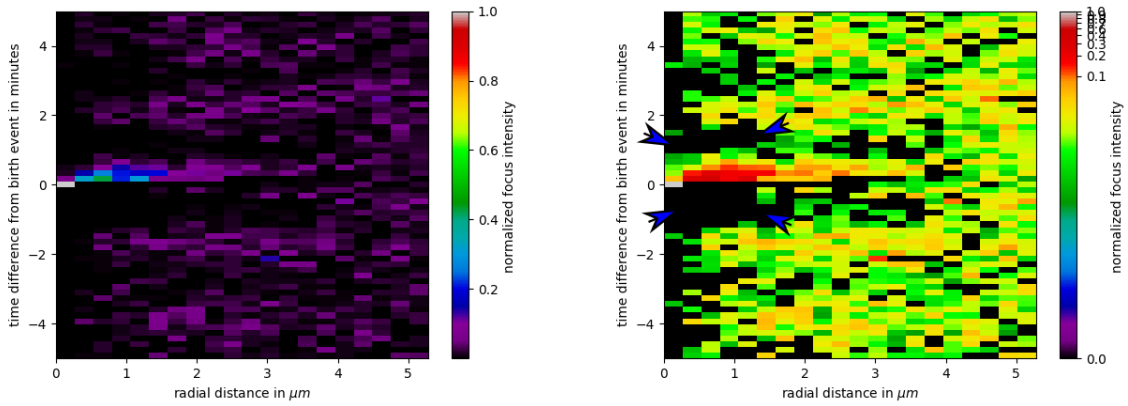

(a) (b)

Figure 4.8: **The birth and propagation of foci:** Panel (a) shows centroid kymograph around a focus birth event, considering only centroids of foci present in the original cell. Panel (b) shows the same figure with colorbar in logscale, to better visualize low Myosin features. Blue arrowheads mark the Myosin depletion region, which is black in this figure. These kymographs contain 1852 events, averaged over 307 cells in 8 tissues.

We see the birth of the 'original' focus, associated with the region of maximum intensity, at origin $t = 0$ and running across the kymograph as a bright stripe that is nearly horizontal. We estimate the speed of this stripe to be in the order of $2.4\mu m/min$, which of course, agrees with the speeds we obtain from the tracking in section 2.4.3.

More interestingly, we find two prominent regions of low focus density that run along the vertical axis at the origin seen as a black vertical bands from about 5 to 0 minutes and from 1 to 5 minutes, and radii smaller than $0.26\mu m$ (corresponding to our minimum spatial resolution). This vertical band is divided by the presence of the original focus stripe. We can think of these as Myosin depletion regions. They are punctuated by four strips of color of area 1 pixel-frame, that imply the presence of foci there at those times (greater than -2 and -4 minutes, and smaller than 2 and 4 minutes).

As we move to greater radii, we also find two narrower depletion regions that follow the trajectory of the focus, across the horizontal axis, both below and above (up to $2\mu m$). Each of these regions has an average width of about 1 minute.

If we assume that these depletion regions are indeed associated a focus presence at previous times, we can explain the wider depletion region for times between 1 and 1.5 minutes and radius smaller than 0.26 μm (after the focus has departed from the point $(0, 0)$), as compared to points with greater r . Since foci have a duration of less than a minute in general, and we fix the origin at focus birth events, we are sure to have a focus departing from the origin, and thus a corresponding depletion region between 1 and 1.5 minutes , for all instances of the averaging process over events. For greater r values, we are not sure of having a focus there for all instances of birth, and so the region becomes narrower.

We can also run this analysis with the radial-Myosin kymograph. Since for now we are only interested in the signal from the cell containing the original focus, we restrict our annular region to iterate only over

tissues are presented in the appendix C.

that cell. This is done by a 'bitwise-and' operator between a binary image of the cell contour with the tissue image at every instant, as explained above.

Performing this over all tissues and averaging in an analogous way, we plot the kymograph 4.9 :

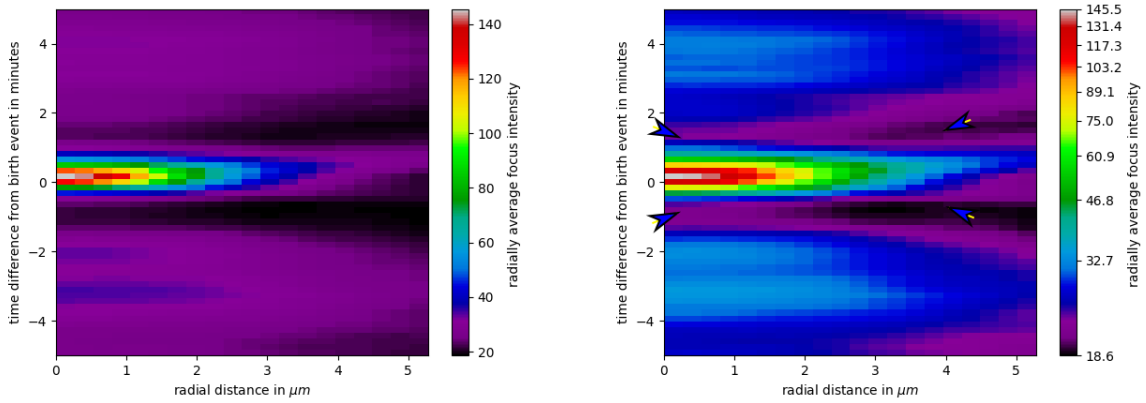

(a) (b)

Figure 4.9: **Depletion regions through radial-Myosin kymograph** Panel (a) shows the average radial-Myosin kymograph with origin centered at focus birth, considering only signal from the cell containing the focus. Panel (b) same figure with colorbar in logscale, to better visualize low Myosin features. The black bands in panel (a), and the purple-black bands in panel (b) (marked with blue arrowheads), show the presence of depletion regions. These kymographs contain 1852 events, averaged over 307 cells in 8 tissues.

We recapture many of the same features as from centroid kymographs, such as original focus birth, and likely radial displacement and attenuation as we move further from the origin. This kymograph has more vertical spread than the centroid one (for example the original focus is spread in time is about a 1 minute), because the centroid kymograph treats the foci as point objects, and so the features present in centroid kymographs are 'squashed' along the vertical axis.

Once again, we find the low-intensity depletion regions before and after all points on the trajectory , we can see more precisely that they occur up to nearly 1 minutes before and after focus motion. Before and after this, the region of space shows signs of higher Myosin that could be foci (this can be seen most clearly at times -2 minutes and ~ -4 minutes in the figure 4.9a).

We also find evidence of the same close to the origin, up to 2 minutes before and 1 minutes after , beyond that interval the tissue recovers up to a quarter of the maximum range of intensities in the plot. Thus, we see these depletion regions of low-Myosin intensity occur in the cell before and after the time of focus birth.

Asking ourselves if these depletion regions are local phenomena due to the focus presence, or cell-wide phenomena due to the pulsation of Myosin content in the cell, we observe the region of space up to a distance of $0.53\mu m$ to the focus birth point, and plot its evolution in time as a line plot, in the figure 4.10. In the same figure, we plot also the average Myosin signal of the cell at the same time instants.

We find that, centered around the maximum focus amplitude (that occurs on this plots to right of $t = 0$, the birth time), the Myosin concentration at that region of cell shows a pulsatile behaviour. We find a drop in the amplitude both right and left of the crest, which correspond to the depletion regions seen in our heatmaps at $r = (0, 0.53\mu m)$. Further away on both sides there are the small peaks that correspond to the bright strips of focus presence in figure 4.8.

We observe also the pulsation of Myosin concentration of the cell, which shows lower amplitude oscillation. However, we note that in these plots, the Myosin concentration at the birth pixels, falls below the average of the cell at that times before and after focus presence [2]. We conclude that these depletion regions are features of the local apical region associated with focus births.

[2] we find this to be the case often, and the plots for the other tissues are given in the appendix C

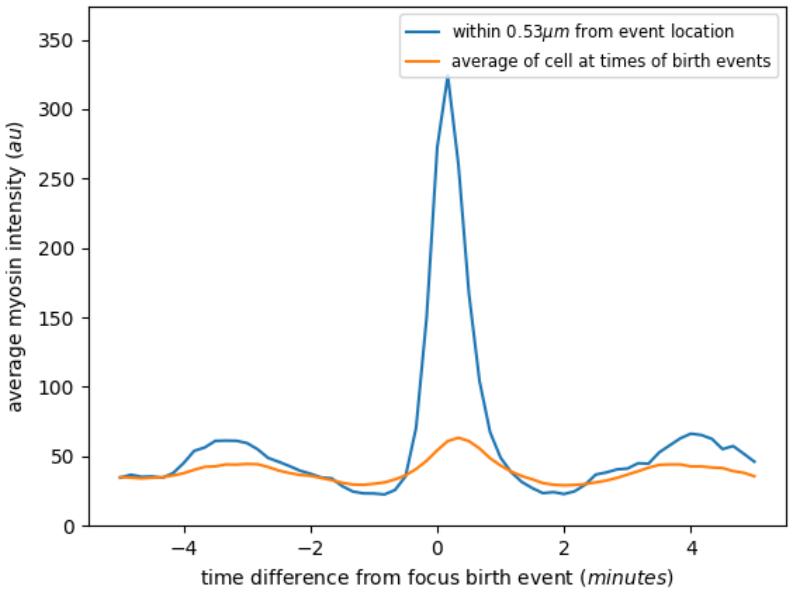

(a) 2a early

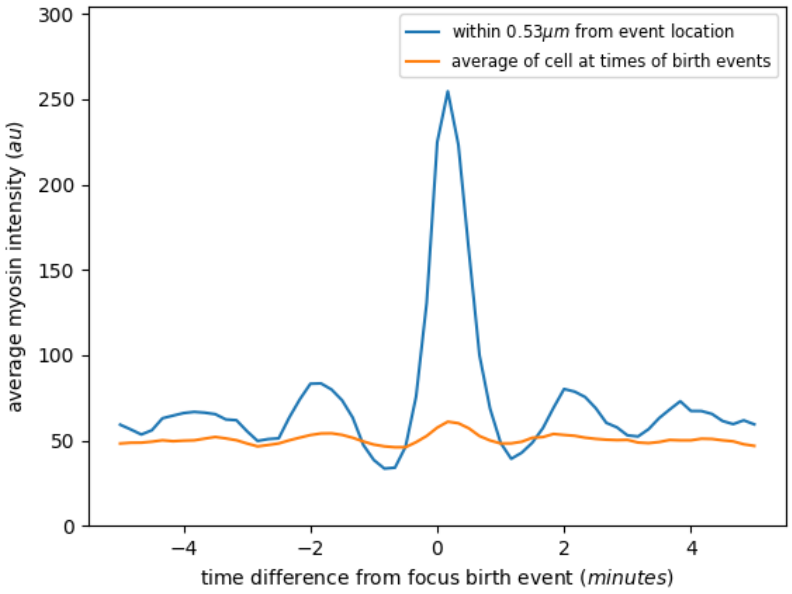

(b) 4a fast

Figure 4.10: **Myosin signal at regions close to focus birth:** For two tissues, from early (Panel(a)) and fast (Panel(b)) phases of dorsal closure, evolution of pixel intensities at distance 0.53 μm from a focus birth event, for 10m centered on the event, shown in blue. Evolution of the average signal in that cell during those times shown in orange.

We can repeat these analyses for death events as opposed to birth events, plotting again, the kymographs for centroid and radial-Myosin, in figure 4.11.

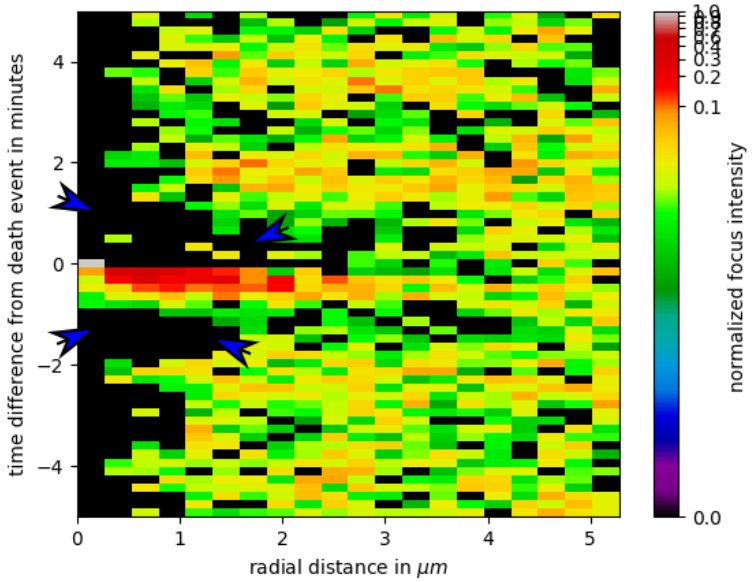

(a) Centroid kymograph with origin centered at focus death, considering only signal from the cell containing the focus. Colorbar in logscale. Blue arrowheads mark depletion regions

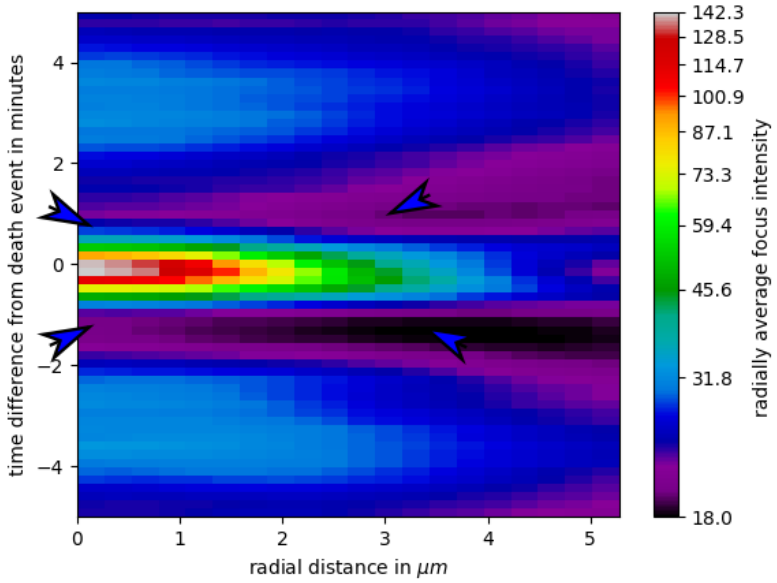

(b) Radial Myosin kymograph with origin centered at focus death, considering only signal from the cell containing the focus. Colorbar in logscale. Blue arrowheads mark depletion regions.

Figure 4.11: **Depletion regions associated with focus death, through centroid and radial-Myosin kymographs:** These kymographs contain 1852 events, averaged over 307 cells in 8 tissues

These kymographs are qualitatively similar to the birth kymographs, but reversed along the time-axis. Depletion regions are seen again, at the origin: after the focus death has occurred, before it arrives at the

position, as well as following its trajectory before and after.

Looking at figure 4.11b, we find that the Myosin signal before the focus is generally lower than after it, and we can verify this by analogously plotting the evolution of pixel intensities close to the focus death points in the figure 4.12. We find that for these tissues, the trough before the focus is deeper than the trough after.

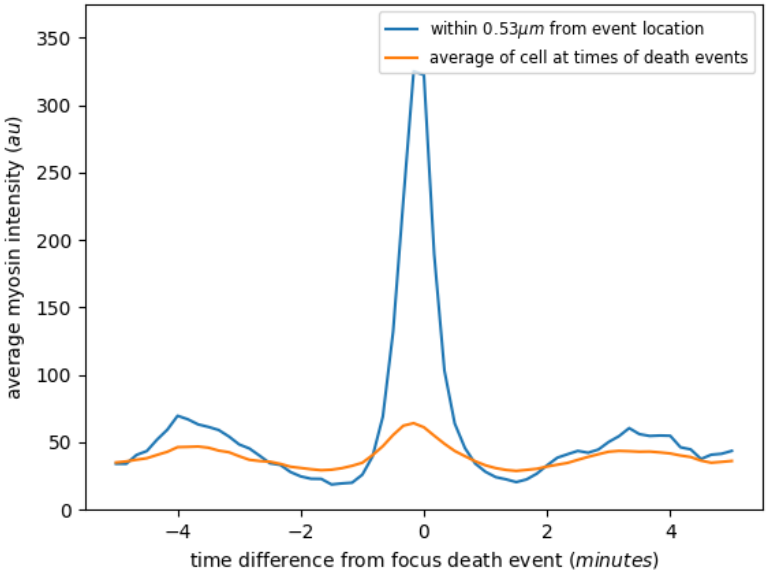

(a) 2a early

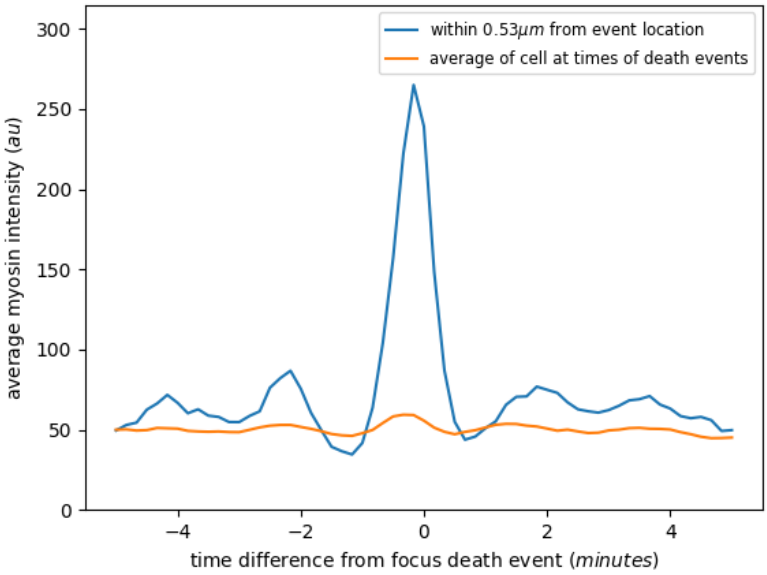

(b) 4a fast

Figure 4.12: **Myosin signal at regions close to focus death:** For two tissues, from early (Panel(a)) and fast (Panel(b)) phases of dorsal closure, evolution of pixel intensities at distance 0.53 μm from a focus death event, for 10m centered on the event, shown in blue. Evolution of the average signal in that cell during those times shown in orange.

4.4.2 Focus Motion at the Tissue Scale

Having looked at the simple case of the behaviour of a focus in a cell, we can now expand the scope of our search to include the whole tissue (condition 4.2.2). To do this, we simply extend the analysis from previous

section by including signal from the whole tissue, and not just the original cell. We are interested in how foci interact with each other, and whether an event happening at one focus in a particular cell affects the other foci in the neighbourhood.

We see in the previous section that Myosin depletion regions precede and follow the trajectory of the original focus at all points in space, and not just the origin, where birth and deaths occur. So, in this section we would also like to change the scope of the search to the points in the trajectory that are not focus birth or death points. This can be done by changing the set $\mathbf{E}'_{\text{event}}$, which we use for the origin in our kymograph, to the set $\mathbf{E}'' = \mathbf{F}' \setminus \mathbf{E}'_{\text{event}}$. We will call this set 'mid' and these kymographs 'mid kymographs' referring to the fact that these are points in the middle of focus birth and death, (or any two events) or the 'normal' points in the focus' life.

As before, we plot the centroid kymograph in the figure 4.13.

At times $t \in (-0.5, 0.5)$ and radii $r \in (0, 3)$, we can see the original focus. Since we are now centered on the mid points, this focus is born at some point in the lower right portion of this region, moves into the origin, and then dies at some point at the upper right. As we move further from the origin, since we are averaging over more and more foci, the focus signal is attenuated and diffused over surface.

We find again that the focus itself is surrounded with the band of depletion region as before. In figure 4.13b, we see that this depletion region is the most pronounced at the center across the horizontal axis, since these are the radial points where the depletion region on top of the focus moving into the origin, overlaps with the one in the bottom of the focus moving out of the origin.

More interestingly, we find the depletion region at the origin, shows an oscillatory pattern, punctuated by focus presence. These were seen as bright strips of area 1 pixel frame in the kymograph 4.8. Now, due to the greater number of 'mid' events, we can see them more clearly. We note that the depletion regions, at their lowest trough, are about 1 minute in temporal length.

We can replot this with the radial-Myosin kymograph in the figure 4.14. This time, since we are checking distances further away from the origin, as compared to the kymographs in the previous section, let us use the maximum radial-Myosin flavour to have contrast at these high radii (panels 4.14c and 4.14d).

Once again, in both flavours, looking at the vertical axis at $r = 0$, we see the original focus moving into and out of the origin. Along the horizontal axes near the origin, we observe the size of the original focus (between 3 and 4 μm, depending on the threshold chosen in units of intensity, 2.6b), and its attenuation as we move further away from the origin. Once again, as in the figure 4.13, we see the focus coming into the origin and moving out in the form of a travelling pulse. As expected, the details at high Myosin signal further away from the origin are clearer under the maximum radial-Myosin flavor, where as details close to the origin and at low Myosin signals are clearer in the average radial-Myosin flavour.

In the maximum radial-Myosin kymograph, we can also see a linear increase of the signal far away from the focus, due to the increase in radius of the annular ring, as seen in the randomised kymograph in figure 4.7c. In fact, we can now use this as background and subtract it from our focus kymograph to clearly reveal the focus properties. We do so in the figure 4.15

In the figure 4.15, we can clearly see the focus travelling across distances as large as $7\mu m$. We also see the evidence of the depletion regions at the $1 - 2$ minute marks above and below the origin (most clearly visible in panel 4.15b). We see, once again, the focus surrounded by a depletion region of low Myosin at all points. We see that the most intense depletion (the deepest trough) is associated with regions before the focus arrives, and a slightly less intense one associated with the regions after leaves.

We now ask ourselves the question whether the presence of the focus in one cell influences the other foci in the proximity.

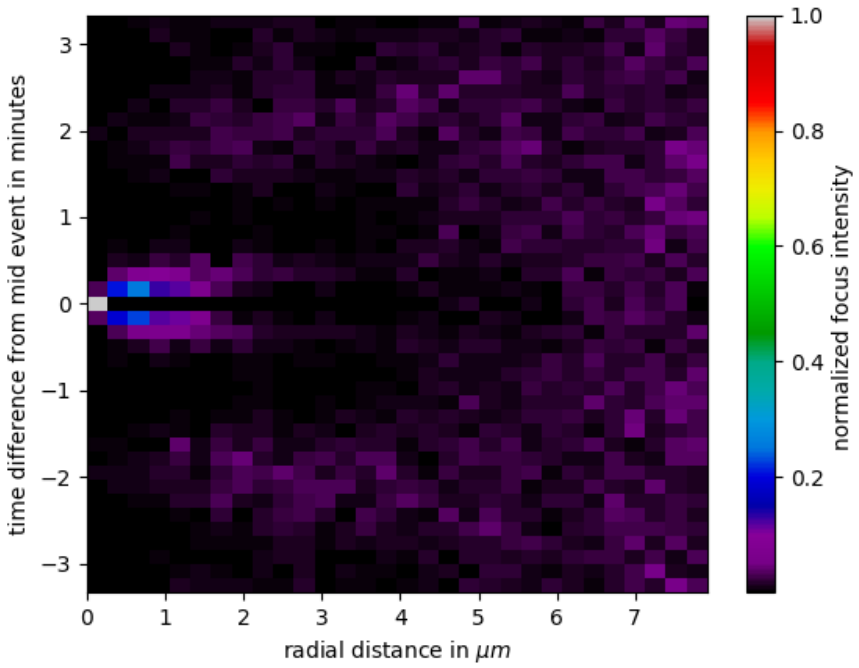

(a)

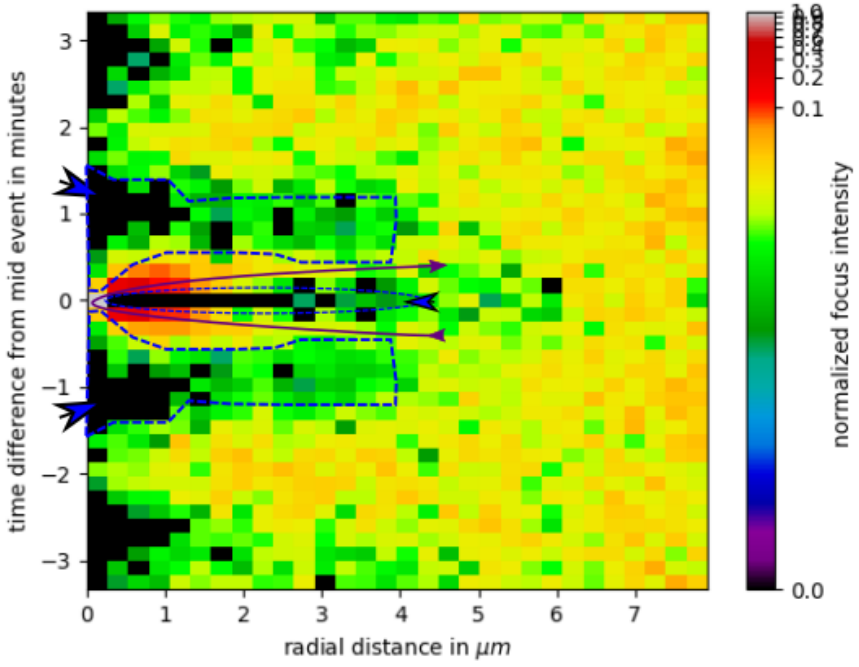

(b)

Figure 4.13: **Motion of focus at tissue scale through centroid kymographs :** Panel (a) shows average centroid presence from mid events. Note the black depletion band at times before and after the original focus moves into, and away from the origin. Panel (b) has the same plot in logscale. The depletion regions are marked with blue dotted lines and arrows, the motion of the original focus marked with purple solid line. These kymographs contain 4237 events averaged over 8 tissues.

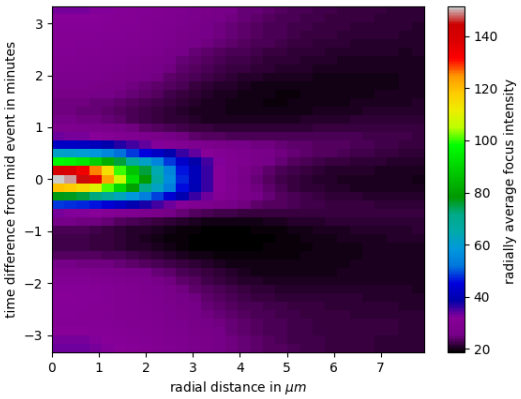

(a) Average radial-Myosin from mid events.

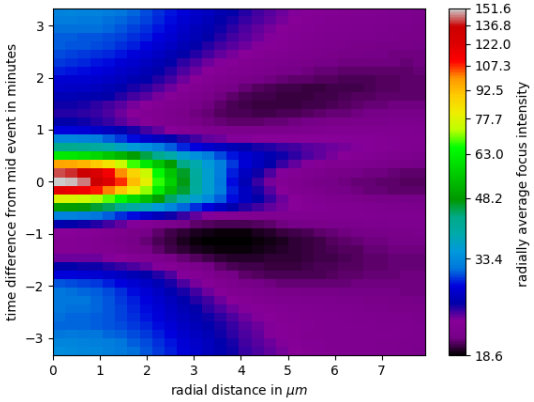

(b) Average radial-Myosin from mid events, colorbar in logscale

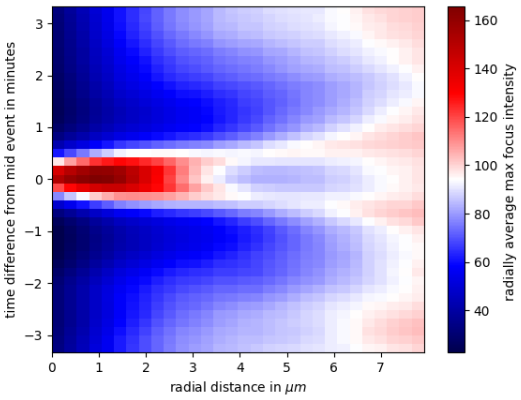

(c) maximum radial-Myosin from mid events

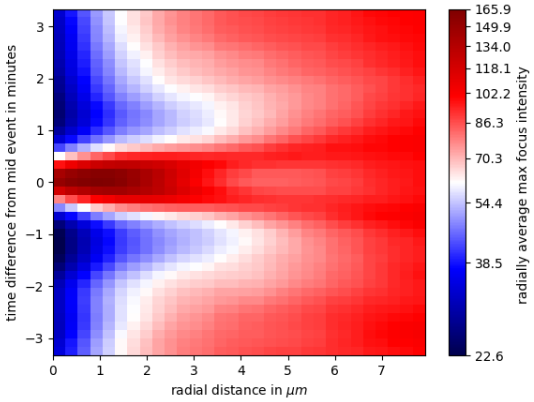

(d) maximum radial-Myosin from mid events, colorbar in logscale

Figure 4.14: **Motion at tissue scale through radial-Myosin kymographs:** These kymographs contain 4237 events averaged over 8 tissues.

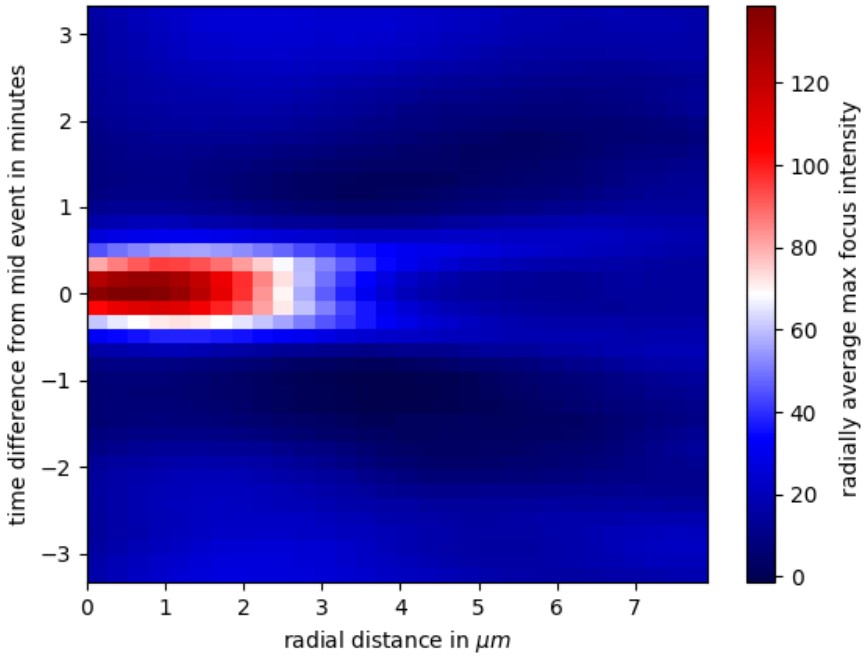

(a) maximum radial-Myosin from mid events, background subtracted

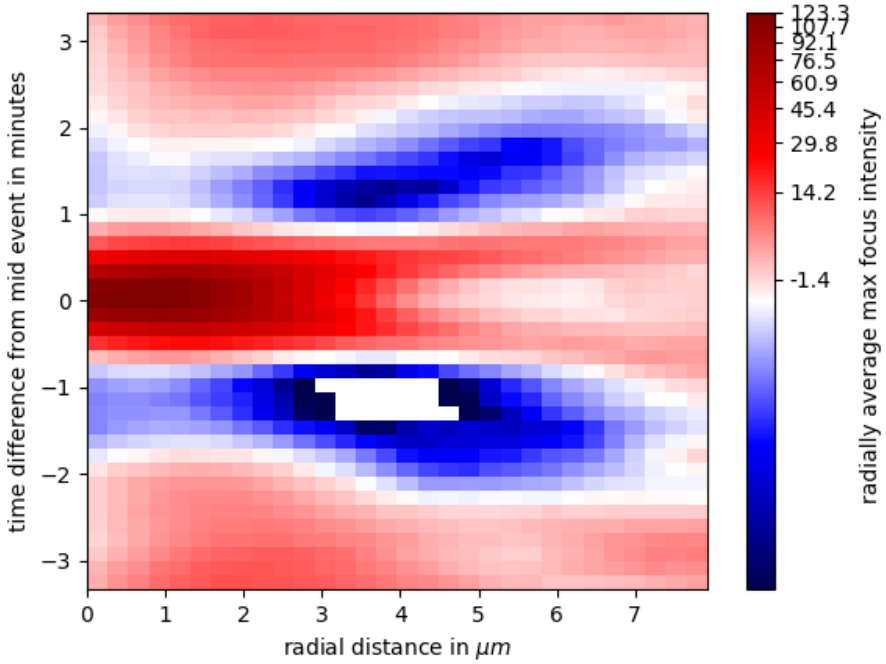

(b) maximum radial-Myosin from mid events, background subtracted, colorbar in logscale. White patch shows where data falls to zero and under, and cannot be logscaled

Figure 4.15: **Motion of focus at tissue scale through background subtracted maximum radial-Myosin kymographs**

4.4.3 Influence of a Focus Beyond the Cell it Belongs to

In the two previous sections, we have looked at kymographs confined to the original cell and those at the tissue scale. In both cases, we observed features of the original focus. However, given that original focus dominates these kymographs, we were not able to see clearly the features of the other foci in response to the presence of this original focus.

In this section we distinguish between the signal (or foci) present in the same cell as the original focus, and signal (or foci) present outside of it, removing the former from our analysis. Our cell segmentation tool allows for us to do this easily, by performing the opposite operation as we did in section 4.4.1, or restricting our signal to all parts of the tissue except the instantaneous contour of the original cell (condition 4.12).

We look at this process with the radial-Myosin kymograph, in the figure 4.16.

We once again find evidence of depletion regions, as before. However, this kymograph is dominated by a bright patch of Myosin in the region $t \in (-0.7, 0.7)$ and $r \in (0.5, 2)$, which is thrice as bright as the surrounding tissue. We has seen this in the figure 4.14, but now we understand that a part of it comes from outside the original cell. This tells us that the original focus presence in one cell co-occurs with the presence of a region of high Myosin in a neighbouring cell, close to it. We see in the panel C.4b, that this patch is connected to the rest of the apical signal through a region of slightly lower Myosin intensity. To better visualize these features, we repeat the process of background subtraction through randomized kymographs and plot the figure 4.17

In the panel 4.17a, we are able to faintly perceive the motion of the focus that constitutes this bright patch, going out of this region. However, the intensity of this motion is only a few units of intensity brighter than its surroundings, and so it must not be considered definitive.

We may repeat this through the centroid kymograph, now updating our look up list to exclude foci from the original cell, in the figure 4.18. Though in these kymographs the same bright patch position is observed to have some focus presence, we find that this is quite low in Myosin signal, (less that 10 % of maximum) so the confirmation of communication of foci across cell membranes remains elusive.

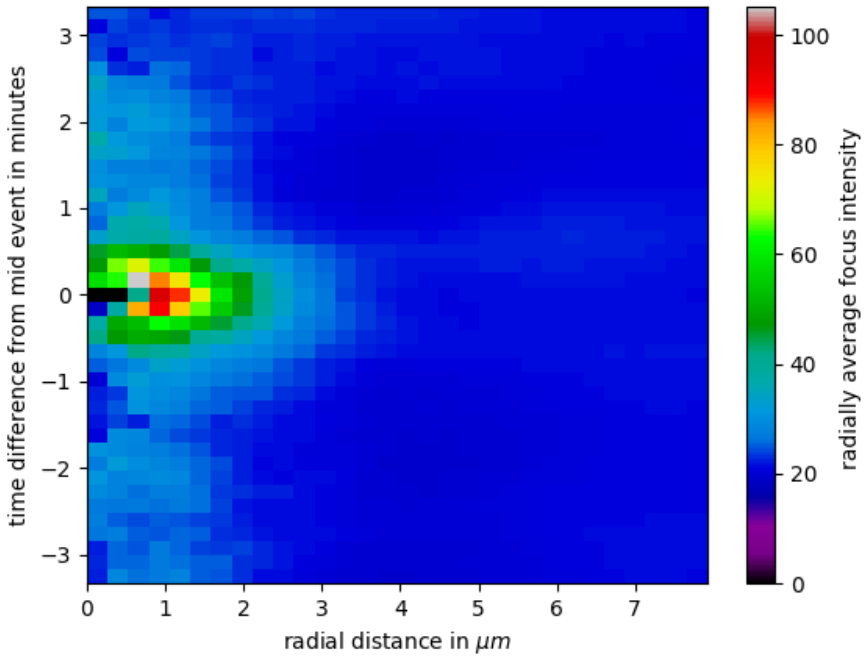

(a) Average radial-Myosin kymograph from mid events without signal from original cell

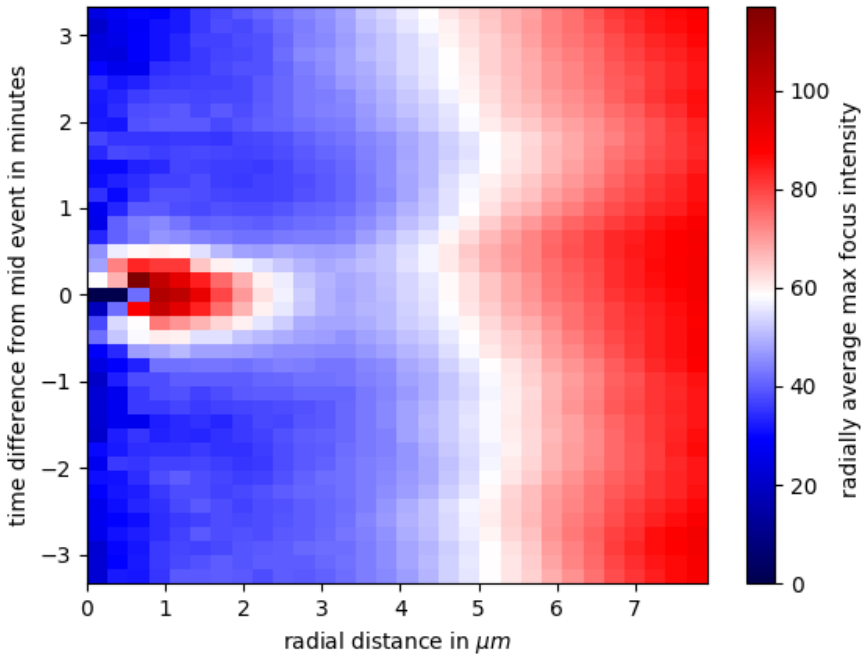

(b) Maximum radial-Myosin kymograph from mid events without signal from original cell

Figure 4.16: **Myosin signal outside the original cell:** These kymographs contain 1403 events averaged over 4 embryos.

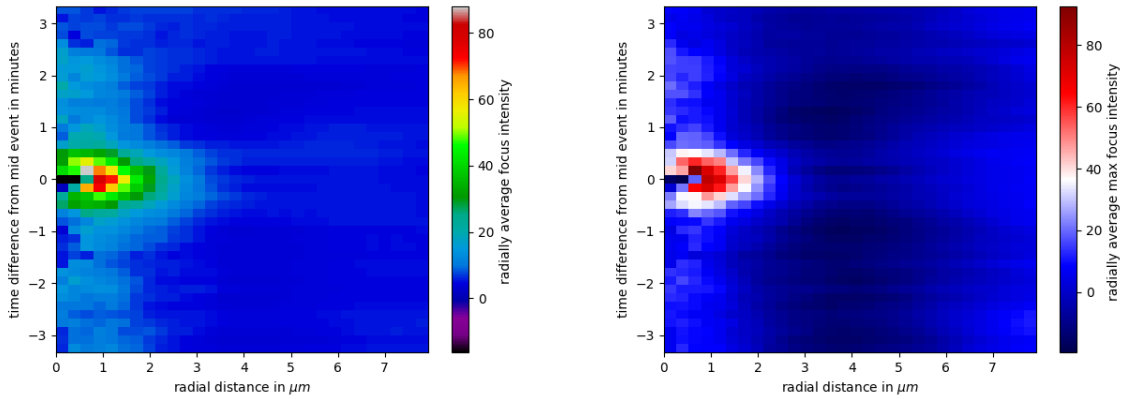

(a) average radial-Myosin from mid events, without original cell, background subtracted

(b) maximum radial-Myosin from mid events, without original cell, background subtracted

Figure 4.17: **Myosin signal outside the original cell through background subtracted average and maximum radial-Myosin kymographs**

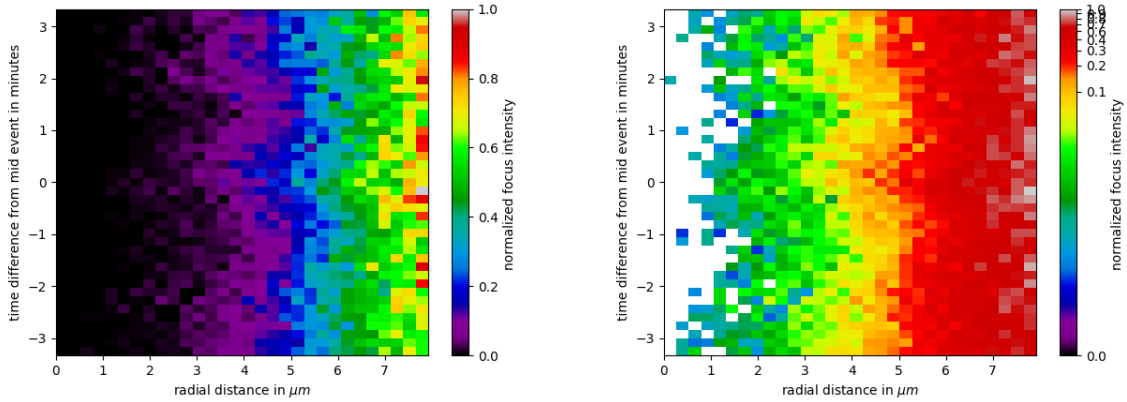

(a) Centroid kymograph without foci from the original cell

(b) Centroid kymograph without foci from the original cell, colorbar in logscale

Figure 4.18: **Centroid kymograph outside the original cell:**These kymographs contain 1403 events averaged over 4 embryos

4.5 Discussion

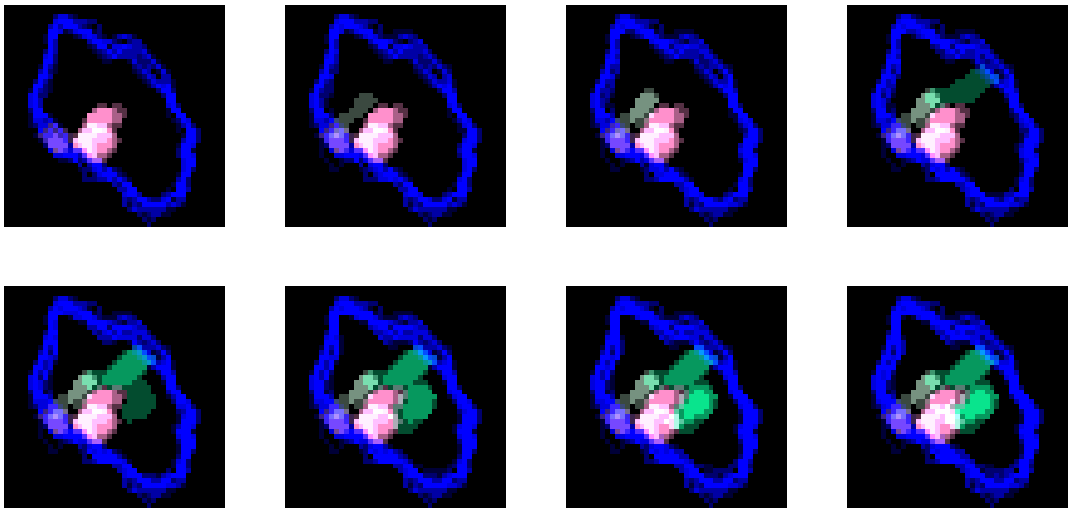

(a)

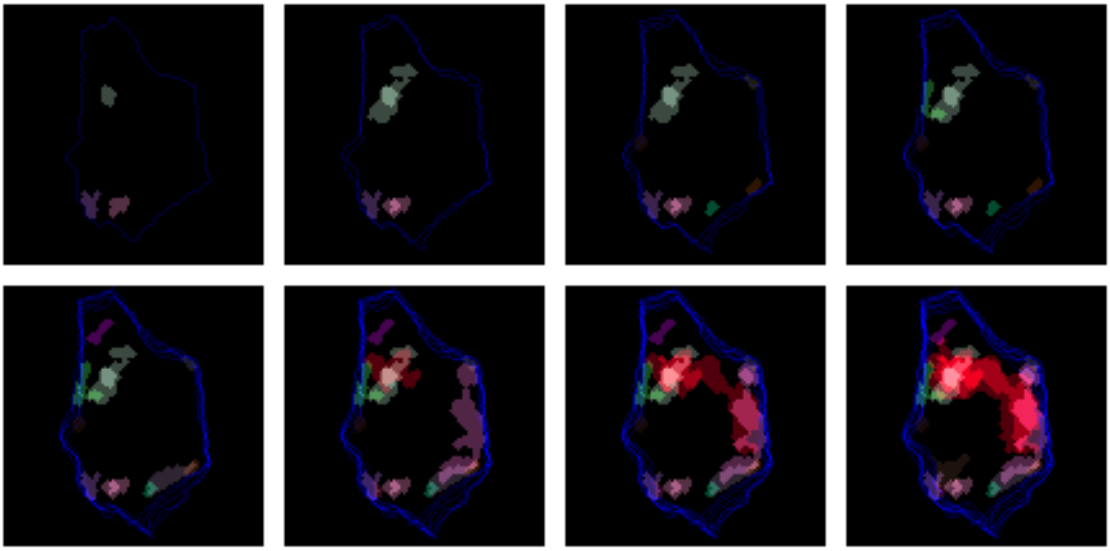

(b)

Figure 4.19: **The evolution of distribution of foci on the apical cellular surface:** Two different cells shown over subsequent frames. In each frame, foci are marked with different colors. At each subsequent panel, foci are overlaid onto the previous panel, thus brighter areas indicate overlap between subsquent frames. The evolution of cell contours are shown in blue.

From the results in chapter 2, we have seen that Myosin focus centroids move with non-zero velocity. In chapter 3, we observed high directionality in the motion of the focus branches, as well as a value for

the median exponent of mean-squared-displacements at a regime that was consistent with a self-avoiding random walk. Together, these observations pointed towards a self avoiding behaviour for focus motion.

Thus, if a focus does not return to its previous positions as a rule, this can be expected to manifest in the kymographs as low expectation value for Myosin intensity in the regions of space close to a focus at the times after the focus has been there. We observe such depletions regions 1.5 minutes later when there has been a focus birth (figure 4.8), death (figure 4.11a) and simple presence (figure 4.13) in our centroid kymographs.

However, the foci are not geometric points, as we have considered in these kymographs (and also in the analysis in chapter 3), and in reality have finite size, (radii up to 4 μm), and travel with finite speeds (mean of 2.5 $\mu m/min$), and are characterized by a high value of Myosin signal on the apical surface of the amnioserosa.

The non-zero size, that we lose in the pointwise-approximation, would mean that as a focus travels, no other centroid could occupy the positions of the original focus centroid up to timescales in the order of a few minutes: explaining the low probability density black regions we see. Thus, we have to verify the claims of self avoidance through a return to the continuous signal description. This is the purpose of our radial Myosin kymographs.

And indeed, we observe the same phenomenon of depletion regions for in figures 4.9, 4.11b and 4.14. The last of these, (corroborated by the analogous centroid figure 4.13), extends our self avoidance rule from the cell occupied by the focus, to the whole tissue . We also observe that stationary foci, which would manifest as vertical bands in the kymographs are absent, confirming our observation that foci always have a finite speed (section 2.4.3).

Thus, we claim that focus propagation is associated with the creation of 'refractory regions' on the apical cortex in its wake, which we define as parts of the cortex that other, newer foci do not venture upon for finite times (few minutes). We denote this time period as the refractory time period of the cortex. a focus cannot stay still because the region it is in becomes refractory, and so it has to propagate, or die out.

We speculate that a local refractory property could imply high rates of Myosin unbinding from the actin substrate in that region. This would have the effect of providing the nearby substrate regions a large pool of unbound Myosin to draw from, promoting concentration at that location. With the promotion of this concentrating phase, this nearby region would eventually become refractory, and the process would repeat itself further and further from the original site, giving us the net effect of a travelling focus.

Self avoidance also implies that this travelling focus would be more likely to propagate to non-refractory regions with low-Myosin values (where the focus is avoiding other foci that are in other regions), thus we would expect to see a drop in the Myosin signal in a region not only after a focus has passed through it, but also before it has been there.

We observe this phenomenon as depletion regions that manifest before the focus presence. As before, it is seen in cases of birth (figures 4.8, 4.9), death (4.11), and presence (4.13, 4.14) in both centroid and radial-Myosin kymographs.

It should be noted at this point that this claim puts us at odds with the backwards steps we observed in the plot 3.1, since this would imply coming back onto the refractory region. However, as mentioned before, in the point wise approximation we lose the spatial features of the focus, the backwards steps could mean the focus passes close to a refractory region. This could happen when a focus encounters a cell membrane, as we see in figure 4.19, in the green branches in both cells. Other mechanisms of backwards steps could be substrate refractoriness proportional to Myosin intensity, and backwards steps observed in low Myosin foci. To understand this, more experiments and imaging of the motion of the substrate are required.

Finally, we posit a possible mechanism for focus birth, through 'infections' from neighbouring cells. We claim that focus birth in one cell might be through the influence of focus presence in another cell, close to the membrane.

This claim is supported by high Myosin expectation value just outside the cell membrane where a focus is born, which we see in the figure 4.17. We find that the presence of a focus coincides with the presence of high Myosin value in another cell, close to the original focus. However, we find the patch is short in radial distances, implying that infections are not always successful in creating travelling foci. Infections could be due to mechanical (for example through the mechanical communication of ratcheted Myosin pulses across neighbouring cells, as studied by [69]) or biochemical cues (for example Ca^{2+} ions, which flow through mechanically gated channels and upragulate Myosin activity, as mentioned in [25]) that flow across the surface of the tissue and across cell junctions . Further work is needed to determine their exact nature.

All these features together combine to give us a phenomenological picture of focus life. A mechanism for birth could be infections from neighbouring cells. If this is true, it is likely that the same mechanical or biochemical effects take place in the same cell enabling focus birth. The foci propagate due to their self avoiding nature, creating refractory regions in their wake. Finally, focus death could be due to the creation of refractory regions all around it, combined with entrapment at a cell edge.

Conclusion and Discussions

5.1 A Summary of Results from Previous Chapters

We briefly review the main conclusions from the previous chapters:

- Chapter 1

  Being equipped with time lapse movies of the amnioserosa during dorsal closure, we briefly reviewed the tool to extract cell membranes from the E-cadherin channel. Using this tool, we explored the basic properties of the cells of the amnioserosa, such as their area fluctuations and their anisotropy in shape. We then used the Myosin channel in the movies, and defined foci in an algorithmic way using two parameters: Myosin binary fluorescence threshold, and a radius for the closing operator for smoothing focus edges and removing small foci. To compare statistics over our entire dataset, we developed a tool to normalize myosin intensities across time and embryos. Using our algorithmic definition and the normalized movies, we used image analysis to identify and obtain a list of foci.

  We described the static features of the foci, including areas and intensities. We observed their distribution on the cell apical surface, noting that they were more probable near membranes than at the centre.

  Our method of focus identification can be applied to a broad variety of biological imaging where foci are present (section 0.3), if there is an intensity difference between the subject and the background. We also develop efficient methods of noise removal and intensity normalization to remove artefacts from phenomena such as photo-bleaching and varying levels of background intensity.

  We note that focus identification is dependent on the lower threshold level, and the radius of the closing operator. In this work, the lower threshold is decided visually, with some additional verification from various parameters elucidated in section 1.7. In choosing our closing radius we are guided by estimates of size of foci found in the literature. However, a strictly mathematical way to decide what constitutes a focus is yet to be articulated.

  Since our method is based on sizes and intensity differences, other large, high intensity features other than foci are also tracked. This includes the junctional myosin at cells, extra-cellular myosin cable on the tissue. We avoid the former by removing data from a 1 *pixel* boundary of the cell membranes, and the later by not not including data from the end of the fast phase of DC, where the cable appears.

  The normalization method is dependent on the relative spacing of quantiles, does not work for 'aberrant' movies, eg: 3LU.

- Chapter 2

  We presented a way to automatically track foci in time and reconstruct their motion. Treating the tracked foci as discrete objects with trajectories, we observed merging and splitting phenomena, thus defining trees and branches. Analysing the focus branches, we described kinematic features of foci speeds ($0.1\ \mu m/s$) , durations ($20s$ to $1min$) end-to-end distances ($1.6\mu m$), and relative changes in area and intensity during the course of their lifetimes. We found that in these branches, foci were never stationary, having a non-zero minimum speed between subsequent frames.

  Looking at the branch trajectories, we defined the angles of deviation at each frame. Finding this distribution to be anisotropic, peaked at 0°, lead us to speculate that motion of foci might be directional, or even ballistic.

Our focus tracking is a non invasive way to analyse focus dynamics *in vivo* in the amnioserosa, and takes into account non-injective dynamics of foci including mergings and splittings. It provides us with data-sets large enough to analyse statistically, with numerous features such as: speeds, sizes, intensities and geneologies. While not used in this work, parallel data-sets can be produced by intracellular and in-tissue tracking.

Our tracking is based on two parameters, maximum speed of foci, and the fractions of area overlap. In choosing both these parameters, we have been guided by the literature. Though the effect of these on branch kinematics is small, the focus genealogies depend on these parameters, as well as the lower threshold and the closing radius.

- Chapter 3

  This chapter saw the continued point particle analysis of the two features of focus branch trajectories: directions and distances. We defined an 'average' direction of focus motion, finding a strong preference for motion along that direction, and a strong abhorrence perpendicular to it. We also calculated the mean squared displacements of the foci, fitting them with a power-law in time to compare them with known regimes of motion, namely diffusive, ballistic and self-avoiding. We found a wide distribution of exponents, with the median around 1.5, the value in literature for self-avoiding random walks. This was a clue to the self-avoiding nature of foci.

  We observed effect of confinement on focus branch motion, in highly eccentric cells foci predominantly travelled along the long axis of the cell. At this point, we were able to reject unconstrained diffusive motion, on the basis of non-zero minimum speed between frames, and high directionality.

  We observed no effect on directionality due to presence of other foci, and no effect on the exponent due to confinement, or developmental time.

  The point-particle analysis performed in this chapter provides a good starting point to understand the kinematics of focus branches. Locating the foci at the centre of its visible myosin intensity mass, we are able to statistically summarize a wide variety of focus features: defining displacements and thus velocities and directions.

  However, one must remember that foci are not point particles, or objects possessing constant shape features. The quantity of myosin in a focus is in a state of flux at all points, the molecules themselves performing complex binding and unbinding dynamics and disappearing from the field of view. Thus, what we observe as motion, could be the combined effect of a number of biochemical and mechanical cues.

- Chapter 4

  In this chapter we returned to analysing the continuous myosin signal on the amnioserosa apex, through radial-myosin kymographs. This enabled us to observe the features of the apical myosin signal in the spatiotemporal neighbourhoods of foci. Our ideas of self avoiding motion of foci were confirmed by the presence of depletion regions before and after focus presence. We observed this phenomenon in the cell, and at the scale of the tissue. We hypothesized a mechanism for focus propagation, through creation of myosin refractory regions at the apical cortex in its wake. We speculated that this could be a factor responsible for both focus disassociation, as well as propagation.

  Noting the high expectation value of myosin just outside the cell-membrane found indications of inter-cellular focus 'infections'. Based on this observation, we speculated on one possible mechanism for focus birth, through infections from neighbouring cells.

  We validated good tracking through correspondence between centroid and the radial-myosin kymographs.

  The method of kymographs allows us the visualize and summarize the space-time features of the apical Myosin over thousands of focus events. Thus, we can extract the identifying features of focus births, deaths and motion.

5.2 Focus Dynamics

In this section, we will review the known hypotheses on actomyosin dynamics and see how far our observations can justify them. We will also present our own hypotheses based on our observations. We divide, for convenience, the dynamics of foci into three phases:

- **Assembly Phase**

  Mechanisms of focus assembly have been studied in various works. Some authors [54] have suggested assembly due to chemical gradients diffusing from the cell membranes (Rok). The high concentration of foci close to cell membranes that we observed in chapter 1, section 1.8.2 is consistent with this hypothesis. In this work, we study the spatio-temporal aspects of assembly through the definition of focus birth events. We note high concentration of birth events close to the cell membrane, in chapter 2, figure 2.14 adding further weight to this hypothesis. The imaging of Rok during DC suggests that it colocalises with foci [49], suggesting that this effect plays a role in DC. In the future, two channel movies with Rok and Myosin imaged could shed light on the temporal differences between these two species, making a more rigorous explanation possible.

  Other authors [51] [58] have cited the effect of a cell-wide Rho1/A clock controlling the assembly and disassembly of Myosin. This would imply a synchonised pattern in the births and deaths at the cell level. We do not observe this effect.

  Other works mention focus assembly due to cooperative actin bundling [67]. Increase in rates of focus events during the later parts of dorsal closure, as seen in chapter 2, section 2.5, which is also the phase of accelerated cell contraction, seen in chapter 1 section 1.4.1, is consistent with the possibility that this effect dominates during late DC. In the future, higher spatial and temporal resolution in imaging could expect to yield better correlations of focus pulsations and cell shape changes that we observe qualitatively in figure 1.2.

  Thus we see that both mechanical and biochemical effects can play a role in focus assembly. We will now posit a mechanism based on infections and substrate refractoriness as the reason for focus assembly, as we cite the literature that supports our claims.

  As we have seen in section 4.4.3, the presence of foci implies the presence of elevated myosin signal across the cell membrane that it is close to. The high number of focus births close to the membrane would also be consistent with this. We suggest that the observation of infections is an indication that diffusion of biochemical species is not the only contribution to the local triggering of Myosin recruitment. Stress could be involved, since it is known that the binding of Myosin on actin is mechano-sensitive [67].

  In *Drosophila* ventral furrow [69], it was noted that mechanical communications occur in neighbouring cells due to ratcheted Myosin pulses, or pulses of Myosin that result in apical constriction of the cell that does not relax afterwards. In the future, a quantification of whether infections are only caused by ratcheted focus pulsation or not, could shed light on this. These pulses would be more prevalent during the slow and fast phases of dorsal closure, and a preliminary visual inspection shows more signs of infections in the kymographs associated with these tissues. However, better quantification is necessary. These authors have suggested the mechanical contact via cortex 'clutch' [1] as a reason for this phenomenon. While we don't directly study the hypothesised presence of such an actin-membrane 'clutch', or whether the focus is connected to cell membrane [55], we qualitatively observe high motion of foci compared to motion of cell membranes, especially during the early and slow phases of dorsal closure. These preliminary observations likely imply that such a clutch is not activated in the amnioserosa.

  Infections could also be of biochemical origin. Biochemical communications between neighbouring cells via the flow of Ca^{2+} ions (a known upregulator of myosin activity in dorsal closure) through mechanically gated channels in cell membranes, has been noted [25]. Manipulations of the available free Ca^{2+} in cells, either upregulation through ultraviolet light induced uncaging, or downregulation through pharmacological means, have already been performed by the same authors. Analysing such a perturbed system through the method of focus identification and kymographs will be able to tell us if this truly has an effect on the infections that we observe.

Whether mechanical or biochemical, we speculate that the mechanisms that trigger focus birth in neighbouring cells would also be valid mechanisms in the same cell. These mechanisms could therefore contribute to the motion phase of foci. The observation of substrate refractoriness in sections 4.4.1 and 4.4.2 also gives as the spatial locations where focus birth is most probable, which are the non-refractory low-Myosin regions in a cell.

Conversely, the locations where the substrate is refractory would see low recruitment of Myosin, giving us a local downregulation effect once concentration has already taken place. Therefore, a combination of these two factors gives us a recipe for pulsatility.

- **Motion Phase**

  During the course of this work, we first rejected random walk as the explanation for focus propagation. In figure 2.7, we find non-zero focus speeds, which is not consistent with the diffusion hypothesis for focus propagation. Further evidence is the highly directional nature of focus branches as seen in chapter 2, figure 3.1 (where we calculated deviation from mean direction), as well as in chapter 3, figure 2.10 (where we calculated deviation in each step of trajectory). The high mean value for exponent of motion seen in D.2 also leads us away from this hypothesis. However, in the future, imaging the spatial dynamics of myosin up and down-regulating species, Rho, Rok, Mbs (and further, up and down regulators of Rho, RhoGEFs and RhoGAPs), followed by temporal tracking, will be able to tell us if which of these chemicals colocalise with, and follow the dynamics of Myosin foci. This could shed light on the role of diffusion in focus propagation. Since focus motion has also been considered to be the combined effect of its advection and binding-unbinding dynamics, a mathematical method to separate these two factors could allow us to isolate the second and discover effective rates.

  A mechanism for the flow of foci has been presented in the *Drosophila* germband as the advection of Myosin by the convergent velocity field of the substrate [49].We find relatively high values of focus displacement as compared to the motion of the cell-membranes, which can be considered a proxy for the radial flow of the substrate. In our drift diffusion analysis (figure D.3), we find that by subtracting a drift field from the motion of the focus branches, we do not obtain a flow that is consistent with diffusive dynamics. We conclude that this explanation is not consistent with our observations and there are likely to be other effects at play during dorsal closure.

  We posit, through our observations in chapter 4, a model of self-avoidance due to substrate refractoriness as a mechanism for focus propagation. Once actomyosin is concentrated at a specific sub-cellular region, it starts to generate a local refractory behaviour in the substrate. The underlying cause can be mechanical or biochemical. Likely candidates include the breakdown of the substrate at high myosin intensities as modelled in [67]. In the future high spatial resolution in the imaging of the substrate could definitively tell us whether there is breakdown of actin at the wake of focus trajectories.

  Refractoriness could also be due to local high concentration of myosin downregulating species such as Mbs which is known to localise with Myosin in *Drosophila* amnioserosa [17]. In the same work Mbs downregulation has also been shown to reduce the integrity of the amnioserosa, causing tears, so perhaps this explanation can be combined with actin breakdown. In the future, simultaneous imaging of Mbs and Myosin, followed by spatio temporal tracking, could shed light on this process.

  We claim that the foci show high directionality in their flow due to the same self-avoidance mechanism, while never quite reaching the persistence expected for driven, ballistic motion. [22] have claimed that cell polarisation causes focus flow along long axis of cell. We found this effect to increase with eccentricity in chapter 3 section 3.2.1. However, we saw in chapter 1 figure 1.4, that cell shape anisotropy decreases with progress of dorsal closure. The same is true for the oriented nature of cells as seen in figure 1.5. But the focus activity increases with the progress of dorsal closure. Thus we see that this effect is present during DC, but is likely linked with other effects that influence directionality of foci. In the future, through higher temporal resolution of imaging, we can hope to achieve better focus tracking, and likely find the other factors influencing directionality (as we attempted to do in the figures 3.5 and 3.7).

- **Disassembly Phase**

The authors [49] submit low advection rates at high concentrations of myosin, as the factor responsible for focus disassembly. They note that myosin foci were assembled by convergent advection with the actin cytoskeleton, and disassembled by the local effect of Mbs. High concentrations of myosin feedback negatively on the advection rates, enabling disassembly. We observe no difference in motion of our foci in based on their myosin concentrations, so this explanation is unlikely to explain focus death in dorsal closure.

Other authors use the cell wide Rho-1/A clock [58], as the factor setting periods of Myosin downregulation. In our analysis, this would likely imply an oscillation in the pattern of focus deaths through dorsal closure. We observe the pattern of focus deaths through DC in chapter 2, figure 2.13, but we do not make this claim. In the future, higher temporal resolution of focus imaging would shed better light on this topic.

We posit substrate refractoriness and geometrical confinement as the reason for focus death. As a general rule, foci follow the longest cellular length dimension, creating a refractory substrate as they pass, and die when they are trapped between a cell membrane and their own trajectory. Indeed, we find in chapter 1, figure 2.14, that death events are more probable close to the cell membranes. As stated before, the substrate refractoriness suggests the existence of a local downregulation effect once concentration has already taken place. The diffusion-reaction model from [54], which predicts a local tuning of Myosin binding and unbinding, is a possible biochemical mechanism for this effect. Following [67], we suggest that mechanics could also play a role in this. It is likely that both play a role, and we will need be able to gauge the relative importance of the two to complete our understanding of these ubiquitous pulsations.

Appendix A

Evolution of Statistics with Lower Threshold

In this appendix we will explore the effect of various lower threshold on the main plots

A.1 Evolution of Number of Tracked Quantities with Threshold

We plot the evolution of the number of foci with the increase in lower threshold from 60 to 130.

We plot the evolution of the number of branches and trees with the increase of lower threshold from 60 to 130, in figure A.1. We find that both of them take a maximum value at 70, and then reduce with increasing threshold.

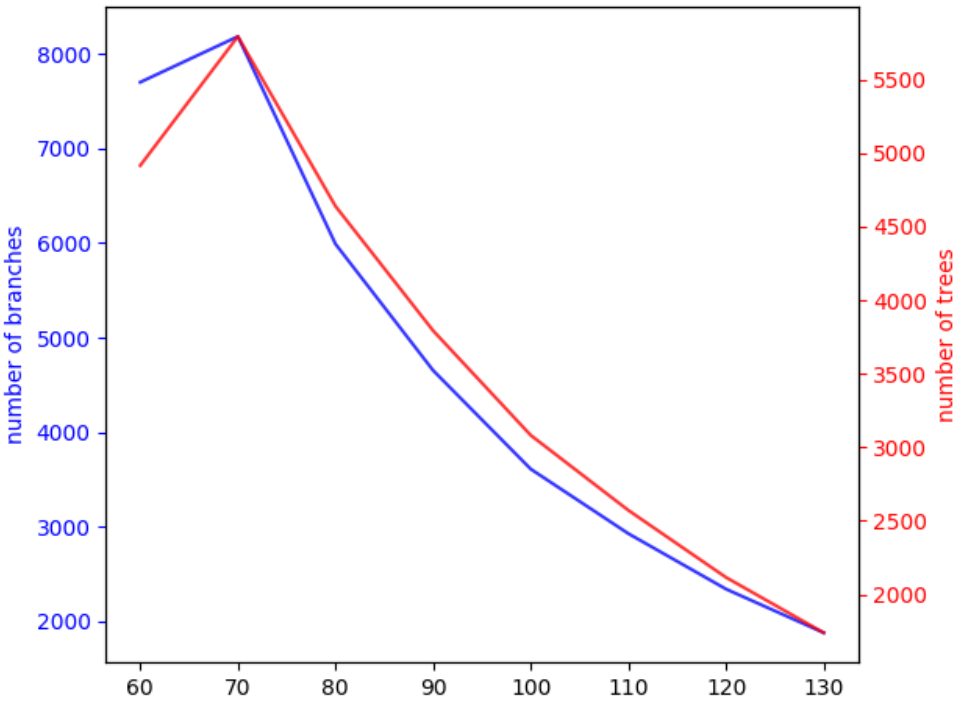

Figure A.1: **Number of trees and branches at different lower thresholds**

A.2 Plots from Chapter 2

A.2.1 End to End Distances

We plot the distributions of the end to end distances of foci for lower threshold values from 60 to 130 in figure A.2. We note that the decay distance changes from 0.44 μm at 60 to 0.56 μm at 130.

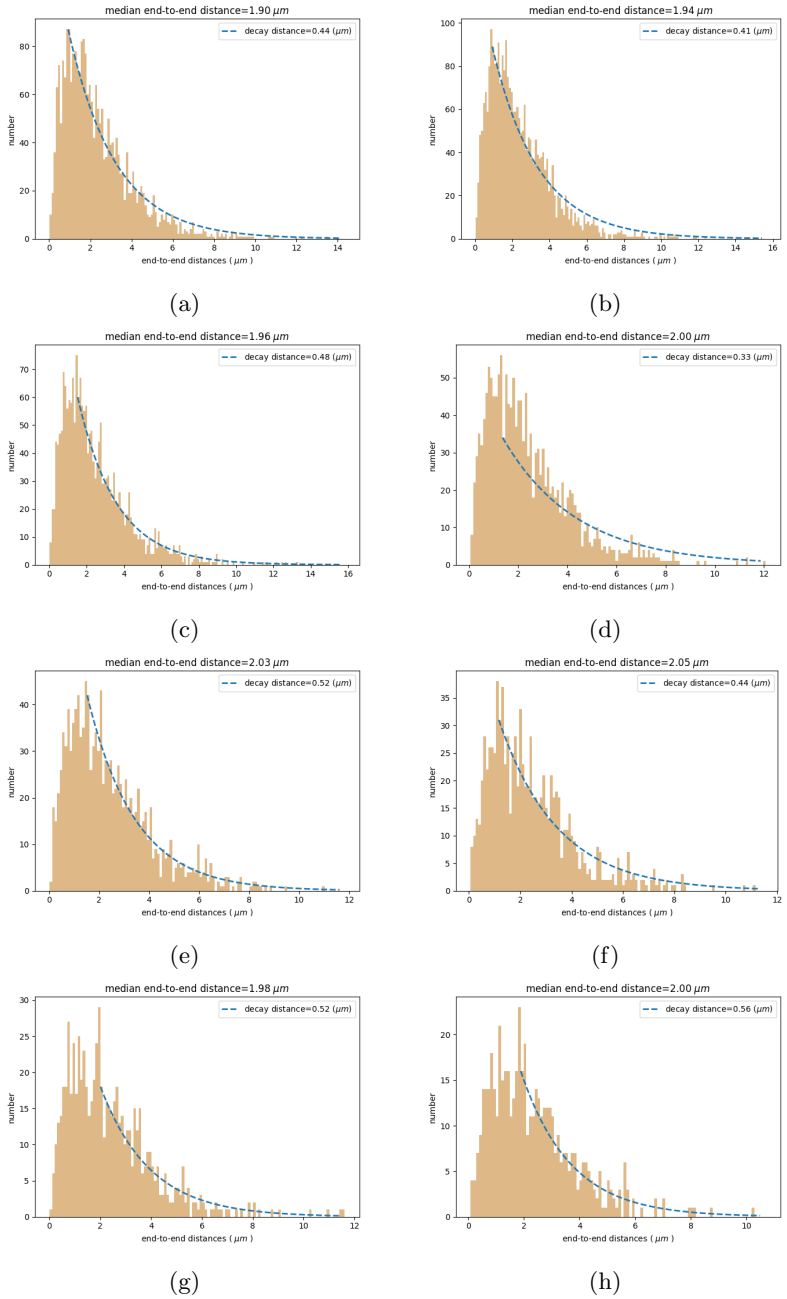

Figure A.2: **Distributions of focus end to end distances with lower thresholds between 60-130**

A.2.2 Speeds

We plot the distributions of the speeds of foci for lower threshold values from 60 to 130 in figure A.3. We note that the mean speed, 0.08 $\mu m/s$ stays the same at all thresholds, where are the minimum speed increases from 0.01 to 0.02 $\mu m/s$ at the very high thresholds.

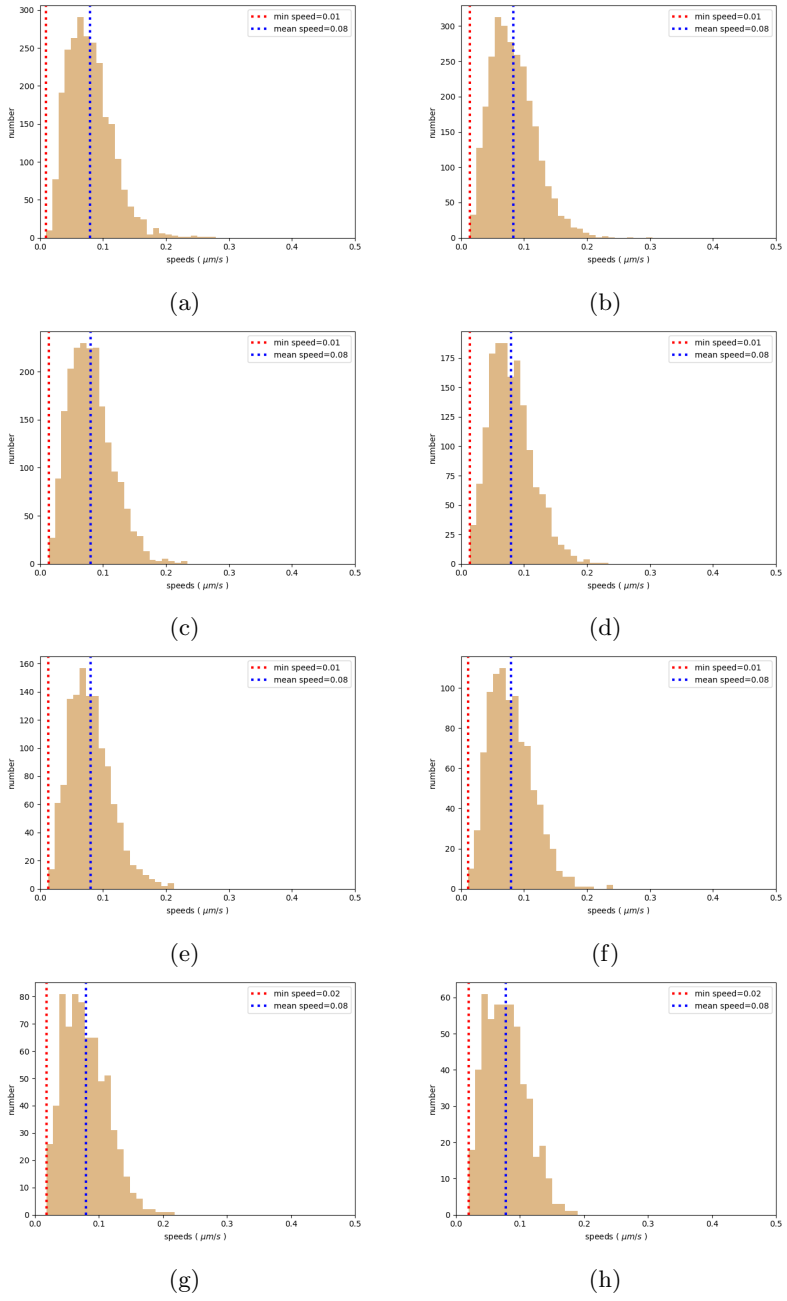

Figure A.3: **Distributions of focus speeds with lower thresholds between 60-130**

A.2.3 Birth and Death Events in Time

We plot the birth and deaths events of foci vs developmental time, for lower threshold values from 60 to 130 in figure A.4. Over the range of these thresholds, we see more than a three fold decrease in the number of

such events detected (5755 at 60 to 1796 at 130).

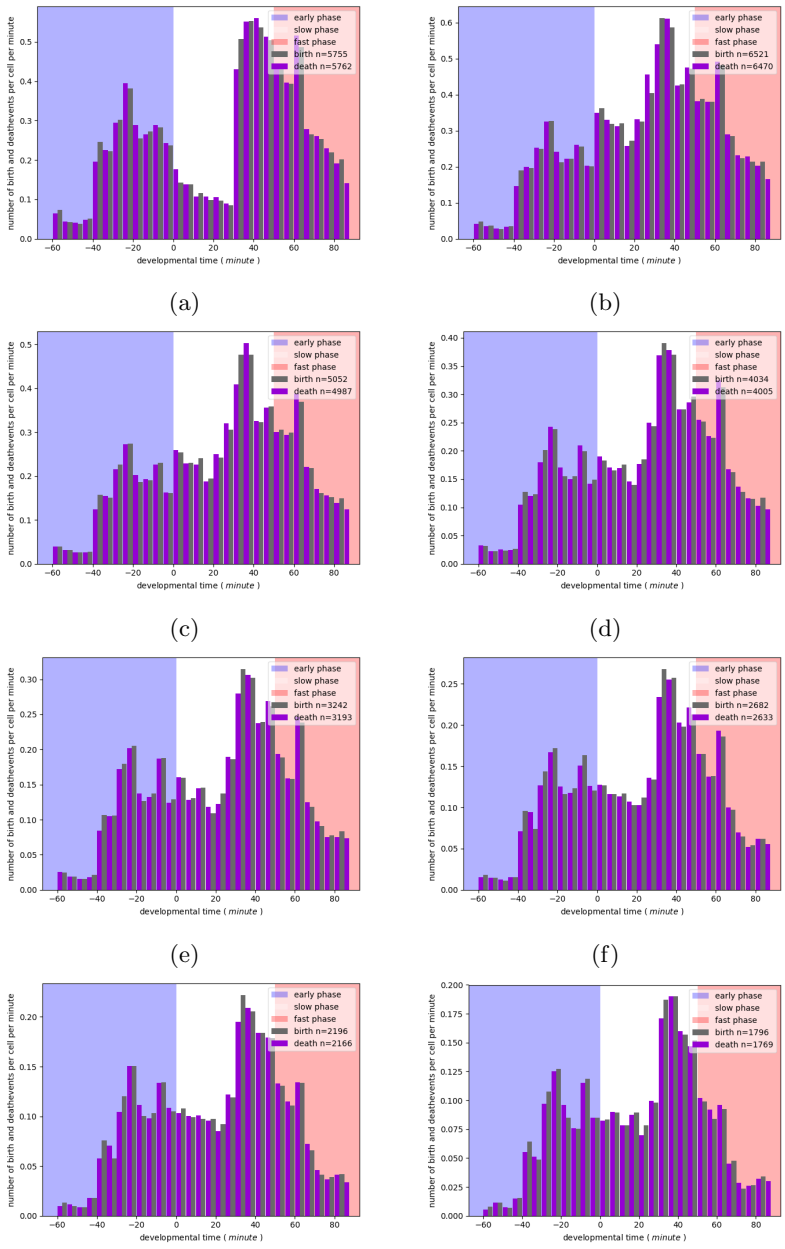

Figure A.4: **Plots of births and deaths with developmental time for lower thresholds between 60-130**

A.2.4 Merging and Splitting Events in Time

We plot the merging and splitting events of foci vs developmental time, for lower threshold values from 60 to 130 in figure A.5. We note that at higher thresholds, we stop progressively detecting these events at the fast phase of dorsal closure. Over this range of thresholds, the number of events detected reduces by an order of magnitude (1916 mergings at 60, compared to 135 at 130)

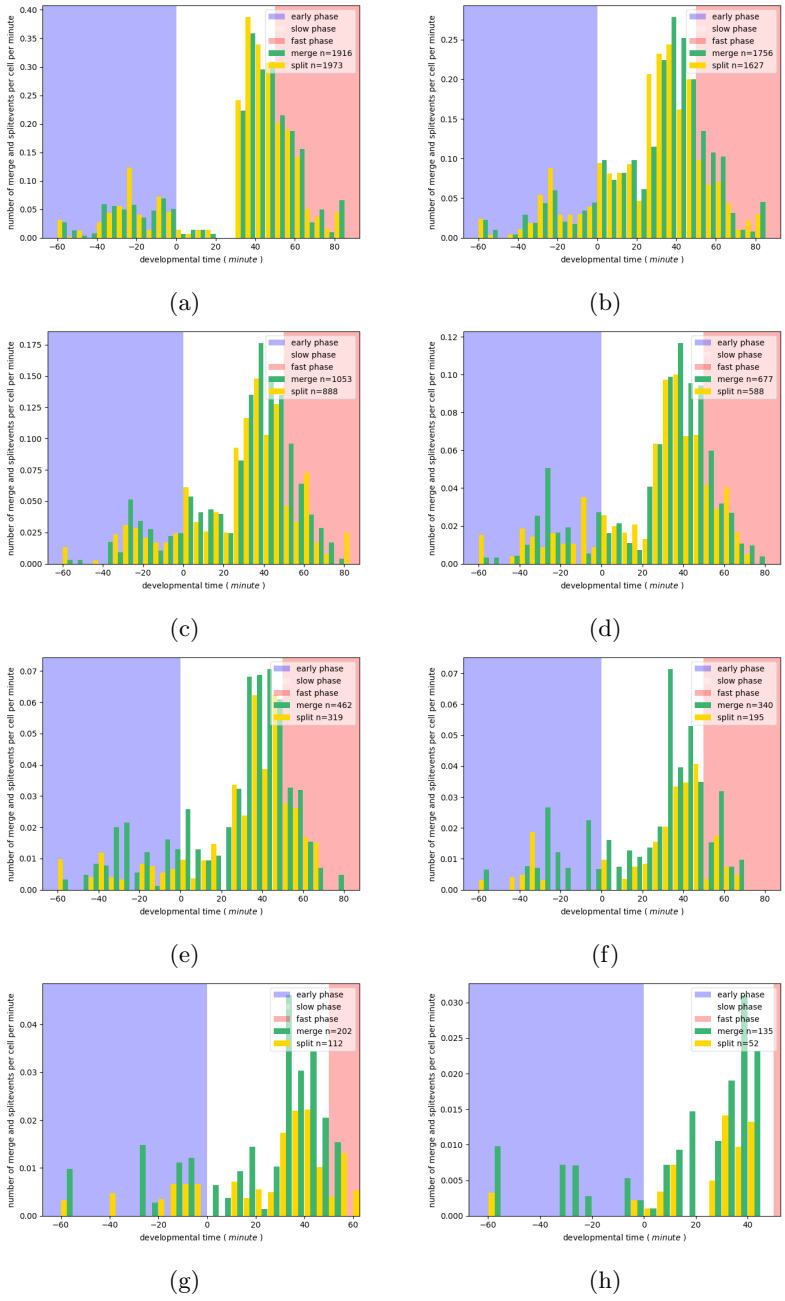

Figure A.5: **Plots of mergings and splitting with developmental time for lower thresholds between 60-130**

A.3 Plots from Chapter 3

A.3.1 Angles of Deviation from Average Focus Direction

We plot the distributions of angles of deviation from the average focus direction, for lower thresholds between 60 and 130. We note that backwards steps at around 180° are found for all thresholds.

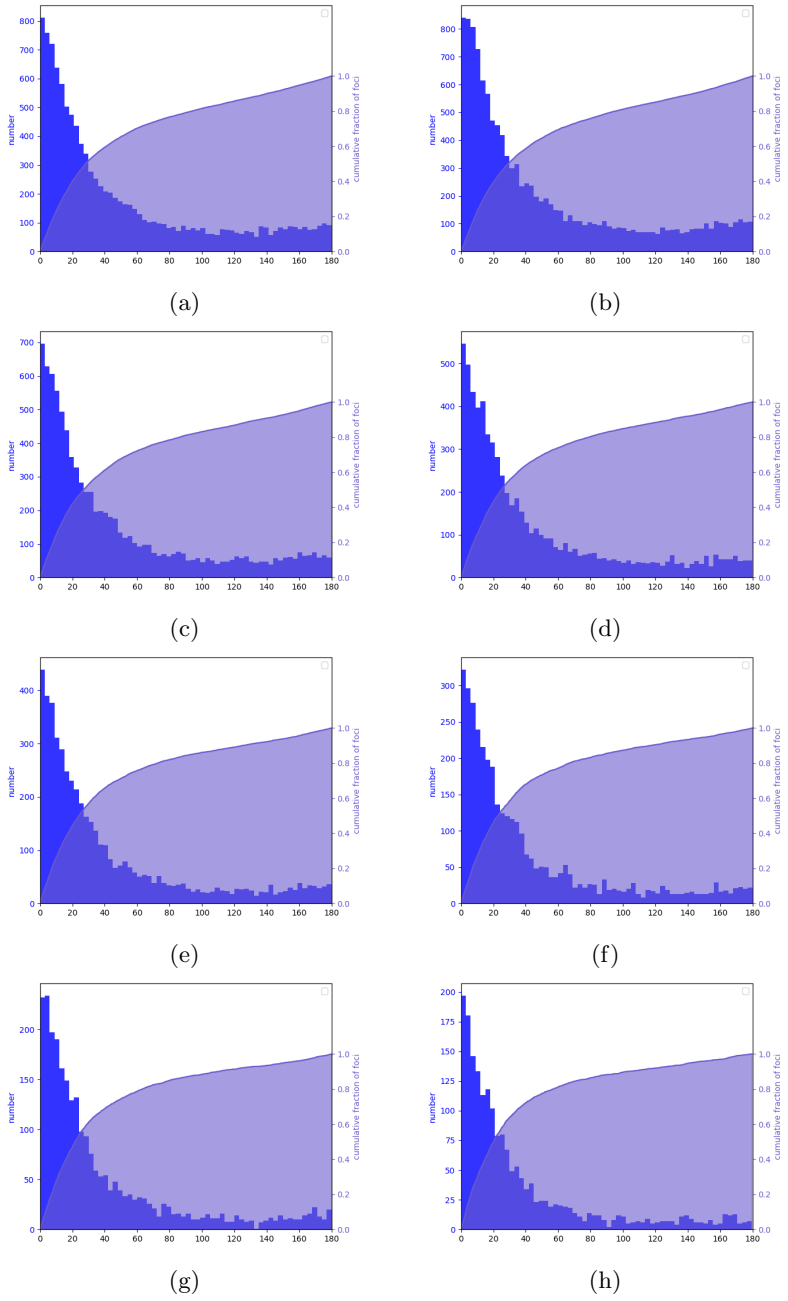

Figure A.6: **Distributions of angles of deviation from average focus direction for lower thresholds between 60-130**

A.3.2 MSD Exponent Distribution

We plot the distributions of exponents of motion for lower thresholds between 60 and 130. We note that the number of branches decreases from 2662 at 70 to 521 at 130. Within this range, the median exponent rises from 1.34 to 1.59.

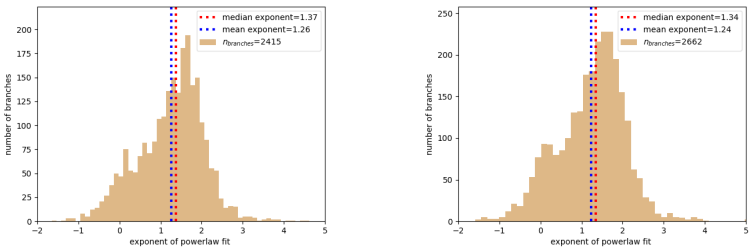

(a)

(b)

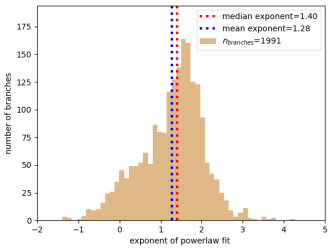

(c)

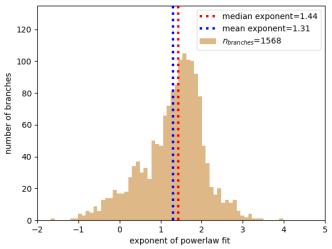

(d)

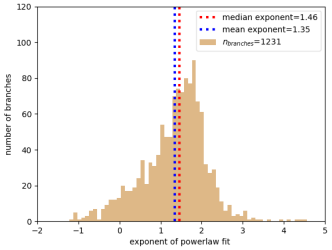

(e)

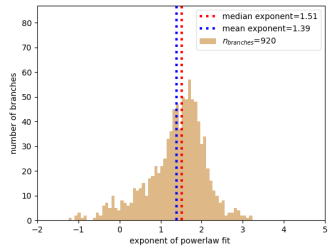

(f)

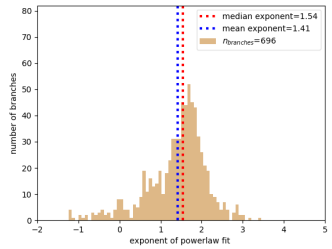

(g)

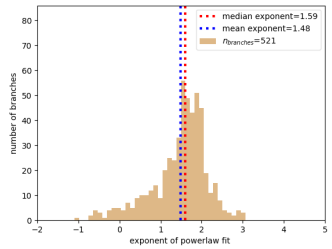

(h)

Figure A.7: **Distributions of exponents of motion for lower thresholds between 60-130**

Appendix B

Evolution of MSD Exponents

In this Appendix we present the evolution of focus mean-squared displacements (MSD) exponents with various cell and focus characteristics, and vice versa.

B.1 Exponent of Motion and Focus Intensities

Plotting against one another, the exponent of focus motion and its end to end distance, in the figure B.1, we find, on one hand, that the increase in end to end distance implies an increase in the median value of the exponent of motion, upto a value around 6 μm. This is to be expected because higher end to end distance implies more directed motion, therefore more ballistic exponents. On the other hand, plotting the end to end distances as function of the exponent, we find a non-monotonic increase in end to end distances from the sub-diffusive to super-ballistic range, with the maximum around 1.9 [1].

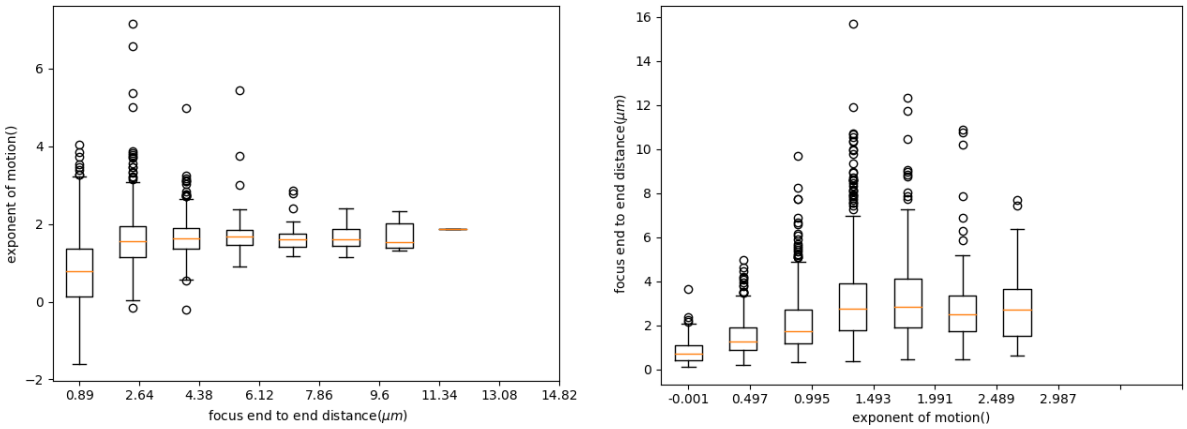

(a) Exponent of motion vs focus end to end distance (b) Focus end to end distance vs exponent of motion

Figure B.1: **Exponents of Focus Motion and Focus End to End Distances**

B.2 Exponent of Motion and Focus Intensities

Plotting against one another, the exponent of focus motion and its average intensity, in the figure B.2, we find, on one hand, that the increase in intensity implies an increase in the median value of the exponent of

[1] in the figure B.1b, only the relevant range of exponents are plotted. on both sides of this range, there are higher and lower exponents that associate with few focus paths. This sub-selection is done for all (b) plots in this appendix, and for none of the (a) plots.

motion, upto a value around 66000 au (after this, the number of foci polled is few). On the other hand, with the increase in exponent from the sub-diffusive to super-ballistic range, the mean focus intensity first rises and then falls, with a maximum around 1.5.

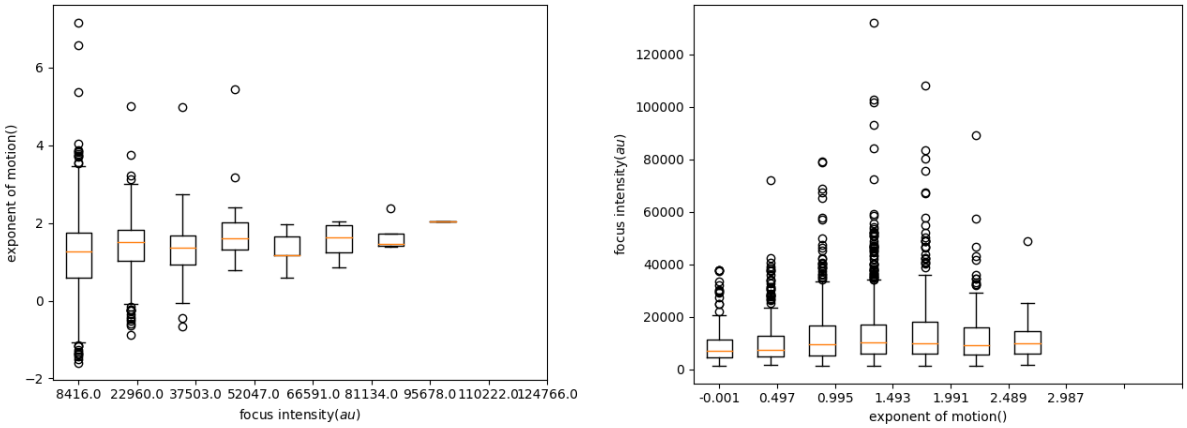

(a) Exponent of motion vs focus intensity

(b) Focus intensity vs exponent of motion

Figure B.2: **Exponents of Focus Motion and Focus Intensities**

B.3 Exponent of Motion and Focus Durations

Plotting against one another, the exponent of focus motion and its duration, in the figure B.3, we find that duration under a minute correspond to the highest median exponent of motion, and also the largest spread in exponents. More than this, the exponents decreases slowly. It rises again for foci of durations greater than two minutes, but such foci are rare in our analysis. On the other hand, the median duration stays relatively constant up at around 50s for the reliable range of exponents of motion.

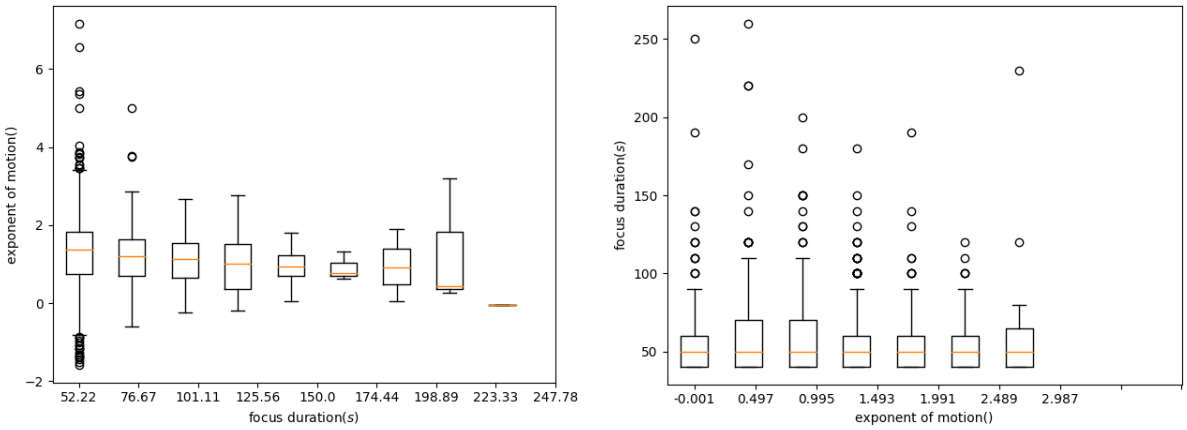

(a) Exponent of motion vs focus duration

(b) Focus duration vs exponent of motion

Figure B.3: **Exponents of Focus Motion and Focus Durations**

B.4 Exponent of Motion and Cell Myosin Concentrations

Plotting against one another, the exponent of focus motion and the mean concentration of Myosin in the cell, over times of focus presence, in the figure B.4, we find, on one hand the median exponent remains relatively uniform with increase in cell Myosin concentrations. On the other hand, we find that as the exponents around increase to the diffusive to ballistic range $(1-2)$, the median Myosin concentration of the containing cell increases also.

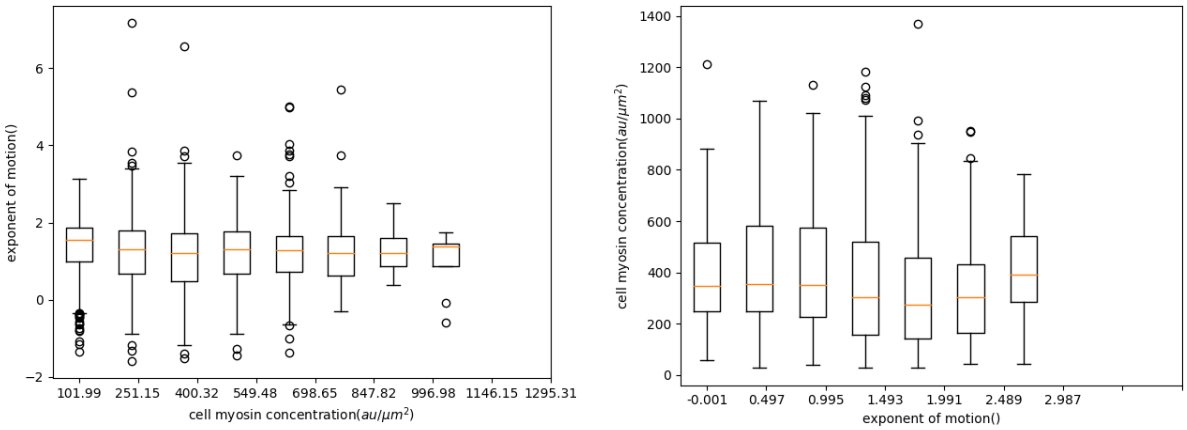

(a) Exponent of motion vs cell myosin concentration (b) Cell myosin concentration vs exponent of motion

Figure B.4: **Exponents of Focus Motion and Cell Myosin Concentration**

B.5 Exponent of Motion and Cell Areas

Plotting against one another, the exponent of focus motion and the mean area of the cell over times of focus presence, in the figure B.5, we find, on one hand the median exponent remains relatively uniform with increase in cell areas. On the other hand, the cell areas also stay relatively uniform for an increase of the exponent in the relevant range.

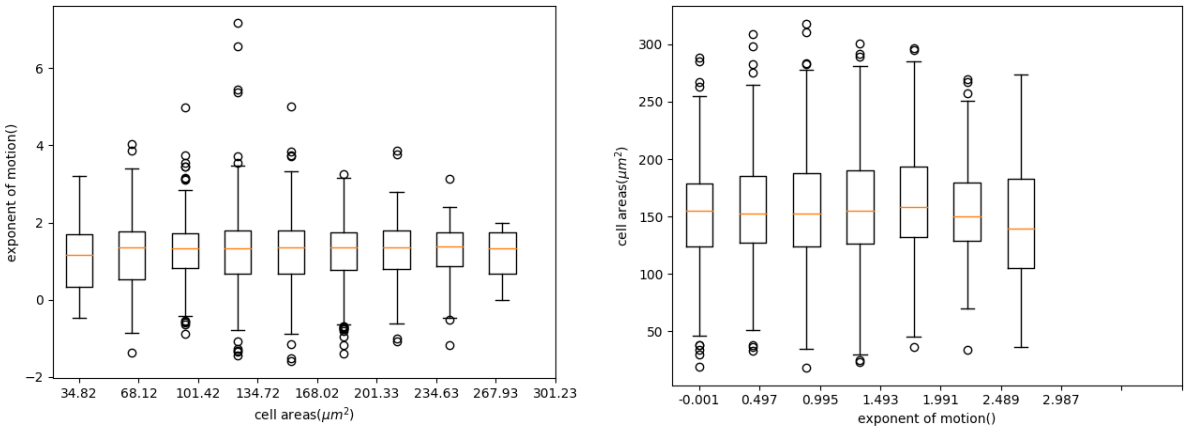

(a) Exponent of motion vs focus duration (b) Focus duration vs exponent of motion

Figure B.5: **Exponents of Focus Motion and Cell Areas**

Here, we also plot against one another in figure B.6 the exponent of focus motion with the mean area strain of cells. Area strain is defined as the change in area in any two frames, normalized by the area in the

first frame. Thus, positive values represent expansion, and negative values represent contraction. We find that large contractions are associated with somewhat higher exponents of motion, and large expansions are associated with slightly larger exponents of motion than small expansions.

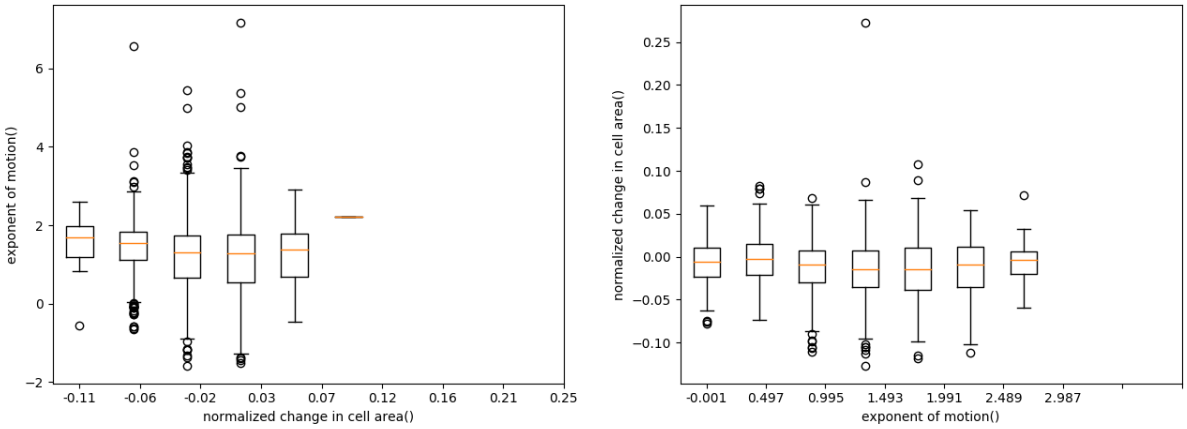

(a) Exponent of motion vs area strain

(b) Area strain vs exponent of motion

Figure B.6: **Exponents of Focus Motion and Cell Area Strain**

Appendix C

Space-Time Kymographs

In this appendix we present the kymographs not presented in the main work.

C.1 Averaged Kymographs over Tissues

We present the averaged kymograph variants not presented in the main work.

C.1.1 Kymographs in Original Cell Only

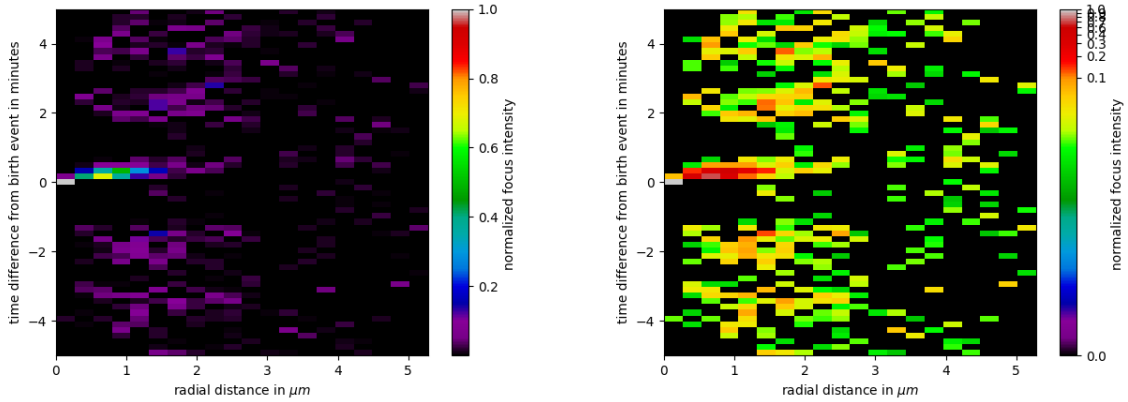

(a) (b)

Figure C.1: **The birth and propagation of foci:** Panel (a) shows centroid kymograph around a focus birth event, considering only centroids of foci present in the original cell. Panel (b) shows the same figure with colorbar in logscale, to better visualize low myosin features. These kymographs contain 613 events averaged over 127 cells in 4 tissues

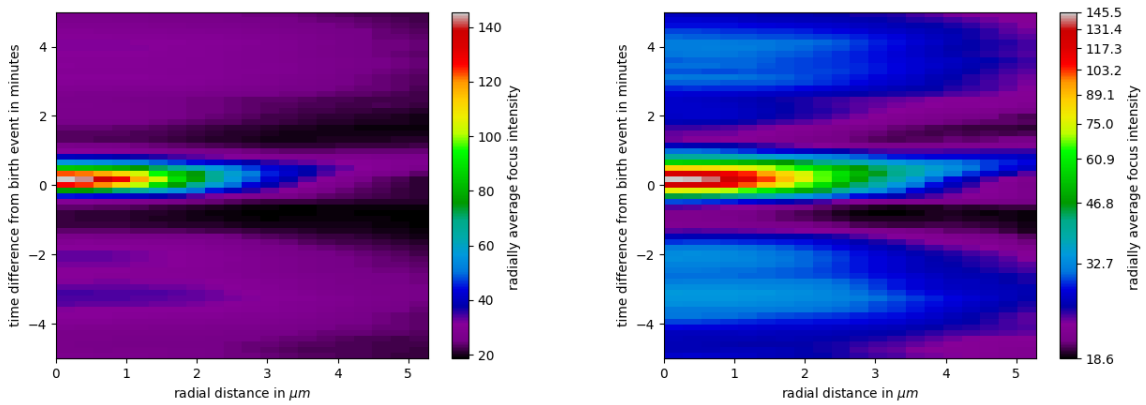

(a) (b)

Figure C.2: **Depletion regions through radial-myosin kymograph:** Panel (a) shows the average radial-myosin kymograph with origin centered at focus birth, considering only signal from the cell containing the focus. Panel (b) same figure with colorbar in logscale, to better visualize low myosin features. These kymographs contain 546 events averaged over 4 tissues

C.1.2 Kymographs in Whole Tissue

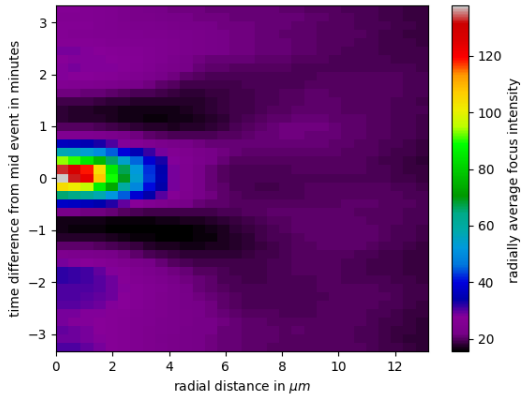

(a) average radial-myosin from mid events

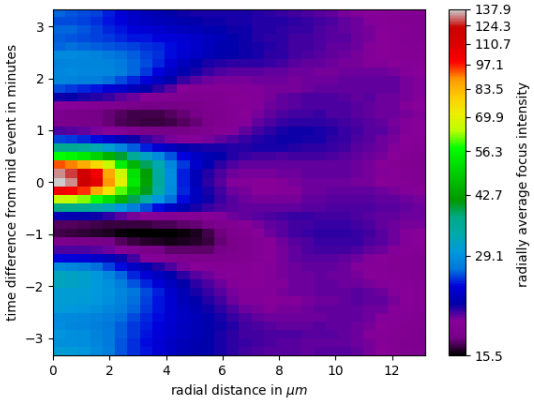

(b) average radial-myosin from mid events, colorbar in logscale

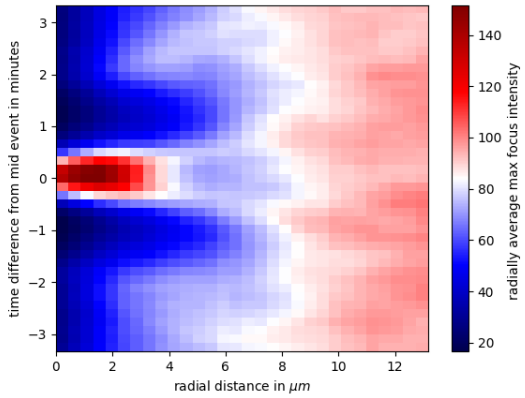

(c) maximum radial-myosin from mid events

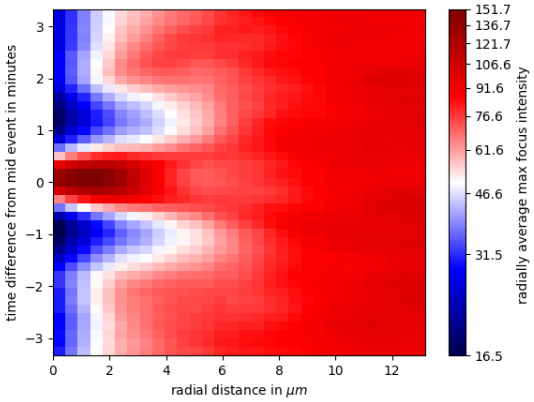

(d) maximum radial-myosin from mid events, colorbar in logscale

Figure C.3: **Motion at tissue scale through radial-myosin kymographs**

C.1.3 Kymographs outside Original Cell

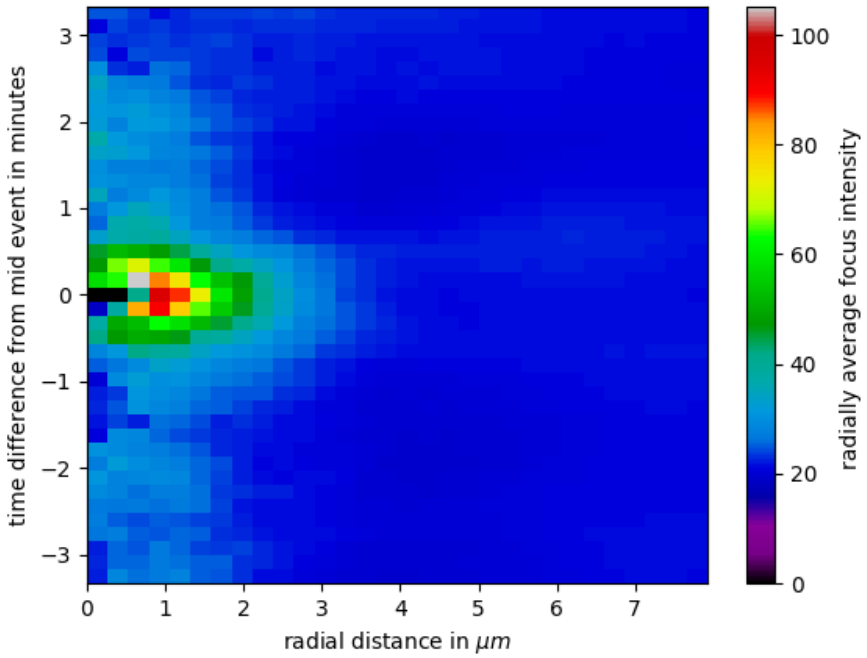

(a) Average radial-myosin kymograph from mid events without signal from original cell

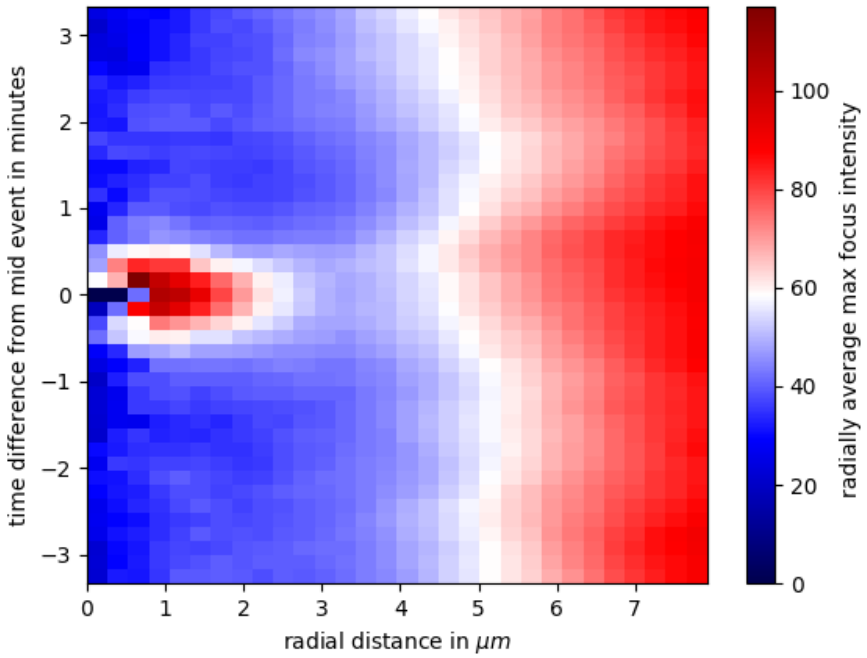

(b) Maximum radial-myosin kymograph from mid events without signal from original cell

Figure C.4: **Myosin signal outside the original cell:** These kymographs contain 4334 events averaged over 8 tissues

C.2 Kymographs of Individual Tissues

We present the Kymographs of individual tissues.

C.2.1 Kymographs with Original Cell Only

Radial-myosin kymographs for original cell: Birth

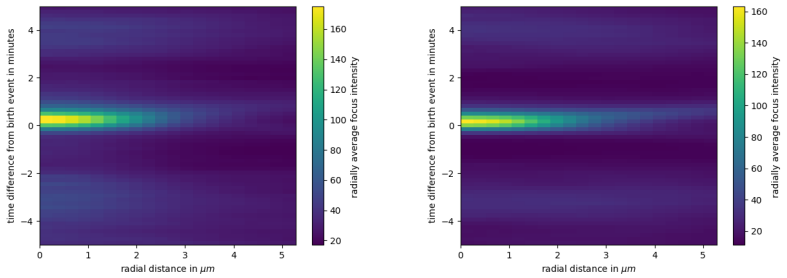

(a) 3a early

(b) 2a early

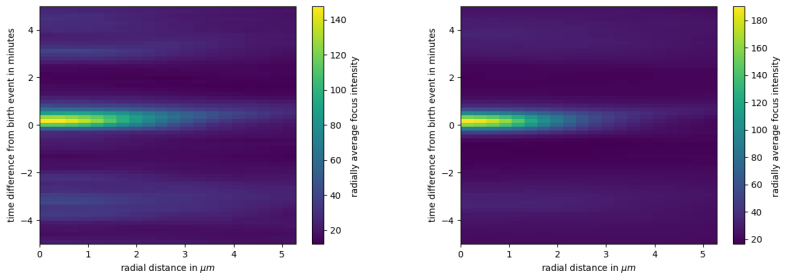

(c) 4a early

(d) slow3

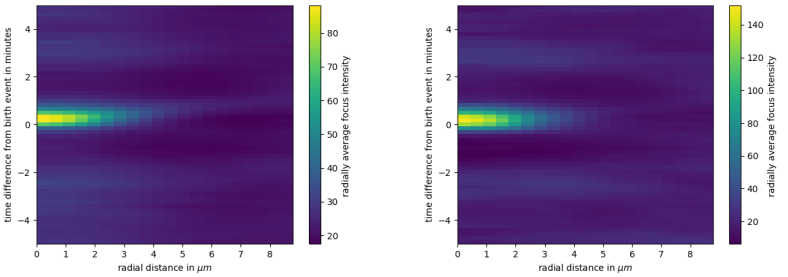

(e) 7LU

(f) 5LU

Figure C.5: **Average radial-myosin kymographs for birth events (original cell only) in individual tissues 1**

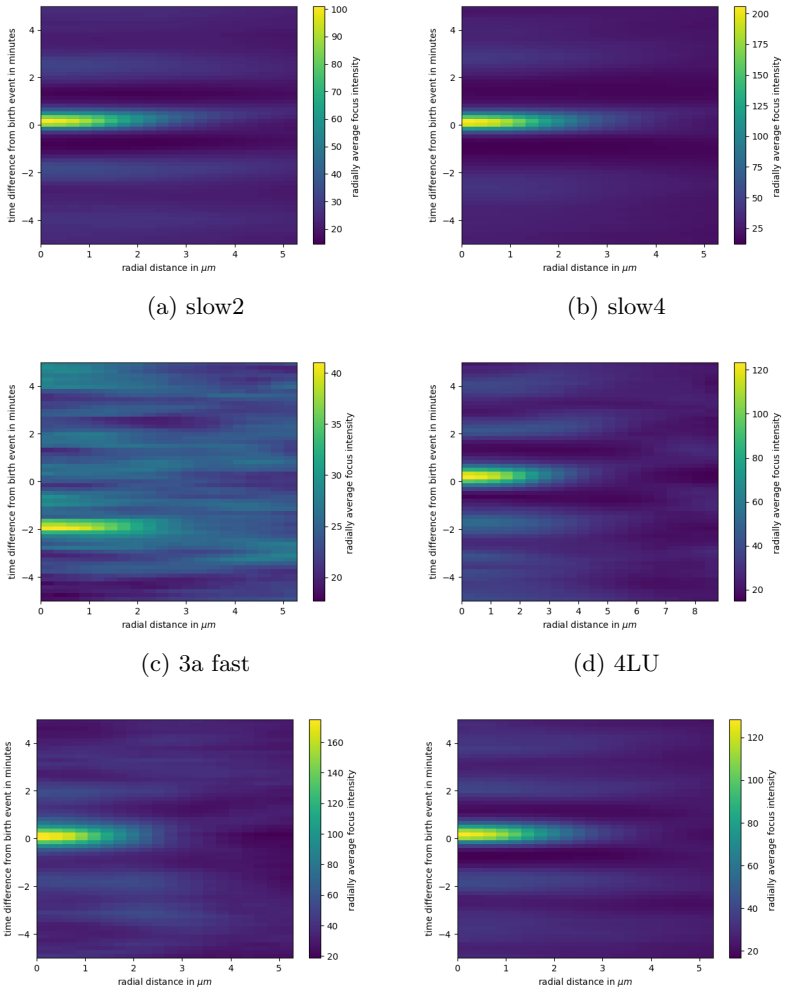

(a) slow2

(b) slow4

(c) 3a fast

(d) 4LU

(e) 2a fast

(f) 4a fast

Figure C.6: **Average radial-myosin kymographs for birth events (original cell only) in individual tissues 2**

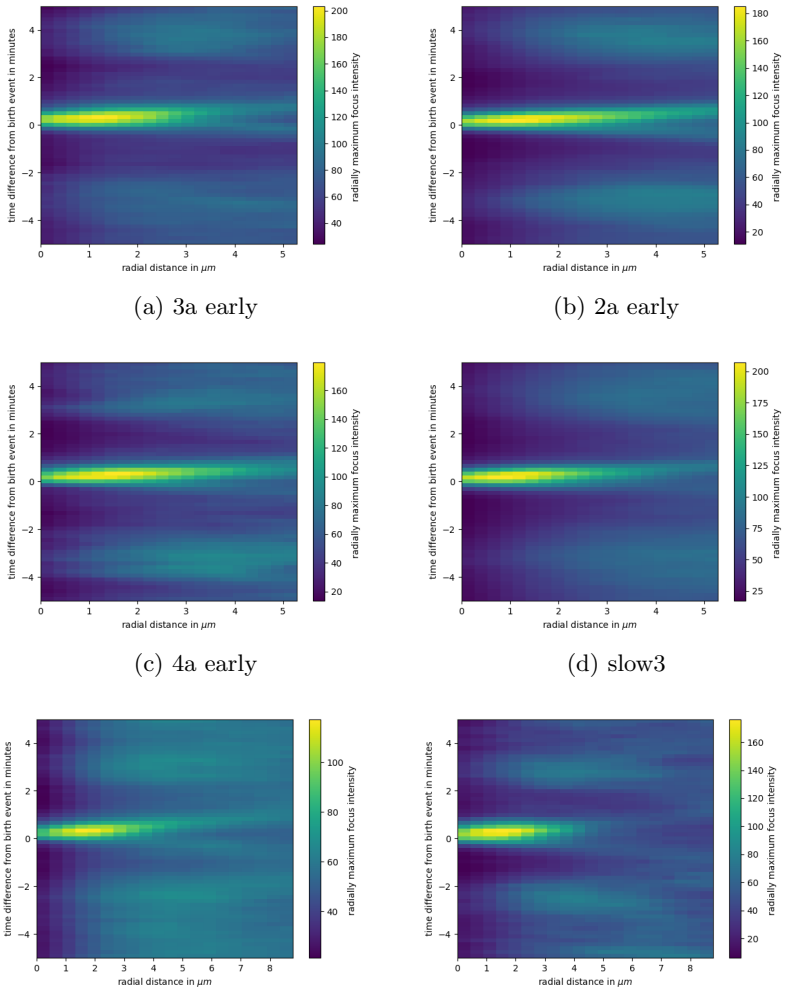

(a) 3a early

(b) 2a early

(c) 4a early

(d) slow3

(e) 7LU

(f) 5LU

Figure C.7: **Maximum radial-myosin kymographs for birth events (original cell only) in individual tissues 1**

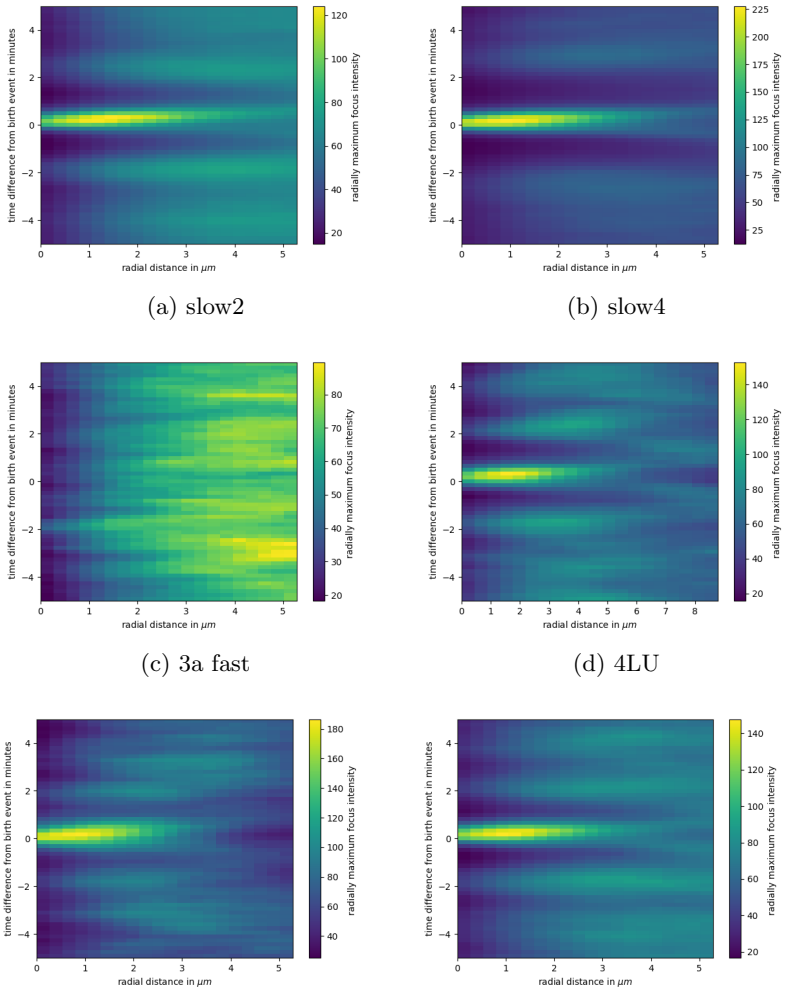

(a) slow2

(b) slow4

(c) 3a fast

(d) 4LU

(e) 2a fast

(f) 4a fast

Figure C.8: **Maximum radial-myosin kymographs for birth events (original cell only) in individual tissues 2**

Line Plots of Myosin intensities close to origin for radial-myosin kymographs for original cell: Birth

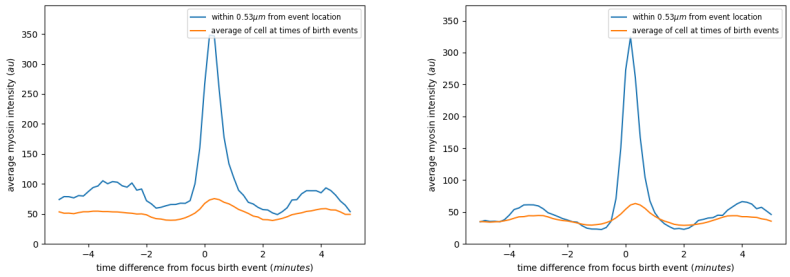

(a) 3a early

(b) 2a early

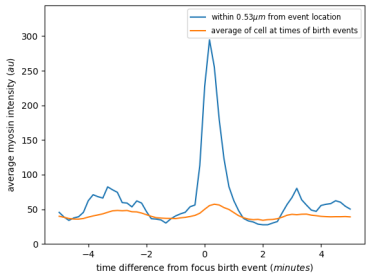

(c) 4a early

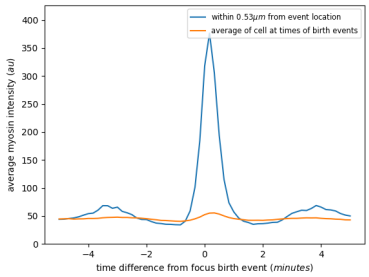

(d) slow3

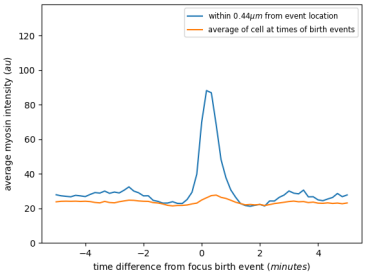

(e) 7LU

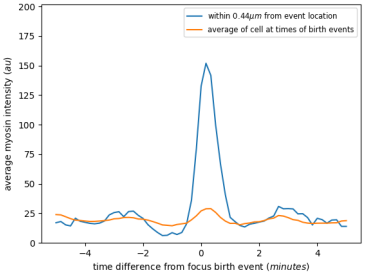

(f) 5LU

Figure C.9: **Line plots close to birth locations 1**

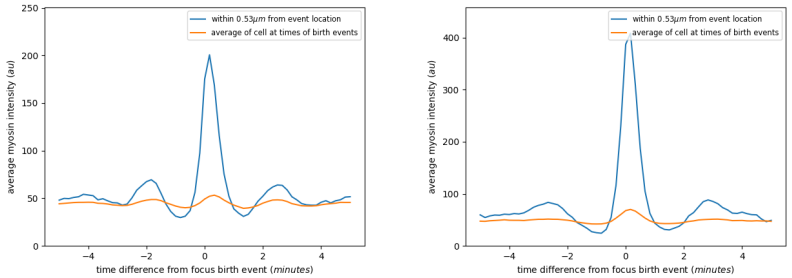

(a) slow2

(b) slow4

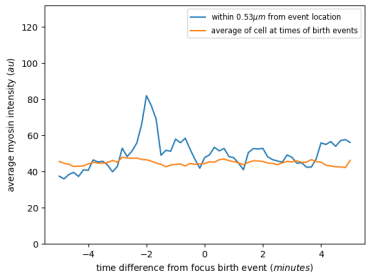

(c) 3a fast

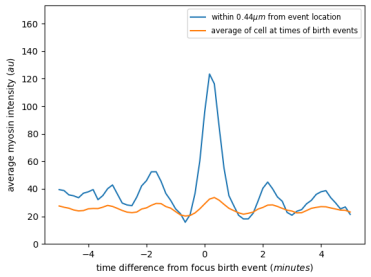

(d) 4LU

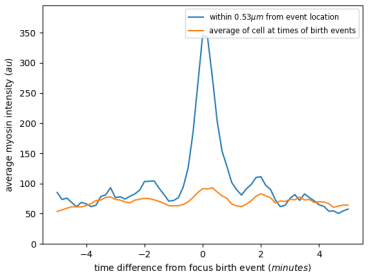

(e) 2a fast

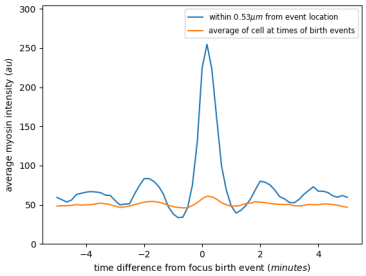

(f) 4a fast

Figure C.10: **Line plots close to birth location 2**

Radial-myosin kymographs for original cell: death

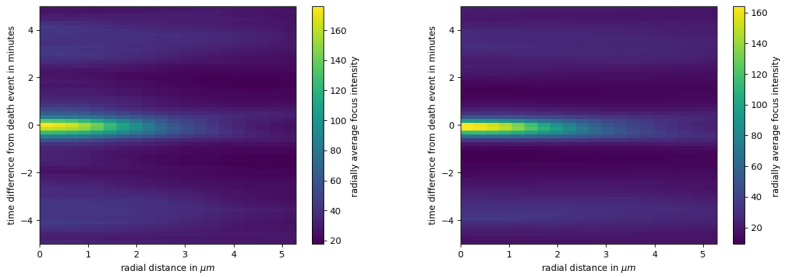

(a) 3a early

(b) 2a early

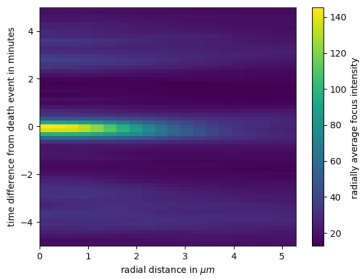

(c) 4a early

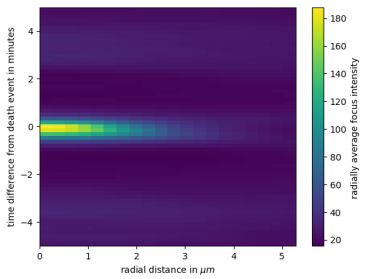

(d) slow3

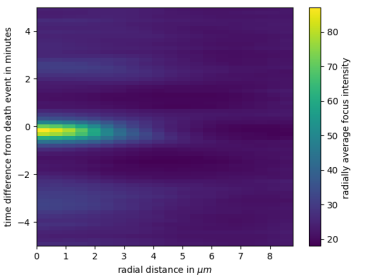

(e) 7LU

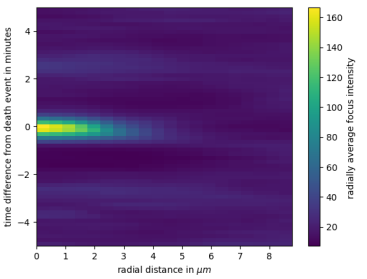

(f) 5LU

Figure C.11: **Average radial-myosin kymographs for death events (original cell only) in individual tissues 1**

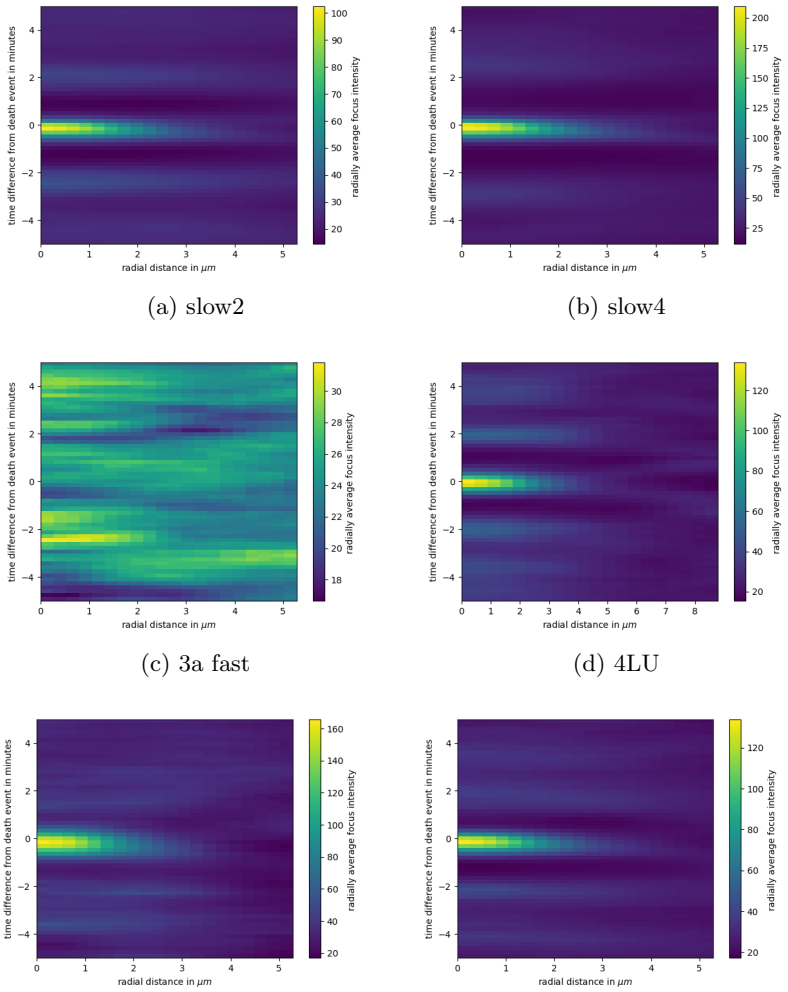

(a) slow2

(b) slow4

(c) 3a fast

(d) 4LU

(e) 2a fast

(f) 4a fast

Figure C.12: **Average radial-myosin kymographs for death events (original cell only) in individual tissues 2**

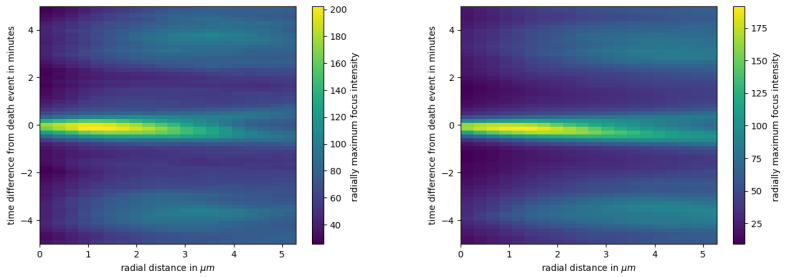

(a) 3a early

(b) 2a early

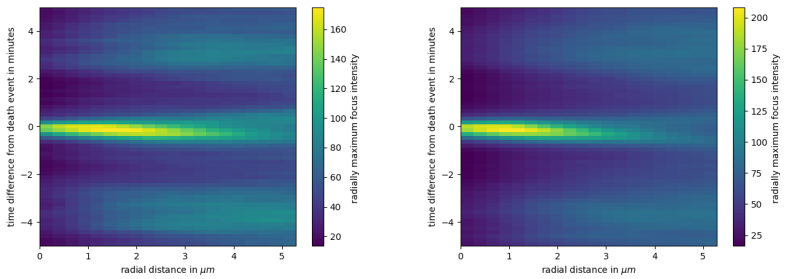

(c) 4a early

(d) slow3

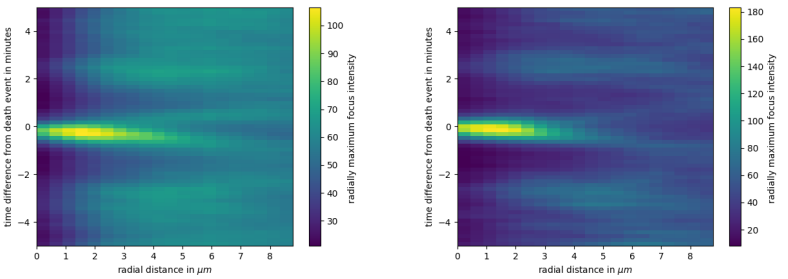

(e) 7LU

(f) 5LU

Figure C.13: **Maximum radial-myosin kymographs for death events (original cell only) in individual tissues 1**

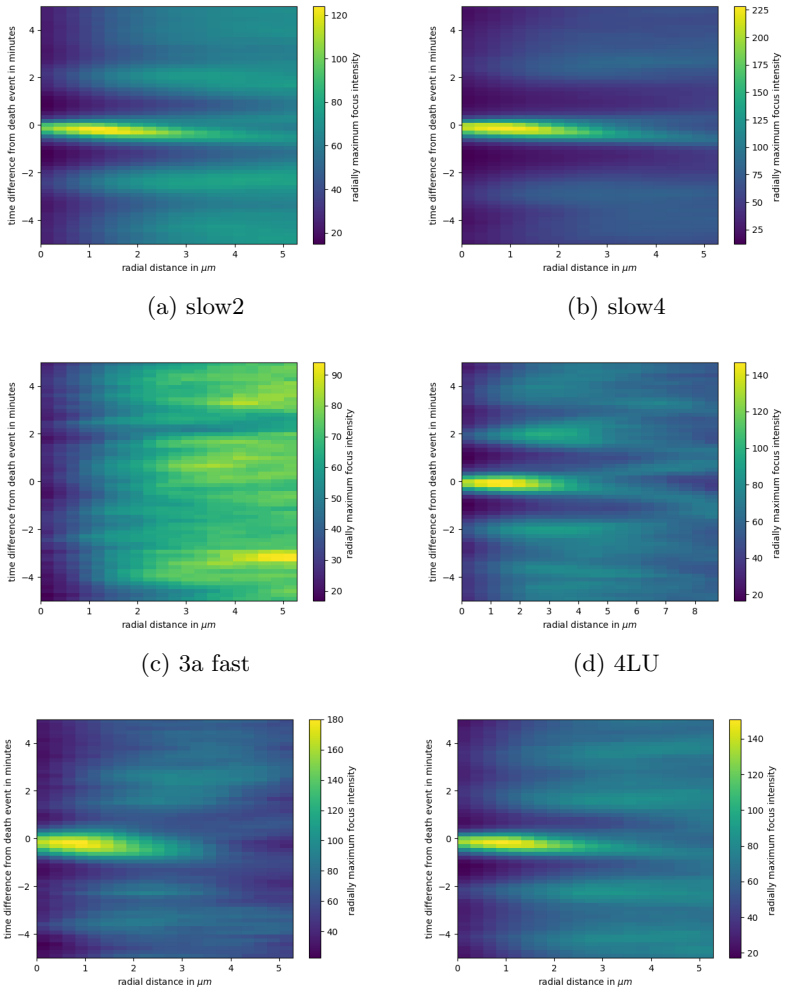

(a) slow2

(b) slow4

(c) 3a fast

(d) 4LU

(e) 2a fast

(f) 4a fast

Figure C.14: **Maximum radial-myosin kymographs for death events (original cell only) in individual tissues 2**

Line Plots of Myosin intensities close to origin for radial-myosin kymographs for original cell: death

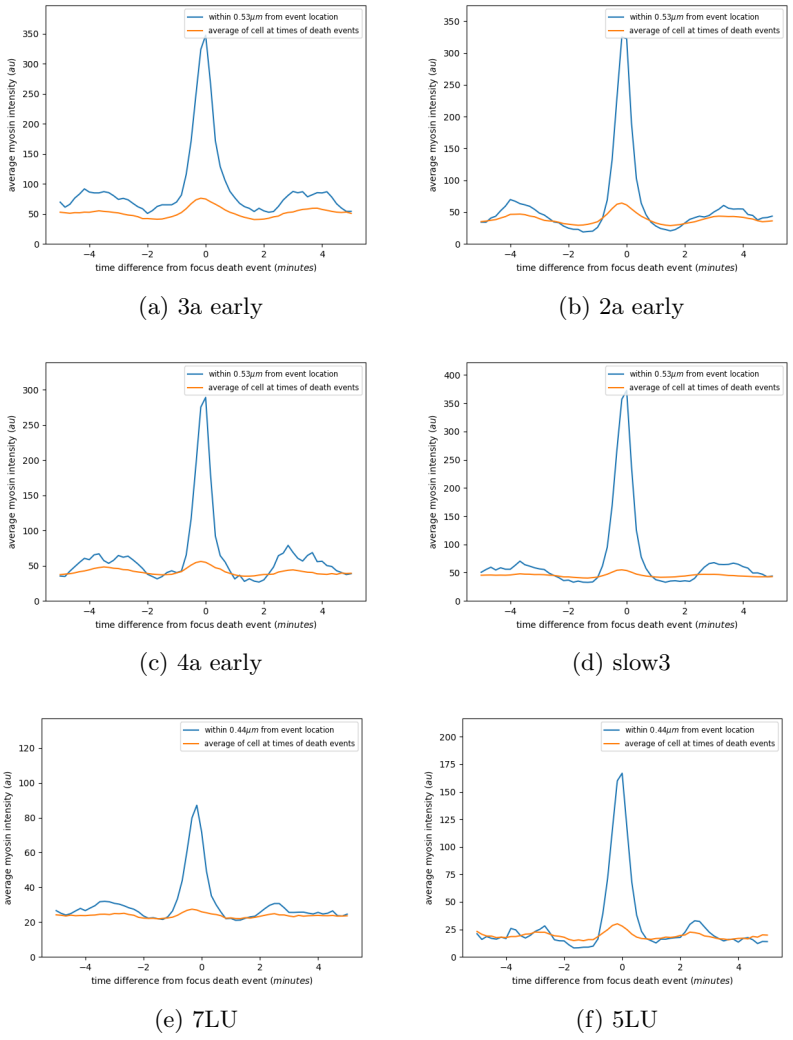

(a) 3a early

(b) 2a early

(c) 4a early

(d) slow3

(e) 7LU

(f) 5LU

Figure C.15: **Line plots close to death location 1**

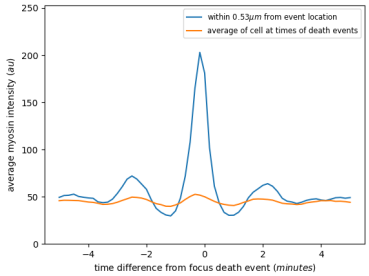

(a) slow2

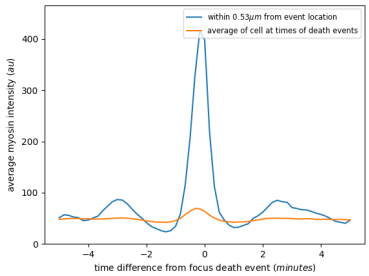

(b) slow4

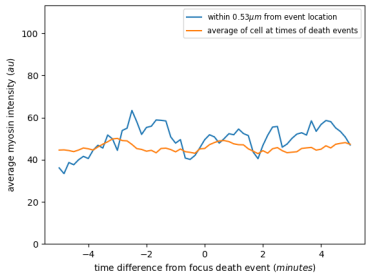

(c) 3a fast

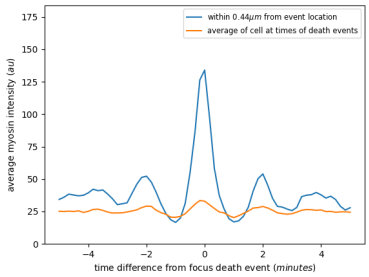

(d) 4LU

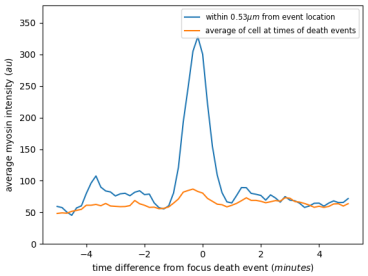

(e) 2a fast

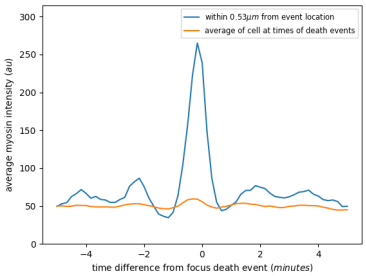

(f) 4a fast

Figure C.16: **Line plots close to death location 2**

Radial-myosin kymographs for original cell: mid

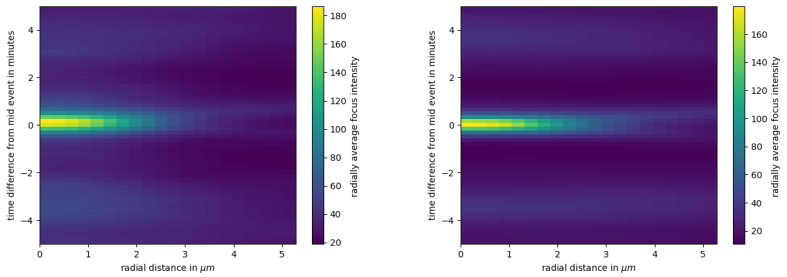

(a) 3a early

(b) 2a early

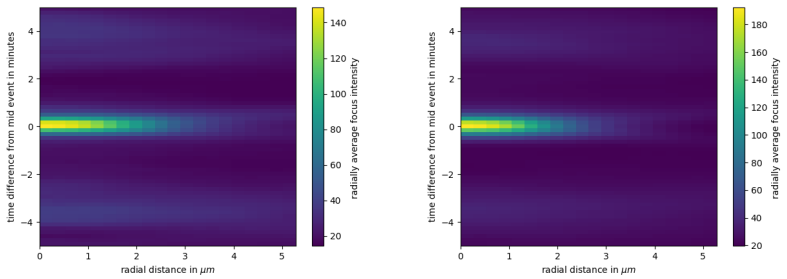

(c) 4a early

(d) slow3

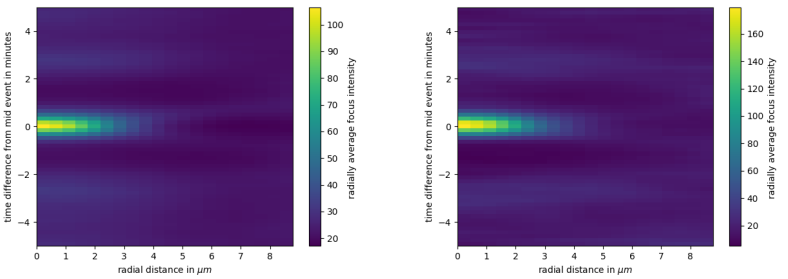

(e) 7LU

(f) 5LU

Figure C.17: **Average radial-myosin kymographs for mid events (original cell only) in individual tissues 1**

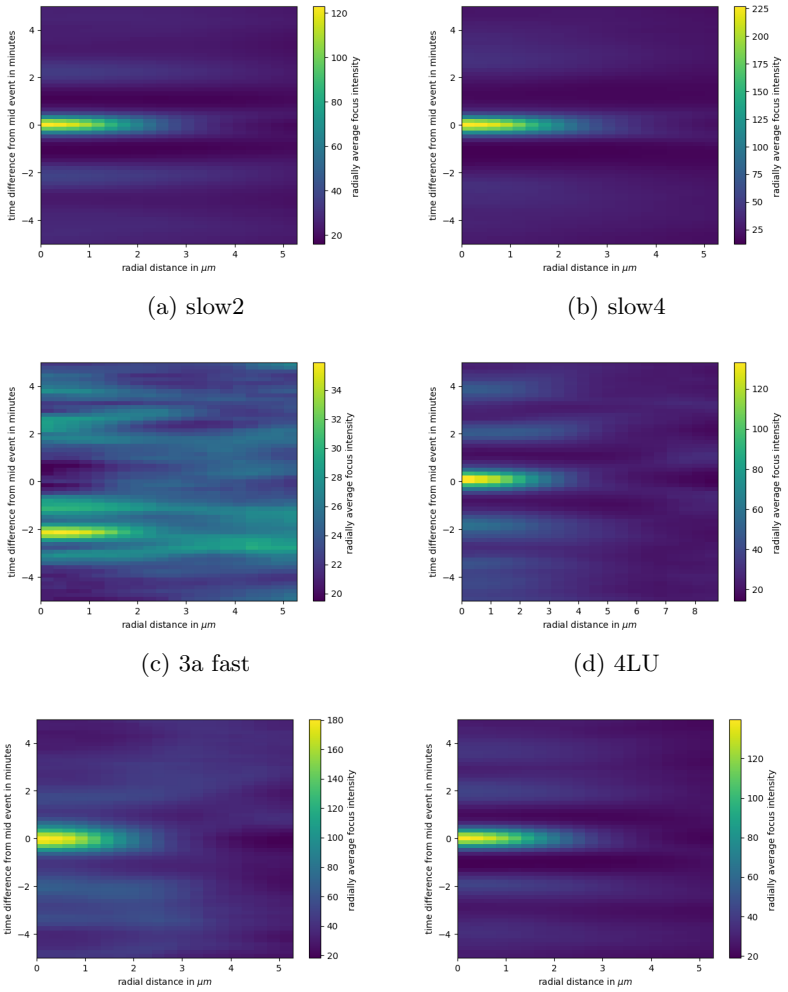

(a) slow2

(b) slow4

(c) 3a fast

(d) 4LU

(e) 2a fast

(f) 4a fast

Figure C.18: **Average radial-myosin kymographs for mid events in (original cell only) individual tissues 2**

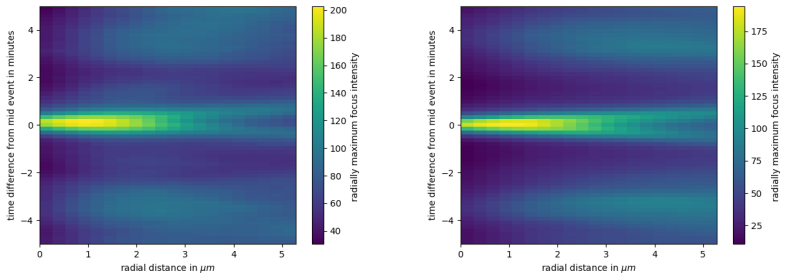

(a) 3a early

(b) 2a early

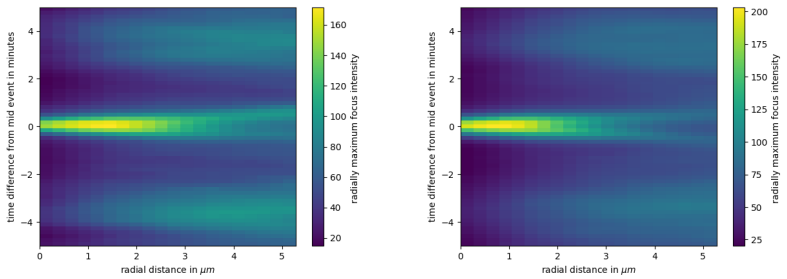

(c) 4a early

(d) slow3

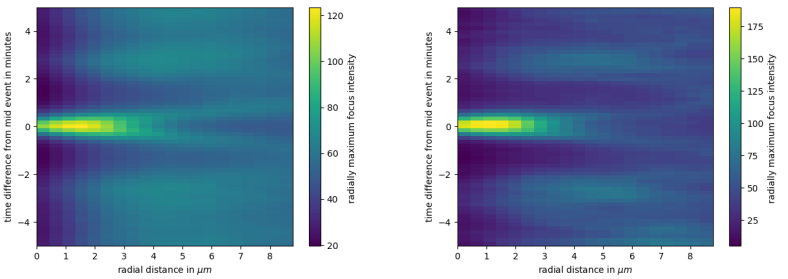

(e) 7LU

(f) 5LU

Figure C.19: **Maximum radial-myosin kymographs for mid events (original cell only) in individual tissues 1**

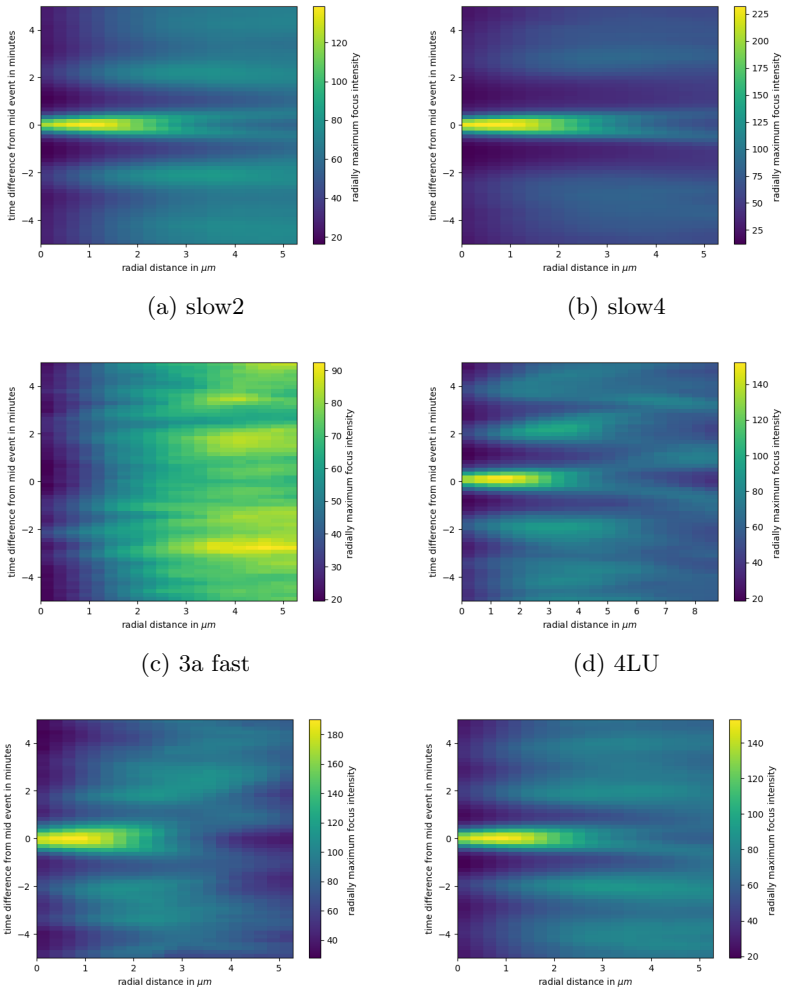

(a) slow2

(b) slow4

(c) 3a fast

(d) 4LU

(e) 2a fast

(f) 4a fast

Figure C.20: **Maximum radial-myosin kymographs for mid events (original cell only) in individual tissues 2**

C.2.2 Kymographs with All Tissue

Radial-myosin kymographs for all tissue: Birth

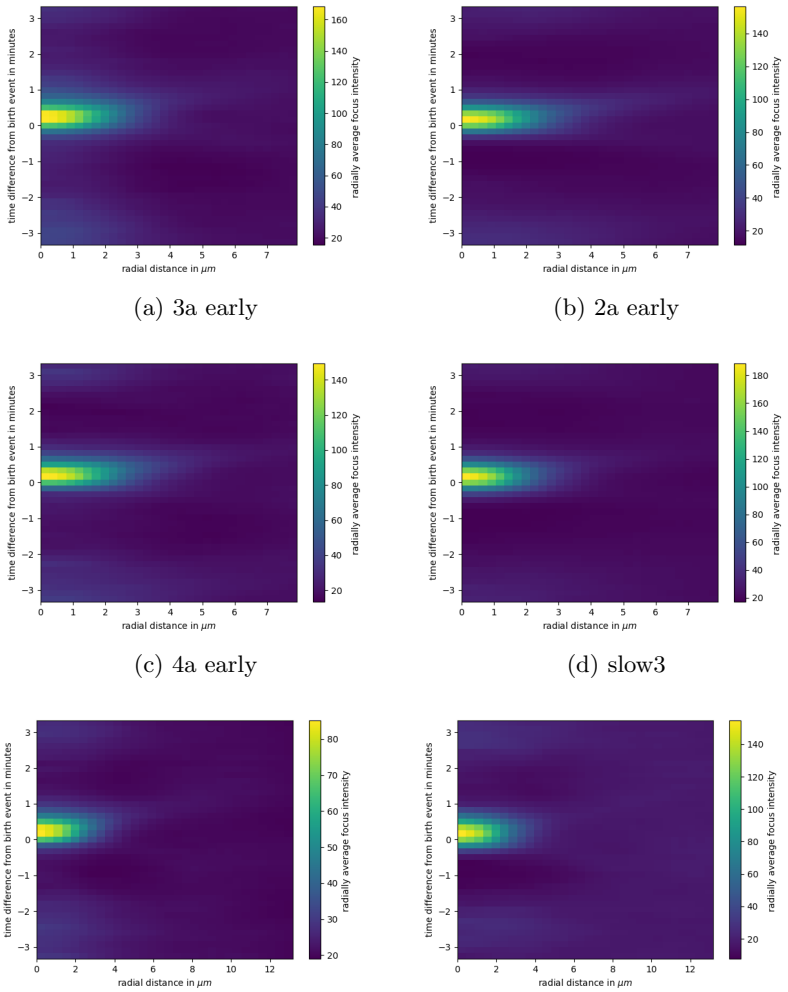

(a) 3a early

(b) 2a early

(c) 4a early

(d) slow3

(e) 7LU

(f) 5LU

Figure C.21: **Average radial-myosin kymographs for birth events in individual tissues 1**

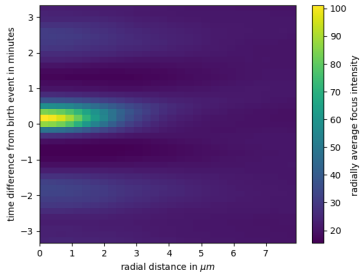

(a) slow2

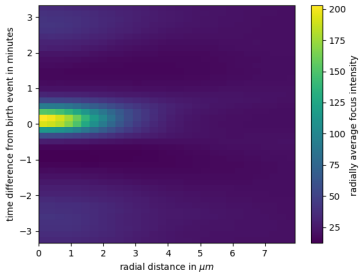

(b) slow4

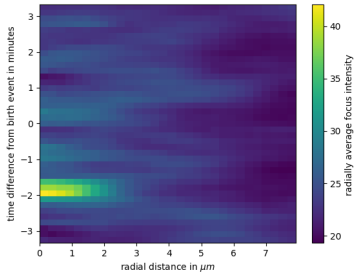

(c) 3a fast

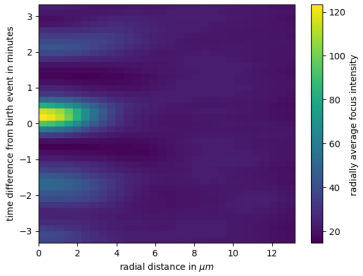

(d) 4LU

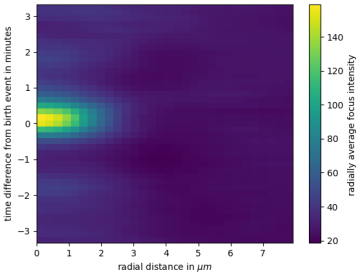

(e) 2a fast

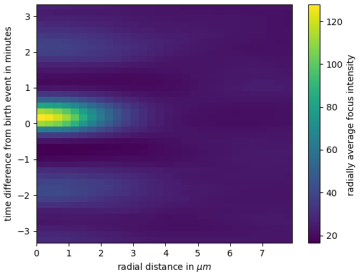

(f) 4a fast

Figure C.22: **Average radial-myosin kymographs for birth events in individual tissues 2**

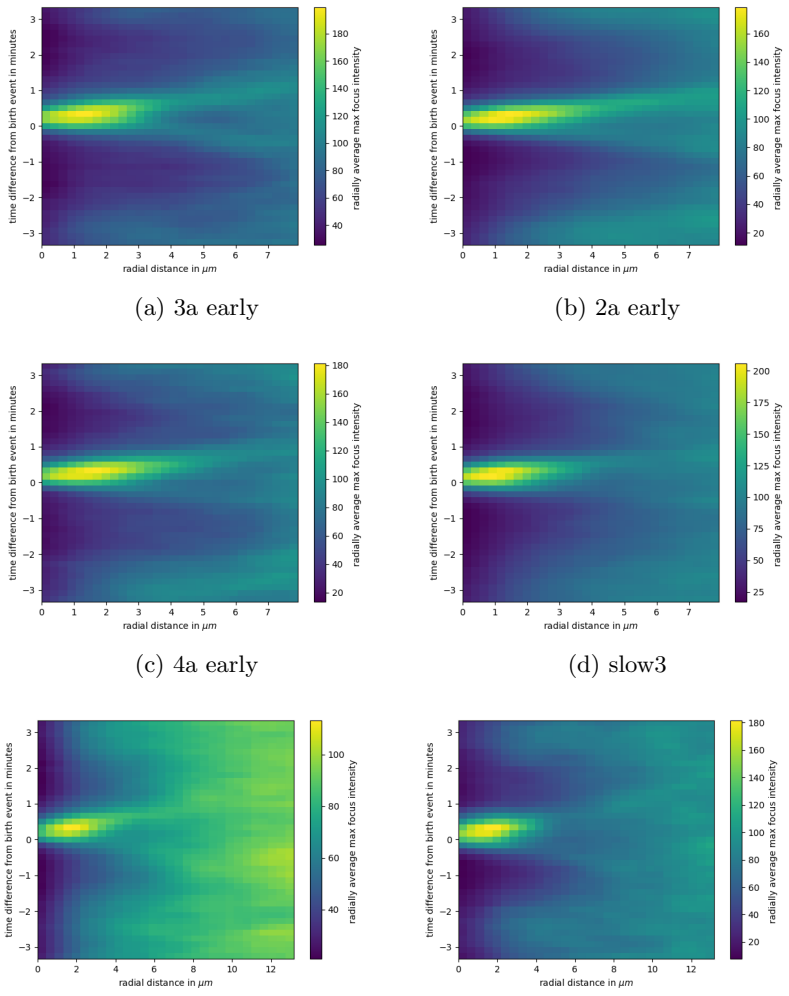

(a) 3a early

(b) 2a early

(c) 4a early

(d) slow3

(e) 7LU

(f) 5LU

Figure C.23: **Maximum radial-myosin kymographs for birth events in individual tissues 1**

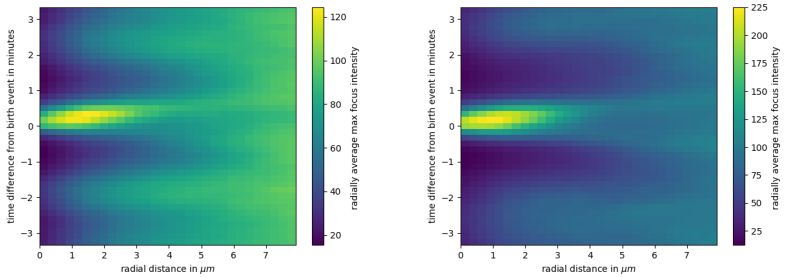

(a) slow2

(b) slow4

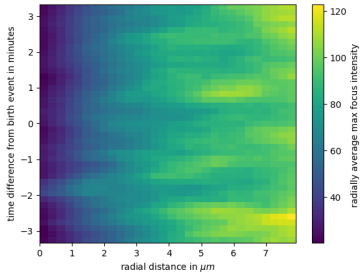

(c) 3a fast

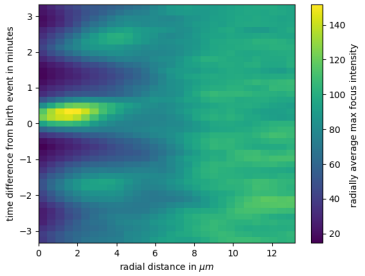

(d) 4LU

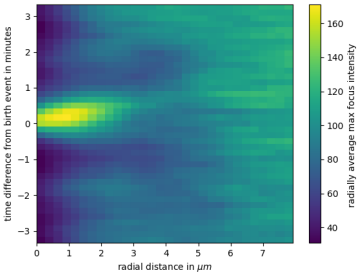

(e) 2a fast

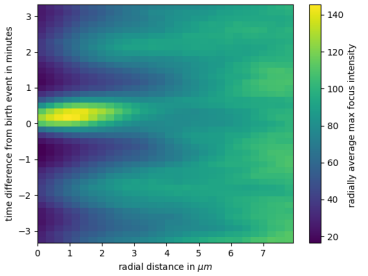

(f) 4a fast

Figure C.24: **Maximum radial-myosin kymographs for birth events in individual tissues 2**

Radial-myosin kymographs for all tissue: death

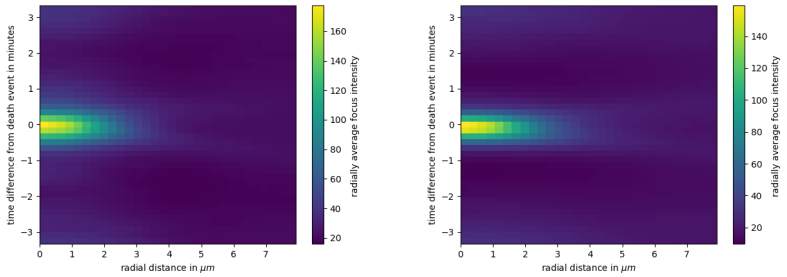

(a) 3a early

(b) 2a early

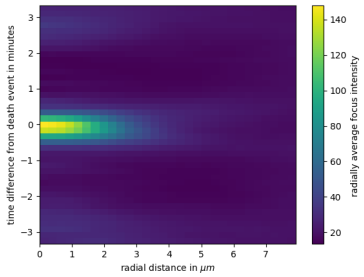

(c) 4a early

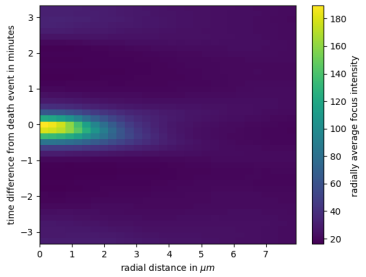

(d) slow3

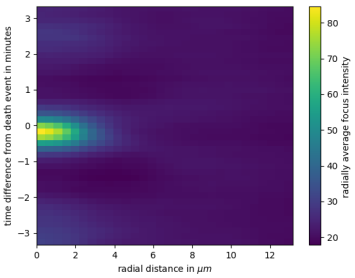

(e) 7LU

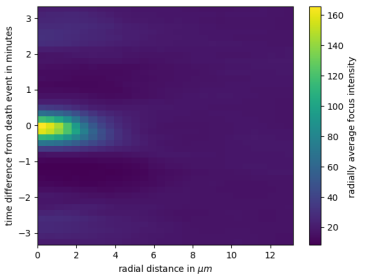

(f) 5LU

Figure C.25: **Average radial-myosin kymographs for death events in individual tissues 1**

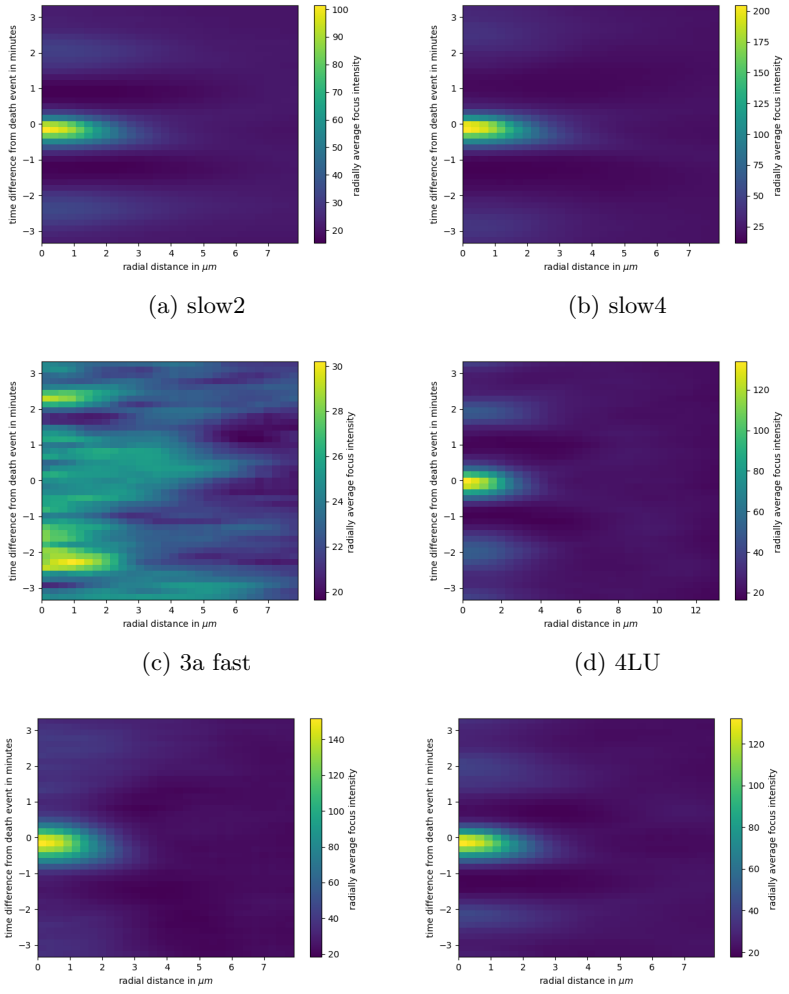

(a) slow2

(b) slow4

(c) 3a fast

(d) 4LU

(e) 2a fast

(f) 4a fast

Figure C.26: **Average radial-myosin kymographs for death events in individual tissues 2**

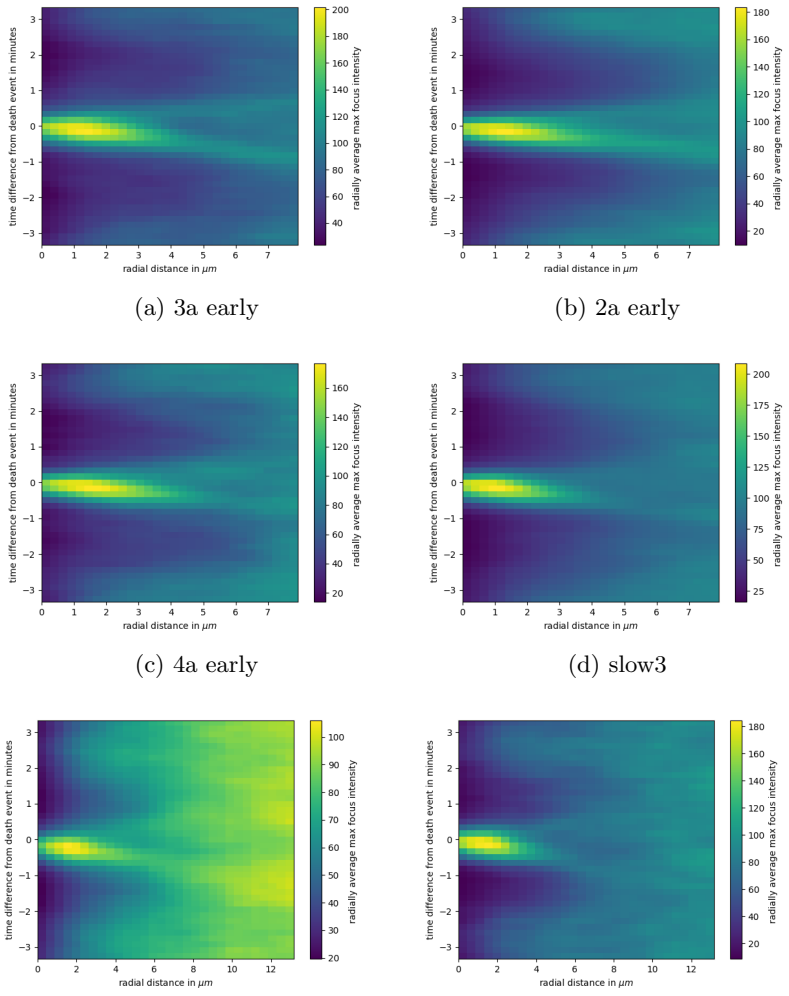

(a) 3a early

(b) 2a early

(c) 4a early

(d) slow3

(e) 7LU

(f) 5LU

Figure C.27: **Maximum radial-myosin kymographs for death events in individual tissues 1**

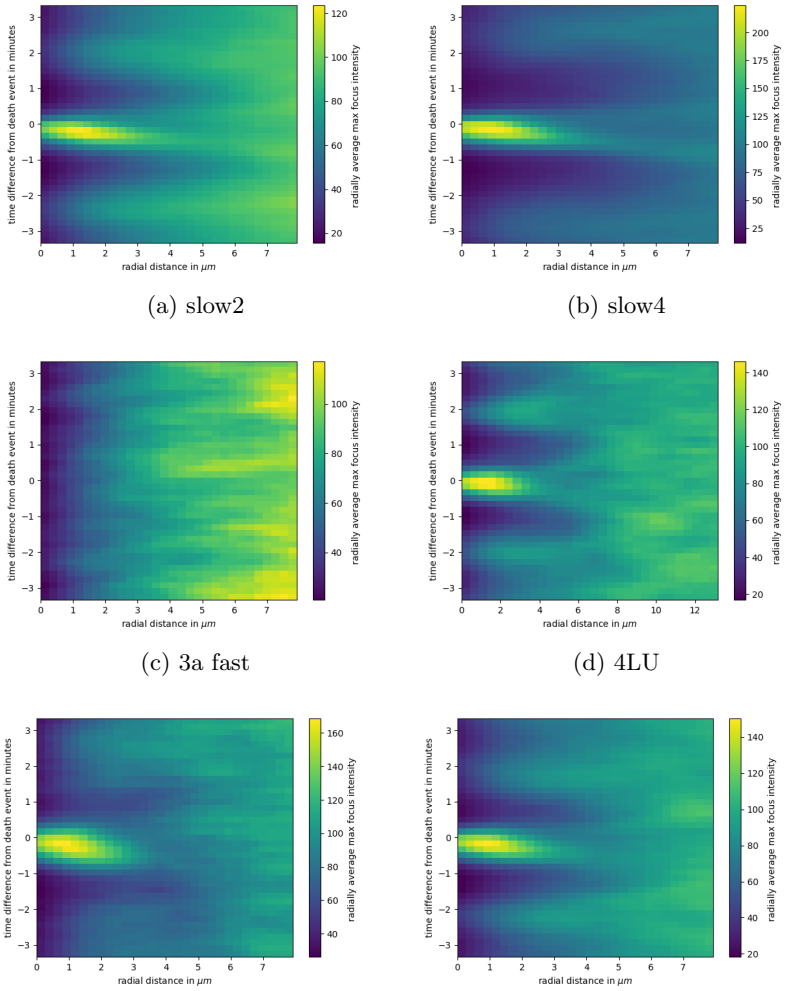

(a) slow2

(b) slow4

(c) 3a fast

(d) 4LU

(e) 2a fast

(f) 4a fast

Figure C.28: **Maximum radial-myosin kymographs for death events in individual tissues 2**

Radial-myosin kymographs for all tissue: Mid

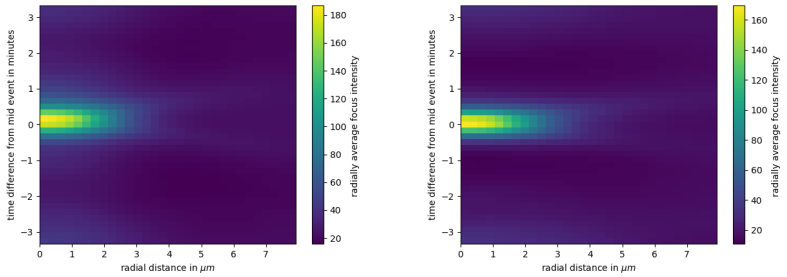

(a) 3a early

(b) 2a early

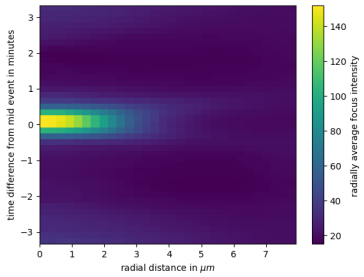

(c) 4a early

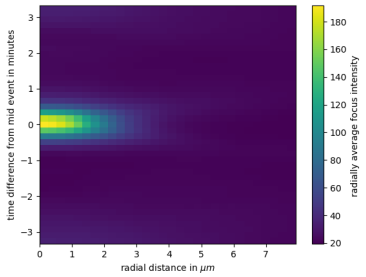

(d) slow3

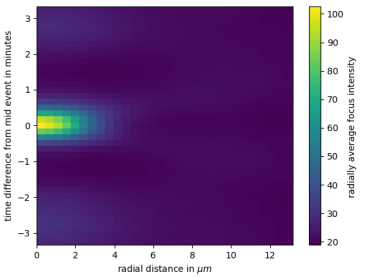

(e) 7LU

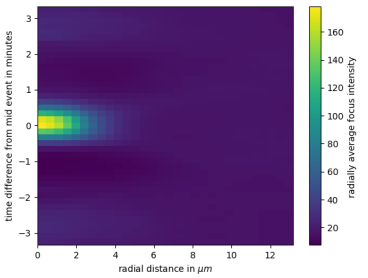

(f) 5LU

Figure C.29: **Average radial-myosin kymographs for mid events in individual tissues 1**

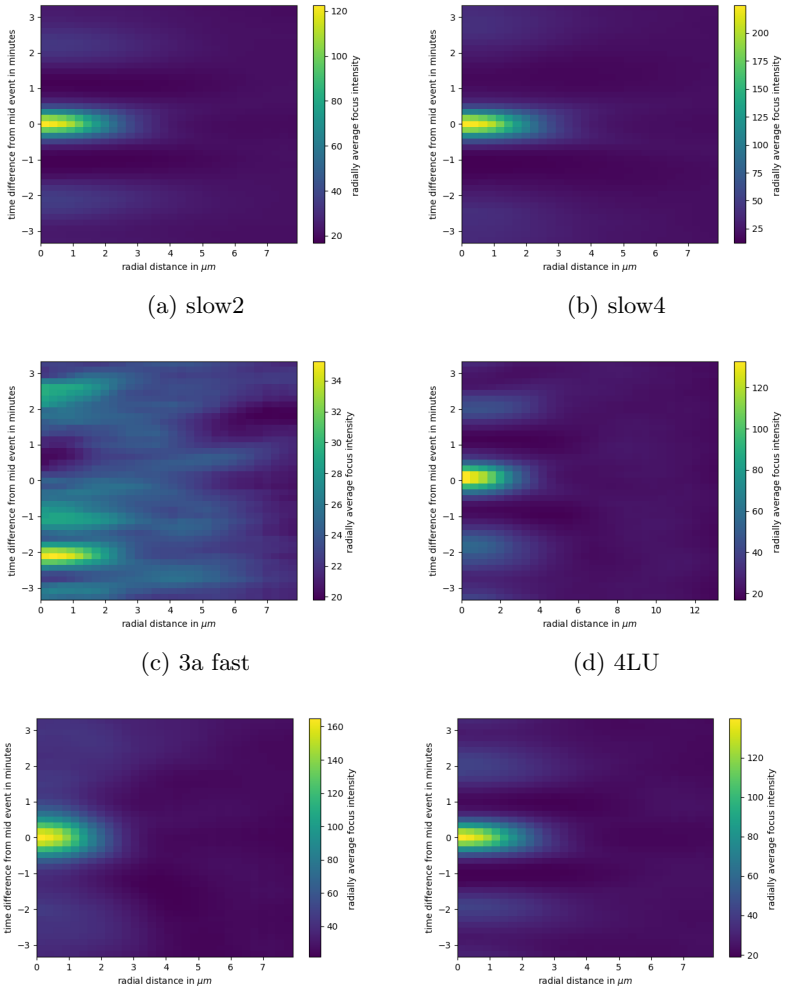

(a) slow2

(b) slow4

(c) 3a fast

(d) 4LU

(e) 2a fast

(f) 4a fast

Figure C.30: **Average radial-myosin kymographs for mid events in individual tissues 2**

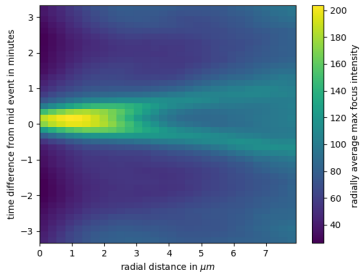

(a) 3a early

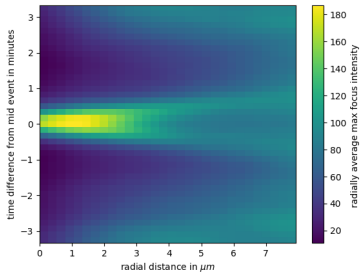

(b) 2a early

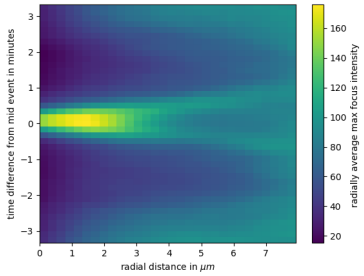

(c) 4a early

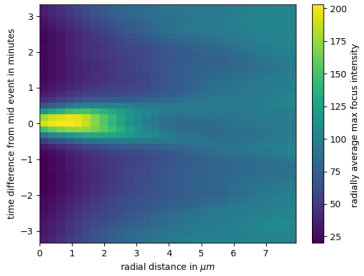

(d) slow3

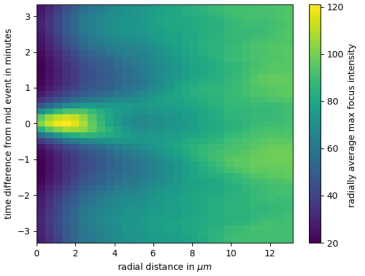

(e) 7LU

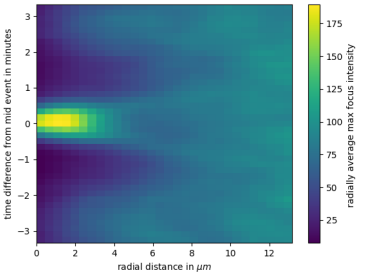

(f) 5LU

Figure C.31: **Maximum radial-myosin kymographs for mid events in individual tissues 1**

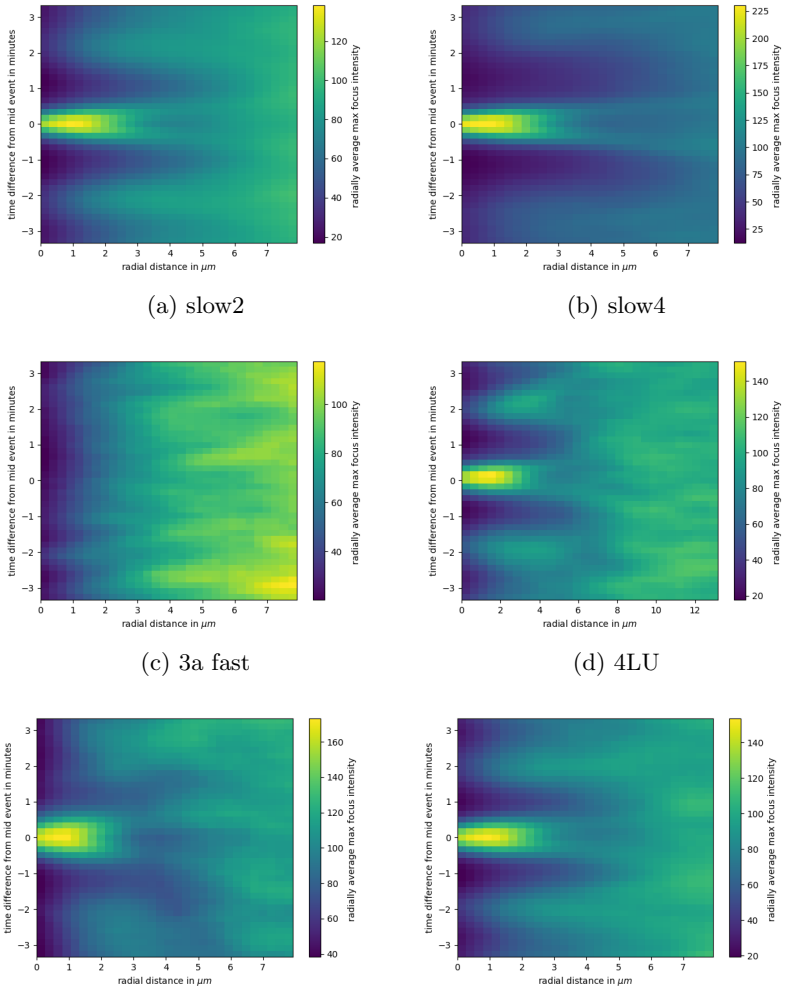

(a) slow2

(b) slow4

(c) 3a fast

(d) 4LU

(e) 2a fast

(f) 4a fast

Figure C.32: **Maximum radial-myosin kymographs for mid events in individual tissues 2**

C.2.3 Kymographs without Original Cell

Radial-myosin kymographs without Original Cell: Mid

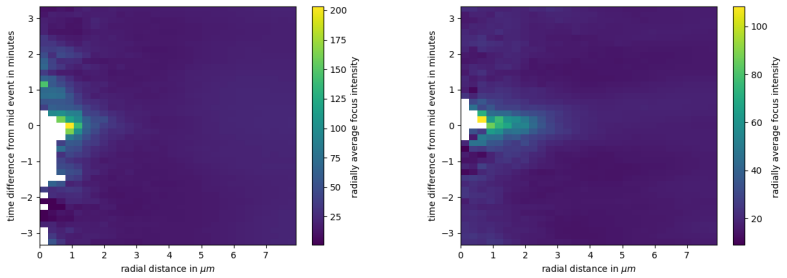

(a) 3a early

(b) 2a early

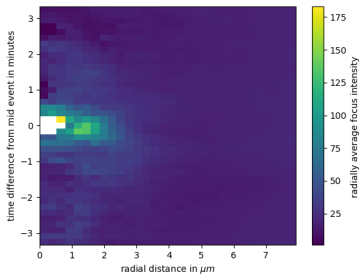

(c) 4a early

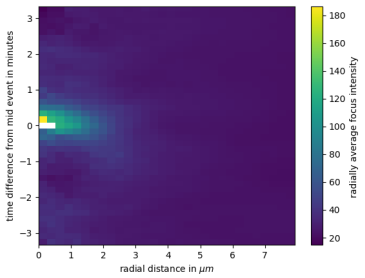

(d) slow3

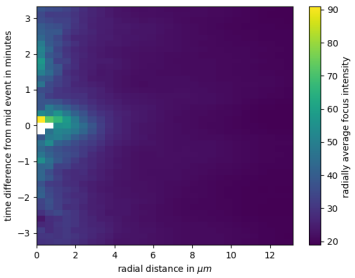

(e) 7LU

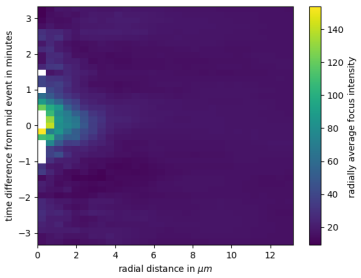

(f) 5LU

Figure C.33: **Average radial-myosin kymographs for mid events (without original cell) in individual tissues 1**

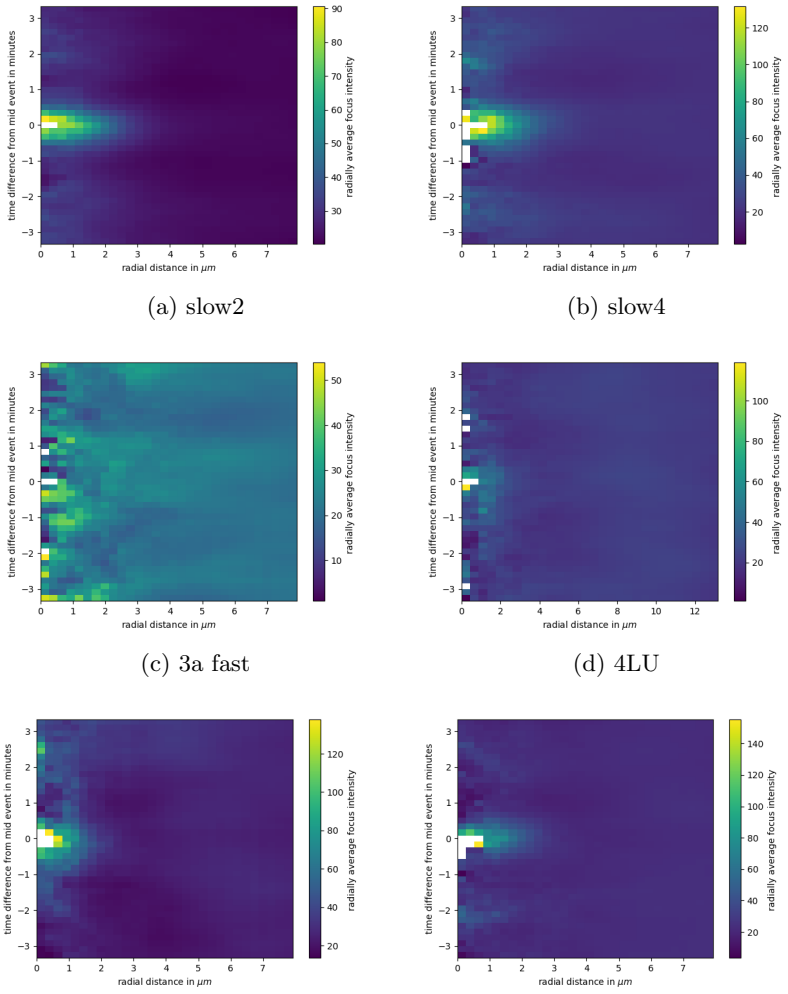

(a) slow2

(b) slow4

(c) 3a fast

(d) 4LU

(e) 2a fast

(f) 4a fast

Figure C.34: **Average radial-myosin kymographs for mid events (without original cell) in individual tissues 2**

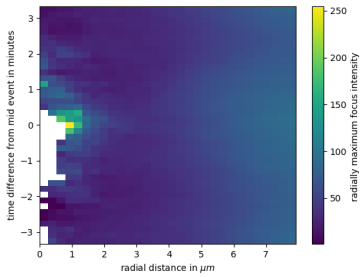

(a) 3a early

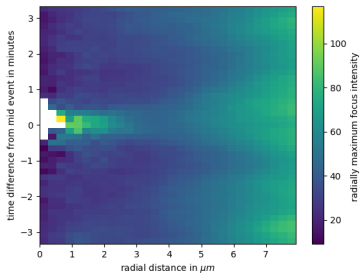

(b) 2a early

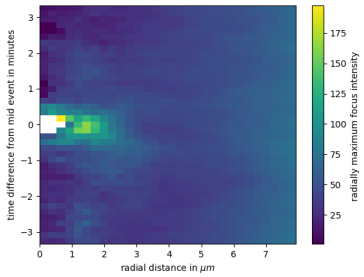

(c) 4a early

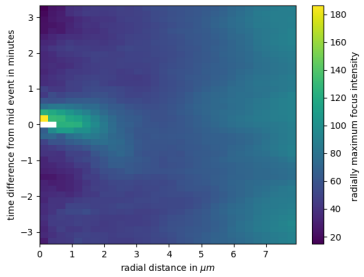

(d) slow3

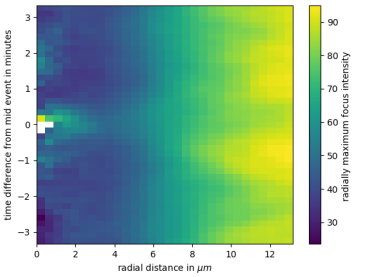

(e) 7LU

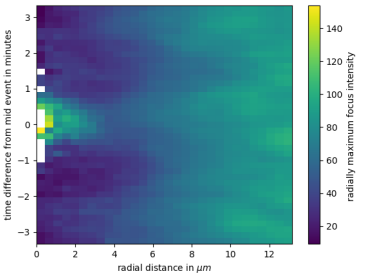

(f) 5LU

Figure C.35: **Maximum radial-myosin kymographs for mid events (without original cell) in individual tissues 1**

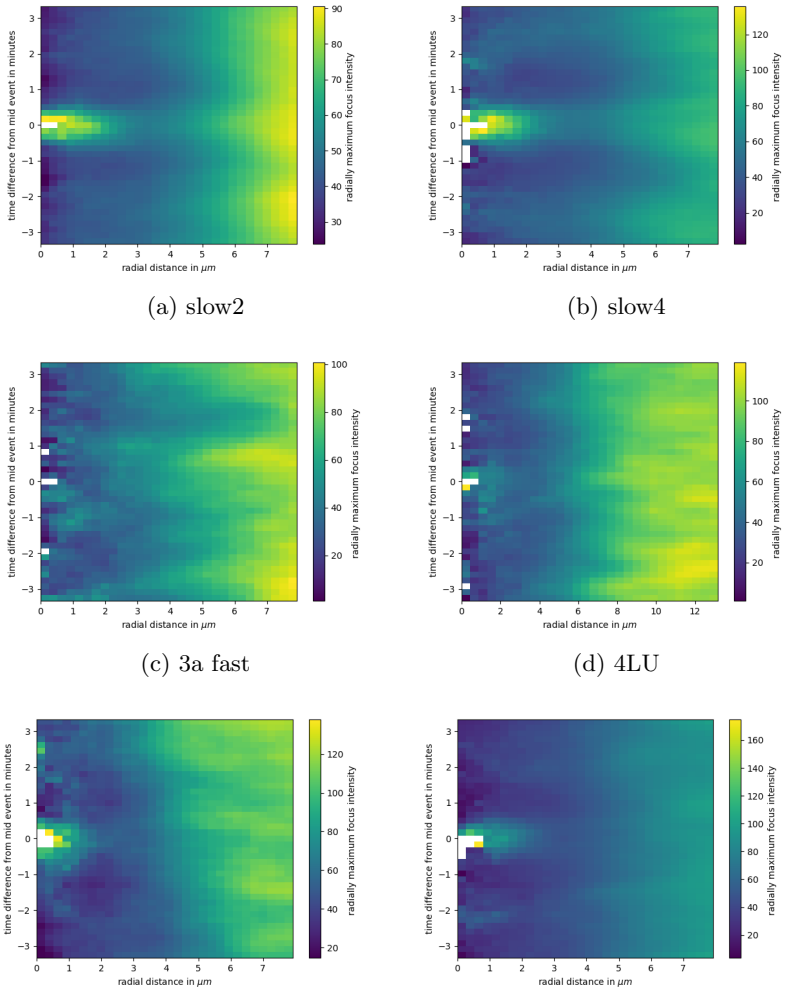

(a) slow2

(b) slow4

(c) 3a fast

(d) 4LU

(e) 2a fast

(f) 4a fast

Figure C.36: **Maximum radial-myosin kymographs for mid events (without original cell) in individual tissues 2**

Appendix D

Corrections of MSD Exponents

During the examination of the thesis, Prof. Francois Gallet noted that the exponents greater than two were mathematically impossible. While I have not been able to prove this yet, on further examination, I noted that by fitting the mean-squared-distances of the focus trajectories with a linear law in the log-space,

$$log(d_i) = log(a) + nlog(t_i)$$

as opposed to a non-linear power-law fitting that I had been performing earlier,

$$d_i = a(t_i)^n$$

(where n is the value of the exponent) , I am able to obtain a distribution of exponents that do not take these super-ballistic values. Thus, this change mainly affects the parts of the distribution that have very low (that are less that 0) or very high values (that are very close to, and ofcourse above 2).

An example of the different exponent values obtained from these to fits is provided in the figure below:

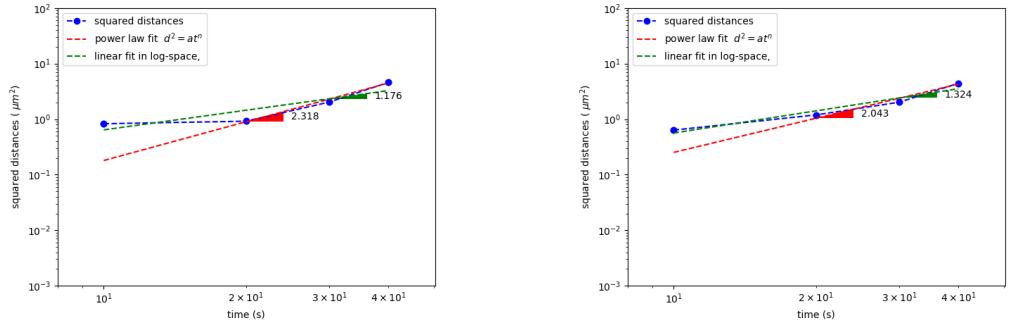

(a) squared distances versus lag for focus trajectory (b) squared distances versus lag for focus trajectory

Difference of exponents through linear and non-linear fitting: Squared distances versus lags for 2 different focus branches illustrating the difference in exponent values obtained through linear fitting in log-space (green) and non-linear fitting with power-law (red).

In the following document, I provide the figures and the text in the thesis that were changed by performing this operation.

D.1 Mean Squared Distances on Focus Trajectories

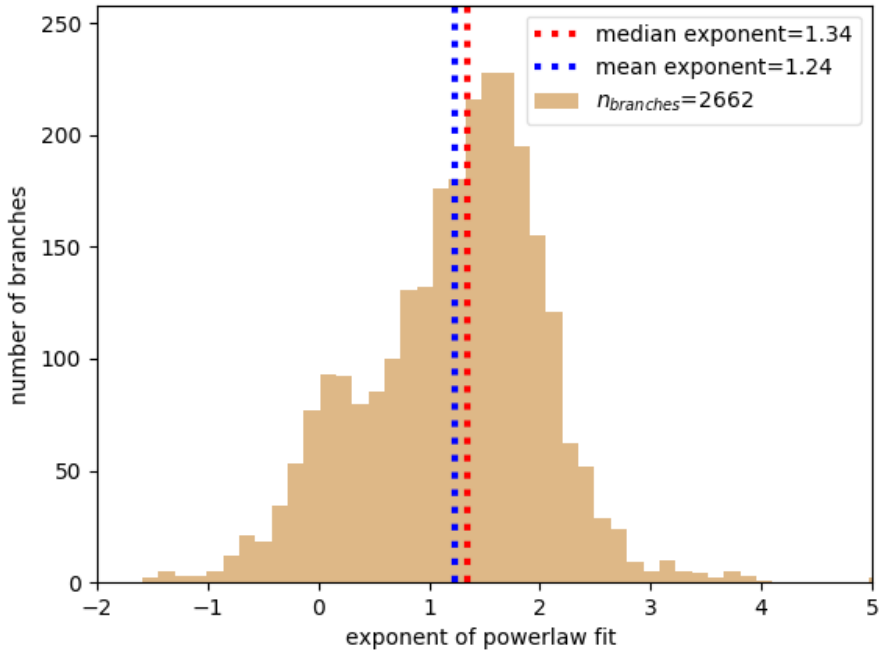

Figure D.2: ***From Thesis:*** **various regimes of motion for focus branches:** The distribution of the exponents of the laws of motion for the focus branches.

In the thesis, section D.1, we had described the distribution of exponents as :

"Plotting the distribution of all n in the form of a histogram D.2, we see wide range of exponents ranging between -2 to 4 implying that behaviour in all three regimes are presented by foci. About a third (34.7%) of foci behave diffusively or sub-diffusively, with an exponent less that 1. Going up to the self avoiding exponent of 1.5 accounts for approximately another third (64.5%), and another 20% are up to the ballistic exponent of 2. The remaining 15% have an exponent more than 2, showing a net acceleration. The median exponent is found to be 1.34, and the mean as 1.24. "

Whereas, now we find that the distribution of exponents ranging from -0.22 to 2.00, still implying that behaviour in all three regimes are presented by foci. We find that 33.47% of foci behave diffusively or sub-diffusively, with an exponent less that 1. Another one third of the foci are accounted for going up to the self avoiding exponent of 1.5 (32.79%). The rest are upto the ballistic exponent of 2. The median exponent is found to be 1.36 and the mean as 1.22.

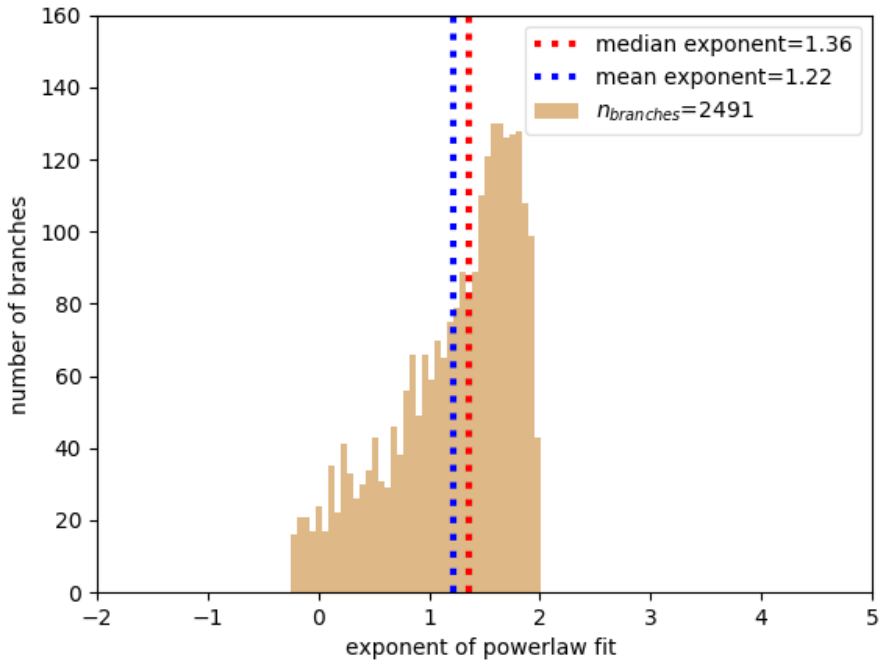

Now changed to: **Various regimes of motion for focus branches:** The distribution of the exponents of the laws of motion for the focus branches.

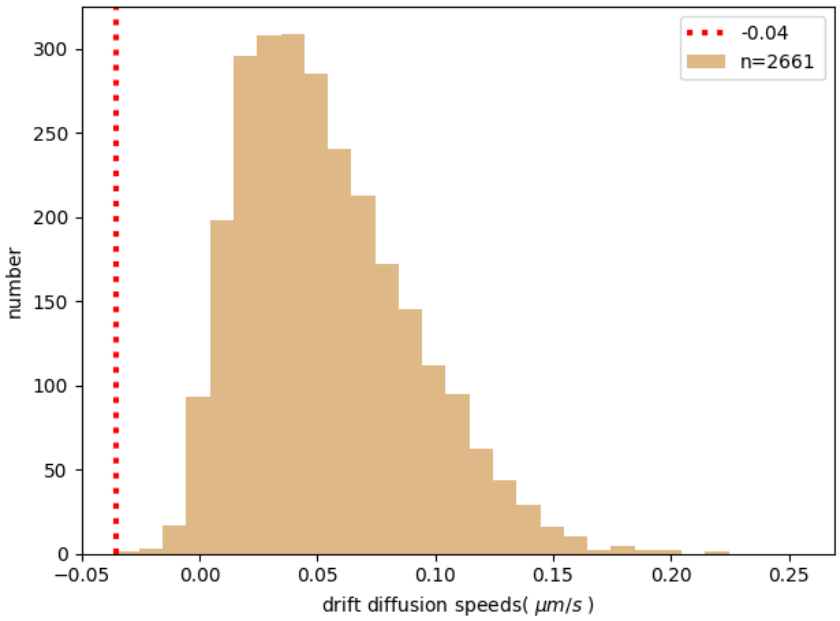

(a) Drift diffusion speeds

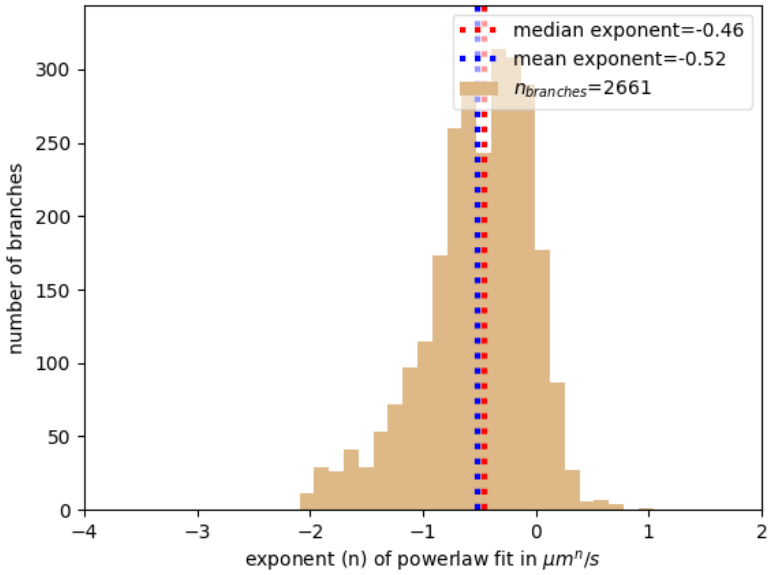

(b) Drift diffusion exponents

Figure D.3: ***From Thesis:*** **Drift diffusion as mechanism of focus propagation**: Panel (a) shows the distribution of the constant speeds of each focus branch along its mean direction. Panel (b) shows the distribution of exponents in a frame of reference that travels with this constant velocity vector.

Since the distribution of drift diffusion exponents are also dependant on the fitting, this is changed too:

In the thesis, we had noted that this distribution was centered at 0, whereas now we find even smaller values, with the distribution being centered at -1.

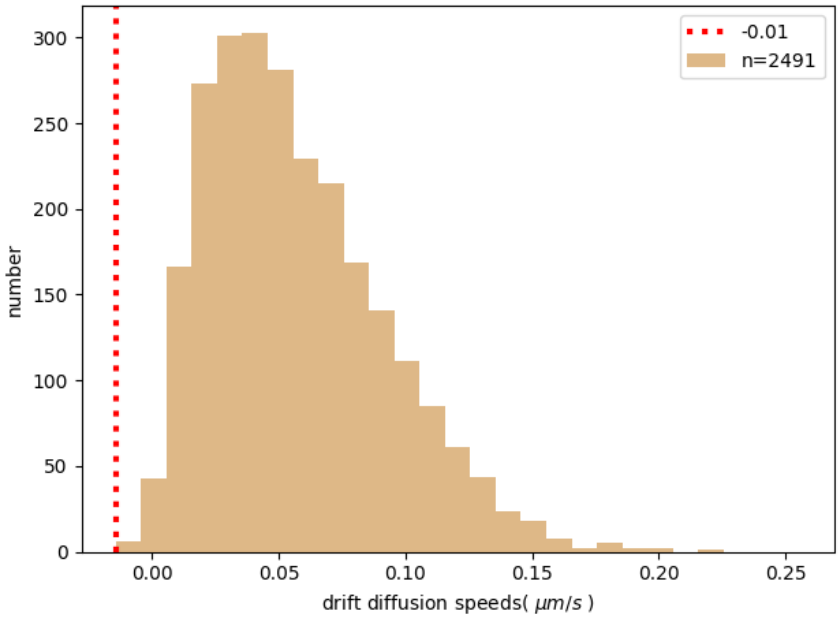

(a) Drift diffusion speeds

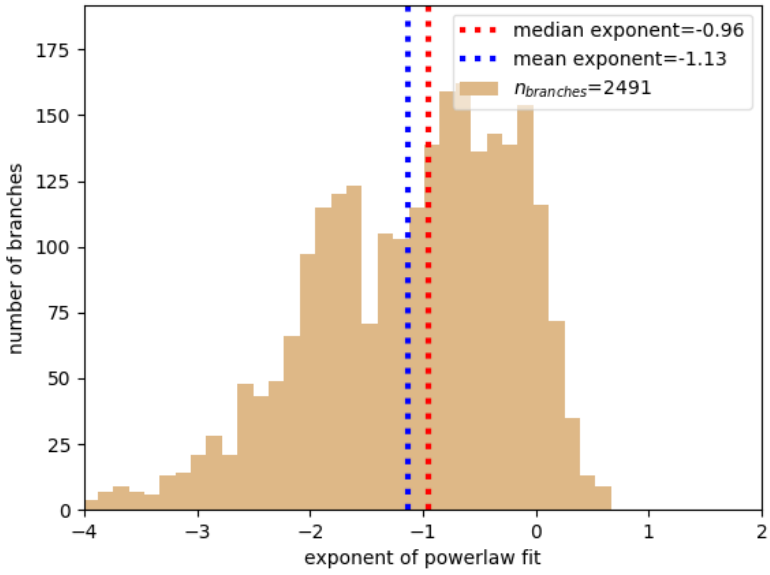

(b) Drift diffusion exponents

Now changed to: **Drift diffusion as mechanism of focus propagation**: Panel (a) shows the distribution of the constant speeds of each focus branch along its mean direction. Panel (b) shows the distribution of exponents in a frame of reference that travels with this constant velocity vector.

In the thesis, we had noted while trying to decompose our distribution of exponents in figure D.2 into two Gaussian distributions in figure D.5:

"Coming back to the figure D.2, another feature of this distribution is that it can be expressed as the sum of two gaussian distributions, a low amplitude, high-variance distribution centered around 0.75, and another, high amplitude, low-variance distribution at 1.5 (figure D.5)."

Whereas now, we see that the low amplitude high variance distribution is centered at 1.25, where as the high amplitude, low-variance distribution is centered at 1.68.

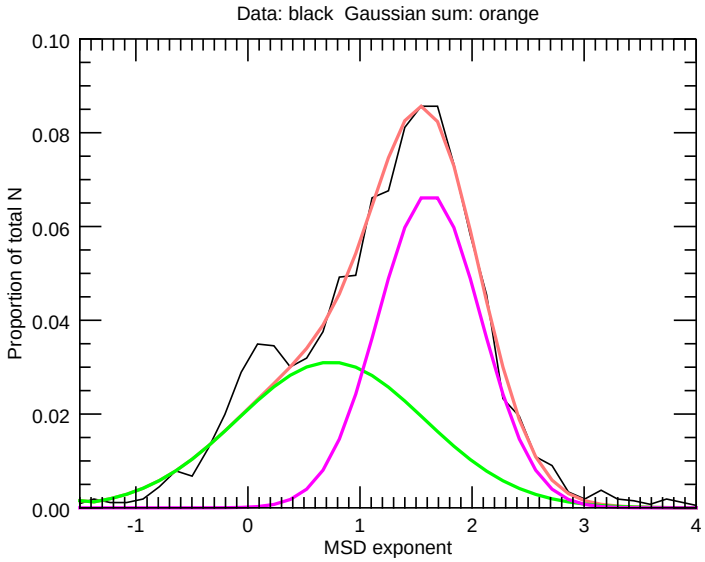

Figure D.5: ***From thesis:*** **Exponents of motion as a sum of two Gaussian distributions:** For the low exponent population $\mu_1 = 0.741, \sigma_1 = 0.833$, and for the high exponent population $\mu_2 = 1.619, \sigma_2 = 0.455$, fraction of area overlap between low and high = 0.843.

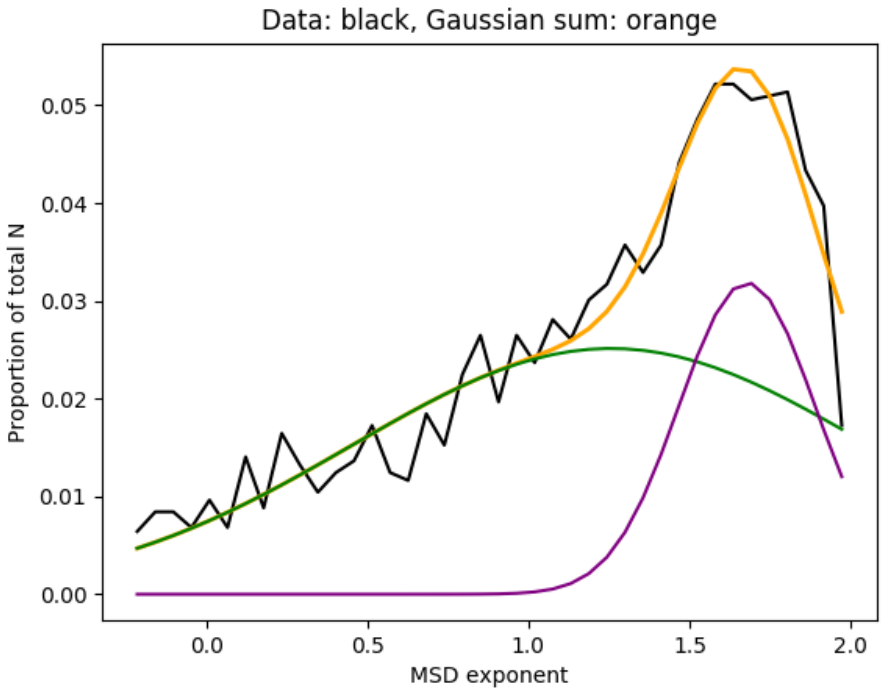

Now changed to: **Exponents of motion as a sum of two Gaussian distributions:** For the low exponent population $\mu_1 = 1.255, \sigma_1 = 0.803$, and for the high exponent population $\mu_2 = 1.679, \sigma_2 = 0.210$, fraction of area overlap between low and high = 0.309.

D.1.1 Trends in MSD due to Confinement

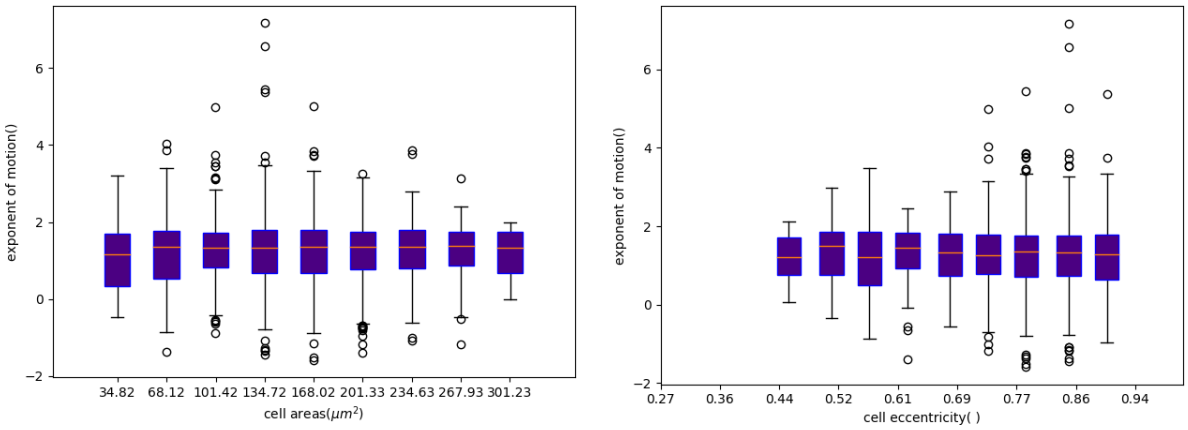

(a) exponents of motion vs cell area

(b) exponents of motion vs cell eccentricity

Figure D.6: ***From Thesis:*** **Exponent of motion of focus branches due to confinement**

The change in the exponent distribution affects its correlation with other quantities, such as cell areas and eccentricities:

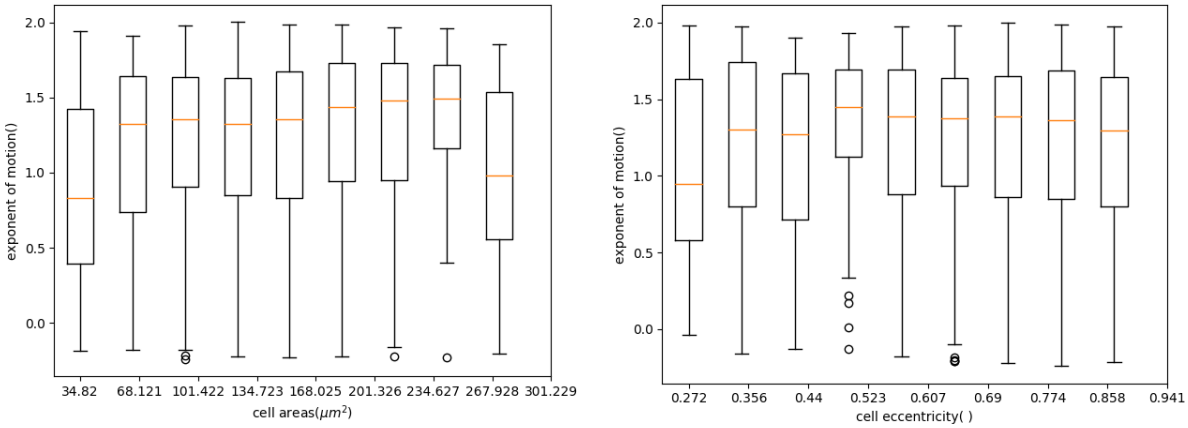

(a) exponents of motion vs cell area

(b) exponents of motion vs cell eccentricity

Now changed to: **Exponent of motion of focus branches due to confinement**

In the thesis, we had found no apparent trends in the plots D.6. Now that the range of exponents is smaller, we can better see the slight evolution of exponents, already present in the thesis. We find the median value of the exponents increases with the increase in area upto around 300 μm^2. We also find that the median value of the exponents increases with eccentricity for more circular cells (upto $\epsilon = 0.5$). After this, the median exponent value shows a slight decrease.

D.1.2 Trends in MSD over Developmental Time

In the thesis, we found no change in the exponent over the course of developmental time. We do not note a great difference in the new plots, except the curtailing of exponents at 2.

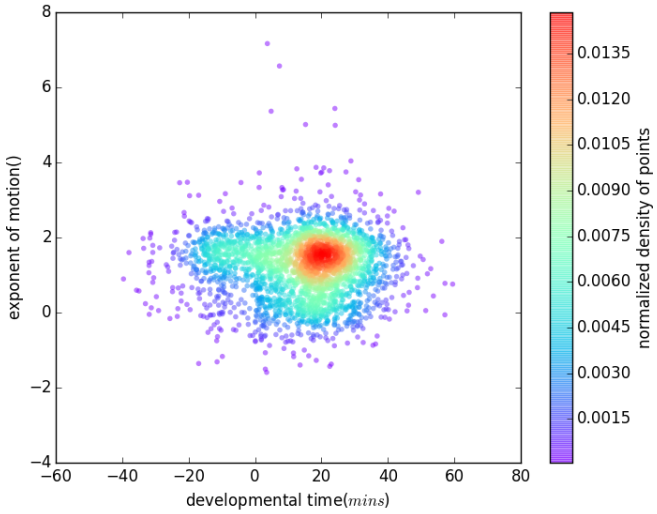

(a) Exponents of focus branches, vs developmental time of branch occurrence. Colorbar indicates the normalized density of points at each coordinate.

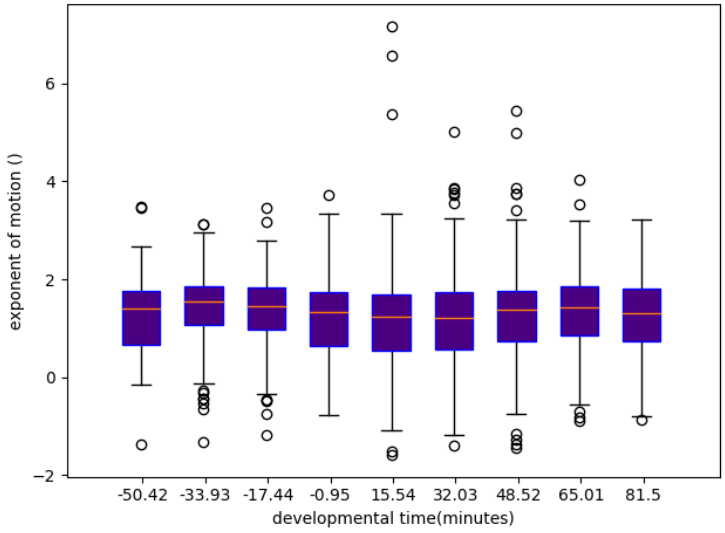

(b) Exponents of focus branches, vs developmental time, box width indicates the upper and lower quartiles, with red line at median

Figure D.8: ***From thesis:*** **Exponent of motion of focus branches with progress of dorsal closure:** Exponents of motions vs developmental times through D.8a scatter plot, showing the density of tracked foci in time. same plot in box and whisker formulation, D.8b showing roughly uniform distribution of exponents across time.

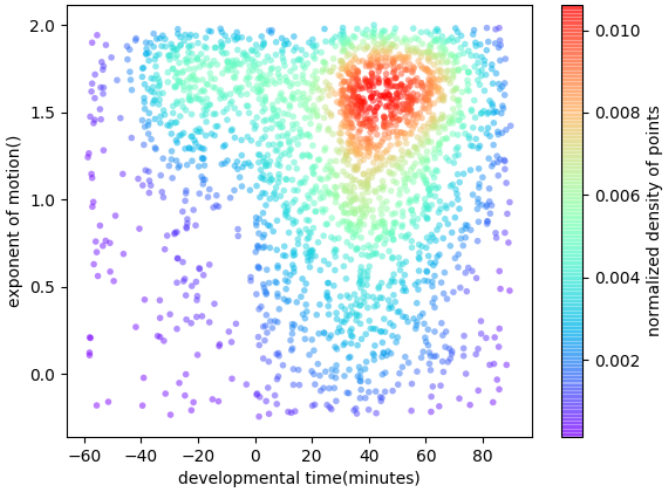

(a) Exponents of focus branches, vs developmental time of branch occurrence. Colorbar indicates the normalized density of points at each coordinate.

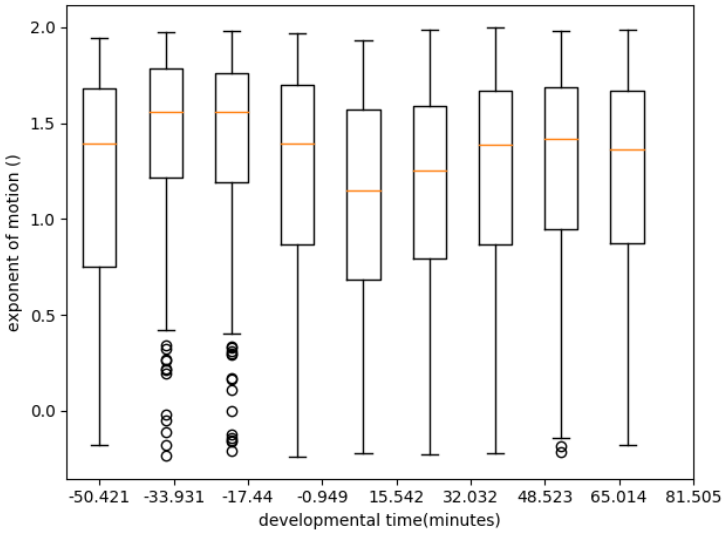

(b) Exponents of focus branches, vs developmental time, box width indicates the upper and lower quartiles, with red line at median

Now changed to: **Exponent of motion of focus branches with progress of dorsal closure:** Exponents of motions vs developmental times through (panel(a)) scatter plot, showing the density of tracked foci in time. same plot in box and whisker formulation, (panel(b)) showing roughly uniform distribution of exponents across time.

D.2 Conclusions

In the conclusions of this chapter, we had noted that :

"Finally, we found no correlation of the exponent of the squared distances with confinement or the change in developmental epoch. "

Whereas, now, having reduced the range of exponents, we find that the exponent does change slightly with confinement, increasing, in general, with the increase in cell area, as well as the increase in eccentricity for circular cells. However, statistical tests need to be performed to note if these changes are significant.

Bibliography

[1] Roh-Johnson M et al. "Triggering a cell shape change by exploiting preexisting actomyosin contractions". In: *Science* 335 (2012), pp. 1232–1235.

[2] Luis Almeida et al. "A mathematical model for dorsal closure". In: *Journal of theoretical biology* 268.1 (2011), pp. 105–119.

[3] Guy B Blanchard, Jocelyn Étienne, and Nicole Gorfinkiel. "From pulsatile apicomedial contractility to effective epithelial mechanics". In: *Current opinion in genetics & development* 51 (2018), pp. 78–87.

[4] Guy B Blanchard et al. "Cytoskeletal dynamics and supracellular organisation of cell shape fluctuations during dorsal closure". In: *Development* 137.16 (2010), pp. 2743–2752.

[5] Guy B Blanchard et al. "Tissue tectonics: morphogenetic strain rates, cell shape change and intercalation". In: *Nature methods* 6.6 (2009), p. 458.

[6] Alan Conrad Bovik, Thomas S Huang, and David C Munson. "The effect of median filtering on edge estimation and detection". In: *IEEE Transactions on Pattern Analysis and Machine Intelligence* 2 (1987), pp. 181–194.

[7] G. Bradski. "The OpenCV Library". In: *Dr. Dobbs Journal of Software Tools* (2000).

[8] G Wayne Brodland et al. "Video force microscopy reveals the mechanics of ventral furrow invagination in Drosophila". In: *Proceedings of the National Academy of Sciences* 107.51 (2010), pp. 22111–22116.

[9] Lucy C Butler et al. "Cell shape changes indicate a role for extrinsic tensile forces in Drosophila germ-band extension". In: *Nature cell biology* 11.7 (2009), p. 859.

[10] Emmanuel Caussinus, Oguz Kanca, and Markus Affolter. "Fluorescent fusion protein knockout mediated by anti-GFP nanobody". In: *Nature structural & molecular biology* 19.1 (2012), p. 117.

[11] Soline Chanet et al. "Actomyosin meshwork mechanosensing enables tissue shape to orient cell force". In: *Nature communications* 8 (2017), p. 15014.

[12] Jonathan S Coravos and Adam C Martin. "Apical sarcomere-like actomyosin contracts nonmuscle Drosophila epithelial cells". In: *Developmental cell* 39.3 (2016), pp. 346–358.

[13] Daryl JV David, Alisa Tishkina, and Tony JC Harris. "The PAR complex regulates pulsed actomyosin contractions during amnioserosa apical constriction in Drosophila". In: *Development* 137.10 (2010), pp. 1645–1655.

[14] Wilhelmine N De Vries et al. "Maternal β-catenin and E-cadherin in mouse development". In: *Development* 131.18 (2004), pp. 4435–4445.

[15] Kai Dierkes et al. "Spontaneous oscillations of elastic contractile materials with turnover". In: *Physical review letters* 113.14 (2014), p. 148102.

[16] Antoine Ducuing and Stéphane Vincent. "The actin cable is dispensable in directing dorsal closure dynamics but neutralizes mechanical stress to prevent scarring in the Drosophila embryo". In: *Nature cell biology* 18.11 (2016), p. 1149.

[17] Julia Duque and Nicole Gorfinkiel. "Integration of actomyosin contractility with cell-cell adhesion during dorsal closure". In: *Development* 143.24 (2016), pp. 4676–4686.

[18] Sabine C Fischer et al. "Contractile and mechanical properties of epithelia with perturbed actomyosin dynamics". In: *PLoS One* 9.4 (2014), e95695.

[19] Andrew W Fitzgibbon, Robert B Fisher, et al. *A buyer's guide to conic fitting*. University of Edinburgh, Department of Artificial Intelligence, 1996.

[20] Bob Goldstein, Steven N Hird, and John G White. "Cell polarity in early C. elegans development". In: *Development* 119.Supplement (1993), pp. 279–287.

[21] Nicole Gorfinkiel and Guy B Blanchard. "Dynamics of actomyosin contractile activity during epithelial morphogenesis". In: *Current opinion in cell biology* 23.5 (2011), pp. 531–539.

[22] Nicole Gorfinkiel et al. "Mechanical control of global cell behaviour during dorsal closure in Drosophila". In: *Development* 136.11 (2009), pp. 1889–1898.

[23] Peran Hayes and Jérôme Solon. "Drosophila dorsal closure: an orchestra of forces to zip shut the embryo". In: *Mechanisms of development* 144 (2017), pp. 2–10.

[24] Irene Hueter. "Formula for the Mean Square Displacement Exponent of the Self-Avoiding Walk in 3, 4 and All Dimensions". In: *arXiv preprint math/0108120* (2001).

[25] Ginger L Hunter et al. "Ion channels contribute to the regulation of cell sheet forces during Drosophila dorsal closure". In: *Development* 141.2 (2014), pp. 325–334.

[26] M Shane Hutson et al. "Forces for morphogenesis investigated with laser microsurgery and quantitative modeling". In: *Science* 300.5616 (2003), pp. 145–149.

[27] DE Ingber, JA Madri, and J Folkman. "A possible mechanism for inhibition of angiogenesis by angiostatic steroids: induction of capillary basement membrane dissolution". In: *Endocrinology* 119.4 (1986), pp. 1768–1775.

[28] Donald E Ingber. "Mechanical control of tissue morphogenesis during embryological development". In: *International Journal of Developmental Biology* 50.2-3 (2003), pp. 255–266.

[29] Aroshan K Jayasinghe et al. "Apical oscillations in amnioserosa cells: basolateral coupling and mechanical autonomy". In: *Biophysical journal* 105.1 (2013), pp. 255–265.

[30] Jeanne N Jodoin et al. "Stable force balance between epithelial cells arises from F-actin turnover". In: *Developmental cell* 35.6 (2015), pp. 685–697.

[31] Jaime Jurado, Joaqun de Navascués, and Nicole Gorfinkiel. "α-Catenin stabilises Cadherin–Catenin complexes and modulates actomyosin dynamics to allow pulsatile apical contraction". In: *J Cell Sci* 129.24 (2016), pp. 4496–4508.

[32] Daniel P Kiehart et al. "Multiple forces contribute to cell sheet morphogenesis for dorsal closure in Drosophila". In: *The Journal of cell biology* 149.2 (2000), pp. 471–490.

[33] Anita T Layton et al. "Drosophila morphogenesis: tissue force laws and the modeling of dorsal closure". In: *HFSP journal* 3.6 (2009), pp. 441–460.

[34] Thomas Lecuit and Pierre-Francois Lenne. "Cell surface mechanics and the control of cell shape, tissue patterns and morphogenesis". In: *Nature reviews Molecular cell biology* 8.8 (2007), p. 633.

[35] Thomas Lecuit, Pierre-François Lenne, and Edwin Munro. "Force generation, transmission, and integration during cell and tissue morphogenesis". In: *Annual review of cell and developmental biology* 27 (2011), pp. 157–184.

[36] Timothy Lenoir. *The strategy of life: Teleology and mechanics in nineteenth century German biology*. Vol. 13. Springer Science & Business Media, 1982.

[37] Thanasis Loupas, WN McDicken, and Paul L Allan. "An adaptive weighted median filter for speckle suppression in medical ultrasonic images". In: *IEEE transactions on Circuits and Systems* 36.1 (1989), pp. 129–135.

[38] Weiwei Luo et al. "Analysis of the local organization and dynamics of cellular actin networks". In: *J Cell Biol* 202.7 (2013), pp. 1057–1073.

[39] Holley E Lynch et al. "Cellular mechanics of germ band retraction in Drosophila". In: *Developmental biology* 384.2 (2013), pp. 205–213.

[40] Xiaoyan Ma et al. "Probing embryonic tissue mechanics with laser hole drilling". In: *Physical biology* 6.3 (2009), p. 036004.

[41] Pedro F Machado et al. "Emergent material properties of developing epithelial tissues". In: *BMC biology* 13.1 (2015), p. 98.

[42] Rohit K Mahajan and Joel D Pardee. "Assembly mechanism of Dictyostelium myosin II: regulation by K+, Mg2+, and actin filaments". In: *Biochemistry* 35.48 (1996), pp. 15504–15514.

[43] Adam C Martin, Matthias Kaschube, and Eric F Wieschaus. "Pulsed contractions of an actin–myosin network drive apical constriction". In: *Nature* 457.7228 (2009), p. 495.

[44] Adam C Martin et al. "Integration of contractile forces during tissue invagination". In: *The Journal of cell biology* 188.5 (2010), pp. 735–749.

[45] Frank M Mason et al. "RhoA GTPase inhibition organizes contraction during epithelial morphogenesis". In: *J Cell Biol* 214.5 (2016), pp. 603–617.

[46] Callie Johnson Miller and Lance A Davidson. "The interplay between cell signalling and mechanics in developmental processes". In: *Nature Reviews Genetics* 14.10 (2013), p. 733.

[47] Callie J Miller et al. "Emergent mechanics of actomyosin drive punctuated contractions and shape network morphology in the cell cortex". In: *PLoS computational biology* 14.9 (2018), e1006344.

[48] Démosthene Mitrossilis et al. "Mechanotransductive cascade of Myo-II-dependent mesoderm and endoderm invaginations in embryo gastrulation". In: *Nature communications* 8 (2017), p. 13883.

[49] Akankshi Munjal et al. "A self-organized biomechanical network drives shape changes during tissue morphogenesis". In: *Nature* 524.7565 (2015), p. 351.

[50] Edwin Munro, Jeremy Nance, and James R Priess. "Cortical flows powered by asymmetrical contraction transport PAR proteins to establish and maintain anterior-posterior polarity in the early C. elegans embryo". In: *Developmental cell* 7.3 (2004), pp. 413–424.

[51] Masatoshi Nishikawa et al. "Controlling contractile instabilities in the actomyosin cortex". In: *Elife* 6 (2017), e19595.

[52] Hiroki Oda and Shoichiro Tsukita. "Real-time imaging of cell-cell adherens junctions reveals that Drosophila mesoderm invagination begins with two phases of apical constriction of cells". In: *Journal of cell science* 114.3 (2001), pp. 493–501.

[53] Stefano Piccolo. "Developmental biology: Mechanics in the embryo". In: *Nature* 504.7479 (2013), p. 223.

[54] Xiang Qin et al. "A biochemical network controlling basal myosin oscillation". In: *Nature communications* 9.1 (2018), p. 1210.

[55] Matteo Rauzi, Pierre-François Lenne, and Thomas Lecuit. "Planar polarized actomyosin contractile flows control epithelial junction remodelling". In: *Nature* 468.7327 (2010), p. 1110.

[56] Matteo Rauzi et al. "Embryo-scale tissue mechanics during Drosophila gastrulation movements". In: *Nature communications* 6 (2015), p. 8677.

[57] Matteo Rauzi et al. "Physical models of mesoderm invagination in Drosophila embryo". In: *Biophysical journal* 105.1 (2013), pp. 3–10.

[58] François B Robin et al. "Excitable RhoA dynamics drive pulsed contractions in the early C. elegans embryo". In: *BioRxiv* (2016), p. 076356.

[59] Laure Saias et al. "Decrease in cell volume generates contractile forces driving dorsal closure". In: *Developmental cell* 33.5 (2015), pp. 611–621.

[60] Guillaume Salbreux, Guillaume Charras, and Ewa Paluch. "Actin cortex mechanics and cellular morphogenesis". In: *Trends in cell biology* 22.10 (2012), pp. 536–545.

[61] Anne Scuderi and Anthea Letsou. "Amnioserosa is required for dorsal closure in Drosophila". In: *Developmental dynamics* 232.3 (2005), pp. 791–800.

[62] Gordon Slade. "Self-avoiding walks". In: *The Mathematical Intelligencer* 16.1 (1994), pp. 29–35.

[63] Marina Soares e Silva et al. "Active multistage coarsening of actin networks driven by myosin motors". In: *Proceedings of the National Academy of Sciences* 108.23 (2011), pp. 9408–9413. ISSN: 0027-8424. DOI: 10.1073/pnas.1016616108. eprint: https://www.pnas.org/content/108/23/9408.full.pdf. URL: https://www.pnas.org/content/108/23/9408.

[64] Jerome Solon et al. “Pulsed forces timed by a ratchet-like mechanism drive directed tissue movement during dorsal closure”. In: *Cell* 137.7 (2009), pp. 1331–1342.

[65] Angughali Sumi et al. “Adherens junction length during tissue contraction is controlled by the mechanosensitive activity of actomyosin and junctional recycling”. In: *Developmental cell* 47.4 (2018), pp. 453–463.

[66] DARI Sweeton et al. “Gastrulation in Drosophila: the formation of the ventral furrow and posterior midgut invaginations”. In: *Development* 112.3 (1991), pp. 775–789.

[67] Andrea Valencia-Expósito et al. “Myosin light-chain phosphatase regulates basal actomyosin oscillations during morphogenesis”. In: *Nature communications* 7 (2016), p. 10746.

[68] Qiming Wang, James J Feng, and Len M Pismen. “A cell-level biomechanical model of Drosophila dorsal closure”. In: *Biophysical journal* 103.11 (2012), pp. 2265–2274.

[69] Shicong Xie and Adam C Martin. “Intracellular signalling and intercellular coupling coordinate heterogeneous contractile events to facilitate tissue folding”. In: *Nature communications* 6 (2015), p. 7161.

[70] PE Young et al. “Morphogenesis in Drosophila requires nonmuscle myosin heavy chain function.” In: *Genes & development* 7.1 (1993), pp. 29–41.

[71] Jian Zhou, Hye Young Kim, and Lance A Davidson. “Actomyosin stiffens the vertebrate embryo during crucial stages of elongation and neural tube closure”. In: *Development* 136.4 (2009), pp. 677–688.